

Advancement and Applications of the Template Matching Approach to Indexing Electron Backscatter Patterns

Alexander James Foden

Imperial College London

Department of Materials

This thesis is submitted for the degree of

Doctor of Philosophy

December 2020

1 Statement of Originality

I declare that all work contained in this document is my own work and that any work that is not my own is appropriately referenced. Figures referenced from another source are appropriately referenced and reproduced under licence from their respective copyright owners

2 Copyright Statement

The copyright of this thesis rests with the author. Unless otherwise indicated,

its contents are licensed under a Creative Commons Attribution-Non

Commercial 4.0 International Licence (CC BY-NC).

Under this licence, you may copy and redistribute the material in any medium

or format. You may also create and distribute modified versions of the work.

This is on the condition that: you credit the author and do not use it, or any

derivative works, for a commercial purpose.

When reusing or sharing this work, ensure you make the licence terms clear to

others by naming the licence and linking to the licence text. Where a work has

been adapted, you should indicate that the work has been changed and

describe those changes.

Please seek permission from the copyright holder for uses of this work that are

not included in this licence or permitted under UK Copyright Law

3 Acknowledgements

Firstly, I would like to thank my supervisor Dr. Ben Britton for his endless patience, support encouragement and friendship throughout my time here at Imperial College. I will be eternally grateful to him for seeing me through this PhD.

I would like to thank all for the members of the experimental micromechanics group, past and present, for their help and support. In particular: Vivian, Jim, Simon, Tom, Yi and Ruth.

Thank you to everyone in the Engineering Alloys theme. To Yi Cui and Chris Gourlay for their discussions and data regarding pseudosymmetry and the Friday meeting crew. And to Abigail Ackerman for introducing me to Ben.

In the wider community, thank you to Angus Wilkinson and David Collins for co-authoring my first paper, and for guidance throughout the process. To Aimo Winkelmann for multiple discussions regarding EBSD. And my viva examiners, Katharina Marquardt, Alex Eggeman and Luc Vandeperre for their helpful discussions and suggestions. These have vastly improved my thesis.

I am indebted to Mahmoud Ardakani for teaching me how to use the Quanta, to Ben Wood for all his technical support in the lab and to Michael Lennon for his help in the development of the direct electron detector stage.

I would like to thank my girlfriend, Diana Neves and her parents Jorge and Fatima for putting up with me and giving me a home whilst in London.

Finally thank you to my parents, Bev and Simon. They have been endlessly loving and supportive in every endeavour I have attempted. I am truly lucky to be their son.

4 Dedication

I would like to dedicate this thesis to my parents, Bev and Simon.

5 Contents

Statement of Originality.....	i
Copyright Statement.....	ii
Acknowledgements.....	iii
Dedication.....	iv
Contents.....	v
List of Figures.....	viii
List of Tables.....	xv
Abstract.....	1
1 Introduction.....	2
1.1 EBSD: A Brief History.....	7
1.2 In this Thesis.....	9
2 Literature Review.....	12
2.1 EBSD Geometry.....	13
2.1.1 Coordinate Systems in Electron Backscatter Diffraction.....	13
2.1.2 Pattern Centre.....	15
2.1.3 Projections of a sphere.....	19
2.2 Simulated Kikuchi Patterns.....	22
2.2.1 Kinematic vs Dynamical Simulation.....	23
2.2.2 Dynamical Simulations.....	24
2.3 The Radon and Hough Transforms.....	33
2.4 Cross-Correlational Methods.....	36
2.4.1 Library Generation for Cross-Correlational Methods.....	38
2.5 Representations of Orientation.....	44
2.5.1 Rotation Matrices.....	45
2.5.2 Euler Angles.....	47
2.5.3 Axis-Angle Pairs.....	48
2.5.4 Rodrigues Vectors.....	49
2.5.5 Quaternions.....	50
2.5.6 Switching Between Orientation Representations.....	51
2.5.7 Advantages and Disadvantages.....	53
2.5.8 Phase Classification Using Electron Backscatter Diffraction.....	56
2.5.9 Detectors.....	61

3	Development and Testing of the Refined Template Matching Algorithm.....	69
3.1	Introduction	69
3.2	Method Overview	73
3.3	Image Cross Correlations	75
3.3.1	Normalised Dot Product	75
3.3.2	Fast Fourier Transform.....	76
3.4	SO(3) Library Generation	78
3.4.1	SO(3) Spacing	79
3.4.2	SO(3) Sampling Frequency	85
3.4.3	SO(3) Library Size and Computational Costs.....	90
3.5	Orientation and Pattern Centre Refinement	92
3.6	Demonstrations	98
3.6.1	Si Single Crystal:	98
3.6.2	Deformed α -Fe Dataset.....	102
3.7	Chapter Summary	105
4	Phase Characterisation Using the Refined Template Matching Approach.....	107
4.1	Introduction	107
4.2	Methodology.....	108
4.3	Phase Classification of a Dual Phase Material	108
4.3.1	Mixed Patterns with an associate Orientation Relationships.....	108
4.3.2	Different Crystal Structures	111
4.4	Experimental Demonstrations	114
4.4.1	Robust Pattern Matching for Phase Classification - Error Analysis.....	116
4.4.2	Phase Contrast	118
4.4.3	Comparison with the Phase Confidence Metric	125
4.5	Chapter Summary	127
5	Application of the Refined Template Matching Approach to Pseudosymmetry.....	129
5.1	Al ₁₃ Fe ₄ Unit Cell	131
5.2	Reference Frames	134
5.3	Representing the Orientation of the Unit Cell	135
5.4	Resolving Pseudosymmetry with Pattern Matching.....	137
5.5	Electron diffraction pseudosymmetries.....	139
5.6	Indexing EBSD Data	144
5.7	Summary	148
6	Direct Electron Detection with a Fixed Detector Angle Stage	149
6.1	Introduction	149

6.2	The Stage.....	150
6.2.1	Stage Design.....	151
6.3	Detector Testing.....	157
6.3.1	Modulation Transfer Function	157
6.3.2	Pattern Centre Determination	158
6.4	Detector exposure	161
6.5	Map reconstruction	167
6.6	Chapter Summary	169
7	Discussion.....	170
8	Conclusions and Future Work.....	180
8.1	Future Work.....	183
8.1.1	The Refined Template Matching.....	183
8.1.2	Phase Characterisation with the RTM.....	184
8.1.3	Pseudosymmetry with the RTM.....	184
8.1.4	Direct Electron Detector Stage	185
9	References	186
	Appendix 1	205

6 List of Figures

Figure 1: Schematic of the standard EBSD setup within the SEM. Reproduced from [2]	2
Figure 2: the typical interaction volume of the incident electron beam and the sample, adapted from [3]	3
Figure 3: The sources of A) secondary and B) backscattered electrons. Adapted from [3]	4
Figure 4: A) A typical EBSP, in this case a single crystal silicon pattern. And B) a line scan of the intensities of the pixels along the blue line indicated in A). The bands are shown as bumps of raised intensity in a smoothly varying background in the form of a gaussian.	5
Figure 5: A) A simulated, unrotated silicon EBSP showing the horizontal {100} plane in green and the vertical {001} plane. And B) the way these bands are projected from the unit cell. Note the red band is parallel to the red face, and the green, parallel to the green face.	6
Figure 6: A) An electron backscatter pattern as captured from a conventional detector. B) the background of the pattern and C) the pattern with the background removed. The bands indicated by green arrows are now visible, along with two HOLZ rings (Red arrows). D) Is a simulated pattern of the same patter, the HOLZ rings are missing due to the simulation software used.	13
Figure 7: The different coordinate systems in EBSD (reproduced from [36]). A) Shows the Gnomonic frame on the detector frame. B) shows the experimental set up, i.e. the tilt of the sample and detector frames and C) shows the same as a cross section.	15
Figure 8: The experimental set up and schematic of a shadow casting experiment. Figure adapted from [13]	16
Figure 9: Experimental set up of a retraction experiment. z^* is the distance between the in position and the source point, and S is the camera displacement. This figure is similar to the derivation in [44].	19
Figure 10: The gnomonic plane shown diagrammatically. Both points P_1 and P_2 will map to point P in the gnomonic frame. Figure adapted from [51]	21
Figure 11: The stereographic projection shown diagrammatically, adapted from [51].	22
Figure 12: A) A Kinematic and B) a dynamic simulation of an orientation of Ferrite. Both images taken from the DynamicS software using standard settings.	23
Figure 13: Elements in a crystal lattice needed for Bragg's law to apply. From [54]	24
Figure 14: The "random walk" of an electron in the crystal. This also shows the disconnect between the incident and outgoing electrons described in [52] that allows us to treat incoming and backscattered electrons independently.	25
Figure 15: Because of the reciprocity principle, in a) the red point emitting D, is equivalent to b) where D enters the lattice and works back to point P. (Reproduced from [52]). (Reprinted by permission from Springer Nature: Springer eBook Electron Backscatter Diffraction in Material Science by R. A. Schwarzer, D. P. Field, B. L. Adams COPYRIGHT (2009))	26
Figure 16: The probability density of an electron being diffracted from a given point in a lattice at pixels a, b, c, d and e. Here light areas show high probability of diffraction (reproduced from [52]). (Reprinted by permission from Springer Nature: Springer eBook Electron Backscatter Diffraction in Material Science by R. A. Schwarzer, D. P. Field, B. L. Adams COPYRIGHT (2009))	32
Figure 17: Flowchart reproduced from [1] showing the standard method for indexing an EBSP. (Reprinted from Materials Today, 15, A. J. Wilkinson, T. B. Britton, Strains, Planes and EBSD in materials science, 366-378, Copyright (2012), with permission from Elsevier)	34
Figure 18: Two graphs reproduced from [37] showing the Hough/Radon transform. A) Shows a line plotted in Cartesian polar coordinates, defined as $\rho = x\cos(\theta) + y\sin(\theta)$. And B) the same line represented as a point in Hough/Radon space. (Reprinted by permission from Springer Nature:	

Springer eBook Electron Backscatter Diffraction in Material Science by R. A. Schwarzer, D. P. Field, B. L. Adams COPYRIGHT (2009))	35
Figure 19: reproduced from [40] showing the use of the Hough transform, and demonstrating the butterfly wing effect. Reproduced with permission of Taylor and Francis Group LLC (Books) US through PLSclear from Introduction to Texture Analysis Macrotexture, Microtexture, and Orientation Mapping, Second Edition by O. Engler and V. Randle.	36
Figure 20: The 14 Bravais lattices reproduced from [40]. The symmetries of these lattices will determine the size of the library that is needed for the generation of the library. Reproduced with permission of Taylor and Francis Group LLC (Books) US through PLSclear from Introduction to Texture Analysis Macrotexture, Microtexture, and Orientation Mapping, Second Edition by O. Engler and V. Randle.	39
Figure 21: The basis vectors for a unit cell. Reproduced from [36].	40
Figure 22: The point group symmetry of a cube. Here the n-fold rotation axis is denoted with An and the mirror planes are shown by dashed lines labelled m. There is also a point of inversion at the centre of the cell. Reproduced from [79]. Reproduced with permission from Prof. S. A. Nelson.	41
Figure 23: The fundamental zone for a cubic cell in Rodrigues space shown as a wire frame (adapted from [5])	42
Figure 24: A) The passive rotation of an axis, (x, y) , about a vector, r , by angle θ to the new axis, (x', y') . B) The active rotation of vector, r , by the same angle to r'	45
Figure 25: The original axis, (x, y) and axis rotated about angle θ to (x', y') . The point p is the endpoint of the vector being passively rotated. (Adapted from [83]).	46
Figure 26 The Euler rotation for angles (ϕ_1, Φ, ϕ_2)	47
Figure 27: Graphical representation of an axis angle rotation about an arbitrary vector (r) by angle θ	49
Figure 28: A vector pre and post rotation. Reproduced with permission of Oxford Publishing Limited through PLSclear. From Interfaces in Crystalline Materials by A. P. Sutton and R. W. Balluffi	52
Figure 29: A typical EDX spectrum. Reproduced from [96]	59
Figure 30: Two distinct but pseudosymmetrically equivalent orientations for $Al_{13}Fe_4$ (A and B) and their dynamical simulations (C and D).	60
Figure 31: Cartoon of the cross section of a typical EBSD detector. Figure reproduced from [106]. (Reprinted from Ultramicroscopy, 111, K. Mingard, A. Day, C. Maurice, P. Quedest, Towards high accuracy calibration of electron backscatter diffraction systems, 320 - 329, Copyright (2011), with permission from Elsevier)	61
Figure 32: Cartoon of the cross-section of a DED (adapted from [111])	63
Figure 33: A schematic of a Timepix 2 pixel, reproduced from [112]. (Reprinted from Nuclear Instruments and Methods in Physics Research Section A: Accelerators, Spectrometers, Detectors and Associated Equipment, 581, X. Llopart, R. Ballabriga, M. Campbell, L. Tlustos, W. Wong, Timepix, a 65k programmable pixel readout chip for arrival time, energy and/or photon counting measurements, 485 - 494, Copyright (2007), with permission from Elsevier)	64
Figure 34: The black line shows an experimental edge function with the red dashes showing an idealised step function. Figure adapted from [117]	65
Figure 35: A) An initial input gaussian. This curve stays stationary and is the reference about which the shifted gaussians are compared. B) 5 examples of mean or phase shifted gaussians. C) The correlation coefficients of the NDP of the shifted vs reference gaussian in real and Fourier space. ...	72
Figure 36: A reference EBSD generated with Euler angles $(15^\circ, 20^\circ, 25^\circ)$, a close match with Euler angles $(15^\circ, 19^\circ, 24^\circ)$ and a far match with Euler angles $(63^\circ, 55^\circ, 30^\circ)$. The 2D Fourier transforms are shown below the respective inputs, and the correlation coefficients below the label. For each simulation the PC is (0.5, 0.3, 0.6) and the material simulated is Ferrite.	73

Figure 37: The template matching method follows the following steps: A) An experimental pattern is imported for indexing. B) A library of templates is searched using an XCF to determine the orientation in SO(3) space (the 3D-rotation group) closest to the experimental pattern (C). D) The best orientation is refined to match the experimental orientation.	74
Figure 38: The gnomonic projections for a rectangular screen for PC = (0.5,0.5,0.5) for A) no rotation, B) rotation about x, C) rotation about y and D) rotation about z. A rectangular screen has been used to show the distortion of the screen and pattern in the Stereographic projection. The blue segments in the stereographs are the shadows of the screen.	79
Figure 39: A) The distribution of misorientations for a 10° sampling frequency. (B) the maximum, mean and mode distributions of similar histograms at varying sampling frequencies. Both figures are for cubic symmetry.	82
Figure 40: Pole figures of a cubic library for a sampling frequency of 10° and 5° and hexagonal and monoclinic unit cells with a sampling frequency of 10°. These show the S2 space is well sampled and the S1 is less so.	84
Figure 41 A) Rotation of a generated pattern, show here for the sample y axis. B) correlation coefficients for the NDP and FFT methods from rotations about the sample axes.	87
Figure 42: A, B and C) The FWHM recorded for a shift in PC (ΔPC) in the x, y and z directions respectively. The screen is 500 x 500 pixels for each of these graphs, with the initial PC = (0.5, 0.3, 0.6). D) Varying the screen size; a screen size of 128 is labelled to identify where the FFT becomes stable for the PC set to (0.5, 0.3, 0.6).	89
Figure 43: The time taken to index a single pattern for the NDP (blue) and the FFT (orange) is shown in A. B shows the time taken to complete the SO(3) search. This, in turn is dependent on the number of images in the library to search through, as is shown in A, B, D and E. As the FFT uses a significantly reduced library size, it is able to index patterns significantly more quickly than the NDP. Figures C and F show the relationship between the time to index a single pattern with respect to the sampling frequency, and C the Log of the sampling frequency vs the log of the time taken. D, E and F show the same for memory usage instead of time. On all graphs, the dashed vertical lines show the respective positions the NDP and FFT libraries occupy.	91
Figure 44: A) A rotation of the crystal becomes a shift in the EBSD pattern. B) As I have the shift in x or y, or in the PC and I know the detector distance, trigonometry can be used to correct for a PC discrepancy should one occur. Finally, Z is corrected as shown in C. C) To determine the z rotation, the EBSD is transformed into log polar space, where a shift in y translates to a rotation about z in real space.	94
Figure 45: A and C show the difference between the generated data and the indexed data for the NDP and the FFT respectively. They show the misorientations after the SO(3) search, a single refinement and the iterated refinement used in this method. B and D show the distribution of misorientations between the indexed and generated data. The distribution for the SO(3) search has been omitted as it makes the single and iterated distributions unreadable.	96
Figure 46: The accuracy of the pattern matching approach a series of EBSPs related to a random set of orientations was generated and the misorientations of the indexed and generated patterns calculated for the NDP and FFT, A and B respectively. From B, it is seen that, using the refined FFT pattern mating approach, an accuracy or $<0.2^\circ$ is possible,	97
Figure 47: Surface maps showing the orientation of small single crystal silicon for Hough (A and B) and FFT pattern matching (C and D) to demonstrate the precision of the pattern matching approach. The coloured orientation maps are shown with respect to the macroscopic X and Z axes. E and G show the misorientation with respect to the central pattern in the map. I shows the distribution of the misorientations shown in E and G. H shows the peak height from the FFT for each point in the map, this can act as an error metric similar to the image quality in the Hough. J shows the captured	

image, cropped and background corrected (a) and the pattern indexed with the refined method (b). The red x on the map in A shows the location from which the pattern was extracted.	100
Figure 48: Surface maps showing the orientation of small single crystal silicon for Hough (A and B) and FFT pattern matching (C and D) to demonstrate the precision of the pattern matching approach. E and G show the misorientation with respect to the central pattern in the map. I shows the distribution of the misorientations shown in E and G. H shows the peak height from the FFT for each point in the map, this can act as an error metric similar to the image quality in the Hough. J shows the captured image, cropped and background corrected (a) and the pattern indexed with the refined method (b). The red x on the map in A shows the location from which the pattern was extracted.	101
Figure 49: Orientation maps of a deformed α -Fe sample, showing the sensitivity of the pattern matching approach (A, B, C and D). E shows the misorientation with respect to Hough as a rough guide to the accuracy of the pattern matching approach, and the distributions of the misorientations are shown in G. F shows the FFT peak heights as a map, analogous to the IQ in the Hough and H shows the distribution of the peak heights. This histogram can be used to determine where the cut off for incorrectly indexed patterns should be. I shows a) The captured image, cropped and background corrected and B the pattern indexed with the refined method. The red x on the map in A shows the location from which the pattern was extracted.	104
Figure 50: Mixed patterns showing the linear mixing of α -Ti and β -Ti patterns for varying percentages of mixing.	109
Figure 51: The correlation coefficient as a function of the α -Ti as a percentage of the pattern for each of the 12 ORs. Results show the CC for the α and β libraries, with the 50% pattern mix indicated with a vertical line.	110
Figure 52: Graphs showing the CC for the top 5% of SO(3) library searches that have been refined against the correct and incorrect libraries for the pattern. The misorientation shown, is the misorientation between the known and correct orientation and the orientation associated with the CC returned. Graph A shows the results for an α -Ti pattern vs an β -Ti library. B is the same pattern vs an α -Ti library and a β -V library. C) shows an Austenitic pattern vs an Austenite and a Ferrite library. And D shows a FCC Cu pattern vs an FCC Cu and FCC Ag library. In all cases the least misorientated CC is the highest. Peaks at higher angles of misorientation show either symmetric or pseudosymmetric orientations of the correct orientation. This suggests the refined template matching can be used to differentiate all three cases of differing phase tested.	113
Figure 53: The dual phase titanium map for, A, the Hough based indexing and B the refined template matching approach. The α and β correlation coefficients for each point are shown in C and D respectively. The red point in A shows the location the pattern in E has been taken from, with F and G showing the indexed patterns with the α and β libraries respectively. Bands of interest in E, F and G are highlighted in an orange dashed line.	115
Figure 54: The results of matching an α -titanium pattern against A) an α -titanium library and B) a β -titanium library and a β -titanium pattern against C) an α -titanium library and D) a β -titanium library.	121
Figure 55: The normalised correlation coefficients for an α titanium pattern library search plotted against A: an α titanium library, B: a β titanium library and C: both libraries. C also shows the locations of the two best matches from the library search. The alpha library is shown to have a better match due to the pattern being further along the x axis.	122
Figure 56: A) An Argus image of the titanium map, with B) the same map as in Figure 53 with the points marked as red below the threshold value	123
Figure 57: A and B show 3-D histograms of the contrast against the CC of a given library for indexing. The contrast is calculated as in Equation 59, with χ_{1i} as the α library for A and β for B. The colours show the number of points in each bin at a given point. The red boxes show the regions that are	

removed within a contrast threshold of 0.1 as read from the base of the large clump in A. The area inside the green highlighted section show points with a high contrast and that have a CC above a threshold of 0.5 for the α library and orange boxes show the same for β . C and D show the phase maps for the contrast threshold and the contrast and CC threshold determination methods respectively. 125

Figure 58: Maps showing the phase confidence described in Equation 60. Map A shows the phase confidence for the initial library search in SO(3) space for an alpha library and B) shows the same for a beta library. The top M patterns from the initial search were then refined and the phase confidence calculated again for the refined step and are shown in map C for the alpha library and D for the Beta. 126

Figure 59: Two patterns exhibiting pseudosymmetry are shown in A and B, with annotations of similar and different features shown in C and D. All highlighted bands would be indistinguishable to the Hough method of indexing. The red highlighted bands are split bands, where the band width and relative intensity differentiate them. The orange circles show the HOLZ rings. 130

Figure 60: An $\text{Al}_{13}\text{Fe}_4$ unit cell, the associated atomic positions and how they relates to the sample frame. 131

Figure 61) The EBSD and respective unit cells for A) $\text{Al}_{13}\text{Fe}_4$ and B) Si in a pseudosymmetric configuration. All of the bands highlighted in A) have a corresponding band in B and it is this symmetry between the two patterns I take advantage of in the modified indexing algorithm. 134

Figure 62: A) The sample plane shown as a circle around a unit cell. The axes show the sample frame and the unit cell frame. The projection of the EBSD in the gnomonic frame is also shown. And B) the rotation (α) about the X axis shared between the sample and gnomonic frames to switch between the two. 135

Figure 63: The controlled rotation and representation of a unit cell for $\text{Al}_{13}\text{Fe}_4$. For the (-30,-10,60) rotation green cross represents the C axis in the positive hemisphere. 136

Figure 64: The modified refined template matching to account for pseudosymmetry. A reduced library is first generated and used to get an initial orientation. This is taken as a starting point and symmetrically equivalent rotations are applied and tested. The best match is taken to be the correct orientation 139

Figure 65: Pole figures showing the full SO(3) library (this is showing a sampling frequency of 8° due to the time needed to plot the full 5° SO(3), however as this is a demonstration, this is sufficient), and initial seed orientation. The results of the first search and thresholding, the refinement and the final result of the first iteration showing a new seed point. 141

Figure 66: The distribution of the correlation coefficients found in A) the initial search of the whole fundamental zone and b) the distributions of the CCs after the refinement of patterns above the cut off value. 142

Figure 67: The electron diffraction symmetries for an input pattern and their respective correlation coefficients. 143

Figure 68: A demonstration of the spread of the symmetric orientations. A) The input pattern leads to an incorrect orientation from B) the sparse library search but is corrected to C) a pattern that matches. The Histogram (D) shows the distribution of the electron diffraction equivalents tested and highlights the main and pseudosymmetric peaks of the distribution. E) Example matches are shown along with their corresponding correlation coefficients. The patterns are labelled such that the peaks they relate to in the histogram are shown. 144

Figure 69: The results of indexing two patterns, the simulated patterns with band overlays are shown for the orientation the indexing returned along with the unit cubes that formed each pattern. The 5 pole figures show the overlapping and similar planes for each pattern, points on the pole figure marked by a black circle are from pattern one and those with a pink x are from pattern two. The axis

shown to the left of the pole figures is the axis for the pole figures and also the sample frame for the unit cubes plotted.	145
Figure 70: The results of indexing the red segment shown in the backscatter image. The habit plane (plane shared between the two orientations) is shown as an orange dashed line . The Hough matching is shown as an indication of the improvement the modified refined template approach has made. The correlation coefficient map supports the smoothness of the refined map and the pole figure is included for completeness.	147
Figure 71: The Timepix 2 detector used throughout this chapter. The detector is covered by a protective screen that is slid out of the way when the detector is in use. The ruler is included as a scale for the detector.	150
Figure 72: The fixed angle direct electron detector set up with a camera at a fixed angle with respect to the sample. The camera will be able to advance and retract upon the sample, which should be able to move in the sample X/Y plane. The whole assembly will also be able to move in the microscope X/Y/Z planes because of the movement of the microscope stage. The black, solid arrows show the coordinate systems as used throughout this thesis. The red unfilled arrows show the directions of movement of the stage	151
Figure 73: Digital CAD renderings of o A) the SmarAct sample x/y stage and B) the detector z stage	152
Figure 74: CAD rendering of the designed DED stage, with) overview of the stage with key parts... 154	
Figure 75A) And example pattern used to obtain an example MTF, shown in B. The line in B is likely not smooth due to the line in A not being entirely straight.	158
Figure 76: The graphs of A) The PCX B) the PCY and C) the PCZ locations at each retraction. And examples of patterns at various points in the retraction.	159
Figure 77: Example pattern with elliptical shadows from ball bearings suspended between the Si sample and the detector. Note the overlaid ellipses misalign with the elliptical shadows due to there being too little of the ellipse showing on the pattern.	161
Figure 78: The collection time of patterns 1-5 and the example patterns 1-5. The red bars indicate time when the detector is capturing an image and the space in between is the associated overhead with each pattern collected.	163
Figure 79: The correlation coefficient with respect to the collection time.	164
Figure 80: Rows 1 and 2 show the patterns as collected from the detector and the background corrected patterns respectively. The intensities of the pixels in each of the patterns were taken and rows 3 and 4 show the histograms of the collected and the background corrected patterns respectively. Rows 5 and 6 show the FFTs of the collected and background corrected patterns respectively. The horizontal and vertical bands prominent in each FFT in row 5 are an artefact from the fact that the patterns are not periodic. Finally, row 7 shows the background of each pattern. A simulated pattern, histogram and FFT have been included as a reference.	165
Figure 81: A line scan perpendicular to the {220} band and running along the {311} band, marked by a red line on the EBSDP.	166
Figure 82: The IPF maps for a single crystal of Si in the A) x, B) y, with the location of the experimental point, and C) z directions and D a map showing the correlation coefficients of each point. A pattern from E) the detector and F) the result of the indexing taken from the red circle on the IPF y map. And finally G) the unit cell orientation.....	168
Figure 83: The standard, pseudosymmetry and phase classification branches of the refined template matching approach.	180
Figure 84: The point D , which is a point on the pattern, with respect to the PC and the unit sphere. Important points and vectors are labelled.	205

7 List of Tables

Table 1: The advantages and disadvantages of each representation of rotation.	53
Table 2: Examples of the three ways in which a crystal lattice can differ	111
Table 3: The properties for the simulation used in DynamicS.....	119
Table 4: Atomic Coordinates of the $\text{Al}_{13}\text{Fe}_4$ unit cell, taken from DynamicS	132
Table 5: The time and memory requirements and number of patterns indexed in each of the demonstrative maps.	173

8 Abstract

Electron backscatter diffraction is a well-established characterisation technique used to determine the orientation and crystal phase of a crystalline material. A pattern is formed by dynamical interaction of electrons with the crystal lattice, which can be understood and simulated by using Bloch wave theory. The conventional method of indexing a diffraction pattern is to use a Hough transform to convert the lines of the pattern to points that are easily accessible to a computer. As the bands of the pattern are direct projections of the crystal planes, the interplanar angles can then be computed and compared to a look up table to determine phase and orientation. This method works well for most examples, however, is not well suited to more complex unit cells, due to the fact it ignores more subtle features of the patterns. This thesis proposes a refined template matching approach which uses efficient pattern matching algorithms, such as those used in the field of computer vision, for phase determination and orientation analysis. This thesis introduces the method and demonstrates its efficacy, as well as introducing advanced methods for pseudosymmetry analysis and phase mapping. A new metric for phase confidence is also proposed and the refined method is shown to be able to correctly determine phases and pseudosymmetric orientations. Finally, preliminary work on a direct electron detector stage is presented. Work on the development, testing the pattern centre reliability, modulation transfer and an example map is shown.

9 Introduction

Electron Backscatter Diffraction (EBSD) is a technique used in a scanning electron microscope (SEM) in the material and geological sciences to measure the crystal orientation, grain shape, size, strain and phase distributions in crystalline materials.

In the SEM, a high voltage (typically 5 – 30 keV) electron beam is focused and scanned across the surface of a highly tilted sample, see Figure 1 [1].

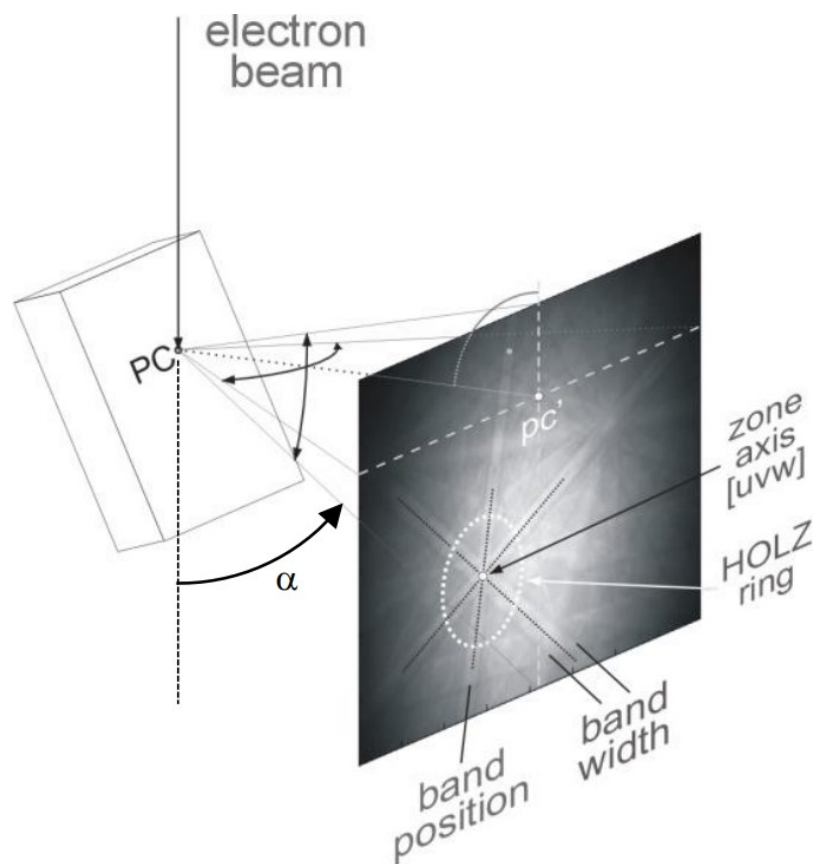


Figure 1: Schematic of the standard EBSD setup within the SEM. Reproduced from [2]

At each point on the sample, the electrons interact with the atoms of the lattice that fall within the interaction volume of the beam, shown in Figure 2. These interactions produce secondary electrons (SE) and backscattered electrons (BSE) [3] .

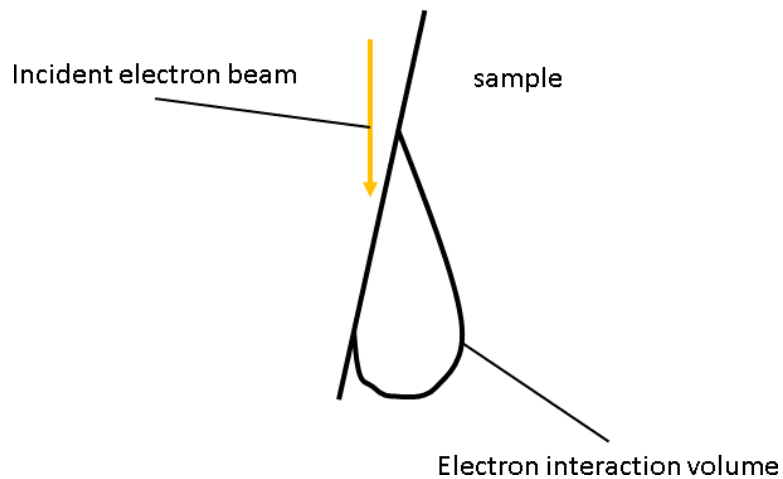


Figure 2: the typical interaction volume of the incident electron beam and the sample, adapted from [4]

A SE comes from the primary beam hitting an atom and dislodging an electron. These electrons are usually low energy. SE formation is shown in *Figure 3*.

The BSEs are the high energy electrons that have interacted in a near elastic manor with the lattice, see *Figure 3* [3]. The BSEs created from the incident beam create a source point inside the lattice. If the interactions of the BSEs from this source point meet Braggs law, the electron is diffracted and an EBSP is formed. An EBSP consists of bands of raised intensity and a smoothly varying background (primarily, the background is composed of non-diffracting BSEs), see *Figure 4*. The bands of raised intensity are usually the focus of an EBSD experiment and, as such, the background is usually removed. The removal of the background is referred to as background correction for this thesis.

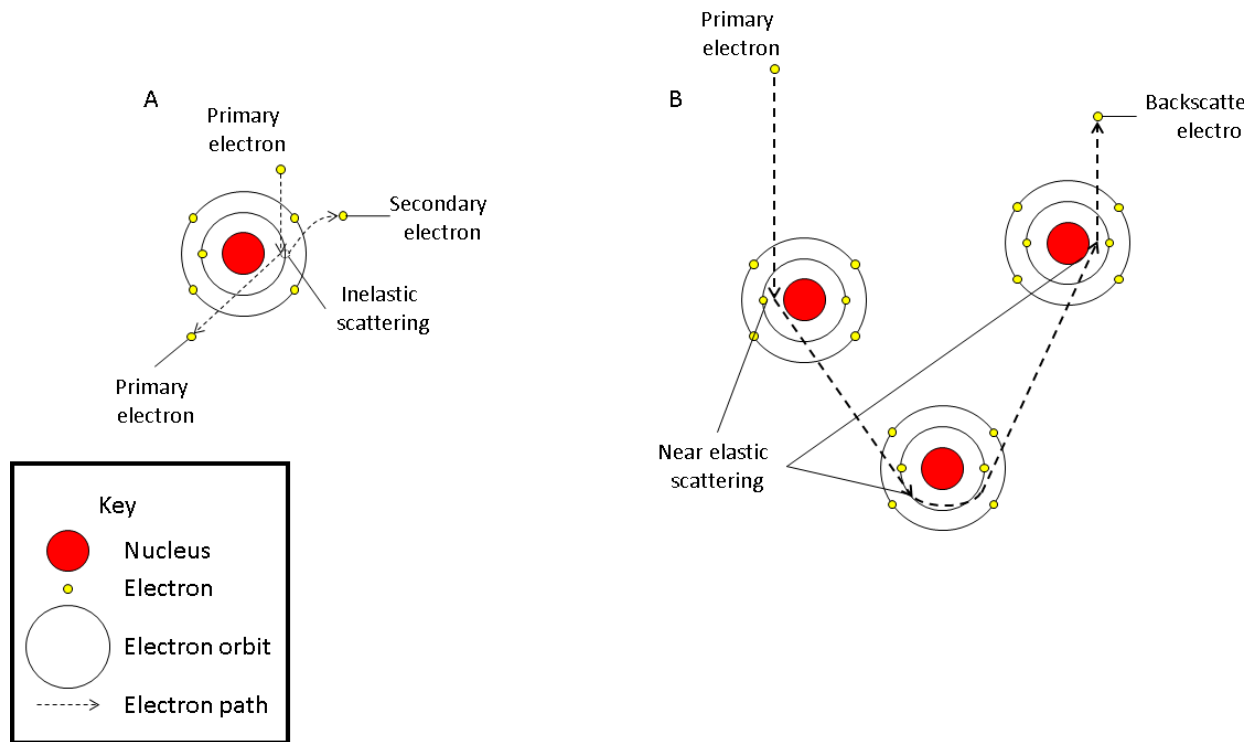


Figure 3: The sources of A) secondary and B) backscattered electrons. Adapted from [3]

Correction of the background is a relatively simple process. The energy spectrum of the whole EBSD, and therefore the intensities of the pixels, follow a mostly gaussian curve with short spikes of raised intensity representing the main bands of the EBSD, this can be seen in Figure 4. As we know how the gaussian behaves, dividing the EBSD by a gaussian curve will remove the background [5].

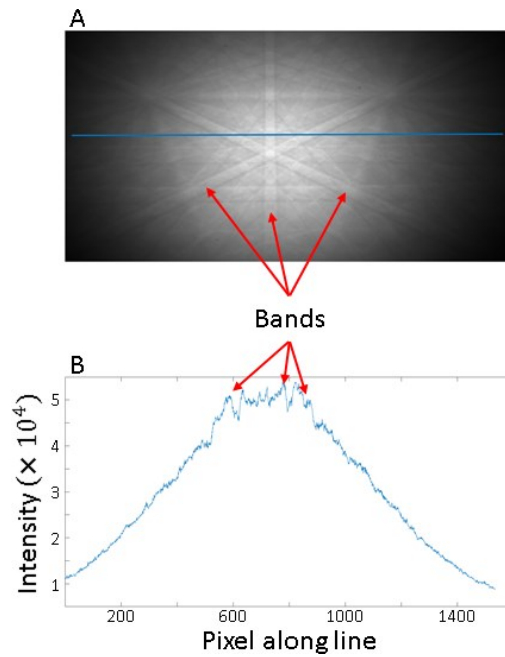


Figure 4: A) A typical EBSD, in this case a single crystal silicon pattern. And B) a line scan of the intensities of the pixels along the blue line indicated in A). The bands are shown as bumps of raised intensity in a smoothly varying background in the form of a gaussian.

Analysis of an EBSD is typically carried out using a Hough transform (or the related Radon transform), which converts the bands of raised intensity to points of raised intensity. These points of raised intensity are more easily identified by a computer. This is important because, due to the nature of the diffraction, the bands on an EBSD are direct projections of the crystal planes, this is shown in *Figure 5* [1].

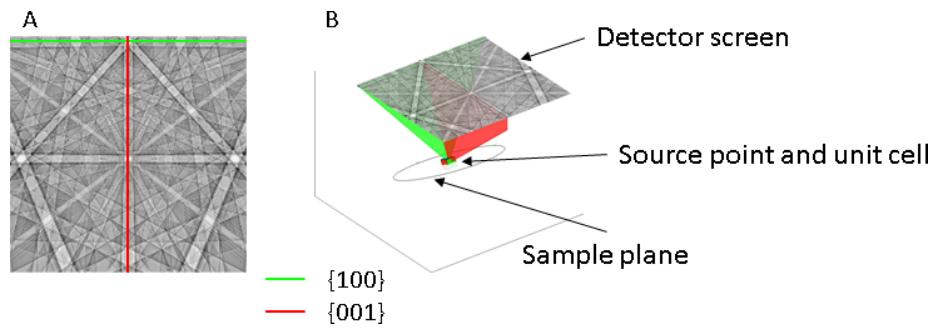


Figure 5: A) A simulated, unrotated silicon EBSD showing the horizontal $\{100\}$ plane in green and the vertical $\{001\}$ plane. And B) the way these bands are projected from the unit cell. Note the red band is parallel to the red face, and the green, parallel to the green face.

Once the bands are identified, it is possible to obtain the interplanar angles of the planes corresponding to the bands detected in the pattern. As the interplanar angles are invariant with rotation, it is possible to compare the obtained interplanar angles with a look up table of expected values and determine the phase and orientation of the unit cell responsible for the pattern [1].

This analysis is quick and well suited to simple crystal structures, such as cubic or hexagonal close packed (HCP) unit cells. However, analysis of more complicated unit cells, such as those of complex intermetallics or minerals bands are actually, requires more subtle features of the EBSD. These features include band width, relative intensity, minor bands or higher order Loue zone HOLZ rings to be considered [6].

To improve on the shortcomings of the Hough based analysis in these situations, the Dictionary indexing (DI) method was developed [7]. In the DI method, a large number of EBSDs at known orientations are generated and stored in a dictionary. An unknown pattern is then compared to each pattern in the dictionary one at a time, using an image cross correlation function (XCF). The XCF quantifies how similar two patterns are (1 for identical patterns and 0 for completely dissimilar images).

The DI approach considers the more subtle features of an EBSP when matching, which makes it more suited to complex unit cells. However, the accuracy of the indexing relies in the orientation being one of those in the dictionary of patterns. This means to improve the accuracy of DI, you need to have a large, closely spaced library to ensure a close enough match in orientation. The size of the library means DI is prohibitively expensive in terms of computational time and computer memory resources [8].

A second drawback is the XCF used in the DI is ill defined and becomes less accurate if two images match, but are shifted or rotated [9].

This thesis aims to develop and test an updated pattern matching approach called the refined template matching approach. It is similar to the DI approach, however there are two main changes (detailed in chapter 11) that lead to a reduced library size, thus a speed up, and the decoupling of accuracy and library search itself. These are:

1. An updated XCF in which the patterns are Fourier transformed and the matching performed in Fourier space. This allows for patterns that match but are shifted to be identified.
2. The addition of a refinement step that uses the shift detected from the updated matching to correct the orientation, and a log polar transform to correct for rotation of the EBSP.

9.1 EBSD: A Brief History

EBSD as we recognise it today, was first recorded by Alam *et al.* [10], who used film to determine the best experimental set up for high contrast EBSPs. The findings of this paper, such as a beam incident to the sample between 20° and 30°, are still used in many EBSD experiments to this day.

In the 1970s, Venables *et al.* [11]–[13] furthered the EBSD technique by implementing EBSD in a scanning transmission electron microscope (STEM). Here patterns were collected on film directly, or via a phosphor screen to the film. This was developed further by Dingley, who was working in the related field of micro-Kossel diffraction [14]–[16] at the time. Dingley made the first step towards automation of EBSD with the addition of a low light level SIT camera to the phosphor screen with the feed connected to a computer [17]–[19].

As a result of the addition of the digital camera, analysis of the EBSPs became partly automated, requiring user input of the location of 3 zone axes for cubic [18] and non-cubic [20] crystals.

At this point, as with today, the main material science challenge with EBSD was grain boundary characterization. An example of this, is identifying significant properties associated with low coincidence site lattice grain boundaries [21]. These properties could involve the energy associated with a given pattern, which will affect relative band intensities and line profiles [22]. Other uses for EBSD include phase identification/characterization using energy dispersive X-ray spectroscopy (EDX) to obtain the chemical properties of the material [23]. More detail about this can be found in the literature review and in chapter 4. Dingley and Baba Kishi also attempted to use EBSD to distinguish different space and point groups from the symmetry elements and systematic reflections in EBSD [24]–[26]. This topic has been revisited more recently thanks to the advancement of image processing techniques, computing power and the development of EBSD detector technology [27].

In the early 1990s, full automation of the EBSD process was attained. Computer control of the electron beam in the SEM allowed for large maps to be collected and the implementation of band detection algorithms allowed for hands off pattern analysis. The

two main early band detection algorithms used were a Burns algorithm (used by the Yale group of Adams, Wright and Dingley) [28] and the Hough transform (favoured by the Risø group of Krieger Lassen, Juul Jensen and Conradsen) [29]–[31]. Eventually the Hough transform was adopted by the Yale group and became the conventional method used to indexing algorithms for EBSD analysis in most commercial EBSD software.

Goehner and Michael [32] then demonstrated phase discrimination (which I will refer to as phase classification) using EBSD is possible. To show this, expected interplanar angles from known crystals were compared to the interplanar angles of the unknown crystal. In order to reduce the number of potential crystals to a manageable number, information about the local chemistry or the primitive lattice of the material is needed.

Recent developments include: the introduction of high angular resolution EBSD (HR-EBSD) by Wilkinson, Meaden and Dingley [33]. In HR-EBSD in which small regions of interest are cross correlated with each other in order to measure the change in lattice strain. The dictionary indexing approach [34], in which patterns are cross correlated to a library of known patterns to determine orientation. And the advancement of detector technology to directly detect the electrons, without the need for a phosphor screen or optics array [35].

9.2 In this Thesis

This thesis explores the use of template matching for improved EBSD analysis, by introduction of an updated algorithm, and applications thereof.

The literature review (Chapter 10) describes current understanding and interpretation of the pattern matching approach to EBSD. Including:

- An overview of the conventional Hough based analysis and the Dictionary Indexing method [34].

- Representations of rotations.
- Simulation of EBSPs.
- Crystal phases and an introduction to pseudosymmetry.
- An overview of metrics used to determine the sensitivity of an EBSD cameras.

Chapter 3 underpins much of the work in chapters 12 and 13 and is a lot of the motivation behind Chapter 14.

Chapter 3 describes the development and testing of the refined template matching (RTM) approach, first published in reference [8]. This chapter shows the refined method can achieve accuracy comparable to, and better than the Hough based indexing method for multiple maps. It also shows the RTM is computationally more efficient than the DI method [34].

Chapter 12 continues the work in Chapter 3 and applies the RTM to multiphase maps and patterns. The chapter also introduces a metric similar to the one proposed in [36] and compares the new algorithm with the existing method.

Chapter 13 then modifies the RTM approach introduced in Chapter 3 to allow it to correctly identify a pseudosymmetric orientation. The modification allows for a significantly reduced library, representing a dramatic speed up in processing.

Chapter 14 explores a new detector set up using a direct electron detector (DED). In this chapter a DED is proposed to be the main tool used to acquire patterns for the RTM approach because of the high sensitivity of the detector. This is demonstrated by measuring the modulation transfer function (MTF) and detective quantum efficiency (DQE) for the Timepix 3 camera. Various example patterns and an example map are then shown to

demonstrate the increase in pattern quality. And a number of calibration tests (shadow casting, screen retraction) are also used to explore the determination of the source point, or pattern centre (PC). The work in this chapter is preliminary in nature and is included for completeness.

10 Literature Review

The main topic of this thesis is developing a pattern matching method, called refined template matching, to classify electron backscatter patterns (EBSPs) and the applications of this method.

The pattern matching approach was developed as an alternative to the more conventional Hough transform-based approach. As such, this literature review explores pattern matching and Hough transform methods for EBSD pattern analysis, and includes details about pattern generation and indexing. Finally, I explore the development of new direct electron detectors and EBSD Indexing an Electron Backscatter Pattern.

An EBSP is usually formed by scintillations on a phosphor screen. An array of optics then transfers this image to a charge coupled device (CCD). The CCD transfers the image to a computer for processing (background correction, hot pixel correction) and determination of phase and orientation [1].

As discussed and shown in the introduction, an EBSP is a smoothly varying background, with bands of raised intensity. Certain bands have a higher intensity than others and are referred to as primary bands, while secondary bands are less intense. In an experimental pattern, there is a background of nondiffracting electrons which can obscure some pattern features, unless a suitable correction is applied. Certain orientations also show higher order Loue zone (HOLZ) rings. Simulated patterns usually do not have a background, unless one is added specifically. An example experimental EBSP, background, corrected EBSP and simulated EBSP can be seen in Figure 6.

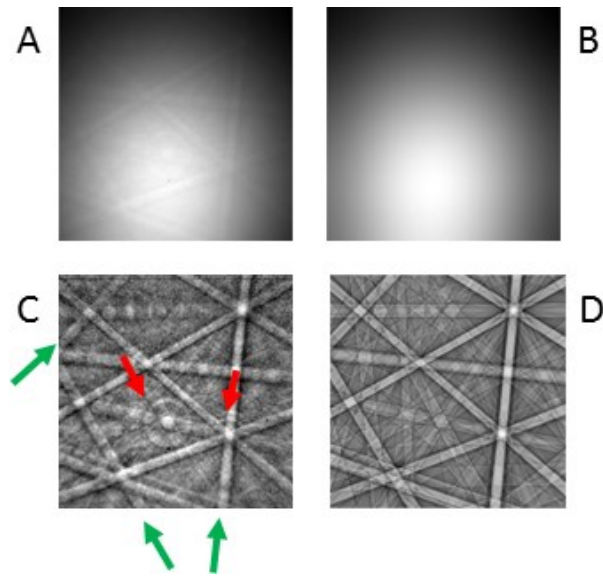


Figure 6: A) An electron backscatter pattern as captured from a conventional detector. B) the background of the pattern and C) the pattern with the background removed. The bands indicated by green arrows are now visible, along with two HOLZ rings (Red arrows). D) Is a simulated pattern of the same patter, the HOLZ rings are missing due to the simulation software used.

10.1 EBSD Geometry

In the introduction, and the start of the literature review, I gave an overview of EBSD

experiments. Before moving forward, it is important to understand the reference frames

and geometry of an EBSD experiment. These reference frames are essential to understand

the analysis of an EBSD, and the geometry is important when discussing the physics of how

patterns form.

10.1.1 Coordinate Systems in Electron Backscatter Diffraction

There are several issues with coordinate systems and reference frames when indexing an

EBSD. The two main causes of this are:

1. The number of different conventions for different indexing software
2. The number of reference frames needed to be kept track of.

This section will focus on the second of these and use the conventions described here

throughout the thesis. This section is a summary of [37].

The main reference frames needed to be considered are:

- The gnomonic frame: The coordinate system defined by the right-handed set (x_g, y_g, z_g) and is located on the phosphor screen. The frame is centred on the pattern centre with x_g extending to the right, y_g upwards and z_g from the crystal. It is in this frame that we look at the EBSP.
- The screen frame: The phosphor screen itself is tilted with respect to the sample and thus has a separate coordinate system to the EBSP. The coordinate system (x_d, y_d, z_d) is centred on the phosphor screen, such that z_d points from the sample to the screen. It is used to calibrate the gnomonic frame such that $x_g = x_d/z_d$ and $y_g = y_d/z_d$.
- The sample frame: This frame (x_s, y_s, z_s) is centred upon the sample with z_s pointing out of the sample towards the screen.
- The crystal frame: This is the frame of the unit cell within the sample and is defined using the same conventions as described in “Crystal Symmetry”

These frames are shown in Figure 7.

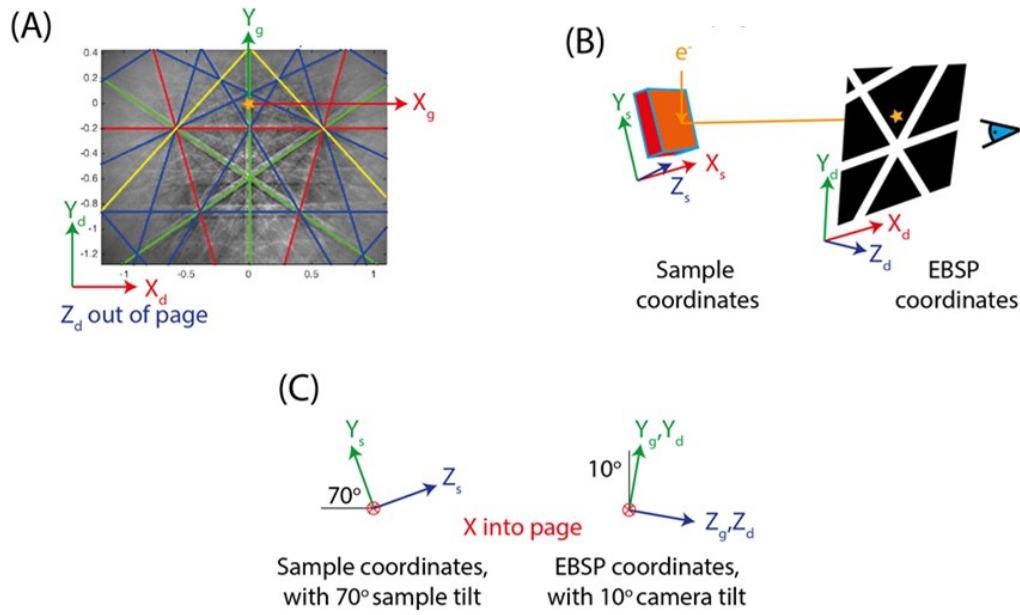


Figure 7: The different coordinate systems in EBSD (reproduced from [37]). A) Shows the Gnomonic frame on the detector frame. B) shows the experimental set up, i.e. the tilt of the sample and detector frames and C) shows the same as a cross section.

10.1.2 Pattern Centre

The pattern centre (PC), also called the source point, is the point, (x^*, y^*) , on the screen closest to where the primary beam hits the sample. The out of plane PC is defined with $z^* = 0$ at the point the beam interacts with the sample, and scatters to form the diffracting electrons [38]. It is also the point on which the gnomonic frame is centred [37]. This can be seen diagrammatically as the orange vector in Figure 7 B.

PC determination is of huge importance experimentally, both for the Hough and XCF approaches. This is because the accuracy of both methods is dependent on the PC for reconstruction of the bands identified in the EBSD [39].

10.1.2.1 Pattern Centre Determination

As the PC needs to be known to a high degree of accuracy for accurate indexing of EBSD patterns, there are several ways in which the PC can be determined. The most commonly used technique is an iterative method [40]. There are, however, several alternatives used primarily for calibration. As background for chapter 3 we will explore the “Pawnbroker’s

balls” or “Dingley’s balls” as it is sometimes known, screen retraction and explore iterative methods. However there are other PC determination techniques such as using a crystal of known orientation [19]. An extensive review of each of these methods, as well as a comparison of advantages and disadvantages of each method can be found in [41].

10.1.2.1.1 Pawnbroker’s/Dingley’s Balls

The “pawnbroker’s balls” (also known as Dingley’s balls) are a shadow casting method for determining the PC. In this method, 3 conductive balls are placed between the screen and the sample, casting three elliptical shadows on the pattern. The major axes of these shadows point towards to the in-plane PC (x^*, y^*) [6], [14], [41], [42]. Determination of z^* is slightly more complex and will be briefly covered in this section, however there is more detail in [14], [42] and [43]. A diagram of a typical set up can be seen in Figure 8.

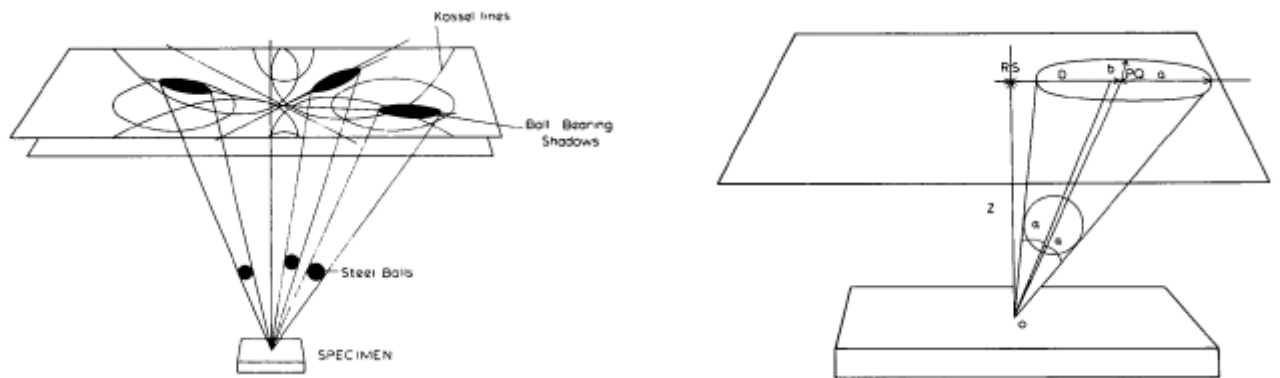


Figure 8: The experimental set up and schematic of a shadow casting experiment. Figure adapted from [14]

Following the method of Dingley [14], we first fit the coordinate values of each ellipse to the general formula:

$$Ax^2 + 2Hxy + By^2 + 2Gx + 2Fy + C = 0 \quad \text{Equation}$$

1

Where A, B, C, F, G and H are constants to be determined with a least squares fitting approach. The angle, γ , between the x axis and the major axis of the ellipse is given as:

$$\gamma = \frac{1}{2} \tan^{-1} \left[\frac{2H}{A - B} \right] \quad \text{Equation 2}$$

And the coordinates of the ellipse centre, PQ are:

$$\frac{HF - BG}{AB - H^2}, \frac{GH - AF}{AB - H^2} \quad \text{Equation 3}$$

Evaluating γ and the centre coordinates allows transposition to the standard equation of an ellipse:

$$\frac{X^2}{a^2} + \frac{Y^2}{b^2} = 1 \quad \text{Equation 4}$$

Where X and Y are the transposed coordinates for the centre of the ellipse, and a and b are the semi lengths of the major and minor axes respectively. Another least squares fitting routine is performed to find values for a and b . A more detailed mathematical analysis is shown in [43].

From here we can take a pair of ellipses and work out the intersection of their major axes, (R, S) , by:

$$R = \frac{\cos \gamma_i (Q_j \cos \gamma_j - P_j \sin \gamma_j) + \cos \gamma_j (Q_i \cos \gamma_i - P_i \sin \gamma_i)}{\cos \gamma_i \sin \gamma_j + \sin \gamma_i \cos \gamma_j} \quad \text{Equation 5}$$

And

$$S = \frac{-\sin \gamma_j (Q_i \cos \gamma_i - P_i \sin \gamma_i) + \sin \gamma_i (Q_j \cos \gamma_j - P_j \sin \gamma_j)}{-\sin \gamma_j \cos \gamma_i + \sin \gamma_i \cos \gamma_j} \quad \text{Equation 6}$$

Where the subscripts i and j denote a given ellipse. It follows, therefore that there are $n!/((n-2)!2!)$ estimates for the (x^*, y^*) pattern centre. Dingley [14] suggests a least squares fitting to determine an estimate.

The Z distance is equal to the length of the normal from this estimated (x^*, y^*) to the source point. And is determined via the equation:

$$z^* = \frac{b_i^2}{a_i} / \tan \alpha_i \quad \text{Equation 7}$$

Where

$$\alpha = \tan^{-1} \left\{ -\frac{a^2}{b^2} + \left[\frac{a^2}{b^2} / \frac{a^2 - b^2}{D^2} \right] \right\}^{\frac{1}{2}} \quad \text{Equation 8}$$

Here, D is the distance between the ellipse centre and the pattern centre, given as $D = [(P - R)^2 + (Q - S)^2]^{\frac{1}{2}}$. And α is the semi-cone angle, shown in Figure 8.

10.1.2.1.2 Camera Retraction

This method, also known as the pattern magnification method [44][45], is when the screen is incrementally stepped away from the source (increasing z^*) and patterns collected. As you move the screen away, the pattern zooms out around an invariant point. That point of invariance is the PC in the gnomonic frame (x^*, y^*) [46]. z^* can be obtained using the following steps, shown in [45].

Firstly, two points in the in position and the out position need to be identified. The in position being when the detector is close to the sample and out being further away. The distance, L , between these points, usually poles, is measured. The camera displacement, h , is also recorded. In order to determine a PC, the diagram in Figure 9 is needed.

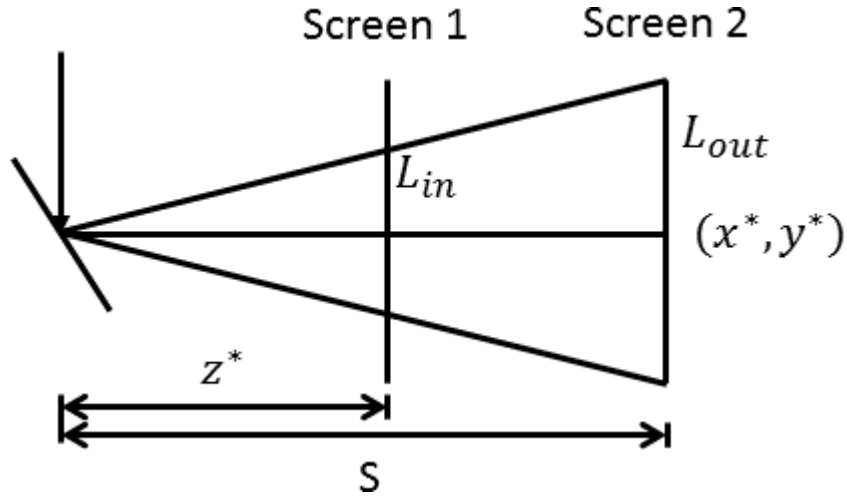


Figure 9: Experimental set up of a retraction experiment. z^* is the distance between the in position and the source point, and S is the camera displacement. This figure is similar to the derivation in [45].

Using Figure 9 we can determine a scale factor, S and use that to determine z^* using similar triangles:

$$z^* = \frac{SL_{in}}{L_{out}} \quad \text{Equation 9}$$

10.1.2.1.3 Iterative Approaches

Iterative approaches to locating the PC are the most common methods used in indexing software available today [40]. The method requires an initial guess at the PC. A pattern is then indexed, and the PC is adjusted to minimize the difference between the detected bands and the bands from the look up table. To increase the accuracy of this method, averages of multiple patterns can be taken [6], [40], [47], [48]. More recently an open source genetic algorithm method for this iterative method was published by Britton *et al.* as a part of the AstroEBSD package [5].

10.1.3 Projections of a sphere

Spherical projections are important in EBSD, and especially in cross correlation-based methods of EBSD classification. This is because electrons diffract radially out from a point

source. This makes a sphere centred on the point at which the incident beam meets the sample, a convenient representation of the diffraction. The electrons are collected on a flat screen[1]. In most cross correlation-based methods, usually the diffraction sphere is stored as a flat projection and the patterns generated by converting between a flat projection and the gnomonic frame that represents the detector [34], [49]. In the spherical EBSD method [50], the diffraction sphere is stored and indexing takes place on the sphere.

There are many spherical projections that can be used to store the diffraction sphere, the stereographic projection is the focus of this literature review, however, other projections would work equally well, such as the modified Lambert projection [51].

10.1.3.1 Gnomonic Projections

The gnomonic projection is essentially taking a flat screen and projecting the points on the sphere radially out to the screen. As we discuss in section 10.1.1, this is the projection in which observed EBSDs are in. We can imagine a sphere, on the surface of which lie the points P_1 and P_2 , at the south pole of the sphere is a flat plane. The projections of the points P_1 and P_2 are the point at which a line going from a point to the surface that passes through the origin meets the surface. If points P_1 and P_2 are opposite each other, they are indistinguishable in the gnomonic plane [52]. This can be seen in Figure 10

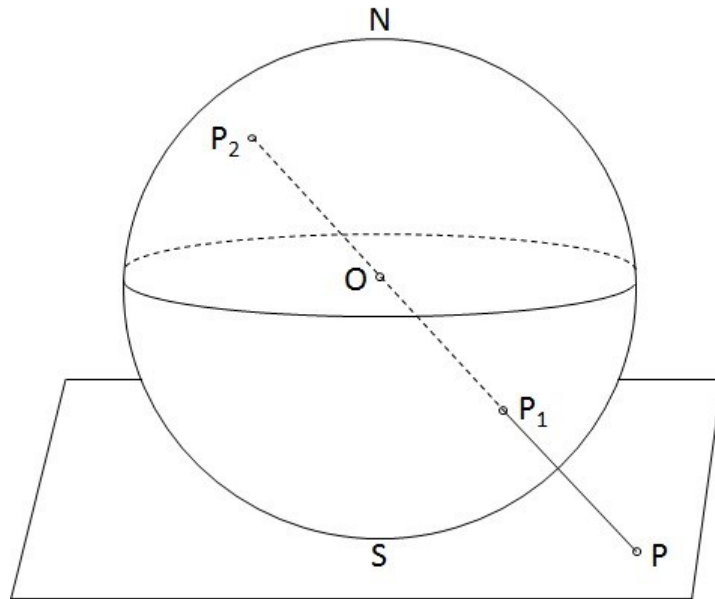


Figure 10: The gnomonic plane shown diagrammatically. Both points P_1 and P_2 will map to point P in the gnomonic frame and would be indistinguishable. Figure adapted from [52]

10.1.3.2 Stereographic Projections

The second way of representing a sphere on a plane is the stereographic projection. In this projection, we imagine the same set up, a sphere has a flat plane at its south pole, and we have the point P' on the sphere. To determine the point on the stereographic plane, take a line from north pole and continue it through point P' to the plane [52]. This is shown in Figure 11

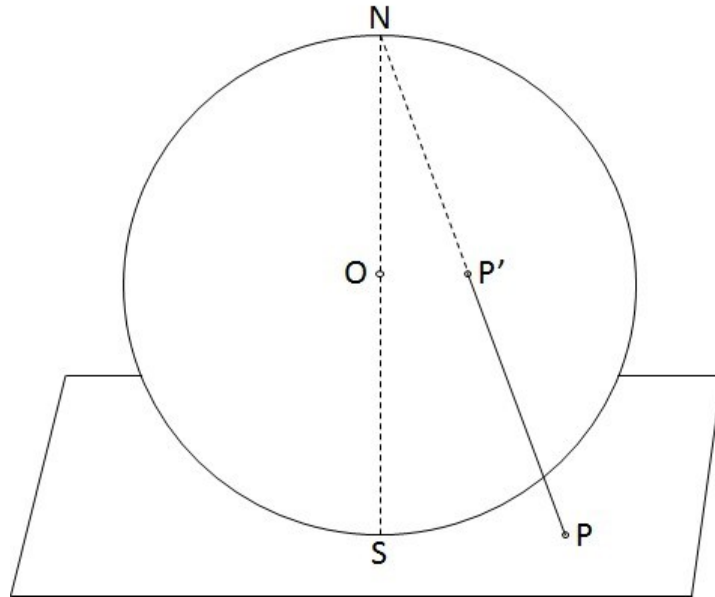


Figure 11: The stereographic projection shown diagrammatically, adapted from [52].

10.2 Simulated Kikuchi Patterns

A brief overview of the generation of EBSPs is included in the introduction, this section looks to expand on the theory behind EBSP generation leading to computer simulations of EBSPs.

The pattern matching approach requires high quality simulated EBSPs of different phases for known orientations. If the simulation is too crude, then there will not be enough information to perform a reasonable pattern match. This could lead to problems with misindexing, such as rogue shifts [40].

There are two main ways to simulate an EBSP, using kinematical or dynamical diffraction theory.

Kinematical simulations are based upon X-ray Bragg diffraction and are very good for predicting the major bands of the diffraction pattern [40], [53]. However, kinematic simulations are insufficient for the high-quality simulations required for the pattern matching approach to EBSD [40].

A better approach is to use a dynamical simulation, which is a quantum mechanical approach and considers the interactions between the diffracting electrons and the lattice of atoms. This provides a simulation with the detail necessary for pattern matching [40]. An example of both can be seen in Figure 12.

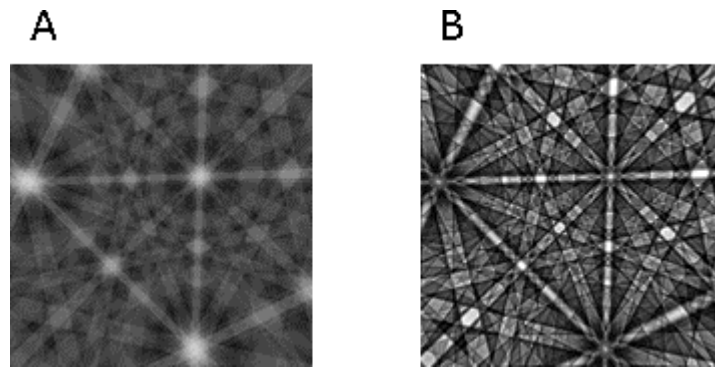


Figure 12: A) A kinematic and B) a dynamic simulation of an orientation of Ferrite. Both images taken from the DynamicsS software using standard settings.

10.2.1 Kinematic vs Dynamical Simulation

10.2.1.1 Kinematic Simulations

EBSD is produced when electrons diffract from the planes of a crystal lattice. This can be approximated to Bragg diffraction, and thus, Bragg's law (Equation 10) can be applied to describe the band edges [54]

$$n\lambda = 2d\sin(\theta) \quad \text{Equation}$$

10

Where n is an integer, λ is the De Broglie wavelength, d is the lattice spacing and θ is the diffracting angle. This is demonstrated below in Figure 13. Treating electrons as waves is good for approximating the locations of the dominant band edges in the EBSP, following Bragg's law. However, electron diffraction is more complex than X-ray diffraction, due to electron interactions with the lattice and other dynamical interactions [53].

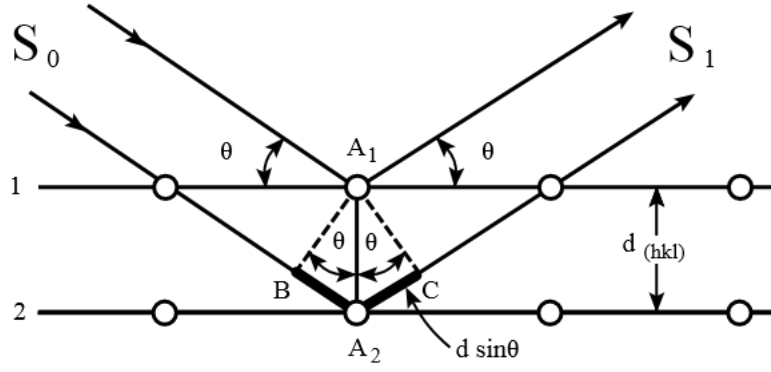


Figure 13: Elements in a crystal lattice needed for Bragg's law to apply. From [55]

10.2.2 Dynamical Simulations

Dynamical simulations are a more in-depth, quantum mechanical model and give the extra detail that is lacking in the kinematical simulation. This is because the model accounts for electron-atom interactions and dynamical effects on the electron from the interaction. As this is a more in depth model, the depth of the diffracting electrons also needs to be considered. Although it is possible to get backscattered electrons as deep as $3 \mu\text{m}$ [3], most electrons that form the EBSD come from a depth of $\sim 15 \text{ nm}$ [56].

The patterns used in this thesis are generated using the Esprit DynamicS software package, and use the standard settings for the simulation unless otherwise stated. The method for simulation used in the software is based on references [53],[57], [58]. The method is described here, and follows reference [53].

Due to the complexities of EBSD, a full quantum mechanical calculation in the form of a quantum mechanical density matrix [59] is impractical. To make the method more usable, the simulation can be simplified using two assumptions.

1. There is no coherence between the incoming (source) electrons and the diffracting electrons.
2. We know the distribution $n_B(\theta, \phi, \theta_{in}, \phi_{in}, E, t)$.

Here, n_B is the distribution of inelastically scattered electrons at energy, E and depth, t . The electrons are scattered in the direction (θ, ϕ) , with incident electrons at (θ_{in}, ϕ_{in}) . In a practical sense, n_B represents the cumulative effects of the elastic and inelastic scattering and necessarily includes electrons lost to the diffracted wave. $n_B(E, t)$, can be approximated to a useful degree of accuracy using Monte Carlo simulations [53]. The typical path the electron takes once inside the atom is known a “random walk” and is shown in Figure 14.

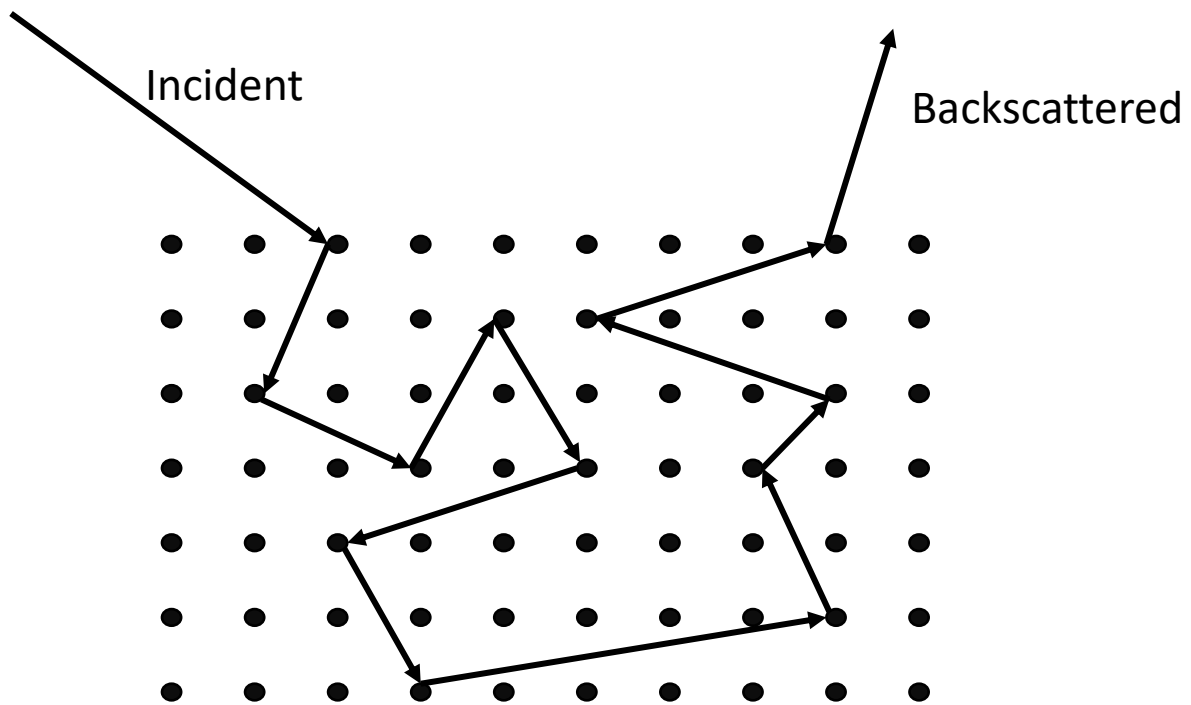


Figure 14: The “random walk” of an electron in the crystal. This also shows the disconnect between the incident and outgoing electrons described in [53] that allows us to treat incoming and backscattered electrons independently.

Usually, in an EBSD experiment, it is not necessary to obtain the absolute intensities of the bands – especially as the signal is rarely absolutely quantified. This means that knowledge of the relative band intensities is sufficient. As such, no detailed assumptions about n_B need to be made. However, it does mean we can symbolically write the observed intensity in the detector, I_B , as such:

$$I_B \propto \int_0^{E_p} dE \int_0^{t_{Max}} dt D[n_B(\theta, \phi, \theta_{in}, \phi_{in}, E, t)] \quad \text{Equation 11}$$

This means the intensity at a given point is a result of the double integral over all energies and all depths. This makes the resultant pattern a superposition of multiple patterns, added together and weighted by n_B .

10.2.2.1 The Reciprocity Principle

The reciprocity principle takes advantage of the time reversal symmetry of EBSD. This means that calculating the intensity emitted at a source and tracing it to where it lands on the screen, is equivalent to calculating the intensity at the screen and tracing it back to where it originated, as shown in Figure 15.

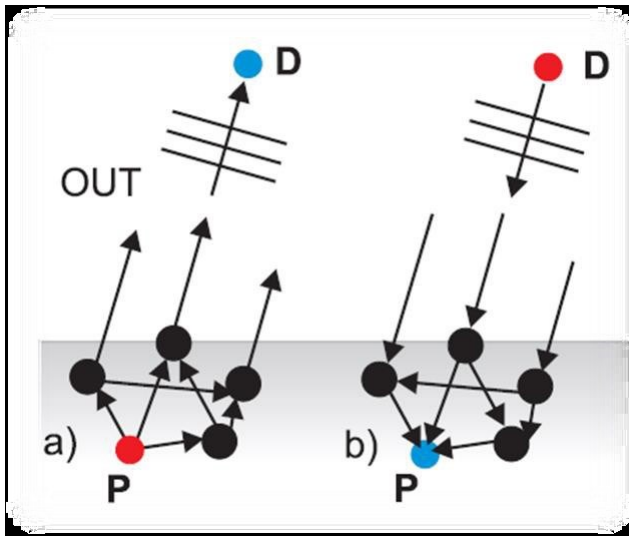


Figure 15: Because of the reciprocity principle, in a) the red point emitting D, is equivalent to b) where D enters the lattice and works back to point P. (Reproduced from [53]). (Reprinted by permission from Springer Nature: Springer eBook Electron Backscatter Diffraction in Material Science by R. A. Schwarzer, D. P. Field, B. L. Adams COPYRIGHT (2009))

Use of the reciprocity principle means we can track single plane waves. If we take a point on the screen, we can choose a single plane wave and work out the scattering that caused it.

10.2.2.2 Bloch Wave Theory

Now we know we can calculate the intensity at a point on the screen, or at a point in the lattice, we need a description of the interactions with the diffracting electrons and the

lattice. The method used in this thesis, is that described by [53], [57], [58] and that is Bloch wave theory.

Bloch waves are a way of describing a periodic wave function, as you would expect in a lattice, and are written in the form $\psi(\underline{r}) = e^{i\mathbf{k} \cdot \underline{r}} u(\underline{r})$ [53]. As crystal lattices are periodic, Bloch waves are a convenient way to represent the wavefunction in the whole crystal. This allows integration of different emitters at different depths and locations within the crystal.

Bethe [60] used a linear superposition of Bloch waves to represent the wave function for the diffracting electrons, which becomes analogous to the nearly free electron model [54], [57], and represents how electrons move in the lattice. This superposition means the wave function takes the form:

$$\psi(\underline{r}) = \sum_j c_j \exp(2\pi i \mathbf{k}^{(j)} \cdot \underline{r}) \sum_g C_g^{(j)} \exp(2\pi i \mathbf{g} \cdot \underline{r}) \quad \text{Equation 12}$$

With \mathbf{g} being the reciprocal lattice vector, and \underline{r} the real space location vector. The aim of this approach is to determine the expansion coefficients, c_j and $C_g^{(j)}$, as well as the wavevector $\mathbf{k}^{(j)}$. With these, the wavefunction becomes known [53].

As the wavefunction is a solution to the Schrödinger equation, this becomes our starting point:

$$\nabla^2 \psi(\underline{r}) + \frac{8\pi^2 m |e|}{h^2} [E + V(\underline{r})] \psi(\underline{r}) = 0 \quad \text{Equation 13}$$

Where m is the relativistic electron mass, h is the Planck constant and $|e|$ is the magnitude of the electron charge. E is the incident electron accelerating potential, such that the total energy of the incident electron is $|e|E$. And $V(\underline{r})$ is the potential [57].

In reference [53], Winkelmann simplifies the equation somewhat, by assuming a plane wave of $\exp\left(2\pi i \underline{K}_0 \cdot \underline{r}\right)$, with corresponding energy $\hbar^2 K_0^2/2m$, thus making the equation:

$$\frac{-\hbar^2}{8\pi^2 m} \Delta \psi(\underline{r}) - |e|V(\underline{r})\psi(\underline{r}) = \frac{\hbar^2 K_0^2}{2m} \psi(\underline{r}) \quad \text{Equation 14}$$

The next step, is to determine the potential term in the Schrödinger equation.

Humphreys [57] derives a term for the crystal potential to be:

$$V_g = \frac{\hbar^2}{2\pi m |e| V_{cell}} F_g \quad \text{Equation 15}$$

Where F_g is the structure amplitude and V_{cell} is the volume of the unit cell. As the crystal lattice is periodic, we follow the method in [53] and take the Fourier transform of the potential giving:

$$U(\underline{r}) = U^c(\underline{r}) + iU'(\underline{r}) = \sum_g U_g \exp\left(2\pi i \underline{g} \cdot \underline{r}\right) \quad \text{Equation 16}$$

Where U is the scaled potential, measured in \AA^{-2} . and is formed from the electron structure factors $U_g^c = 2m|e|V_g/\hbar^2$, with V_g being a Fourier coefficient of the crystal potential in volts and the relativistic electron mass, m . The loss of electrons due to inelastic effects are taken into account with the corresponding Fourier coefficients U'_g of an imaginary part of the crystal potential.

Substituting into the wave function and the Schrödinger equation gives the standard dispersion relation:

$$\left[\underline{K}^2 - \left(\underline{k}^{(j)} + \underline{g} \right)^2 \right] c_g^{(j)} + \sum_h U_{g-h} c_h^{(j)} = 0 \quad \text{Equation 17}$$

Where \underline{K} is the incident electron wavevector inside the crystal. If we examine an infinite number of values for \underline{g} , i.e. an infinite number of reflectors are examined, Equation 17 becomes exact. Suitable levels of accuracy can be attained by analysing many values for \underline{g} . A convenient way of doing this is to transform the equations into a matrix and turn it into an eigenvalue problem. We can do this by considering $K_0^2 = K^2 - U_0^c$, where U_0^c is the mean inner potential and \underline{K}_0 is the electron wave vector in a vacuum.

This means $\underline{k}^{(j)}$ can be written as:

$$\underline{k}^{(j)} = \underline{K} + \lambda^{(j)} \underline{n} \quad \text{Equation 18}$$

Where \underline{n} is a vector normal to the surface. This gives eigenvalues $\lambda^{(j)}$ with eigenvectors containing the elements $c_g^{(j)}$ [58]. This formulation includes the effects due to the tilt of the outgoing direction with respect to the surface [53], and is also valid for values of \underline{g} in higher order Laue zones (HOLZ). The boundary conditions at the surface determine $c^{(j)}$. The quantities for $c^{(j)}$ can be found by taking the elements in the first column of the inverse matrix containing the values of $c_g^{(j)}$. With this information, the wave function is known.

A two-beam approach can be seen in [57], [61]. However, two beams are not sufficient to reproduce the intensity variations you would expect to find in an experimental EBSD, with sufficient detail for high quality matching [40]. They are especially poor for the intensity distributions of the zone axes (where many bands cross).

To calculate the intensity of many beams, the wave function must be worked out for each reflector. This method of calculating the pattern, scales as N^3 , where N is the number of reflectors considered in the simulation. As such, these calculations rapidly become too computationally expensive to be useful. We can overcome this problem by using the Bethe perturbation scheme, which allows the inclusion of the effects of weak reflections U_h , by transformation into an effective potential of strong beams U_g^{eff} , where:

$$U_g^{eff} = U_g - \sum_h \frac{U_h U_{g-h}}{2KS_h} \quad \text{Equation 19}$$

Here $2KS_h = K^2 - (\underline{K} + \underline{h})^2$, which contains the excitation error term, S_h . For the Bethe perturbation, beam selection criteria for strong and weak reflectors have been developed by [62]. Strong and weak beams are selected based on their structure factor and the excitation error, which describe how much influence a certain reflecting plane has at a given point in an EBSP.

10.2.2.3 The Backscattering Process

Using the Bloch wave approach described above, it is possible to determine the diffraction induced changes in the electrons as the exit from a position, \underline{r} , inside the crystal. Allen and Rossouw 1989 [63] state that the backscattered electrons predominantly originate at the atoms in the lattice. This means we need to calculate the probability density of electrons ($\psi\psi^*$) around the atomic positions, \underline{P} . As we have already calculated the wavefunction, this is straightforward.

In the case of EBSD, we take the generalised potentials to be delta functions (point sources), which are broadened by thermal vibrations. This means the backscattered intensity can be given by [64]:

$$I_{DYN} \propto \sum_{n,ij} Z_n^2 B^{ij}(t_1, t_2) \sum_{g,h} C_g^{(I)} C_h^{(j)*} \times \exp(-B_n s^2) \exp[2\pi i (\underline{g} - \underline{h}) \cdot \underline{P}_n] \quad \text{Equation 20}$$

Where $\exp(-B_{ns}^2)$ are the Debye-Waller factors and $B^{ij}(t_1, t_2)$ is the depth integrated interference term made up of the Bloch waves i and j , such that:

$$B^{ij}(t_1, t_2) = c_i c_j^* \frac{\exp[2\pi i (\lambda^i - \lambda^{j*}) t_2] - \exp[2\pi i (\lambda^i - \lambda^{j*}) t_1]}{2\pi i (\lambda^i - \lambda^{j*})} \quad \text{Equation 21}$$

Using the method described above, you can calculate an EBSD, pixel by pixel, each describing a well-defined wavevector direction, \underline{K}_0 . Using the Bethe perturbation in this way allows for inclusion of a sufficiently large number of reflectors. Thus enabling this method to handle the large viewing angles of EBSD [53].

Using the above method, Winkelmann [53] has shown it is possible to work out the electron probability densities that produce points on an EBSD. To demonstrate this, Winkelmann used a simplified (9 reflector) EBSD from BCC iron to generate Figure 16.

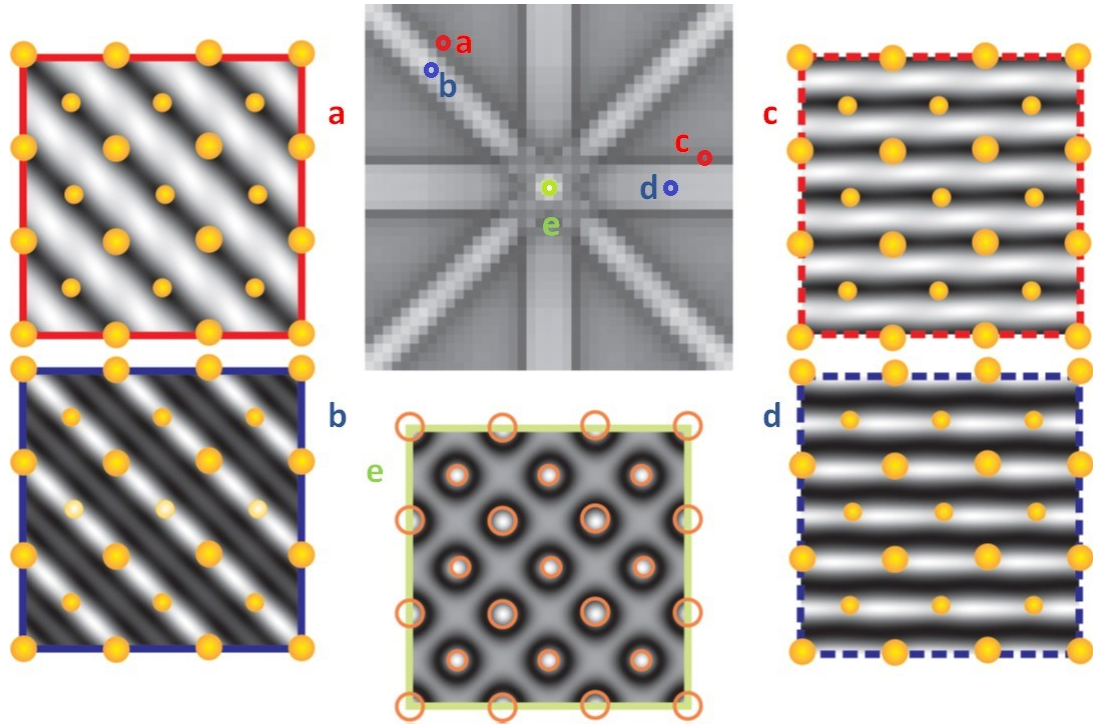


Figure 16. The probability density of an electron being diffracted from a given point in a lattice at pixels a, b, c, d and e. Here light areas show high probability of diffraction (reproduced from [53]). (Reprinted by permission from Springer Nature: Springer eBook Electron Backscatter Diffraction in Material Science by R. A. Schwarzer, D. P. Field, B. L. Adams COPYRIGHT (2009))

Figure 16 shows that, for bright points in the pattern, such as a pole or one of the Kikuchi bands, the electrons are mostly diffracted from points close by atoms, and points of lower intensity come from points where there are fewer atoms. This implies, physically, that if an electron has a path free of atoms it is unlikely to diffract from or interact with an atom and will likely penetrate more deeply into the material.

A similar approach is taken by Callahan and De Greaf [51], who split the problem into 3 stages. Using a similar Bloch wave-based theory, a “master pattern” is generated in the modified Lambert equal area projection. This master pattern is then sampled to produce a gnomonic projection of a pattern at a given orientation for a screen. Finally, a Monte Carlo simulation is applied to the pattern to describe the energy distribution of the pattern. As this method is not used in this thesis, I will not detail it further.

For more information on the dynamical scattering of electrons, please see references [61], [65]–[67].

Note that all patterns simulated in this thesis are for a fixed energy which corresponds to the energy of the primary electron beam. Recent analysis by Winkelmann *et. al.* implies the energy spread across an experimental EBSP is <1 keV [56].

10.3 The Radon and Hough Transforms

To obtain useful information from the pattern, the bands are usually identified, and the orientation determined. This process is called pattern indexing and a general outline of the indexing process is shown in Figure 17.

To find the bands, the captured patterns are transformed using the Radon [68], [69] or Hough transform [70] (the Hough transform is essentially a discrete Radon transform). This transform converts the bands to points, which can be found more easily by a computer [38]. As the bands are a direct projection of the crystal planes, this means the interplanar angles can be found and compared to a look up table (LUT). The results from the LUT can then be used to identify crystal phase and orientation.

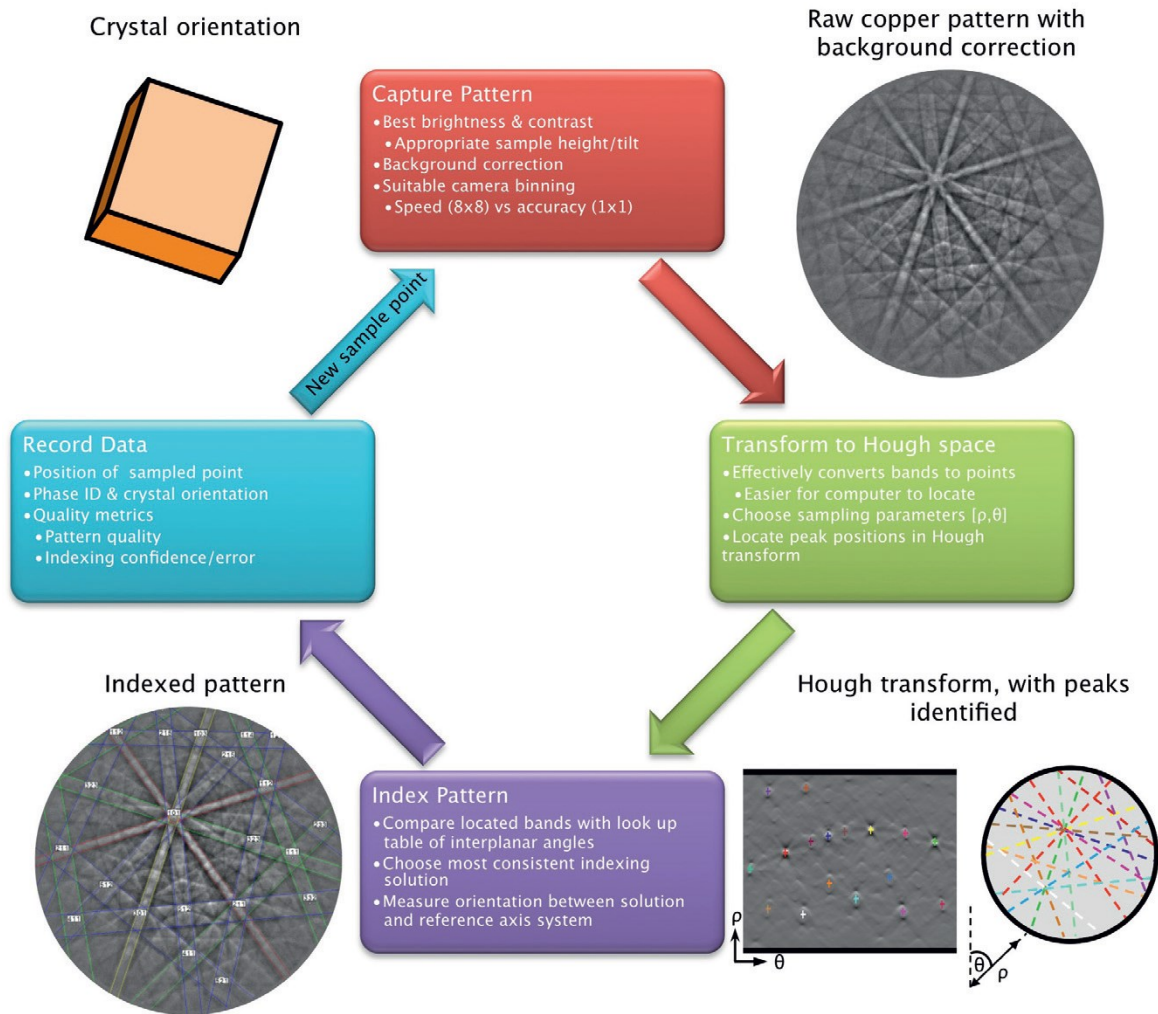


Figure 17: Flowchart reproduced from [1] showing the standard method for indexing an EBSD. (Reprinted from *Materials Today*, 15, A. J. Wilkinson, T. B. Britton, *Strains, Planes and EBSD in materials science*, 366-378, Copyright (2012), with permission from Elsevier)

The Hough transform has been widely used since it was first introduced for EBSD analysis by Krieger Lassen [30], [71], and is very similar to the Radon transform used in the open source AstroEBSD package developed by Britton *et. al.* [5]. To perform a Hough/Radon transform, an arbitrary origin is taken, and a line drawn from that point to a band such that the line bisects the band at 90° . The length of the line, ρ , from the point and the angle rotated from the x axis, θ , are recorded. Conventionally, the angles are measured from the horizontal moving in an anticlockwise direction, meaning angles and lengths are both always positive. These can be plotted on the graph (ρ, θ) , known as Hough or Radon space and is shown in Figure 18.

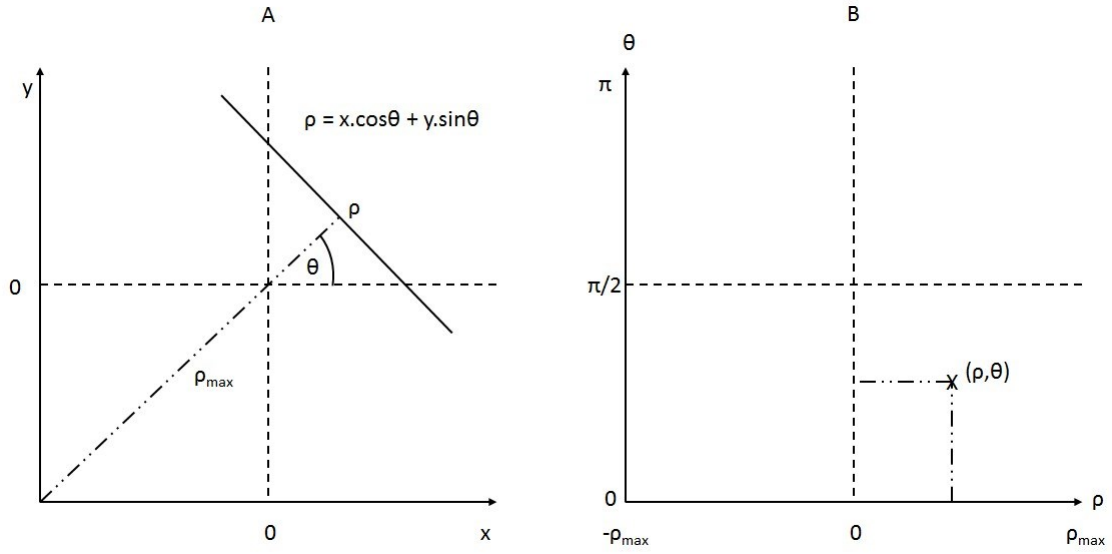


Figure 18: Two graphs reproduced from [38] showing the Hough/Radon transform. A) Shows a line plotted in Cartesian polar coordinates, defined as $\rho = x \cos(\theta) + y \sin(\theta)$. And B) the same line represented as a point in Hough/Radon space. (Reprinted by permission from Springer Nature: Springer eBook Electron Backscatter Diffraction in Material Science by R. A. Schwarzer, D. P. Field, B. L. Adams COPYRIGHT (2009))

If we take a 2-D function ($f(x, y)$), representing the intensity of a pixel located at point (x, y) , we can mathematically represent the Radon transform as:

$$R(\rho, \theta) = \int_{-\infty}^{\infty} \int_{-\infty}^{\infty} f(x, y) \cdot \delta(\rho - x \cos \theta - y \sin \theta) dx dy \quad \text{Equation 22}$$

With the kernel $\delta(\rho - x \cos \theta - y \sin \theta)$ [38]. As the integral sweeps through the values for ρ and θ it converges on the actual bands in the pattern, creating a characteristic butterfly peak as seen in Figure 19 [41]. The algorithm for a Hough transform is similar, but it uses an accumulated array to achieve a comparable output.

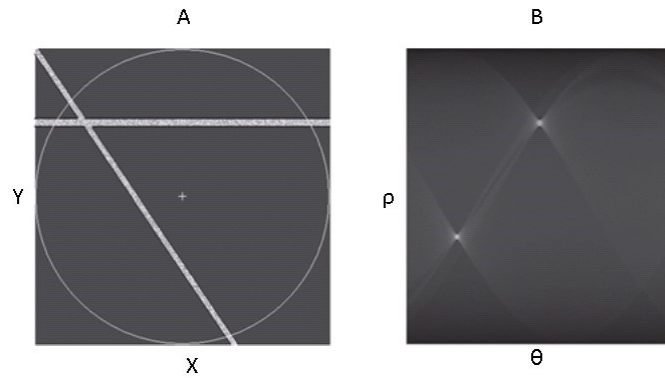


Figure 19: reproduced from [41] showing the use of the Hough transform, and demonstrating the butterfly wing effect. Reproduced with permission of Taylor and Francis Group LLC (Books) US through PLSclear from Introduction to Texture Analysis Macrotexture, Microtexture, and Orientation Mapping, Second Edition by O. Engler and V. Randle.

The limit of the accuracy on the Hough transform is based on how well the individual peaks can be identified in Hough space [71]. Another source of error comes from the fact that the bands are actually slightly curved: the bands look straight, but are, in reality, the intersections of cones on a plane making them hyperbola [72]. These hyperbola can cause an error in the location of the points corresponding to the bands in Hough space [73].

10.4 Cross-Correlational Methods

The Hough transform typically only looks at the locations of the primary band centres. This is suitable for relatively simple crystal structures. However, in more complex crystal structures, phase classification and accurate orientation determination can be dependent on the presence of secondary bands, the relative band intensities and even band widths. One of the strategies to improve the Hough based indexing method, i.e. to consider secondary bands and relative band intensities, is pattern matching with good quality simulations. This process is called template matching and one such example is the Dictionary Indexing approach [7], [49].

In this method, reference patterns are taken from the 2D intensity distribution within EBSPs derived from high quality dynamical simulations. Patterns are calculated for select

orientations to form a large library (or dictionary) of potential templates. In a captured map, the experimental patterns are sequentially template matched (i.e. compared) with the template library and the closest match is taken to be orientation of the unit cell. Matching in the Dictionary Indexing approach is performed via a pixel by pixel comparison, with the “normalised dot product” (NDP). The orientation precision is ultimately limited to the sampling of the orientation space used to generate the library and therefore the library size. It follows that a very large library is required for good orientation resolution. Further, the relatively narrow width of the local peak in the NDP [8] [74] as a function of misorientation from the true crystal orientation sets a minimum requirement on the sampling. This leads to the requirement of a substantial library size for a close match [8]. This limits wide scale implementation due to the high computational costs and memory requirements associated with generating, storing, and matching with the library.

To be more precise, in traditional template matching, we usually generate a library (\mathbf{M}_i^k) of k potential templates and compare these with our experimental observation. The library is generated to populate orientation space with finely spaced sampling. For the Dictionary Indexing method, each experimental pattern (E_i) is compared with each pattern from the library (in turn) via the average inner product, where each pattern is written as a linear vector of pixels (indexed from $i = 1$ to d , where d is the number of pixels in the vector):

$$C^k = \frac{1}{d} \sum_{i=1}^d \frac{\mathbf{M}_i^k \mathbf{E}_j}{|\mathbf{M}_i^k| |\mathbf{E}_j|} \quad \text{Equation 23}$$

The objective of this comparison is to subsequently find the best match, i.e. highest value of C^k , where each experimental pattern and the respective library pattern are most similar [7], [49].

Until the De Graef group published the dictionary indexing method [7], for EBSD analysis cross-correlation was usually limited to high angular resolution EBSD (HR-EBSD). The specifics of HR-EBSD are beyond the scope of this thesis. However, a summary is that regions of interest in the EBSP are compared (via a cross correlation function) between test and reference patterns. This comparison extracts the lattice strain and relative orientation changes, relative to a reference pattern [75], [76].

10.4.1 Library Generation for Cross-Correlational Methods

For cross-correlation based methods of phase and orientation determination, a large library of images usually needs to be generated. An exception to the large library requirement is the spherical EBSD method published by Hielscher *et al.* 2019 [50] (based off of work shown in [77]). Also, recent work by Lenthe [78], where the pattern matching is performed directly on the diffraction sphere.

As the ultimate accuracy of most pattern matching approaches depends on the angular separation of orientations used to generate the library, it is usual for libraries to become large and slow down the indexing process [8]. Methods of reducing the library size are discussed below and in Chapter 3.

10.4.1.1 Crystal Symmetry

The first step in reducing a library is to take advantage of crystal symmetries.

A crystal's unit cell can be described by a Bravais lattice, of which there are 14 [41], as shown in Figure 20.

Name	Conditions	Primitive	Base centered	Body centered	Face centered
Triclinic	$a \neq b \neq c$ $\alpha \neq \beta \neq \gamma$				
Monoclinic	$a \neq b \neq c$ $\alpha = \gamma = 90^\circ \neq \beta$				
Orthorhombic	$a \neq b \neq c$ $\alpha = \beta = \gamma = 90^\circ$				
Tetragonal	$a = b \neq c$ $\alpha = \beta = \gamma = 90^\circ$				
Rhombohedral (trigonal)	$a = b = c$ $\alpha = \beta = \gamma \neq 90^\circ$				
Hexagonal	$a = b \neq c$ $\alpha = \beta = 90^\circ, \gamma = 120^\circ$				
Cubic	$a = b = c$ $\alpha = \beta = \gamma = 90^\circ$				

Figure 20: The 14 Bravais lattices reproduced from [41]. The symmetries of these lattices will determine the size of the needed for cross correlation. Reproduced with permission of Taylor and Francis Group LLC (Books) US through PLSclear from Introduction to Texture Analysis Macrotexture, Microtexture, and Orientation Mapping, Second Edition by O. Engler and V. Randle.

Each primitive lattice can be described by three vectors, **a**, **b** and **c**, the lengths of which determine size of the lattice, and three angles, α , β and γ . Usually, the origin is taken to be the back-left atom in the lower corner of the primitive cell, with the **a** vector pointing forward (out of the page) the **b** vector pointing to the right, and the **c** vector pointing up,

making a right-hand set. The angle α is between \underline{b} and \underline{c} , β between \underline{a} and \underline{c} , and finally, γ is between \underline{a} and \underline{b} [37], [79], as seen in Figure 21.

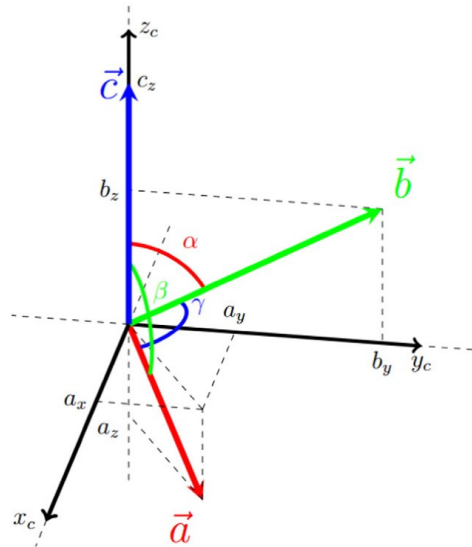


Figure 21: The basis vectors for a unit cell. Reproduced from [37]

Typical values for \underline{a} , \underline{b} , \underline{c} , α , β and γ are shown in the “conditions” column in Figure 20.

For many of the primitive cells, there is significant symmetry and this results in equivalent crystal orientations which are (necessarily) indistinguishable from each other. Take, for example, the cubic primitive cell, pictured in Figure 22, with its planes of symmetry, axes of symmetry and point of inversion. It contains 9 mirror planes (3 parallel to the faces and 6 parallel to the face diagonals). It also has three tetrad (four-fold) axes of rotational symmetry, perpendicular to each face. Four triad (three-fold) axes of rotational symmetry running along the diagonals of opposite corners. And six diad (two-fold) axes of rotational symmetry running between the centres of opposite edges. These mirror planes and axes of rotational symmetry are called the “point group symmetries” for the unit cell, because each of the axes and planes pass through a point at the centre of the unit cell. The point group symmetries differ for each unit cell, with the cubic primitive cell having the most symmetries i.e. being most symmetric [79].

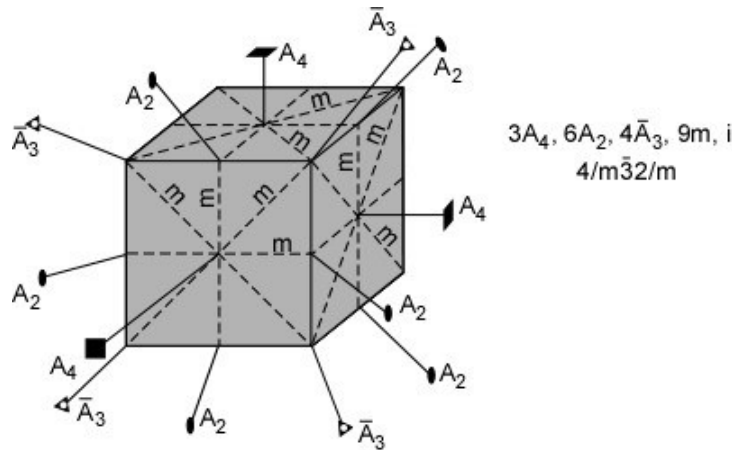


Figure 22: The point group symmetry of a cube. Here the n -fold rotation axis is denoted with A_n and the mirror planes are shown by dashed lines labelled m . There is also a point of inversion at the centre of the cell. Reproduced from [80]. Reproduced with permission from Prof. S. A. Nelson.

10.4.1.2 The Fundamental Zone

The most convenient way to generate a library such that no orientation repeats itself, is to populate the library with orientations within the “fundamental zone.”

The fundamental zone, is often described in terms of Rodrigues vectors (which I will describe in the section 10.5.4) as such, we will do so here.

The entirety of Rodrigues space contains all possible orientations of the unit cell. However, as we saw above, each orientation is not unique crystallographically. A fundamental zone is defined as a set of orientations that are not repeated, or are unique, meaning there are multiple. In this thesis, when we refer to the fundamental zone, we refer to the fundamental zone containing the origin, i.e. the least misoriented of each of the representations [39], [41].

It is convenient now to define the **R** vector. The direction of which is a given axis of rotation, and the length of which is proportional to the angle of rotation. Choosing the shortest **R** for a given crystallographically related orientation gives the fundamental zone in Rodrigues

space [41]. Plotting the end points of these R vectors makes a polyhedron which contains all of the unique orientations. It is worth noting that any point on the surface of this polyhedron can be mapped to a point on the opposite face of the polyhedron [39]. The shape of this polyhedron for a cubic system is a cube with truncated corners [41]. These can be seen in Figure 23

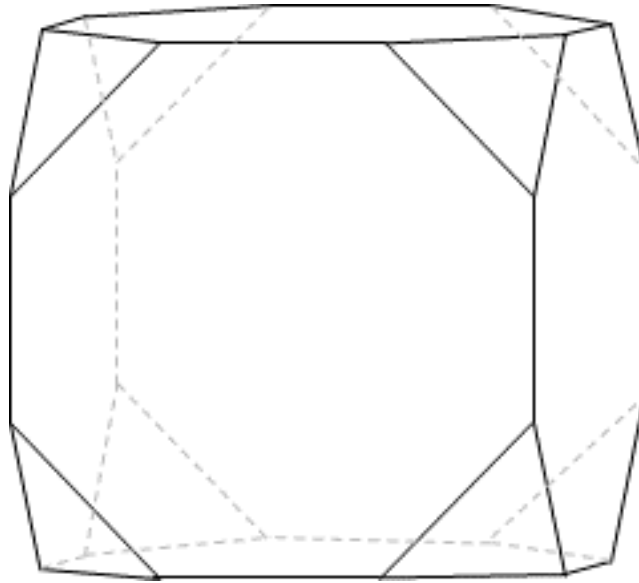


Figure 23: The fundamental zone for a cubic cell in Rodrigues space shown as a wire frame (adapted from [6])

In this thesis, I populate the library with group of rotations called the $SO(3)$ group. I detail the $SO(3)$ group in chapter 3 when discussing library generation for the pattern matching approach to indexing an EBSD. Briefly, the $SO(3)$ rotation group (special orthogonal), is the set of 3×3 rotation matrices with determinant = +1. The $SO(3)$ group is a set of all rotations (equivalent to a triclinic fundamental zone) however, by removing equivalent orientations for primitive cell symmetries it is possible to reduce the size of the group to the fundamental zone required.

10.4.1.3 Library Generation

There are multiple ways in which you can populate the library, such that the orientations are evenly distributed within orientation space, and from within the fundamental zone. One

such method, used by the De Graef group for the dictionary indexing approach, is the cubochoric method. This is described briefly here for completeness, however Chapter 3 describes the method used in this work.

10.4.1.3.1 Cubochoric Library Generation

To understand this method, I need to define the following:

- Homochoric vector: A vector (\underline{h}) defined as $\underline{h} = \hat{n} \left[\frac{3}{4} (\omega - \sin \omega) \right]^{\frac{1}{3}}$ where \hat{n} is a unit vector describing an axis of rotation and ω is an angle of rotation [81], [82].
- Homochoric ball: A ball, in which the radius (r) is equal to the maximum allowed value for \underline{h} . Given as $r = \max(|\underline{h}|) = \left(\frac{3\pi}{4} \right)^{\frac{1}{3}}$ [82].
- Cubochoric cube: A cube with a volume (V) equal to the volume of the homochoric ball. Thus $V = \pi^2$, giving a cube side length of $\pi^{\frac{2}{3}}$ [49].
- Cubochoric vector: A vector (\underline{c}) describing a rotation associated with a point on the cubochoric cube. For a full definition see the appendix of [49].
- Quaternion: A 4-D complex number, that can represent a rotation, given as $q = q_0 + q_1 \underline{i} + q_2 \underline{j} + q_3 \underline{k}$. Where q, q_1, q_2 and q_3 are related to the axis angle orientation (see section 10.5.3) by $q_0 = \cos \frac{\omega}{2}, \begin{pmatrix} q_1 \\ q_2 \\ q_3 \end{pmatrix} = \hat{n} \sin \frac{\omega}{2}$ and $|\underline{i}|^2 = |\underline{j}|^2 = |\underline{k}|^2 = -1$ [83].

The cubochoric method of generating a library, is to inscribe an equispaced grid on a cubochoric cube. Using an equal volume projection, it is then possible to transpose a \underline{c} vector associated with each point on to a \underline{h} vector. Then extend the \underline{h} vector to the homochoric ball. The homochoric ball, by its nature, contains the information about the unit quaternions associated with the point at which \underline{h} meets the homochoric ball [77]. Because

of the equal volume projection, the equispaced mapping on the cube generates a well spaced orientation distribution on the homochoric ball [49], [81]. For contrast, Chapter 3 uses a less in-depth method to generate the library.

10.5 Representations of Orientation

One of the prime uses of EBSD, is to determine the orientation of crystals in a lattice relative to a frame of reference or to another orientation. Therefore, it is important to have a consistent way of describing an orientation. A crystallographic orientation can be described using the operation to take a crystal with a reference orientation into a test configuration, i.e. using a rotation.

The five main ways of describing a rotation are:

1. Rotation matrices.
2. Bunge-Euler angles (hereafter referred to as Euler angles).
3. Axis-angle pairs.
4. Rodrigues vectors (related to the axis angle orientation).
5. Quaternions [83].

However, there are many more, less common representations, such as the homochoric or cubochoric vectors [81] or different Euler angle conventions [41].

Deciding which to use can be important for several reasons. 3-D rotation matrices, for instance, are a 3x3 matrix, thus need 9 numbers to describe what an axis angle pair does in 4 (x, y, z and rotation) or an Euler angle can do in three, thus taking up valuable computer memory and computer cost. They can also be hard to manipulate and are hard to move between/vary in a controlled manner and it is not always obvious what the misorientation between two matrices is. However, they are often convenient and efficient to use for

mathematical operations [83]. It is also possible to convert between all descriptors of orientation, thus meaning one can be used for calculation and another to store the information.

10.5.1 Rotation Matrices

A rotation matrix, is a matrix which when multiplied to a vector, rotates the vector without scaling or translating it i.e, the length of the vector remain invariant and there is an invariant point in space. Thus, for any rotation matrix ($\underline{\underline{G}}$), we know $\text{DET}(\underline{\underline{G}}) = 1$ (no volume change) and $\underline{\underline{G}}^T = \underline{\underline{G}}^{-1}$ (orthogonal) [83].

A vector, for instance a screen normal, can be rotated in 2 ways using a rotation matrix, either by pre-multiplication with a row vector or post-multiplication with a column vector. These are passive and active rotations respectively. An active rotation rotates the vector around an arbitrary axis, whereas a passive rotation rotates the reference axis around a stationary vector [83]. An active and passive rotation are shown in Figure 24.

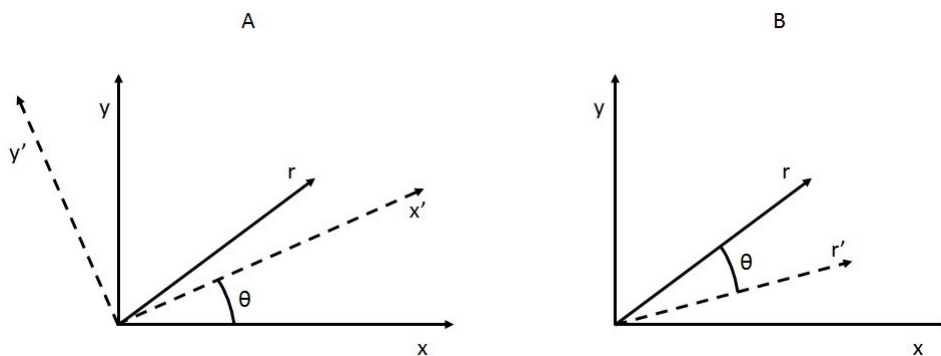


Figure 24: A) The passive rotation of an axis, (x, y) , about a vector, r , by angle θ to the new axis, (x', y') . B) The active rotation of vector, r , by the same angle to r' .

To derive the rotation matrix in 2-D, we start with a diagram (Figure 25) of a rotation coordinate frame.

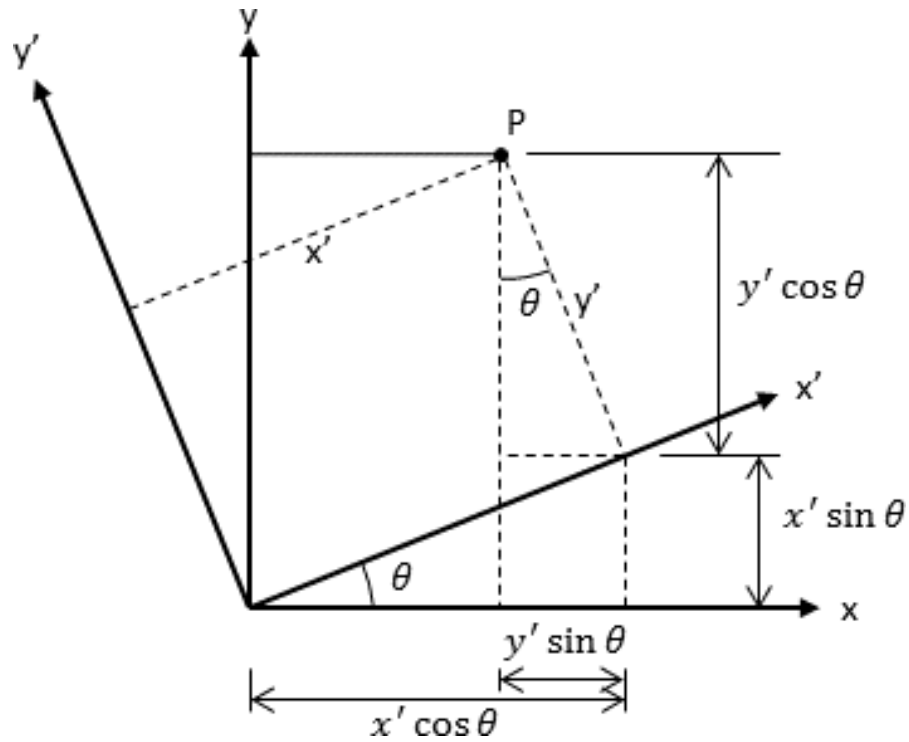


Figure 25: The original axis, (x, y) and axis rotated about angle θ to (x', y') . The point p is the endpoint of the vector being passively rotated. (Adapted from [84]).

Writing (x, y) in terms of (x', y') gives:

$$x = x' \cos \theta - y' \sin \theta \quad \text{Equation}$$

$$y = x' \sin \theta + y' \cos \theta \quad 24$$

And in matrix form:

$$\begin{pmatrix} x' \\ y' \end{pmatrix} = \begin{pmatrix} \cos \theta & \sin \theta \\ -\sin \theta & \cos \theta \end{pmatrix} \begin{pmatrix} x \\ y \end{pmatrix} \text{ Thus } \underline{\underline{G}} = \begin{pmatrix} \cos \theta & \sin \theta \\ -\sin \theta & \cos \theta \end{pmatrix} \quad \text{Equation}$$

25

Where θ is the angle of rotation. It is relatively trivial to extend this rotation to 3-D by

holding the rotation axis constant:

$$\underline{\underline{\mathbf{G}_x}} = \begin{pmatrix} 1 & 0 & 0 \\ 0 & \cos \theta & \sin \theta \\ 0 & -\sin \theta & \cos \theta \end{pmatrix}, \underline{\underline{\mathbf{G}_y}} = \begin{pmatrix} \cos \theta & 0 & \sin \theta \\ 0 & 1 & 0 \\ -\sin \theta & 0 & \cos \theta \end{pmatrix}, \quad \text{Equation 26}$$

$$\underline{\underline{\mathbf{G}_z}} = \begin{pmatrix} \cos \theta & \sin \theta & 0 \\ -\sin \theta & \cos \theta & 0 \\ 0 & 0 & 1 \end{pmatrix},$$

The rotation axis is denoted here by the subscript [84]. By combining different rotations about different axes, it is possible to represent any rotation about any vector with the origin remaining fixed. The combination of these rotation matrices can then form a single matrix describing any rotation, one way of doing so is described in section 10.5.6.1.

As matrix multiplication is non-commutative, the order in which you multiply the matrices matters. This is why you multiply right to left for an active rotation, and for passive, left to right [83].

10.5.2 Euler Angles

Euler angles describe a rotation by describing three rotations about 3 different axes.

There are multiple conventions with Euler angles (Bunge-Roe, Bunge-Kocks etc.) however,

the most common representation in EBSD is the Bunge convention. In the Bunge convention, the rotation is described as three angles, (ϕ_1, Φ, ϕ_2) . These angles describe the angle rotated about z axis, the updated x axis and the updated z axis as shown in Figure 26

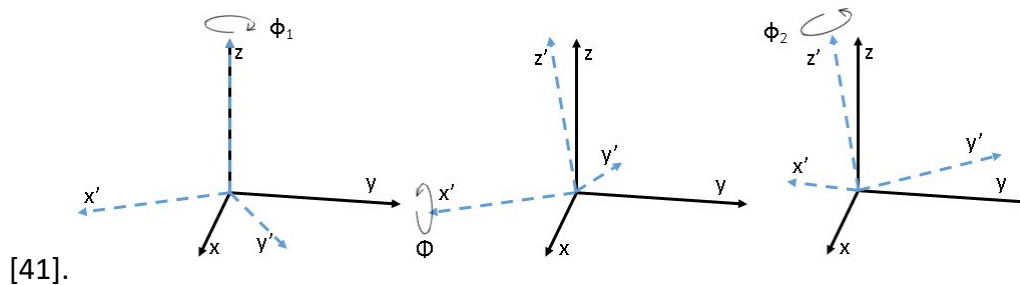


Figure 26 The Euler rotation for angles (ϕ_1, Φ, ϕ_2) .

In general the limits on the Euler angles are given as $0^\circ \leq \phi_1, \phi_2 \leq 360^\circ$ and $0^\circ \leq \Phi \leq 180^\circ$. Note that due to the periodic nature of the sine and cosine functions, other angles can be used and are equivalent.

Euler angles suffer from two main drawbacks. Firstly they can be imprecise when small angles are described. Secondly they can suffer from gimble lock, which is when one or more of the rotation matrices relating to an Euler angle is an identity matrix and the information about the rotation about that axis is lost as a result [41].

10.5.3 Axis-Angle Pairs

The axis-angle representation is important in Chapter 11 for determination of how large the angular separation of the library should be. An axis-angle pair maps a rotation through an angle, θ , about an arbitrary unit vector, $\hat{\mathbf{r}}$. Therefore, any rotation can be described by $(\theta, \hat{\mathbf{r}})$, and can be seen in Figure 27.

Decomposition into an axis-angle for a misorientation is often useful, as then a scalar value (the angle) can be used to express the magnitude of the rotation. Note that for small angles of rotation, the axis can be poorly defined.

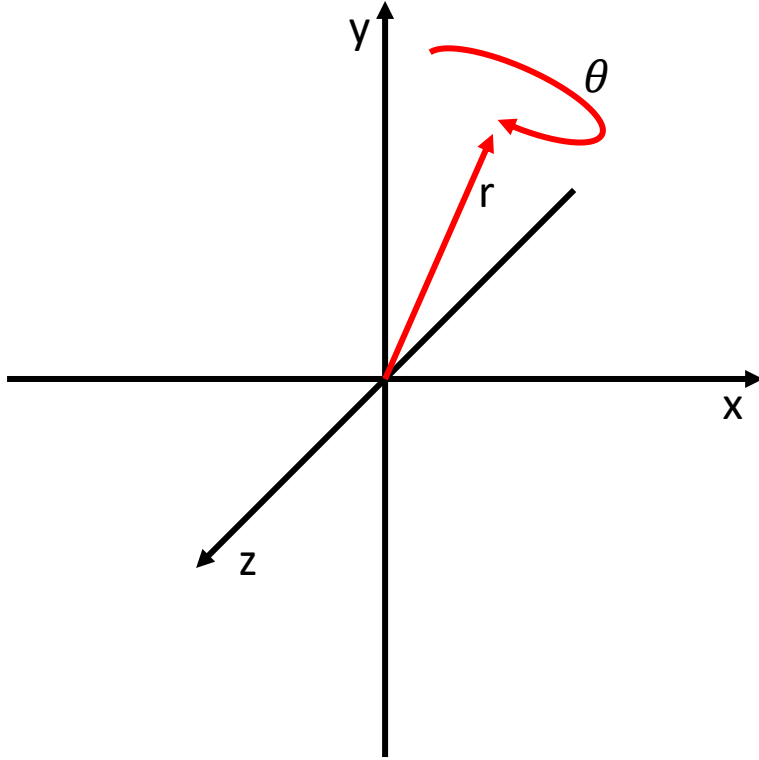


Figure 27: Graphical representation of an axis angle rotation about an arbitrary vector (r) by angle θ .

10.5.4 Rodrigues Vectors

A Rodrigues vector is similar to an axis angle pair, in that it describes the rotation angle, θ , about an axis. However, the main difference is the length of the Rodrigues vector is proportional to the angle of rotations. Therefore, describing the rotation in three digits as opposed to 4 [41]. According to [41], a Rodrigues vector, \underline{R} is written as:

$$\underline{R} = \underline{\hat{r}} \tan \frac{\theta}{2} \quad \text{Equation}$$

27

Where $\underline{\hat{r}}$ is a unit vector representing the axis of rotation.

10.5.5 Quaternions

A quaternion is essentially a 4-D complex number, made up of one real part and three complex parts and can be written in a vector-like fashion with three basis quaternions, \mathbf{i} , \mathbf{j} and \mathbf{k} . Therefore, any quaternion, q , can be written:

$$q = [q_0; q_1, q_2, q_3] \equiv q_0 + q_1\mathbf{i} + q_2\mathbf{j} + q_3\mathbf{k} \quad \text{Equation 28}$$

Where $\mathbf{i}^2 = \mathbf{j}^2 = \mathbf{k}^2 = \mathbf{ijk} = -1$. The $\mathbf{ijk} = -1$ relation derives from the basis vectors (\mathbf{i} , \mathbf{j} and \mathbf{k}) being orthogonal to each other i.e. $\mathbf{ij} = \mathbf{k} \Rightarrow \mathbf{ijk} = (\mathbf{ij})\mathbf{k} = \mathbf{k}^2 = -1$.

To use quaternions as a rotation, consider an axis angle rotation $(\alpha, \hat{\mathbf{r}})$. The rotation quaternion for this axis-angle pair can be written as:

$$q_0 = \cos \frac{\alpha}{2} \text{ and } \begin{pmatrix} q_1 \\ q_2 \\ q_3 \end{pmatrix} = \hat{\mathbf{r}} \sin \frac{\alpha}{2} \quad \text{Equation 29}$$

For a rotation in the SO(3) group, the equivalent quaternion will be of unit length.

The conjugate of a quaternion is denoted as q^* and is obtained by reversing the axis of rotation (or performing a negative rotation along the same axis). Thus:

$$q^* = [q_0; -q_1, -q_2, -q_3] \text{ or } [-q_0; q_1, q_2, q_3]. \quad \text{Equation 30}$$

Quaternion multiplication (denoted as \times_q), like matrix multiplication, is non-commutative, i.e. for two quaternions p and q , $p \times_q q \neq q \times_q p$. For the same two quaternions, the quaternion multiplication is given as:

$$\begin{bmatrix} p_0 \\ p_1 \\ p_2 \\ p_3 \end{bmatrix} \times_q \begin{bmatrix} q_0 \\ q_1 \\ q_2 \\ q_3 \end{bmatrix} = \begin{bmatrix} p_0q_0 - p_1q_1 - p_2q_2 - p_3q_3 \\ p_0q_1 + p_1q_0 + p_2q_3 - p_3q_2 \\ p_0q_2 - p_1q_3 + p_2q_0 + p_3q_1 \\ p_0q_3 + p_1q_2 - p_2q_1 + p_3q_0 \end{bmatrix} \quad \text{Equation 31}$$

Using the definitions for the elements of the quaternions in Equation 29, it is possible to rotate a vector, \underline{v} , about the axis angle pair (α, \hat{r}) either actively:

$$\underline{v}_{rot} = q \times_q \underline{v} \times_q q^* \quad \text{Equation}$$

32

Or passively:

$$\underline{v}_{rot} = q^* \times_q \underline{v} \times_q q \quad \text{Equation}$$

33

For more information on quaternions please see [83].

10.5.6 Switching Between Orientation Representations

It is often necessary to convert between the different types of representations of orientation. For instance, rotations and orientations are often stored as Euler angles, but computed as a rotation matrix [82].

10.5.6.1 Converting Between Euler Angles and Rotation Matrices

To convert from Euler angles to a rotation matrix, we follow the convention $\underline{\underline{G}} =$

$\underline{\underline{G}}_z(\phi_2)\underline{\underline{G}}_z(\Phi)\underline{\underline{G}}_z(\phi_1)$, where $\underline{\underline{G}}$ is a general rotation matrix and $\underline{\underline{G}}_n(\theta)$ is a rotation matrix

about axis n by angle θ . The matrices are multiplied from right to left for a passive rotation and left to right for an active rotation [37]. Written out fully:

$$\underline{\underline{G}} = \begin{pmatrix} \cos \phi_2 & \sin \phi_2 & 0 \\ -\sin \phi_2 & \cos \phi_2 & 0 \\ 0 & 0 & 1 \end{pmatrix} \begin{pmatrix} 1 & 0 & 0 \\ 0 & \cos \Phi & \sin \Phi \\ 0 & -\sin \Phi & \cos \Phi \end{pmatrix} \begin{pmatrix} \cos \phi_1 & \sin \phi_1 & 0 \\ -\sin \phi_1 & \cos \phi_1 & 0 \\ 0 & 0 & 1 \end{pmatrix} \quad \text{Equation}$$

34

$$\underline{\underline{G}} = \begin{pmatrix} \cos \phi_2 & \sin \phi_2 & 0 \\ -\sin \phi_2 & \cos \phi_2 & 0 \\ 0 & 0 & 1 \end{pmatrix} \begin{pmatrix} \cos \phi_1 & \sin \phi_1 & 0 \\ -\cos \Phi \sin \phi_1 & \cos \Phi \cos \phi_1 & \sin \Phi \\ \sin \Phi \sin \phi_1 & -\sin \Phi \cos \phi_1 & \cos \Phi \end{pmatrix} \quad \text{Equation}$$

35

G

Equation

$$= \begin{pmatrix} \cos \phi_1 \cos \phi_2 - \cos \Phi \sin \phi_1 \sin \phi_2 & \cos \phi_2 \sin \phi_1 + \cos \Phi \cos \phi_1 \sin \phi_2 & \sin \Phi \sin \phi_2 \\ -\cos \phi_1 \sin \phi_2 - \cos \Phi \sin \phi_1 \cos \phi_2 & -\sin \phi_1 \sin \phi_2 + \cos \Phi \cos \phi_1 \cos \phi_2 & \sin \Phi \cos \phi_2 \\ \sin \Phi \sin \phi_1 & -\sin \Phi \cos \phi_1 & \cos \Phi \end{pmatrix} \quad 36$$

Converting back to Euler angles from a rotation matrix is not trivial because of the mismatch in

possible angles for Euler angles and the range of allowed values for sine or cosine. If we let

element $G_{31} = \sin \Phi \sin \phi_1 = 0.439$, and $\Phi = 35^\circ$, the possible values for ϕ_1 are 50° and 130° .

Thus to resolve we need to take into account other elements such as G_{32} [41].

10.5.6.2 Converting Axis-Angle Pairs to a Rotation Matrix

To convert to a rotation matrix from an axis angle pair, we follow the method outlined in

[85]. To begin, we sketch the rotation and label as in Figure 28

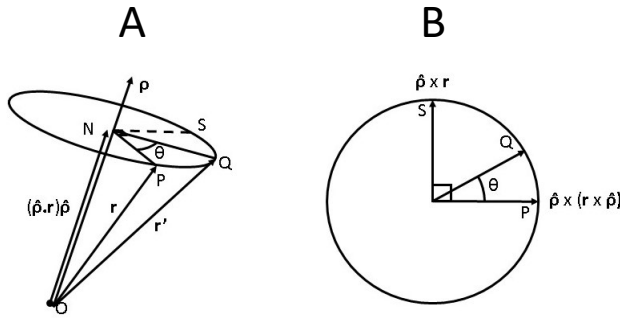


Figure 28: A vector pre and post rotation. Reproduced with permission of Oxford Publishing Limited through PLSclear. From *Interfaces in Crystalline Materials* by A. P. Sutton and R. W. Balluffi

**_

$$\underline{r}' = \underline{OQ} = \underline{ON} + \underline{NQ} \quad \text{Equation}$$

$$= (\hat{p} \cdot \underline{r}) \hat{p} + \cos \theta [\underline{r} - (\hat{p} \cdot \underline{r}) \hat{p}] + \sin \theta (\hat{p} \times \underline{r}) \quad 37$$

$$= \underline{r} \cos \theta + (\hat{p} \cdot \underline{r}) \hat{p} (1 - \cos \theta) + \sin \theta (\hat{p} \times \underline{r})$$

By expressing this in component form, it is possible to retrieve the rotation matrix, R:

$$r'_i = \sum_{j=1}^3 R_{ij} r_j \quad \text{Equation 38}$$

Where

$$R_{ij} = \cos \theta \delta_{ij} + \rho_i \rho_j (1 - \cos \theta) - \sum_{k=1}^3 \epsilon_{ijk} \rho_k \sin \theta. \quad \text{Equation 39}$$

δ_{ij} is the Kronecker delta:

$$\delta_{ij} = \begin{cases} 1, & \text{if } i = j \\ 0, & \text{else} \end{cases} \quad \text{Equation 40}$$

And ϵ_{ijk} is the permutation tensor such that:

$$\epsilon_{ijk} = \begin{cases} 1, & \text{if } i, j, k \text{ are an even permutation of } 1, 2, 3 \\ -1, & \text{if } i, j, k \text{ are an odd permutation of } 1, 2, 3 \\ 0, & \text{else} \end{cases} \quad \text{Equation 41}$$

It follows that $\text{trace}(\underline{\underline{\mathbf{R}}}) = 1 + 2 \cos \theta$ and the rotation axis is parallel to $[R_{32} - R_{13}, R_{13} - R_{31}, R_{21} - R_{12}]$.

10.5.7 Advantages and Disadvantages

Knowing the advantages and disadvantages of each type of representation is important when deciding which to use in a given situation.

Table 1 lists the main advantages and disadvantages of each type of representation used in this thesis.

Table 1: The advantages and disadvantages of each representation of rotation.

Representation	Advantages	Disadvantages

Rotation matrix	<p>Easy to separate into component form</p> <p>Computationally efficient – calculations with rotation matrices require a 3x3 array and a 1 x 3 vector, with little calculation or converting needed.</p> <p>Easy regulation of floating-point variables</p>	<p>Information redundant, 9 digits needed to store an orientation.</p> <p>Imprecise with small angles</p> <p>Hard to determine misorientation without calculation.</p>
Euler angles	<p>Efficient to store – three digits to store a rotation</p> <p>Computationally efficient – one calculation is needed to convert to a rotation matrix</p>	<p>Difficult to visualise or directly calculate misorientations, prone to rounding errors</p> <p>Gimble lock – When one or more rotation matrices is an identity, rotational degrees of freedom are lost.</p>

		1° steps in angles do not equate to 1° steps in orientation space.
Axis angle pair	<p>Intuitive and easy to visualise</p> <p>Efficient to store – four digits for a rotation.</p>	<p>Mathematical manipulation usually requires transformation to another representation, e.g. a rotation matrix.</p>
Rodrigues Vectors	<p>Efficient to store – a rotation angle and a 3-D vector.</p> <p>Easy to convert to Euler angles [86]</p> <p>Easy to construct and visualise fundamental zones and crystal symmetries graphically</p>	<p>Rounding errors can be missed leading to a cumulative error throughout calculations.</p>
Quaternions	Efficient to store.	<p>Computationally less efficient than Euler angles – rotation of a 3-D vector requires 32 scalar</p>

	<p>The mean orientation is easy to estimate (arithmetic mean of the terms) [87]</p> <p>Quaternions related by crystal symmetry are easy to identify via inspection</p>	<p>multiplications and 24 additions.</p>
--	--	--

The main source for this table is [83], with contributions from [20], [23], and [27] with any additional sources stated.

10.5.8 Phase Classification Using Electron Backscatter Diffraction

As well as orientation, EBSD can also be used to determine the phase of a unit cell in a crystal. There are several ways each unit cell can differ, and which can potentially be detected using EBSD. These are:

1. Different primitive cells (e.g. hexagonal vs cubic)
2. Different Bravais lattice (e.g. FCC vs BCC)
3. Same Bravais lattice, different lattice constants (e.g. FCC silver vs FCC copper)

Section 10.4.1 has more detail on crystal phases.

Again, the standard method of determining the phase of a lattice is to use the Hough based indexing approach. But this is still limited as, especially in case 3, more subtle features of the pattern are important [36].

10.5.8.1 Hough Based Methods

As previously discussed, Hough based analysis of EBSPs focuses on a comparison of the interplanar angles of diffracting lattice planes, using a look-up-table [1]. Phase classification, with this method, is performed through finding the library that best matches the pattern for indexing the bands [27], [41]. These libraries of interplanar angles come from an associated list of candidate phases. Selection of the best match is done through either a selection of the best ‘confidence index’ (associated with voting for the best index of band triplets, as per [5]) and/or the best angular fit between matched solution and the input crystal structure. Once the phase of the crystal is ascribed, the crystal orientation can be measured [1].

10.5.8.2 Pattern Matching Methods

Pattern matching approaches follow a similar method to the Hough and template matching approaches described earlier, for phase classification. In this method, multiple libraries of images are generated and both libraries are searched, analogous to the look up tables in the Hough based approach. The library that returns the best match (highest CC) is generally taken to be the library that correctly identifies the phase of the pattern [7], [36], [89].

In the Dictionary Indexing method [7] template matching is performed using the ‘dot product’ between the vectorised forms of the simulated and experimental patterns, and the highest value of the dot product for a phase and orientation is selected. As an addition to this, Ram *et al.* 2018 [36] devised a metric to determine the accuracy of this matching approach. This is discussed in more detail in Chapter 12.

A variation on pattern matching has been introduced by Winkelmann *et al.* [90], which has been used for phase classification and pseudosymmetry based orientation determination.

Another notable variant is the mixture of high angular resolution (HR-) EBSD and pattern

matching for martensite-based orientation determination and tetragonal distortion analysis as demonstrated by [91].

While this thesis was conducted, Hieschler *et al.* [50] used non-equispaced Fourier transforms to perform cross correlation on the sphere, and this was based upon an idea introduced by Day [77]. There is also recent work on this method in [78]. The spherical approach has been used with a linear mixing of the reference spheres to attempt to correlate this with phase fraction, though the validation of this newer variant is limited.

10.5.8.3 EDX and its use with EBSD

Energy dispersive X-ray spectroscopy (EDX) is the analysis of the bremsstrahlung emitted when electrons are diffracted. The spectrum consists of two main features, a noisy background spectrum, with large peaks at “characteristic wavelengths.” These wavelengths correspond to the energy of the transitions of electrons moving between energy levels that occur because of the electron – atom interactions. These energy spikes are usually characteristic of certain elements that are present, see Figure 29. Artifacts in the spectrum not associated with the characteristic peaks can include: electromagnetic interference (such as ground currents or those generated by components of the machine). Direct entry of electrons into the detector. Spurious X-rays and peaks can be lessened by detector saturation [92].

EDX can be performed at the same time as EBSD allowing for data about the chemistry to be collected and used to aid with phase identification [93]–[96].

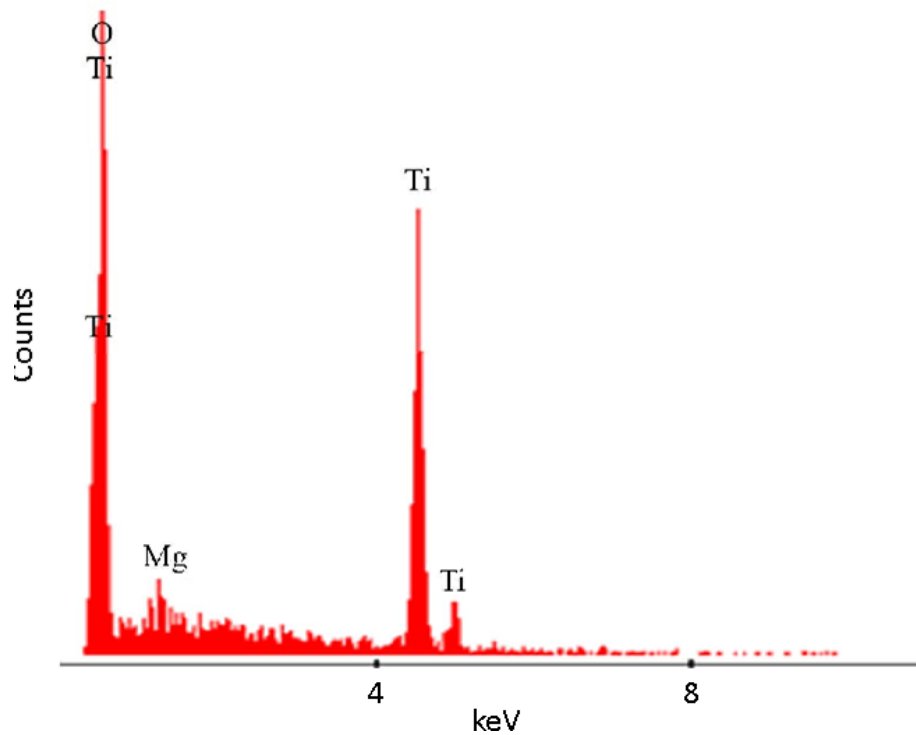


Figure 29: A typical EDX spectrum. Reproduced from [97]

A more recent approach to combining EBSD and EDX was introduced by McAuliffe *et al.* [98]. The method makes use of the principal component analysis (PCA) introduced by Wilkinson *et al.* [99]. In this approach the EDS data is stitched to the end of the EBSD PCA data and a weighting applied to suppress the EDX data. The data is then analysed as per the PCA approach.

The most modern techniques even take advantage of machine learning algorithms to determine phases [100]. In these machine learning approaches it has been shown the algorithm focuses on key features of the EBSD, such as zone axes [101].

10.5.8.4 Pseudosymmetry

Pseudosymmetry occurs where a lower order of symmetry (see section 10.4.1.1) has values for \hat{a} , \hat{b} and \hat{c} and α , β and γ close to values of that for a higher order of symmetry. This leads to crystallographically distinct orientations having similar EBSDs [102]. This is demonstrated in Figure 30. These similar EBSDs are indistinguishable in the conventional

Hough based approach to orientation determination because of similarly placed bands. This means the Hough based approach essentially mistakes an n -fold symmetry axis for a $2n$ -fold symmetry axis and misidentifies the orientation [103], [104].

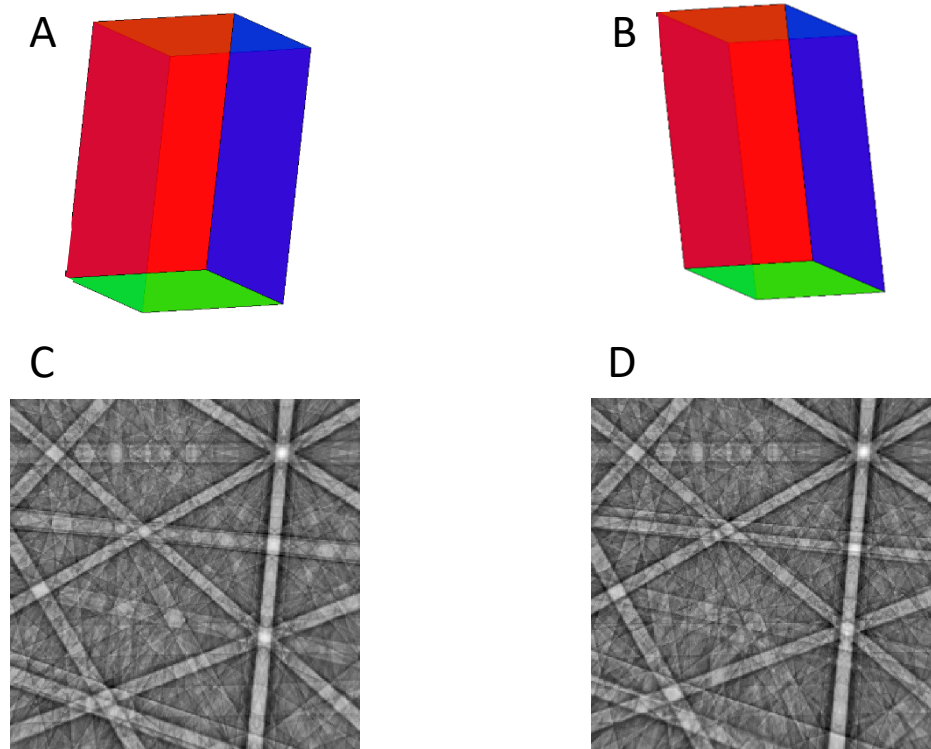


Figure 30: Two distinct but pseudosymmetrically equivalent orientations for $\text{Al}_{13}\text{Fe}_4$ (A and B) and their dynamical simulations (C and D).

There are multiple solutions to obtaining the correct orientation when dealing with pseudosymmetry. For purely Hough based solutions you can decrease your z^* value (bring the sample closer to the screen) or change the lower number of bands needed to index the pattern [105], [106]. It has also been shown the dictionary indexing method can be applied to pseudosymmetry [89], [104]. However this requires a large library size, which makes the process slow [8], [102]. Pang *et al.* [102] suggest a combination Hough and dictionary approach, in which the Hough based indexing is used to select potential orientations and the library of patterns built up around a select few candidate orientations.

This thesis also proposes a solution in contrast to all of the above and discusses it more in Chapter 13.

10.5.9 Detectors

10.5.9.1 Standard detectors

Standard EBSD cameras consist of three main components: A scintillator, with an optical coupling to a 2-D, photon sensitive computer chip. It is usual for the scintillator to be a phosphor screen, the optical array to be a lens and the chip to be a charge coupled device, CCD [1]. This setup has remained mostly unchanged since the early 1990s for most commercially available detectors [35] and is shown in Figure 31.

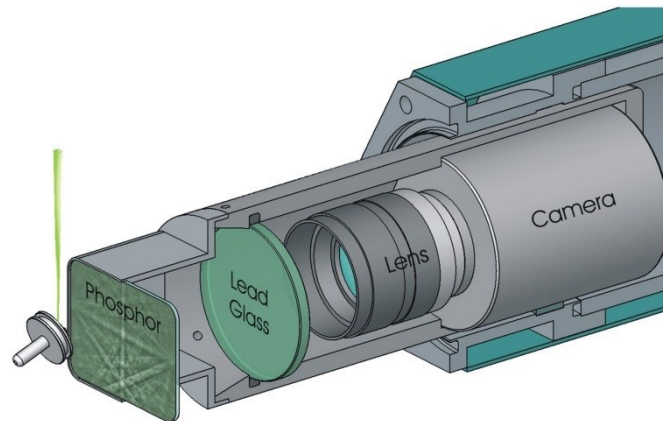


Figure 31: Cartoon of the cross section of a typical EBSD detector. Figure reproduced from [107]. (Reprinted from *Ultramicroscopy*, 111, K. Mingard, A. Day, C. Maurice, P. Quested, Towards high accuracy calibration of electron backscatter diffraction systems, 320 - 329, Copyright (2011), with permission from Elsevier)

One of the drawbacks to this detector set up, is the fact that the lens can distort the image, thus distorting the EBSP. This distortion can be measured and corrected for by applying a checkerboard pattern to a clean phosphor and shining a light through it for the CCD to correct this image [107]. However, removing the lens and replacing it with a fibre optic array can reduce the lens distortion [1], [35].

Another drawback to the standard set up is the trade-off between speed of capturing the EBSPs and image quality. An increase in capturing speed is usually gained via binning of the

patterns. Larger bins leads to a larger electron dose per pixel and result in a lower signal to noise ratio, but this corresponds to a reduced image quality. This is because the angular resolution within the pattern is reduced. Smaller bins lead to sharper patterns, but require more time to acquire [108], [109]. Note that most Hough-based routines will resize the pattern prior to the Hough-transform, and thus many ‘high resolution’ patterns just result in a higher electron dose. To overcome this speed/quality trade off, Oxford Instruments recently redesigned a camera around a complimentary metal-oxide semiconductor (CMOS) chip and fibre-optic coupling, and claim that updated chip allows for fast and high quality image collection [109].

A CMOS chip is similar in many ways to the older CCD chip. The main difference that allows the CMOS to be faster is the way in which the images are read. In a CCD the charge is transported to a corner and read via analogue to digital converter. A CMOS has many transistors near each pixel, thus allowing for individual pixels to be read [110] but these detectors are difficult to spatially bin and may be subject to high image read-out noise.

10.5.9.2 Direct detectors

More recent developments in capturing an EBSD are to use a direct electron detector (DED) thus removing the need for an optics array and scintillator [35].

A hybrid-pixel DED consists of a thin semiconductor with n-type and p-type contacts on opposing sides. A reverse bias is applied across these contacts. When an electron is incident on the semiconductor, an electron-hole pair is formed, which is accelerated towards the contacts because of the bias. The contacts are connected to conductive strips which transport the charge for signal processing. These contacts and conductive strips are arranged in a grid allowing for 2-D spatial resolution [111]. A cartoon of a DED can be seen in Figure 32.

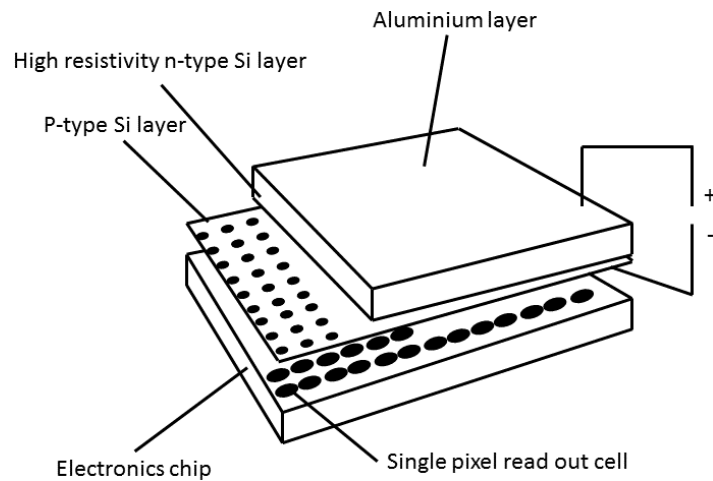


Figure 32: Cartoon of the cross-section of a DED (adapted from [112])

10.5.9.3 Timepix 2 Detector

The Timepix 2 camera is an advancement to the detector style described above. In the Timepix 2, the three main differences are:

1. There is a single threshold with 4 bits threshold adjustment.
2. Each pixel has three operation modes (counting, time over threshold and arrival time).
3. The counting clock is synchronized to an external clock.

For general EBSD, only the counting mode is important.

Each pixel in the Timepix 2 detector is comprised of two main components. The analogue half collects and amplifies an incoming signal, provided the input signal strength is above a threshold set by the user. The digital half buffers and gates the analogue signal. The digital part also synchronises the counts to the reference clock to allow for glitch free counting

[113][114]. This can be seen in Figure 33

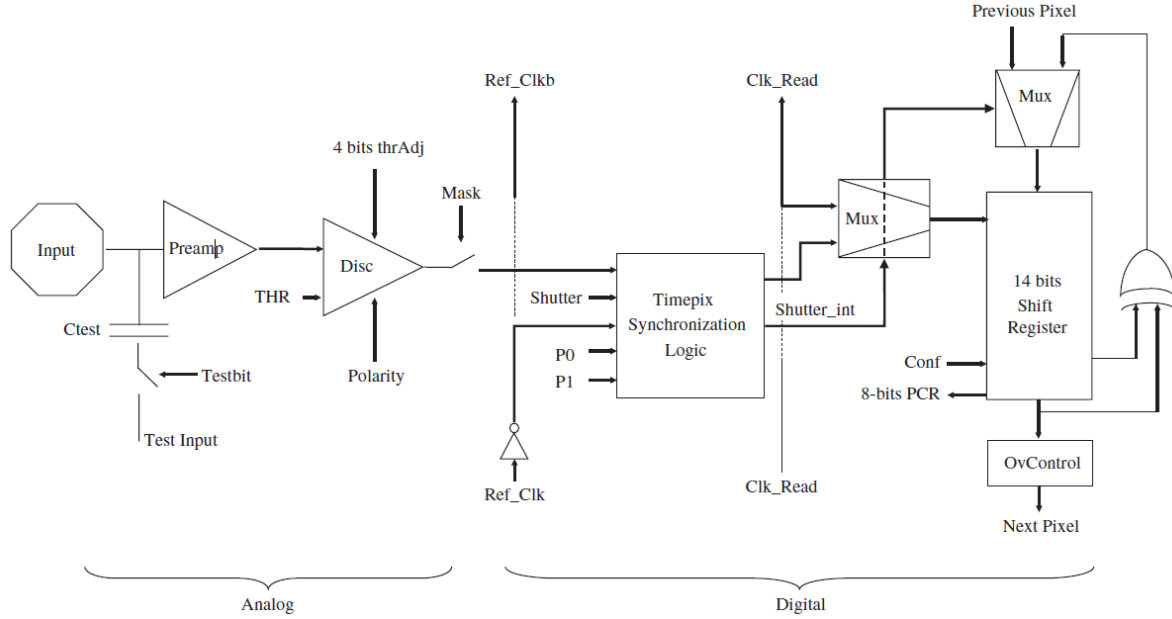


Figure 33: A schematic of a Timepix 2 pixel, reproduced from [113]. (Reprinted from *Nuclear Instruments and Methods in Physics Research Section A: Accelerators, Spectrometers, Detectors and Associated Equipment*, 581, X. Llopart, R. Ballabriga, M. Campbell, L. Tlustos, W. Wong, *Timepix, a 65k programmable pixel readout chip for arrival time, energy and/or photon counting measurements*, 485 - 494, Copyright (2007), with permission from Elsevier)

This allows the detector to count events rather than giving an output proportional to the energy of an input. Hybrid detectors, such as the Timepix 2 also have a separate detector and electronic array, meaning a choice of detectors are available [115] .

10.5.9.4 Detector Properties

Chapter 6 looks at the development of a Timepix DED based EBSD system. Thus it is

important to define important quantities that quantify how well a detector can capture EBSD information, similar to [116].

10.5.9.4.1 Modulation Transfer Function

The modulation transfer function (MTF), is the special frequency response of an imaging system. For EBSD, the MTF determines how capable an imaging system is at detecting a small shift [117].

In this thesis, the MTF of a system is calculated using the method derived by Meyer and Kirkland [118], outlined here:

An aluminium stub is polished, but not to a mirror finish. This allows for an even spread of background electrons with no EBSPs. A conductive, non-magnetic wire is placed between the sample and the screen, at an $\sim 30^\circ$ angle, this creates a shadow of a line on an even background of the detector.

The edge of this shadow creates a step function, which is convenient to use here as the Fourier transform of a step function contains all spatial frequencies. Taking an edge profile of the shadow will not give a perfect step function. To smooth out the edge profile, multiple profiles are taken and averaged together. A typical and theoretical edge profile are shown in

Figure 34.

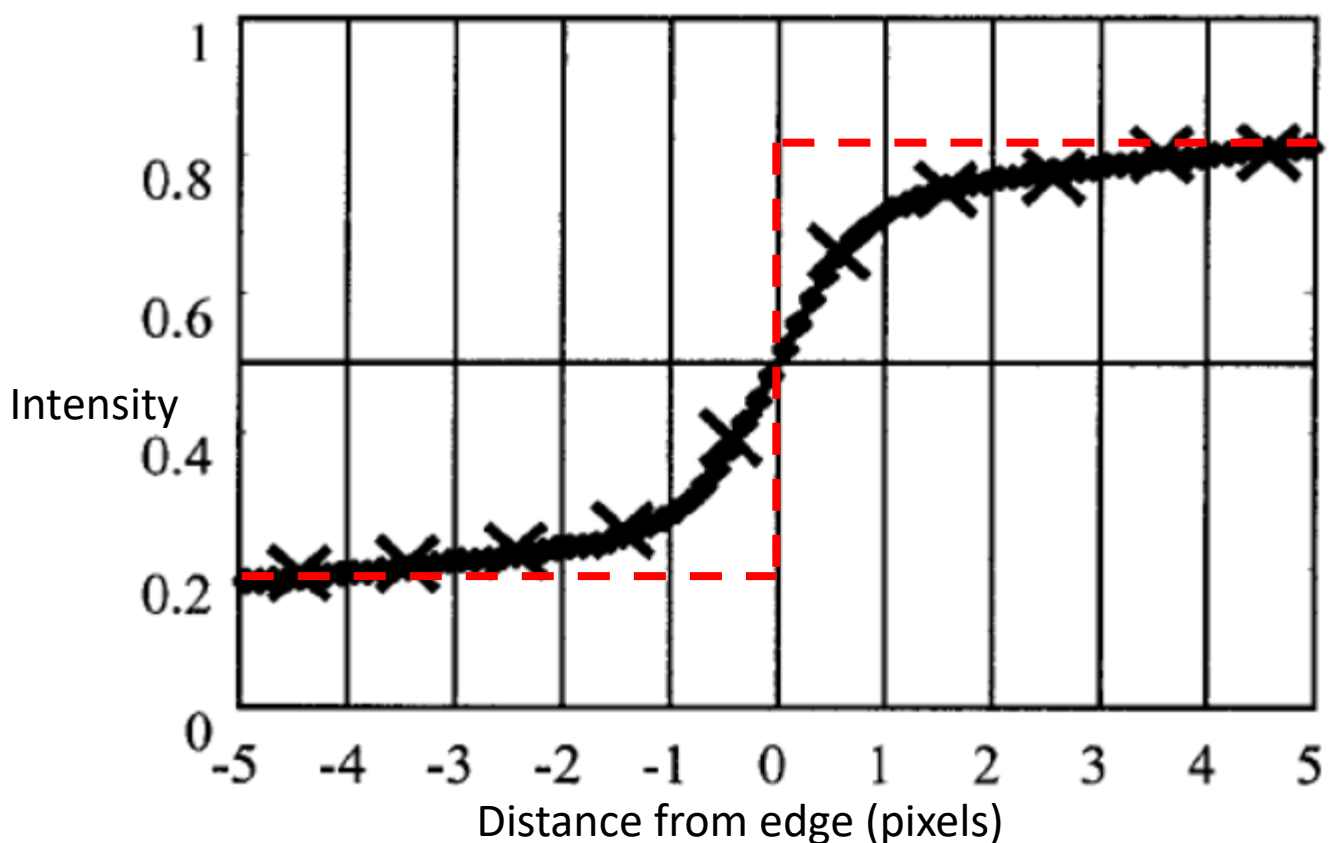


Figure 34: The black line shows an experimental edge function with the red dashes showing an idealised step function. Figure adapted from [118]

The deviation of the measured step from an idealised step can be defined as the line spread function, LSF, the Fourier transform of which is the MTF. Mathematically, this goes as follows:

The edge profile is made to be symmetric:

$$\tilde{f}(x) = \frac{w(x)f(x) + w(-x)(1 - f(-x))}{w(x) + w(-x)} \quad \text{Equation 42}$$

Where the weighting factor $w(x) \propto 1/\sigma(x)$, where $\sigma(x)$ is the mean deviation of the values for x from the average line profile.

To calculate the Fourier transform of the LSF, we set:

$$\tilde{f}(x) = LSF(x) \otimes \chi_{[0,\infty]}(x) \quad \text{Equation 43}$$

Where $\chi_{[0,\infty]} = 1$ for $x \in [a, b]$ and 0 elsewhere and \otimes is the mathematical convolution operator.

Numerical differentiation gives

$$\begin{aligned} g(x) &= \tilde{f}(x + 0.5) - \tilde{f}(x - 0.5) \\ &= LSF(x) \otimes \chi_{[0,\infty]}(x) \otimes (\delta(x + 0.5) - \delta(x - 0.5)) \\ &= LSF(x) \otimes \chi_{[-0.5,0.5]}(x) \end{aligned} \quad \text{Equation 44}$$

Taking the Fourier transform of both sides gives the MTF to be:

$$MTF(k) = \frac{G(k)}{\text{sinc } \pi k} \quad \text{Equation 45}$$

Where $G(k)$ is the Fourier transform of $g(x)$.

Correcting for integration over the pixel size gives the MTF of the scintillator, MTFs to be:

$$MTFs = \frac{MTF(k)}{\text{sinc } \pi k} \quad \text{Equation}$$

46

10.5.9.4.2 Detective Quantum Efficiency

The detective quantum efficiency (DQE) quantifies how efficiently the detector can transfer data. For a given input signal N , there is an output signal, $S(N)$, defining the DQE as:

$$DQE = \left(\frac{d\bar{S}}{d\bar{N}} \right)^2 \frac{\text{var } N}{\text{var } S} \quad \text{Equation}$$

47

Where the bar denotes an average value and var is the variance. For an ideal detector,

$$DQE = 1 \text{ [119].}$$

In [35] the DQE is defined as:

$$DQE(u, v) = DQU(0, 0) \left(\frac{MTF(u, v)}{NTF(u, v)} \right)^2 \quad \text{Equation}$$

48

Where $DQE(0,0) = DQEs(0,0)$ assuming equal pixel size and spacing and where $DQEs$ is the DQE at the scintillator. NTF is the noise transfer function given as:

$$NTF(u, v) = \left\{ \sum_{m,n} NTFs(u + m, v + n) \right. \quad \text{Equation}$$

49

$$\left. \cdot \text{sinc}^2(\pi(u + m)) \text{sinc}^2(\pi(v + n)) \right\}^{\frac{1}{2}}$$

Where m and n take the values of -1, 0 and 1 $NTFs$ is the NTF at the scintillator given as:

$$NTFs(u, v) = \sqrt{\frac{V_{out}(u, v)}{V_{out}(0,0)}} \quad \text{Equation}$$

50

Where V_{out} is the variance in output signal.

Comparisons of the MTF and DQE of various detectors can be found in refs [120]–[123], however, it should be noted these deal with lower electron doses than would be found in a typical EBSD experiment.

11 Development and Testing of the Refined Template Matching Algorithm

11.1 Introduction

In this chapter, I will introduce a refined template matching approach (RTM) to EBSD

analysis. This algorithm and analysis approach underpins work in subsequent chapters

within this thesis. Note, this work has been previously published on ArXiv

(<https://arxiv.org/abs/1807.11313>) and later published in reference [8].

The RTM uses a Fourier domain based pattern matching method [124] and a fast refinement of the orientation, from which several advantages can be demonstrated:

1. A more robust matching than the normalised dot product (NDP) is attained. This enables comparison with a sparser template library (i.e. fewer patterns within the library).
2. The fast Fourier transform (FFT) based cross correlation function (XCF) enables whole pattern translations to be accounted for. These can accommodate large changes and/or uncertainties in the pattern centre (PC) as well as orientation changes.
3. A refinement of the orientation can be rapidly calculated to provide an orientation precision which is substantially better than the precision of library sampling.

Traditional template matching usually generates a library (\mathbf{M}_i^k) of k potential templates and compares these with an experimental EBSD to find the closest match and assign classification of the crystal orientation and/or phase. The library is generated to populate orientation space with finely-spaced sampling to improve orientation resolution.

In prior work, within the Dictionary Indexing method, each experimental pattern (E_i) is compared with each pattern from the library (in turn) via the average inner product, where each pattern is written as a linear vector of pixels (indexed from $i = 1$ to d , where d is the number of pixels in the vector):

$$C^k = \frac{1}{d} \sum_{i=1}^d \frac{\mathbf{M}_i^k \mathbf{E}_j}{|\mathbf{M}_i^k| |\mathbf{E}_j|} \quad \text{Equation 51}$$

This thesis extends this idea substantially, noting that the inner product is related to a special case (the point at the origin) of a frequency based cross correlation. A frequency based cross correlation also contains information about the (translational) shift in each pixel (m, n) between two image arrays, such that:

$$C_{m,n}^k = \sum_{i,j} M_{x+m,y+n}^k E_{x,y}. \quad \text{Equation 52}$$

The information about these shifts can be extracted within the frequency domain via the 2D-FFT which is computationally inexpensive and enables frequency based pattern filtering (i.e. removal of high spatial frequency noise and long range low frequency intensity gradients).

$$C_{m,n}^k = \text{iFFT}(\text{FFTM}^k \odot \text{FFTE}) \quad \text{Equation 53}$$

Where FFT and iFFT are the fast Fourier transform and inverse fast Fourier transform respectively and \odot is described fully by Equation 55 and Equation 56.

In this chapter, I demonstrate that by including the shifts as a degree of freedom I can broaden the sampling of orientation space and normalise the cross correlation more formally. The additional shift information can then be used in multiple ways to improve the matching procedure, details are given in later sections of the chapter.

The major benefit of the FFT based correlation, is that a shift in the input patterns can be accounted for. This can be visualised in 1D, if a gaussian signal is considered, as shown in Figure 35. It is possible to take a gaussian and alter the mean, generating an identical, shifted gaussian. This is equivalent to two patterns matching with a shift or as a phase shift in the input signal. Performing an NDP for the shifted gaussians against the unshifted gaussian in both the real and Fourier domains gives a stark contrast in reliability, as shown in Figure 35.

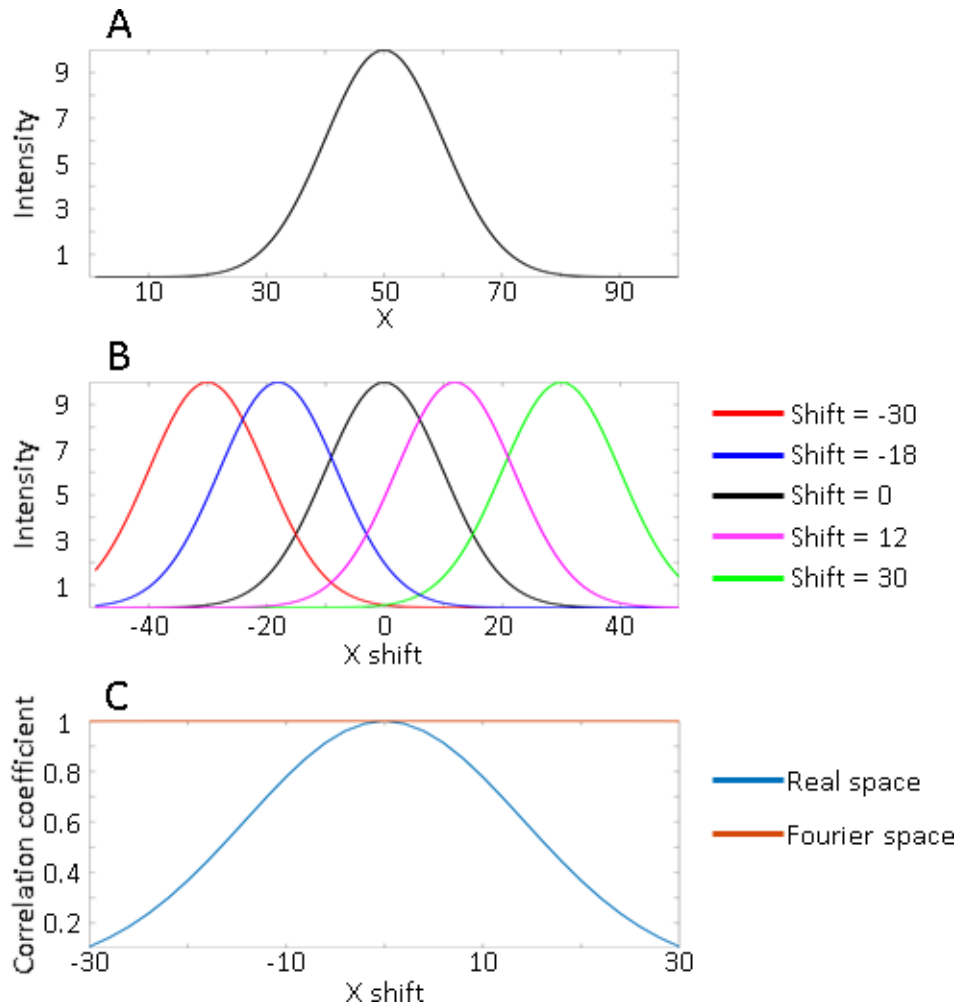


Figure 35: A) An initial input gaussian. This curve stays stationary and is the reference about which the shifted gaussians are compared. B) 5 examples of mean or phase shifted gaussians. C) The correlation coefficients of the NDP of the shifted vs reference gaussian in real and Fourier space.

Figure 35 shows the matching performed in Fourier space, at the most basic level, is phase independent, while the shift measured in real space rapidly declines in accuracy as the shift increases.

Applying a 2D Fourier transform to an EBSD generates a 2D Fourier power spectrum, upon which the match and shift of phase is calculated. Examples of the input patterns and their respective spectra can be seen in Figure 36.

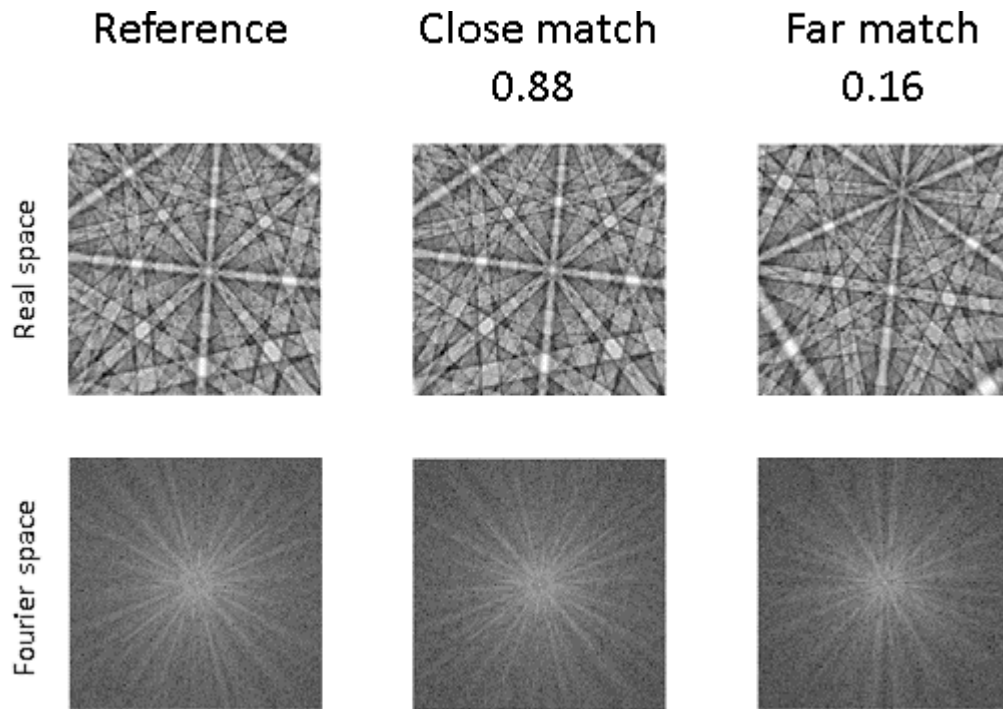


Figure 36: A reference EBSP generated with Euler angles ($15^\circ, 20^\circ, 25^\circ$), a close match with Euler angles ($15^\circ, 19^\circ, 24^\circ$) and a far match with Euler angles ($63^\circ, 55^\circ, 30^\circ$). The 2D Fourier transforms are shown below the respective inputs, and the correlation coefficients below the label. For each simulation the PC is (0.5, 0.3, 0.6) and the material simulated is ferrite.

11.2 Method Overview

Figure 37 outlines the template matching methodology, which is introduced briefly here.

Each step is subsequently described in greater detail.

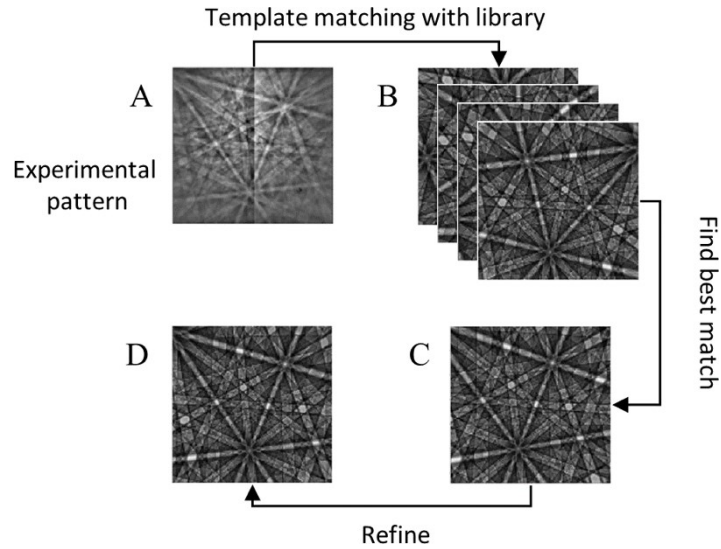


Figure 37: The template matching method follows the following steps: A) An experimental pattern is imported for indexing. B) A library of templates is searched using an XCF to determine the orientation in $SO(3)$ space (the 3D-rotation group) closest to the experimental pattern (C). D) The best orientation is refined to match the experimental orientation.

Firstly, methods of template matching, based upon the NDP (fixed templates) and 2D-FFT correlation (template translation allowed) approaches are introduced.

Next the generation of a library of EBSPs (templates), generated using a uniform sampling of the 3D-rotation group (hereon denoted as $SO(3)$ space), with the MTEX 5.0.1 package for MATLAB [125] is introduced. The patterns in the library are compared to a pattern to be indexed using an image XCF. The crystal orientation of the test pattern is defined from the pattern with the closest match from the library. For the comparison, EBSPs are read in and background corrected, the patterns are then cropped to be square (optimal for a 2D FFT).

The discrete (and for the 2D-FFT case relatively sparse) nature of the library has prompted the creation of a refinement step to interpolate from the best templated orientation to a more precise ultimate orientation. The refinement step approach also enables the pattern centre of the library and the experiment to be different and subsequently corrected (which is important for large area maps). The refinement is applied to the best match from the library search, comprising a translation in the plane of the detector (x and y translations,

after correcting for pattern centre changes across the map) and a rotation about the normal to the detector (z - from a log-polar transform); this is iterated until a sufficiently good match is found and the final orientation is calculated.

11.3 Image Cross Correlations

Pattern matching can be performed using either the NDP [67], [126], [127], or alternatively the 2D-FFT [75], [128]–[130].

11.3.1 Normalised Dot Product

The Dictionary Indexing method of pattern matching uses the inner product, which is also called the normalised dot product (NDP) [34]. This is calculated using Equation 51. Chen et al. [34] introduces the Dictionary Indexing method and comments that this index is used as a ranking to determine the best match from the dictionary of patterns. The inner product is calculated to have a value of 1, when the intensity distributions in both patterns are equal. It is not clear what the value of the NDP should be for two patterns with a similar spatial features within the diffraction patterns, and therefore crystal structures, but different intensity values. Furthermore, Chen et al. [34] suggests only a SVD based background correction and they do not suggest significant image processing (e.g. contrast normalisation) which is typically performed for cross correlation and this may result in difficulties in evaluating the relative quality of the matching.

For the present work, I utilise contrast normalisation (as the intensity distribution within the experimental pattern is a near arbitrary unit) and utilise software based background correction for our experimental patterns. With the NDP, two identical images have $r_{fg} = 1$, and two completely dissimilar images have $r_{fg} = 0$. Unfortunately, two images of similar structure, but different intensity values will unlikely to have $r_{fg} = 0$ and the contrast range and stability of the NDP has not been systematically established.

11.3.2 Fast Fourier Transform

In the FFT method, I perform a comparison in the frequency domain. This enables translation shifts in the spatial domain to be represented as phase shifts in the frequency domain. These shifts extend the cross correlation to enable comparisons with spatial offsets between the template and experimental patterns. In physical reality, these shifts can be a combination of an incorrect pattern centre and/or a misorientation. The misorientation freedom enables a greater offset in orientation between our template and experimental pattern, which in turn enables a sparser orientation sampling of our library, i.e. fewer points in SO(3) needs to be sampled. A reduction in the library size has a significant computation advantage (a smaller library and fewer cross correlation calculations).

In preparation for the FFT-based cross correlation, both images are cropped to be square¹ and the pattern centre of the cropped image is updated accordingly². I then convert the images to be compared into the Fourier domain, using the FFT (Equation 54)

$$F(u, v) = \sum_{x,y} \frac{f(x,y)}{\sqrt{MN}} \exp \left[-2i\pi \left(\frac{ux}{M} + \frac{vy}{N} \right) \right]. \quad \text{Equation}$$

54

Where the capital letters F denotes the Fourier transform of an image (e.g $\text{FFT}(f) = F$), M and N are the image dimensions in Fourier space and the FFT coordinates are (u, v) .

Comparison is performed in the frequency domain, after the application of filters, windowing and upsampling of the peak to enable subpixel shift resolution, as described

¹ Non-square patterns can be compared but this can be computationally difficult, as the FFT combined with the filters I use is easier to employ for a $2^n \times 2^n$ field of view.

² The PC is defined in units of screen size, with the PC in the x direction being in units of screen width. Cropping the screen to be square, thus, changes the screen width and hence the fraction of the screen used for the PC. E.g. if the screen is cropped from 200 to 128 pixels and the PC in x was 0.4 pre crop, post crop it would be 0.34.

previously by Wilkinson et al. [75]. This process enables background correction (through a high pass filter), removal of high frequency noise (through a low pass filter) and management of alias artefacts via windowing and leaves high contrast Kikuchi patterns remaining.

Cross correlation using a 2D-FFT approach also allows freedom to measure suitable correlations if there is a horizontal and/or vertical translation of the two images (and that translation can be measured from the XCF peak position). Cross correlation of the 2D FFT is performed using:

$$\frac{\partial |r_{fg}(x_0, y_0)|^2}{\partial x_0} = 2\text{Im} \left\{ r_{fg}(x_0, y_0) \sum_{u,v} \frac{2\pi u}{M} F^*(u, v) \times \right. \quad \text{Equation} \\ \left. G(u, v) \exp \left[-2i\pi \left(\frac{ux_0}{M} + \frac{vy_0}{N} \right) \right] \right\}, \quad 55$$

where,

$$r_{fg}(x_0, y_0) = \sum_{x,y} f(x, y) g^*(x - x_0, y - \quad \text{Equation} \\ y_0) = \sum_{u,v} F(u, u) G^*(u, v) \exp \left[-2i\pi \left(\frac{ux_0}{M} + \frac{vy_0}{n} \right) \right]. \quad 56$$

and f^* , g^* , F^* and G^* represent the complex conjugates of f , g , F and G (and a capital letter refers to the FFT of the lower case function, as earlier $\text{FFT}(f) = F$) respectively and (x_0, y_0) are the translations between the two images in the spatial domain that give the best match. This freedom of translational correlation is important when there is a difference in pattern centre between the test and the library, and when there are subtle changes in orientations (which will be explored shortly). I note that Equation 55 is a formalization of Equation 53 and both are included for readability and completeness.

Normalizing the FFT correlation coefficient, by the autocorrelation functions for F and G , means the two XCFs can be compared as the coefficients for both range from 0 to 1.

The correlation is performed in the Fourier domain and these correlation functions are calculated using the 2D FFT, therefore for convenience this is referred to as the “FFT method” to distinguish this from the single value normalised inner product, which is called the “NDP” (normalised dot product) to reflect the Dictionary Indexing literature.

11.4 $SO(3)$ Library Generation

Template matching requires a library of candidate simulated templates. Ideally these are well spaced and efficiently generated. To achieve this, I use a reprojection of an EBSD pattern (the reference pattern), which is generated using the Bruker DynamicS package. The package uses Bloch wave theory and the reciprocity principle to determine the reflectors and to generate a dynamical simulation, as described in the literature review. A script was then written to generate a gnomonic projection of a crystal orientation for a given screen size and position following the conventions detailed in Britton et al. [37]. Intensities on the gnomonic projections were calculated through bicubic interpolation of the reference pattern, similar to the work of Wilkinson et al [99]. An example of creating gnomonic projections from a stereographic projection, for different crystal orientations, is shown in Figure 38: The gnomonic projections for a rectangular screen for $PC = (0.5, 0.5, 0.5)$ for A) no rotation, B) rotation about x, C) rotation about y and D) rotation about z. A rectangular screen has been used to show the distortion of the screen and pattern in the Stereographic projection. The blue segments in the stereographs are the shadows of the screen.

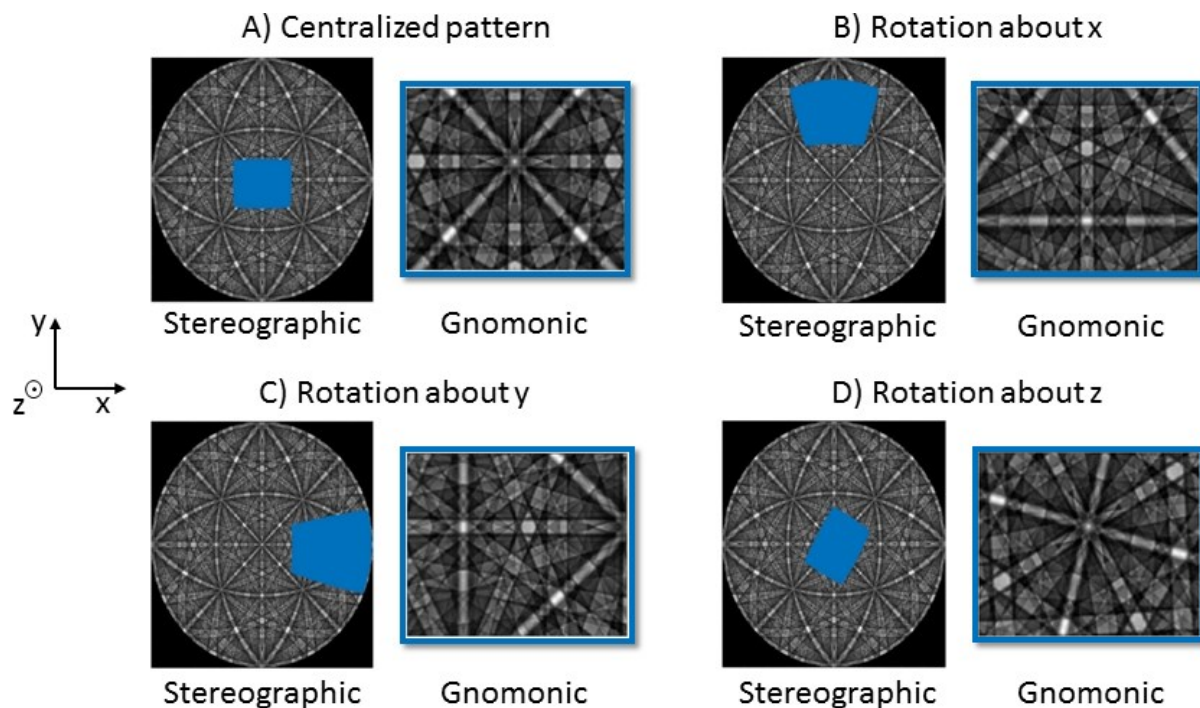


Figure 38: The gnomonic projections for a rectangular screen for $PC = (0.5, 0.5, 0.5)$ for A) no rotation, B) rotation about x, C) rotation about y and D) rotation about z. A rectangular screen has been used to show the distortion of the screen and pattern in the Stereographic projection. The blue segments in the stereographs are the shadows of the screen.

The maths detailing this conversion can be found in Appendix 1.

11.4.1 $SO(3)$ Spacing

The $SO(3)$ rotation group (special orthogonal), is the set of 3×3 rotation matrices with determinant = +1. A well-spaced $SO(3)$ sampling improves the efficiency of the template matching method, ensuring the library has a (near) uniform distribution of orientations which are equispaced. This optimises the likelihood of finding a template and it also improves the reliability of the precision obtained. To avoid duplication and speed up computation, I use the fundamental zone within $SO(3)$ and thus the spacing of the $SO(3)$ sampling is dependent on the crystal symmetry being used (to avoid oversampling due to symmetrically equivalent orientations). The MTEX 5.0.1 orientation generator was used to generate equispaced crystal orientations in $SO(3)$ space. The generator does this by splitting $SO(3)$ into $S^2 \times S^1$. MTEX samples S^2 (the surface of a sphere) by splitting the polar angle

equidistantly and sampling the azimuthal direction as required. Any rotation about points on the sphere are captured with S^1 , which is linearly split.

To ensure a near uniform distribution is used in this work, a list of orientations was generated with a target sampling within MTEX. This generates a library of orientations within the fundamental zone of the cubic crystal system within $SO(3)$. For every point in the library, the disorientation between this point and all the other points in the library (excluding itself) was tested.

The uniformity of this spacing was tested for cubic symmetry. I define SF as the input sampling frequency for the MTEX library generator. For each SF, the disorientation (the minimum angle of misorientation between two orientations) from every orientation of sampling, to every other orientation of sampling, is calculated and compared from decomposing the expected disorientation matrix, calculated using

$$\Delta g_{AB} = \min\{S_i g_A g_B^{-1} S_j, S_i g_b g_A^{-1} S_j\}, \forall \{S_i, S_j\} \in \mathcal{S} \quad \text{Equation}$$

57

Where Δg_{AB} is the measured disorientation matrix between the orientation matrices, g_A and g_B , which belong to the sampling orientations in the $SO(3)$, and \mathcal{S} is the symmetry operator (of which there are 24 for cubic crystals). The symmetry operator is included to ensure the misorientation between the two orientations is at a minimum, thus I am measuring the disorientation.

The SF is essentially the mean disorientation of the angles sampled in $SO(3)$ space, as generated by MTEX. This means if you set the SF to be 10° , the actual disorientations might

be in a large range with a mean of 10° . The spacing of the angles to generate the library needs to be near uniform to ensure an initial guess at an orientation close enough to the actual orientation to be refined. To this end, a test was carried out to determine the spread of orientations in the $SO(3)$ for a given SF.

The distribution of the measured disorientation angles for as a SF of 10° , for cubic symmetry, is shown in Figure 39A. For all orientations within the sampling, the measured disorientation angle to its closest neighbour was at most 10° . In fewer than 20% of samples, the measured SF was significantly less. The distribution of the measured disorientations to their closest neighbour is shown in Figure 39B. The MTEX algorithm has a linear relationship between input spacing and output mode, mean and maximum misorientations for each $SO(3)$ data set. The sampling misorientation only exceeds the input by 0.182° at most (which compares well with the alternative sampling approach used in the study by Ram et al [131]).

The utility of the sampling for the RTM method requires us to determine the minimum misorientation between the $SO(3)$ orientations and the final pattern, such that the peak can be found and that the refinement step works.

The testing of the $SO(3)$ sampling is presented to demonstrate that $SO(3)$ space can be sufficiently populated such that enough (but not too many) orientations create a library with a target SF contains a peak that corresponds to an orientation close to the actual orientation of the crystal (and that it can be refined). The mode, mean and median of these distributions are provided as indicators of the distribution shape within each target bin. Formal analysis of the sampling of orientation space can be more involved, for example by evaluating the gap ratio [132], Riesz energy [133] and discrepancy [134]. However this is beyond the scope and need of this work.

In Figure 39 B, I also observe that number of orientations and therefore templates increases significantly with a decrease in sampling frequency ($10^\circ = 618$, $5^\circ = 4958$, for cubic symmetry). This prompts the exploration what the optimal sampling frequency should be.

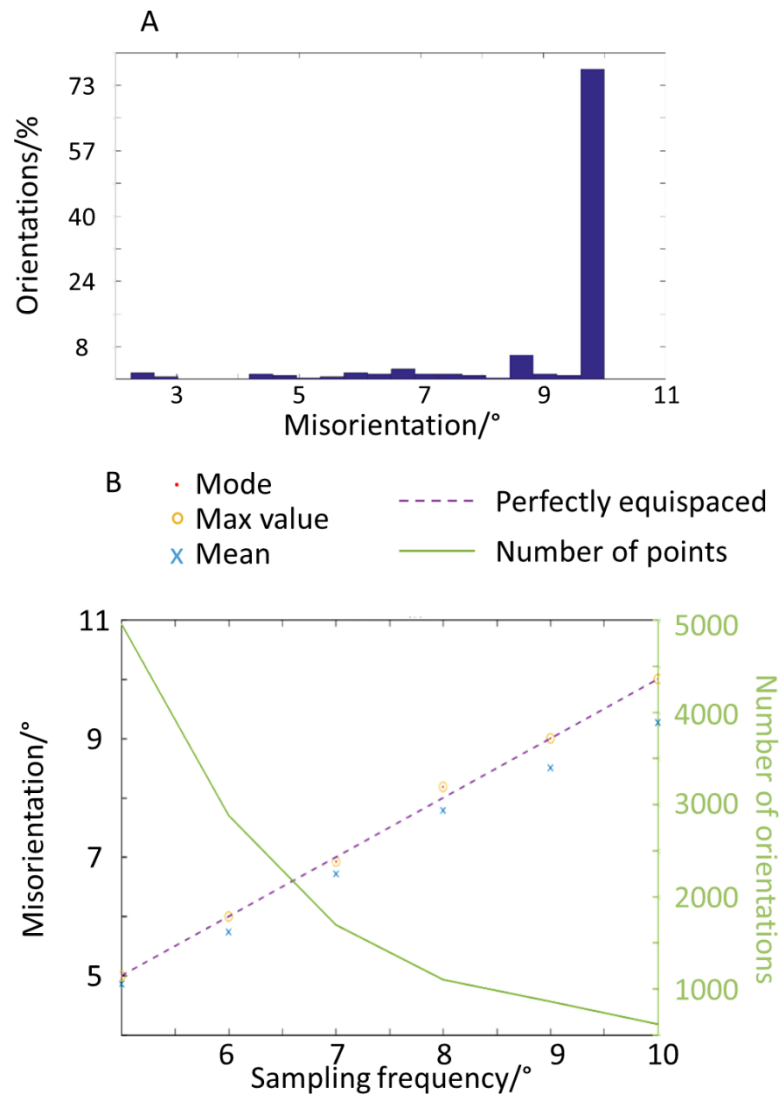


Figure 39: A) The distribution of misorientations for a 10° sampling frequency. (B) the maximum, mean and mode distributions of similar histograms at varying sampling frequencies. Both figures are for cubic symmetry.

It is important to note that the sampling frequency is the term used throughout this thesis to describe the average angular separation of the points in orientation space. As there is finite area in a given fundamental zone, a sampling frequency of 10° means the average angular separation of the points in the fundamental zone is 10° and thus there are fewer and more widely separated points in the library than for a sampling frequency of 2° .

To aid with the visualisation of what the orientation space, I have made a series of stereographs showing how the fundamental zone and distribution changes for different crystal symmetries and sampling frequencies. This is shown in Figure 40.

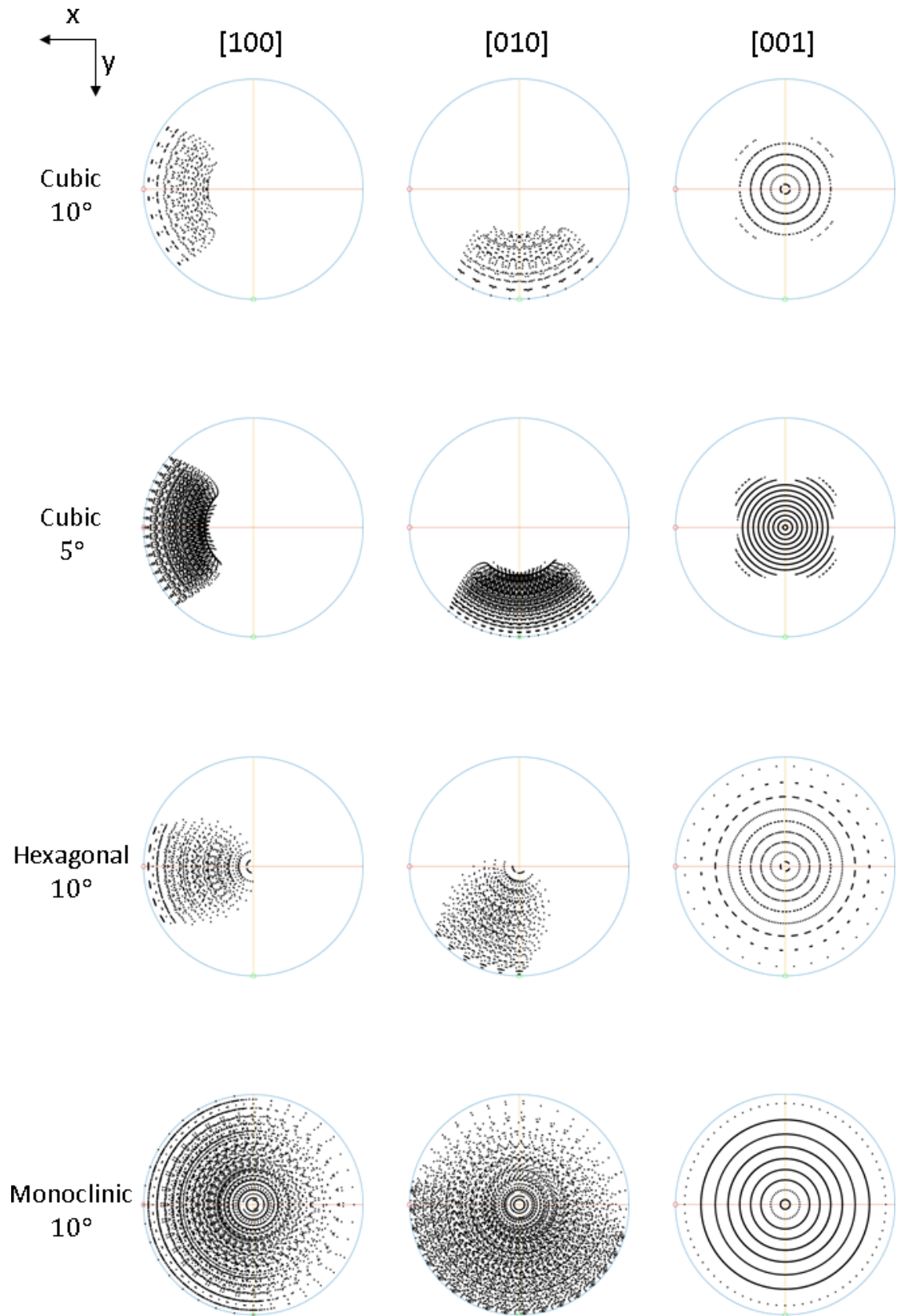


Figure 40: Pole figures of a cubic library for a sampling frequency of 10° and 5° and hexagonal and monoclinic unit cells with a sampling frequency of 10°. These show the S^2 space is well sampled and the S^1 is less so.

Figure 40 shows the different shapes of the fundamental zones for different unit cells. It also shows how the number of points in the library, their spacing and distribution are affected by changing the sampling frequency. The most notable feature of the pole figures is that in all cases the points are well distributed in the $[100]$ and $[010]$ directions. This suggests that points in S^2 space (as described earlier) are well distributed i.e. points are well distributed on the surface of a sphere. The distribution of points in S^1 is less well defined i.e. the sampling of rotations about a point is less well defined. This is unsurprising as the S^1 sampling is a rotation about the points in S^2 space and are therefore constrained by it. This is not a problem for the refined method due to the correction step and therefore the necessity of the library is to get a “close enough” seed orientation to correct.

11.4.2 $SO(3)$ Sampling Frequency

As I have a near equispaced distribution of points in the $SO(3)$ space, I need to work out how dense or sparse the population of orientations in the library (i.e. SF) should be spaced for suitable pattern matching. A lower SF, such as 2.5° , means that each pattern in the library is ideally misorientated by 2.5° from its nearest neighbour. As SF increases, the number of orientations in the library reduces (as per Figure 3B) reducing the number of computations required.

In this section the maximum SF that allows for approximate but robust determination of the pattern orientations via the template matching approach needs to be determined. This can be done via a simulation-based experiment, where a reference pattern is compared to rotations of the library patterns about the three principal axes of rotation. For an example reference pattern, the pattern centre was selected to be (0.5,0.3,0.6) with a pixel resolution

for each pattern of 500 x 500 pixels (descriptions of the geometry are discussed in the literature review). Test patterns were generated by rotating the crystal about the x, y and z axes (in the detector frame) in increments of 0.5° and sampling the same Euler angles at these rotations.

In practice, to perform the NPD, the experimental patterns are cropped, resized, and background corrected (using AstroEBSD [5] routines, from 1600 x 1200 pixel patterns to 128 x 128 pixels) and the dynamical patterns are loaded from the reference pattern (using a cubic based reprojection in MATLAB). This correction draws out the Kikuchi bands and zone axes, suppressing the background signal. For simulations, it also renders the mean of the pixel intensities within each pattern to 0 and the standard deviation is fixed to 1. The templates from the reference pattern have their contrast adjusted in the same manner.

For the NPD method, the correlation coefficient for the pair of patterns is calculated using Equation 51. To perform the FFT method, the experimental and library patterns are windowed, transferred to the Fourier domain using the 2D FFT, and bandpass filtered. The peak correlation coefficient is extracted from the 2D cross correlation function using Equation 55.

Template matching was performed to compare each test image with the reference image.

The correlation coefficient of rotations about X, Y and Z axes are shown in Figure 41 (the NDP coefficient is computed from Equation 51 and the FFT is computed from Equation 55).

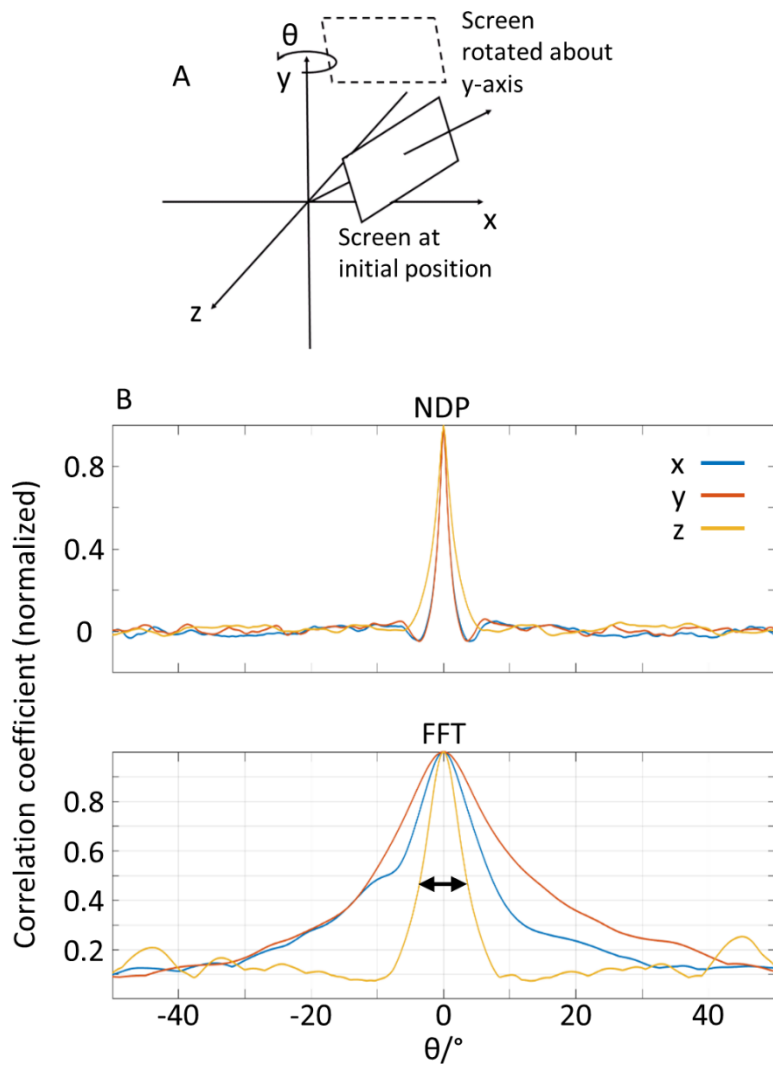


Figure 41 A) Rotation of a generated pattern, show here for the sample y axis. B) correlation coefficients for the NDP and FFT methods from rotations about the sample axes.

Figure 41 B shows the FFT approach is less angularly sensitive, and thus a larger step, i.e. a larger SF can be used.

To match the experimental pattern with a template, the contrast between the correlation coefficient for the best match should be significantly higher than the correlation against pattern generated from a random crystal orientation, and therefore the best match can be identified from an incorrect match. This motivates sampling with a frequency that matches the full width half maximum (FWHM) of the narrowest correlation peak in Figure 41B.

The value of FWHM for successful matching is different for matching patterns rotated about the three axes. In practice, sampling in $SO(3)$ space is limited by the width of the narrowest peak. In the NDP method this is a rotation about x or y and is $\sim 2.5^\circ$. In the FFT analysis this is a rotation about z of $\sim 10^\circ$. The precise width of this peak will vary with screen position, crystal symmetry, and screen size.

The FFT based cross correlation includes an up-sampling of the central peak such that the peak of the cross-correlation function can be for the best translational maximum (and this is sampled with a higher orientation resolution than the $SO(3)$ sampling). Furthermore, as previously noted, the FFT method directly enables the use of windows and filters, which can directly suppress EBSD pattern artefacts (e.g. high frequency noise and background gradients). The range of correlation values extends from 1 (near auto correlation) to 0.1 (correlation of two diffraction patterns of different orientation).

For the NDP case, the maximum value will depend on the offset between the exact solution and an orientation with a misorientation of 0° (i.e. it should be close to 1, subject to small numerical fluctuations). The miscorrelation is less well defined and may not be stable.

The quality of matching can also be affected by an incorrect PC and the size of the patterns used in matching. An incorrectly defined PC can impact the correlation between two images and also result in a systematic misorientation [37]. Furthermore, if a screen has too few pixels there will be insufficient information for matching. These two factors can affect the FWHM of the peak and associated SF. The sensitivity of the two methods for these problems in Figure 42 by systematically adjusting the PC position in x, y or z, shown in A, B and measuring the FWHM (from graphs similar to figure 4) is now to be explored.

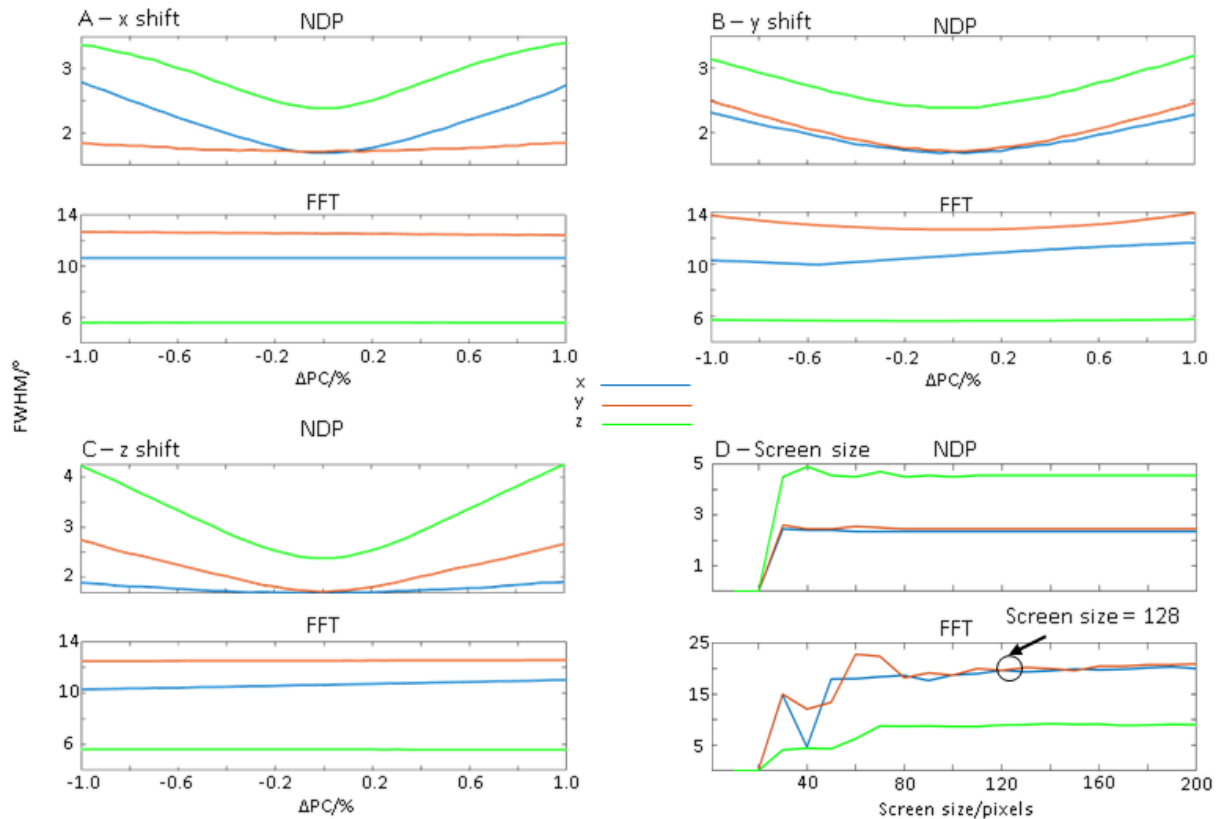


Figure 42: A, B and C) The FWHM recorded for a shift in PC (ΔPC) in the x, y and z directions respectively. The screen is 500 x 500 pixels for each of these graphs, with the initial PC = (0.5, 0.3, 0.6). D) Varying the screen size; a screen size of 128 is labelled to identify where the FFT becomes stable for the PC set to (0.5, 0.3, 0.6).

Figure 42 shows the FWHM for the FFT is consistently greater than that of the NDP, for both PC changes and changes in screen size, as shown in Figure 42D. The ‘U’ shape seen in the NDP, but not in the FFT functions shows that as the error in PC increases, the width of the gaussian describing the spread of CCs widens. This makes the peak of the NDP harder to identify and determine. The lack of this shape in the FFT suggests the FFT is less dependent on the PC being correct for accurate indexing, being mostly reliant on a correctly identified PCZ. For a screen size above 120 x 120 pixels, the limiting angular range of the FWHM is at a maximum of $\sim 6^{\circ 3}$. This motivates the selection of a pattern size of 128 x 128 pixels⁴ (e.g. binning from 512 x 512 pixel images by a factor of 4). Although the FFT has not completely

³ I am using a rotation about the z axis here as Figure 42B Shows this is the smallest SF I can use to resolve the peak.

⁴ This is the closest $2^n \times 2^n$ pixel screen size to 120 x 120 pixels, allowing for a more efficient FFT and more simple windowing, which is important for the refinement step.

stabilised by this screen size, the added computational cost of moving up to 256 x 256 pixels is not offset by the increase in reliability in the FFT. Based on Figure 42 A, B and C, a SF of $\sim 2^\circ$ is needed, to find a near match, for the NDP XCF and a SF of $\sim 6^\circ$ is needed for the FFT XCF. The SF stated here is slightly lower than the 10° mentioned earlier. This is based on Figure 42 showing a SF of $\sim 6^\circ$ is necessary to account for variations in PC. Note that without refinement of the orientation, a high SF would limit the ultimate angular resolution of the indexing method.

The library sampling was chosen to determine the bounds on the peak height and contrast for an allowable orientation difference between patterns in the template library and the experiment. I have performed this sampling in the detector frame of reference as this establishes a bound on the maximum allowable SF required to find a reasonable orientation from within the template library. The full width half maximum is indicative of an appropriate selection for the SF required and as the contrast of our peaks is high a slightly larger SF, of 7° is selected for this work.

11.4.3 $SO(3)$ Library Size and Computational Costs

In a template matching approach, searching the library for the best pattern is computationally expensive.

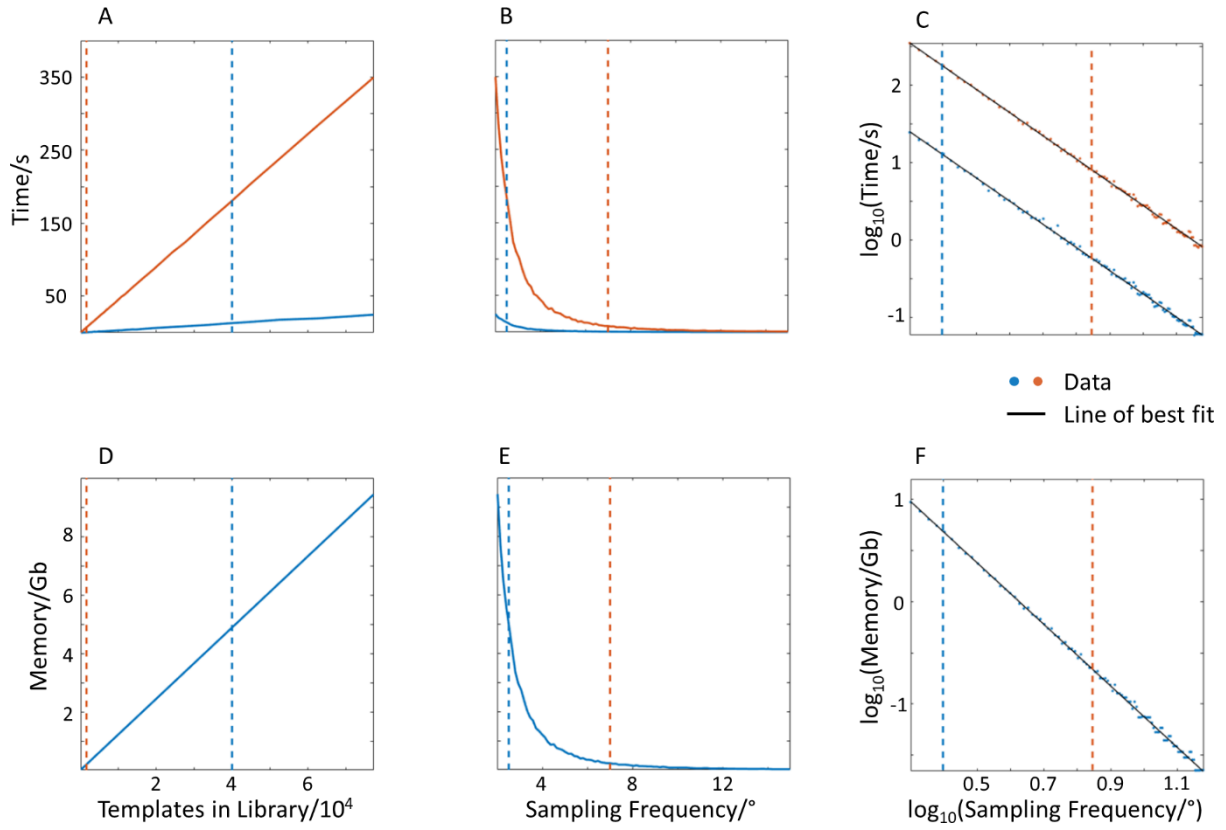


Figure 43: The time taken to index a single pattern for the NDP (blue) and the FFT (orange) is shown in A. B shows the time taken to complete the $SO(3)$ search. This, in turn is dependent on the number of images in the library to search through, as is shown in A, B, D and E. As the FFT uses a significantly reduced library size, it is able to index patterns significantly more quickly than the NDP. Figures C and F show the relationship between the time to index a single pattern with respect to the sampling frequency, and C the Log of the sampling frequency vs the log of the time taken. D, E and F show the same for memory usage instead of time. On all graphs, the dashed vertical lines show the respective positions the NDP and FFT libraries occupy.

Figure 43 shows the relationship between the SF, time and memory requirements for 128 x 128 patterns and cubic symmetry. Graphs C and F all show a gradient of ~ -3 , which shows the time taken to index an EBP is proportional to the SF by a factor of 10^3 . This extra cost of using the FFT for matching is therefore offset due to the significant reduction in the library size, thus accounting for the speed up. It also needs less memory in the computer to store and use the library. It is important to note that these figures represent a single pattern being indexed. The time difference between the NDP and FFT is only slight, however when this extra time is added to all of the patterns in a complete map, the resultant indexing time is sufficiently long to be unusable.

Further analysis shows the average time to search the SO(3) for a sampling frequency of 2° is ~ 5 s. This is significantly more than the ~ 0.6 s for the FFT method with a sampling frequency of 7° . For a small map of 2000 points, the NDP method would take 10,000 s (~ 2 hours and 45 minutes) The same map with the FFT method would take ~ 1200 s (~ 20 minutes). This is a dramatic speed up using the refinement method.

In practice this motivates the use of a method that can use a higher SF. It is worth noting that, although for a given library size, the time taken for the FFT to index a pattern is higher (due to costs in performing FFTs) but I note that a reduced library size (compare the intersections of the vertical lines for each method) has a significant impact on the total time required to find a good match.

11.5 Orientation and Pattern Centre Refinement

It is now assumed that the initial library match provides us with a close approximation to the true orientation, requiring only minor refinement of the crystal orientation to obtain the true orientation. I assume the correction needed is usually within $\pm 7^\circ$ misorientation of the crystal about the X, Y and Z axes of the EBSD detector (i.e. to within the sampling frequency of our SO(3) library).

For small rotations, I exploit the fact that there is a duality in the gnomonic projection, as a rotation about the x or y axis in the sample frame, creating a vertical or horizontal shift in the pattern (Figure 44A, provided the rotations are $< \sim 10^\circ$). The 2D FFT cross correlation can measure this shift precisely (Equation 54 and Equation 55). This shift can be measured using a projection of the pattern with the correct pattern centre. I can approximate this misorientation provided the PC is located within the detected diffraction pattern using basic trigonometry, see Equation 57, to correct the orientation.

$$\theta = \frac{\text{shift}}{\text{detector distance}}.$$

Equation

58

Refinement of the Z rotation is more difficult as it cannot be approximated by a simple translation of the pattern. It would be possible to use the High Resolution EBSD (HR-EBSD) method, described in [33] to calculate the rotation, however this could be computationally expensive. Instead, I propose an alternative refinement where I convert the images to log polar space. The log polar transformation changes a pattern described in square $[X,Y]$ pixel coordinates to $[\log r, \eta]$ space, where r is a distance from the image centre and η is the angle counter clockwise from the positive X axis (see Figure 44). This transformation enables rotations about the image centre to be transformed into linear shifts along the η direction in the log-polar diagram. The log-polar transform is often used for zoom ($\log(r)$) and rotation (η) image registration. This is described in more detail elsewhere ([135], [136]). The rotation of a crystal about the Z axis between template and experimental pattern from the shift along the η axis using FFT based cross correlation of multiple windows, extracting only the shift along η . For this transformation, I place the centre of the log-polar transform at the

screen centre (placing it at the pattern centre adds significant computational complexity).

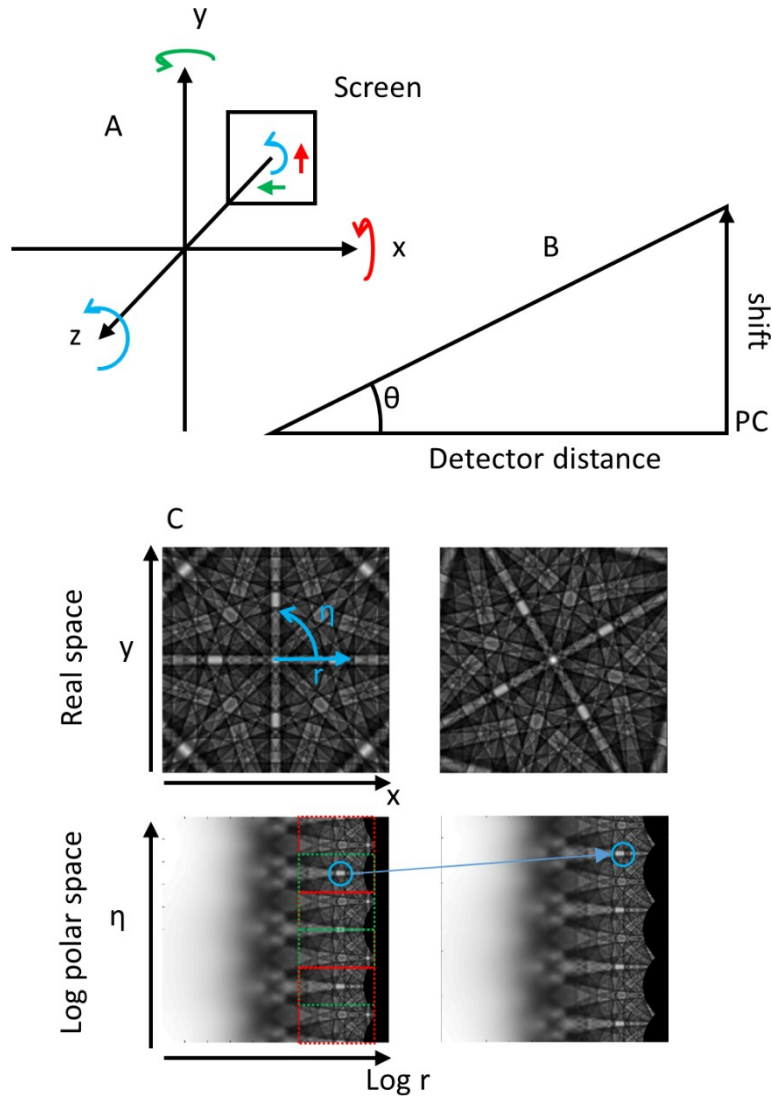


Figure 44: A) A rotation of the crystal becomes a shift in the EBSD pattern. B) As I have the shift in x or y, or in the PC and I know the detector distance, trigonometry can be used to correct for a PC discrepancy should one occur. Finally, Z is corrected as shown in C. C) To determine the z rotation, the EBSD pattern is transformed into log polar space, where a shift in y translates to a rotation about z in real space

The shift used to calculate the misorientation using Equation 57 can be updated to remove the impact of the electron beam induced shift, and therefore only 1 reference pattern library needs to be generated.

The maths used in the log polar transform and conversion of the x and y shifts to rotations assumes the PC is centred on the screen, however, this is rarely the case. Fortunately, it is trivial to address this issue, if the pattern centre is on the screen, by iterating the correction

step with the template being replaced by a pattern obtained calculated for the correct pattern centre and orientation.

The errors associated with the difference between the screen centre and the pattern centre are second order [137] and convergence to the exact solution of the measurement is demonstrated in Figure 45. The calculation is quick and computationally inexpensive (It is found that ~two iterations are typically sufficient). For each refinement “step”, I measure the shift in X and Y, calculate the rotation about Y and X respectively, and then perform the log-polar cross correlation for measurement of the Z rotation.

In Figure 45 I demonstrate that a first match with the closest point in our $SO(3)$ library results in a small disorientation error between the accurate orientation and the measured orientation, as expected. A single correction of the orientation results in a closer alignment of the orientation between test and reference pattern, but there is a smaller linear error associated with the ‘second order’ terms (i.e. that the pattern centre is not at the image centre) and that a second correction results in an improved accuracy. This results in the ultimate disorientation between simulated pattern and measured pattern orientation which is (typically) less than 0.1° . The ultimate precision of the NDP is less than the FFT, as the refinement step benefits from the FFT based imaged shifts which are measured in the initial pattern match.

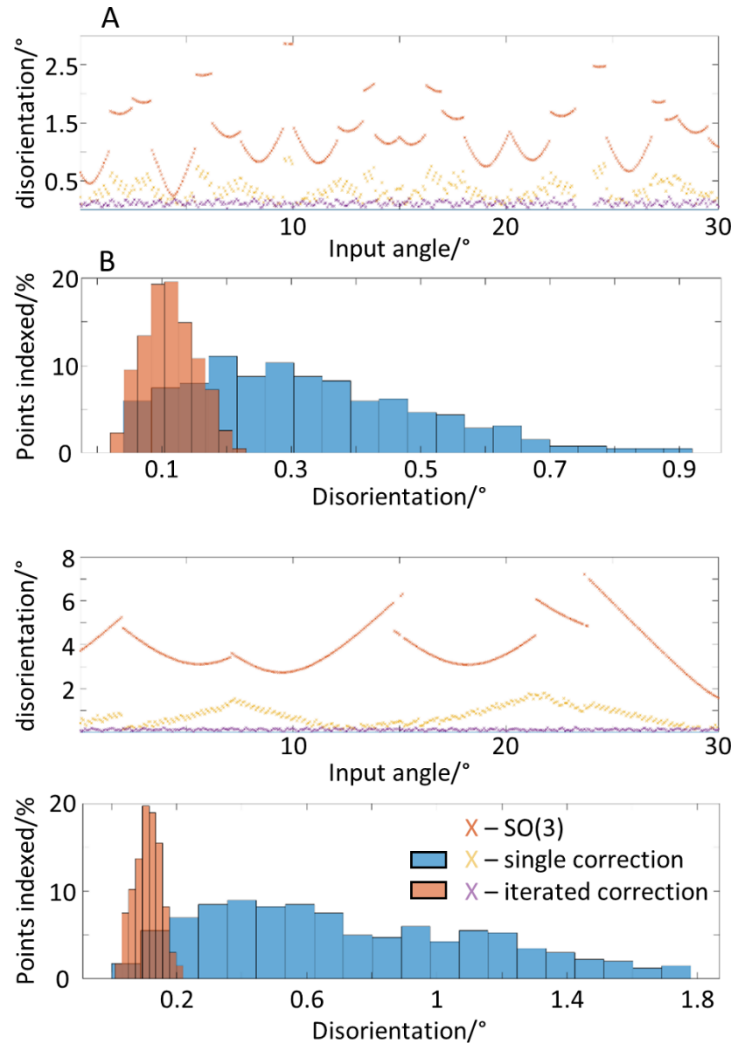


Figure 45: A and C show the difference between the generated data and the indexed data for the NDP and the FFT respectively. They show the misorientations after the SO(3) search, a single refinement and the iterated refinement used in this method. B and D show the distribution of misorientations between the indexed and generated data. The distribution for the SO(3) search has been omitted as it makes the single and iterated distributions unreadable.

For this test, the time taken for the NDP approach to match each pattern was significantly greater than the 2D-FFT approach as the SF is higher for the FFT (a few hours for the NDP as opposed to a few minutes for the FFT). This lower SF requires less correction than the FFT match, however, after two iterations of correction the results show similar accuracy between the two image comparison methods (figure 9). It is worth noting that with each refinement, the stepping in both graphs (which is related to the SF) is reduced.

A further test of accuracy was made in which 100 randomly orientated simulated EBSPs were generated (sampled from a low SF SO(3) orientation set) and then indexed with each

method using a SF of 2.5° for the NDP and 7.5° for the FFT. In both cases two refinement steps were employed to interpolate from the best fit template orientation. The misorientation between the actual and indexed orientations is shown in Figure 46 for the two methods and a similar accuracy is achieved (better than 0.1°).

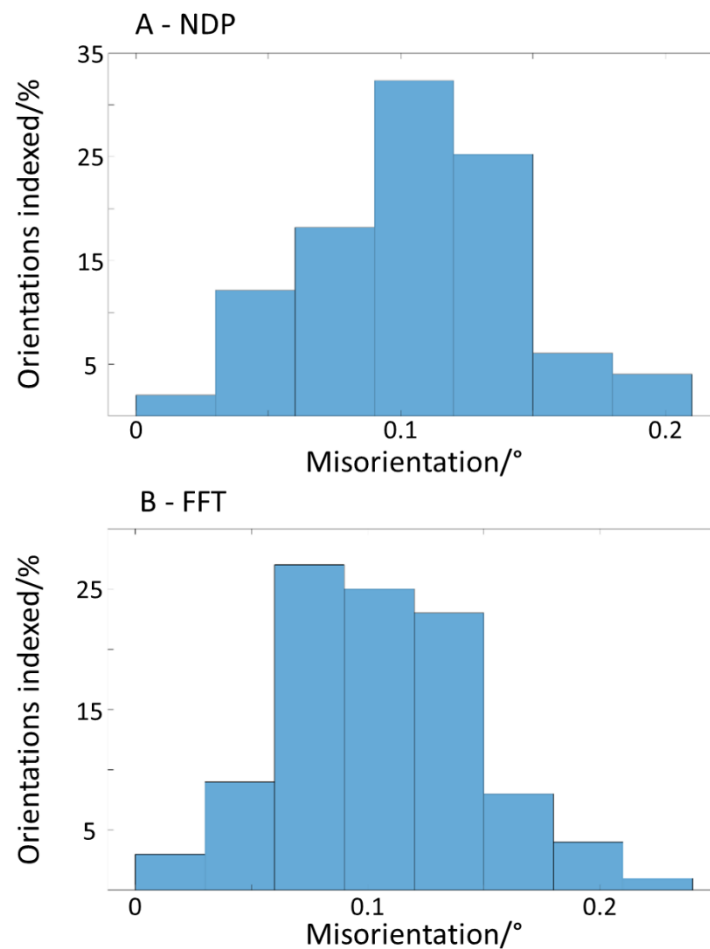


Figure 46: The accuracy of the pattern matching approach a series of EBSs related to a random set of orientations was generated and the misorientations of the indexed and generated patterns calculated for the NDP and FFT, A and B respectively. From B, it is seen that, using the refined FFT pattern mating approach, an accuracy or $<0.2^\circ$ is possible,

Two results for the NDP indexing have had to be omitted due to a misorientation of 60° obscuring the data of a lower misorientation. Due to the misorientation it is suspected that this is a case of pseudo-symmetry (as this is cubic geometry). The FFT, in this case, seems more adept at dealing with cases of pseudo-symmetry. This is an idea explored in chapter

13. The methods ultimately have similar accuracy, as the refinement step is the same in both cases. The FFT in this case returned the results faster than the NDP, and with similar levels of accuracy attained due to the refinement step makes it a sensible alternative.

11.6 Demonstrations

Up to this point, comparisons have been made using simulated patterns. In order to demonstrate the precision of the FFT indexing method, two maps of a single crystal silicon wafer, and one map of an α -iron polycrystal deformed to 4% strain were generated. These were indexed using the refined template matching approach and compared to Hough based measurements indexed using eSprit 2.1. All maps were indexed within this software using default settings: Hough resolution of 60, and an automatic maximum of 12 bands. For these tests, the pattern centre was measured using eSprit 2.1 which employs an iterative pattern centre solver to fit the pattern centre and orientation. For these maps, the PC in the maps varies substantially across the map in both of the silicon maps.

For the template matching approach, a SF of 7° (~1600 templates), was used for the FFT, with 2 iterations of the refinement step. The NDP was not used for these examples as this chapter is demonstrating the use of the new FFT method. All three demonstrations are for cubic crystals and therefore the numerical results may vary slightly if a different symmetry is present within the crystal.

11.6.1 Si Single Crystal:

Two maps of the Si wafer are presented, with one spanning 0.28 mm x 0.21 mm, with a step size of 10 μm and the second 3 mm x 2 mm, with a step size of 50.76 μm . These maps have a large variance in the PC due to electron beam shifts. I note that this method of precision assessment is similar to the one employed by Humphreys et al. [138].

Orientation maps in Figure 47 and Figure 48 (parts A, B, C, & D) indicate that the sample is a single crystal and is oriented as expected (orientations are presented in the sample frame, utilising knowledge of the camera and sample tilt). Consistency of orientation assessment was performed through comparison of the Hough based indexing method and the pattern matching approach (Figure 47 and Figure 48 part F).

Precision for each method was estimated through analysis of the misorientation with respect to a central pattern within each map and results are also shown in Figure 9 and 10 parts E & G. Histograms of the misorientation angles with respect to the central point for both Hough and XCF were also generated (Figure 47 and Figure 48 part I).

Finally, for quality assurance the XCF peak height map for matching is also presented (Figure 47 and Figure 48 part H) and this can be used as a filtering metric for removing suspect points, similar to the image quality in the Hough based method [139]. The XCF peak heights can be used as a rough measure of pattern quality as a better quality (less noisy) pattern will give a higher peak than a low quality (high noise) pattern [140].

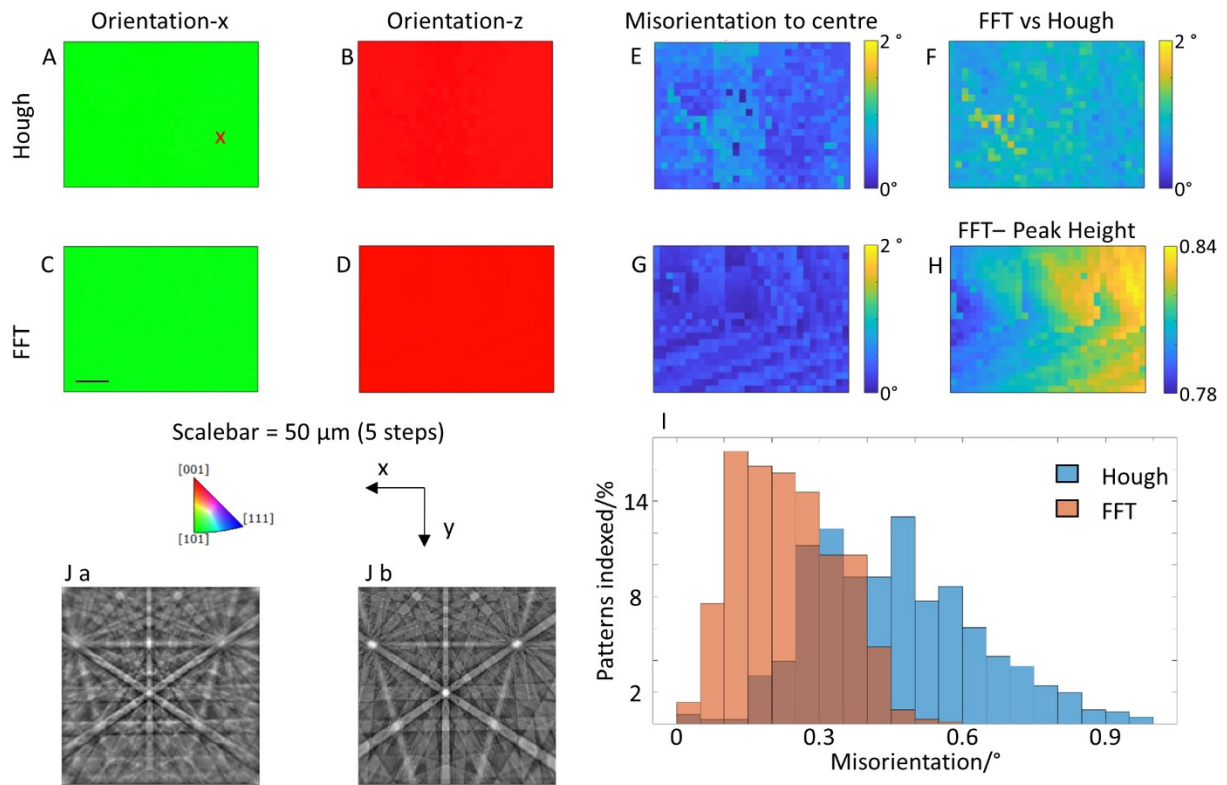


Figure 47: Surface maps showing the orientation of small single crystal silicon for Hough (A and B) and FFT pattern matching (C and D) to demonstrate the precision of the pattern matching approach. The coloured orientation maps are shown with respect to the macroscopic X and Z axes. E and G show the misorientation with respect to the central pattern in the map. I shows the distribution of the misorientations shown in E and G. H shows the peak height from the FFT for each point in the map, this can act as an error metric similar to the image quality in the Hough. J shows the captured image, cropped and background corrected (a) and the pattern indexed with the refined method (b). The red x on the map in A shows the location from which the pattern was extracted.

Figure 47 A, B, C and D show results from the refined template matching approach. It is shown to give similar indexing to the Hough based approach ([110] points along X and [001] points along Z). Figure 47 E and G show that the FFT method has a flatter spatial distribution of misorientations across the map, which is represented also the histogram analysis in I. Figure 47 I shows the FFT indexing has a lower average misorientation, from each point to the centre point, compared to the Hough indexing ($\sim 0.1^\circ$ as opposed to $\sim 0.4^\circ$).

The map was collected in a standard EBSD set up, with a beam acceleration voltage of 20 keV, a detector distance of 14.3 mm, a beam current of $\sim 1 \times 10^2 \mu\text{A}$, and a total collection time of 10 minutes 36 seconds (~ 9 ms per pattern).

Figure 47 G Shows an apparent structure in the FFT, that is missing the Hough misorientations. This variance is likely caused by an incorrect PC. In this instance, the PC for the map was determined by the Bruker eSprit 2.0 software. This model is an iterative approach to determining PC and optimises for PC or rotation. As the map is a Si single crystal, the orientation is optimised in the Hough case and the artifact is hidden. The refined approach shows the artefact due to the equivalence of a shift in PC and a rotation of the crystal.

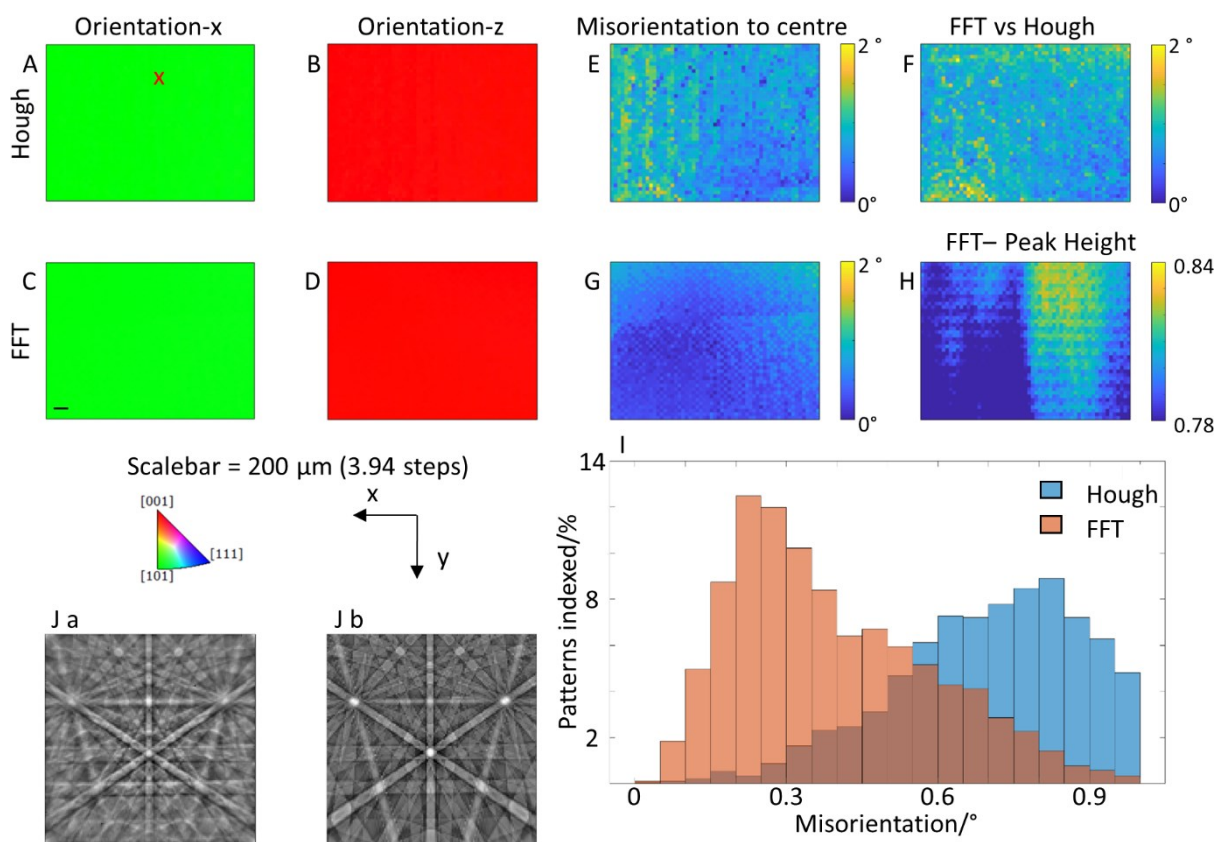


Figure 48: Surface maps showing the orientation of small single crystal silicon for Hough (A and B) and FFT pattern matching (C and D) to demonstrate the precision of the pattern matching approach. E and G show the misorientation with respect to the central pattern in the map. I shows the distribution of the misorientations shown in E and G. H shows the peak height from the FFT for each point in the map, this can act as an error metric similar to the image quality in the Hough. J shows the captured image, cropped and background corrected (a) and the pattern indexed with the refined method (b). The red x on the map in A shows the location from which the pattern was extracted.

The map was collected in a standard EBSD set up, with a beam acceleration voltage of 20 keV, a detector distance of 14.35 mm, a beam current of $\sim 1 \times 10^2 \mu\text{A}$, and a total collection time of minutes 17 seconds (~ 9 ms per pattern).

Figure 48 G shows some structure in the misorientation with respect to the centre. The misorientation here indicates the experimental precision of the method. In an ideal map, the misorientation should be stochastic and not vary systematically with position. For the very large (2.3 mm x 3.2 mm map) shown here, variations in the orientation are likely due to errors in the pattern centre model. Due to the duality of X and Y shift errors, variation in the pattern centre with position (due to electron beam scanning) which are not precisely accounted for will result in apparent changes in orientation. The variation in illumination, due to the change in source point position with respect to a fixed detector, also results in a variation in CC seen in Figure 48 H (The variation in which is only small but seems larger due to the size of the map). A final contributing factor that could be responsible for the apparent structure is the stability of the beam and positioning accuracy of the electron beam during scanning.

If more complete indexing is required, I have also indexed this map through using a bespoke library (results not shown) for each point with an updated PC. This approach is not advised, however, as it significantly increases the time taken to index each EBSD (as time and memory saving is achieved through the generation of only one reference pattern library).

Figure 48 E, G and I all show the refined template matching approach has an improved precision compared to the Hough approach. Figure 48 G shows the misorientation from the central point varies radially with distance, implying that the PC variation model imported from eSprit is not quite correct for this dataset and this systematic problem is only revealed in the template matching approach.

11.6.2 Deformed α -Fe Dataset

The next test is to determine the sensitivity of the pattern matching approach and to select a cut off peak height for incorrect indexing. For this, an EBSD map of α -Fe Polycrystal was

obtained from a lightly deformed sample, the dataset can be found at <https://zenodo.org/record/1214829#.X8Ysy2X7TmE>. The map was collected on a Bruker eFlash HR (1st generation) with full pattern resolution on a FEI Quanta instrument, using the standard EBSD set up described in the introduction. The beam voltage was 20 keV. Patterns were acquired and indexed to show the sensitivity of the method. The deformed iron dataset is used here as there is a slight orientation gradient within the grains as a result of the deformation. The ability of the pattern matching to detect this gradient shift is a good measure of the sensitivity of the method. The distribution of the CCs of the iron dataset shown in Figure 49 H shows a main peak in a Gaussian shape, with an elongated tail. Any point in the elongated tail can be seen as being misindexed. In the case of the Iron dataset here, the misindexed points all come from the spec of dust near the scalebar.

This map covers 16.5 by 12.3 μm at a step size of 0.15 μm and has been described in more detail in [5]. This dataset contains abrupt misorientations across grain boundaries and smaller lattice curvatures within the deformed grains. It is more useful in determining the sensitivity of the pattern matching approach and selecting a cut-off peak height for misindexing.

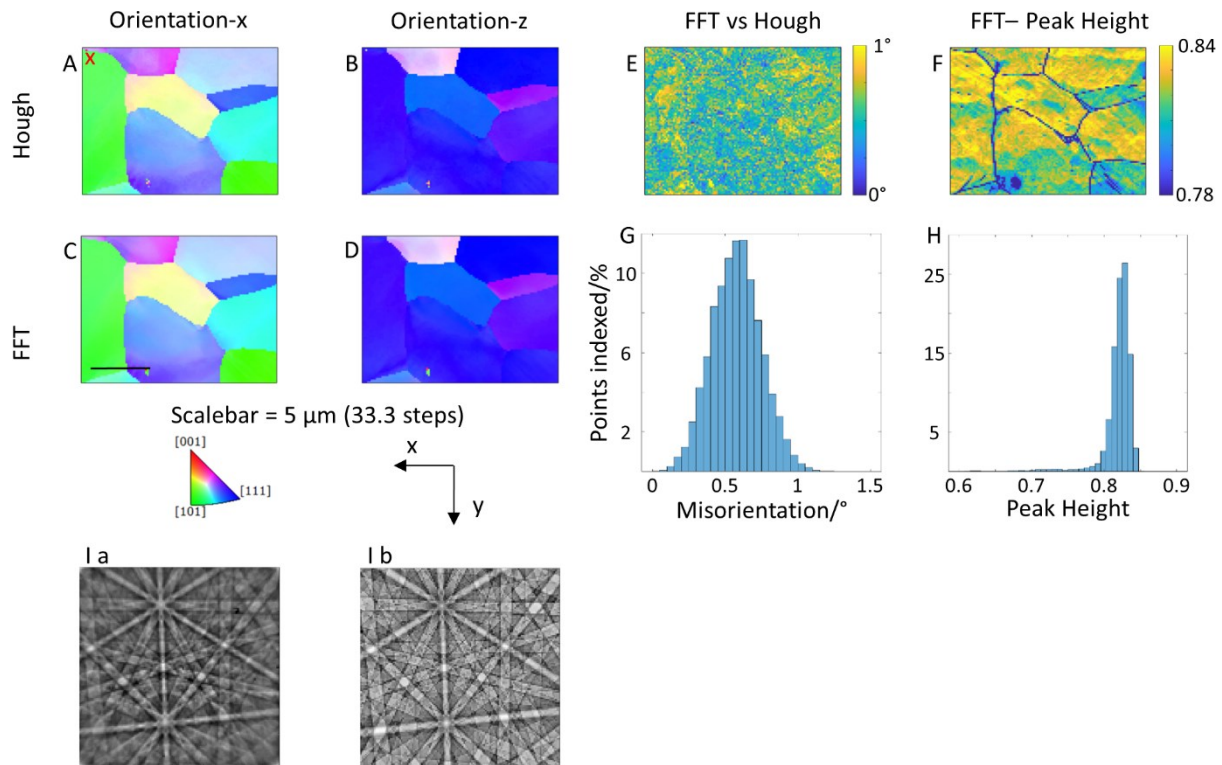


Figure 49: Orientation maps of a deformed α -Fe sample, showing the sensitivity of the pattern matching approach (A, B, C and D). E shows the misorientation with respect to Hough as a rough guide to the accuracy of the pattern matching approach, and the distributions of the misorientations are shown in G. F shows the FFT peak heights as a map, analogous to the IQ in the Hough and H shows the distribution of the peak heights. This histogram can be used to determine where the cut off for incorrectly indexed patterns should be. I shows a) The captured image, cropped and background corrected and B the pattern indexed with the refined method. The red x on the map in A shows the location from which the pattern was extracted.

Figure 49 A,B,C and D shows how closely the two methods index the orientations of the grains in the sample. This is shown further in E and G where the misorientation between the Hough based method and the template matching method are shown (note this illustrates precision between the methods and not accuracy in either case).

Figure 49 F shows the peak height map for the template matching. This can work as an error metric as it reveals through low values regions where patterns may be misindexed. This map also reveals other features, such as slip bands which can be useful for deformation assessment.

The histogram in Figure 49 H, shows a high frequency of points with peak heights > 0.8 and a mode peak height of ~ 0.84 which could be used to filter out misindexed points (such as the speck of dust near the scalebar in Figure 49 F).

The map was collected in a standard EBSD set up, with a beam acceleration voltage of 20 keV, a detector distance of 14.48 mm, a beam current of $\sim 1 \times 10^2 \mu\text{A}$, and a total collection time of 2 hours 19 minutes 28 seconds (~ 9 ms per pattern).

11.7 Chapter Summary

This chapter has presented a pattern matching based algorithm for EBSD pattern indexing.

The approach uses a fast Fourier transform-cross correlation function, which requires a significantly smaller library to be used to fully represent the $\text{SO}(3)$ orientations. This results in a significant speed up in indexing compared to a normalised dot product approach. The DI method has been freely available as a software package since 2017. The work in this chapter was conducted pre-general release of the software, as such the DI approach was not available as a software package at the time of generating these figures. As such the figures and data shown here reflect my own work in replicating the DI from the progenitor paper [34]. I do not, however, believe this affects the speed up. The work in this chapter is preliminary and could easily be sped up by exporting a lot of the heavy-duty calculations to a low-level coding language, such as C. When compared in the same computer language, on the same machine the FFT is faster. The NDP will still need a large library regardless of language, and the computers used for indexing will still need to be sufficiently powerful. The use of a refinement step is attractive to speed up the method as it allows for a sparse library without loss of accuracy. The accuracy possible from this technique has been shown to be

$<0.2^\circ$, for 128x128 pixel EBSPs captured in a conventional geometry. This has been demonstrated on two example data sets from a Si single crystal and a deformed sample of α -Fe. The method is shown to be invariant to PC differences and sensitive enough to identify subtle changes in orientation, within a grain. Figure 47, Figure 48 and Figure 49 all show a variance in CC, This variance is especially noticeable in Figure 49, where the bottom right grain has a slightly lower CC when compared to other grains in the map. This variance is related to the quality of the EBSP. A Low-quality pattern will result in a low CC. The quality of the pattern might be affected by a number of things, beam drift and focus, polishing finish and even orientation of the unit cell. As, for Figure 49, the misorientation with respect to the Hough is flat, I suspect this is the reason for the lower CC. A methodological reason for the drop in CC, could be that the seed orientation from the SO(3) is close to the limit of what is possible for the refinement step to correct. In the case of Figure 49, the CCs are sufficiently high, and the misorientation with respect to the Hough sufficiently low that this is no cause for concern. Should this become a problem, a slight lowering of the SF, and thus a slightly larger SO(3) library can be used.

12 Phase Characterisation Using the Refined Template Matching Approach

12.1 Introduction

In this chapter, I introduce a phase classification method using refined template matching.

EBSD is often used to characterise the crystal phase, as described in the literature review section of this thesis. Typically, this is performed through finding the best ‘index’ via the Hough transform, where the indexing route is used (real pattern → Hough transform → band identification → crystal orientation determination) and the phase with the best quality metric is selected as an appropriate solution. This can be based upon the misfit between the measured and expected interplanar angles, or perhaps the number and/or quality of Hough peaks found. To refresh on this please see section 10.5.8. This method can be problematic if the phases are very similar in structure, or due to the incorrect localisation of a band within the Hough transform.

Firstly, I use simulated data to show the effectiveness of this method for phase characterisation, as this enables the correct result to be known *a priori* and systematic issues to be explored. This includes mixed patterns, patterns with differing crystal structures (hexagonal titanium vs cubic titanium or cubic vanadium), different Bravais Lattices (BCC iron vs FCC iron) and different lattice constants (FCC silver vs FCC copper), following the examples from [36].

The highly automated nature of a typical EBSD analysis requires well characterised error metrics for confident use of the technique, and these metrics should be can be calculated quickly and add minimal extra overhead. One such metric has been developed by Ram and De Graef (2018) [36], however, the use of this metric is difficult to use with the refined template matching approach, as I will discuss later in the “Comparison with the Phase

Confidence Metric” section, and this has led to the development and testing of an error metric specific to the use of the refined template matching approach.

Finally, I will apply the method and error metric to correctly classify phases with an experimental map of dual phase titanium and compare the phase classification provided from this new method with the more conventional Hough based approach.

12.2 Methodology

In brief, patterns will be tested against the template library, simulated using dynamical diffraction theory, and the ultimate orientation refined. This will be repeated for multiple candidate phases, and the pattern can be classified as one of the candidate phases, via the correlation coefficient of each match.

I stress that this is a classification approach, as the template matching method will only select the best phase match amongst the candidate libraries. This is different to a phase identification method, e.g. one where the symmetry of the crystal is evaluated.

Furthermore, the generation of the classification list assumes prior knowledge of potential phases in the material.

12.3 Phase Classification of a Dual Phase Material

12.3.1 Mixed Patterns with an associate Orientation Relationships

In a dual phase material, it is important to determine the phase of each diffraction pattern.

In dual phase titanium alloys, there is the HCP α -phase and the BCC β -phase. Ambiguity can arise in determining orientations within the β -phase due to pseudo symmetry associated with $\langle 111 \rangle$ zone axis. Misclassification for the dual phase microstructure can be complicated further by the Burgers orientation relationship between the two phases, which results in one parent β -crystal having twelve child α -variants, each of which have sharing of $(0001)_{\alpha} || (110)_{\beta}$ and $\langle 11\bar{2}0 \rangle_{\alpha} || \langle 1\bar{1}1 \rangle_{\beta}$. This results in shared features within the

diffraction patterns and similar interplanar angles, which complicates phase classification significantly.

To test how this impacts the cross correlation-based pattern matching, I first generate a random orientation for the β -phase. From this orientation, we calculate the 12 associated α -titanium crystal orientations, according to the BOR.

As mis-classification can occur when the interaction volume extends across an α - β interface, it is important to establish which phase can be separated from these overlapping patterns.

To simulate overlapped patterns, I linearly mix the intensities from the simulated patterns in 10% increments, starting with the β -titanium pattern and each of the associated α -titanium patterns in turn. This results in 11 patterns per OR pair, examples of which are shown in Figure 50.

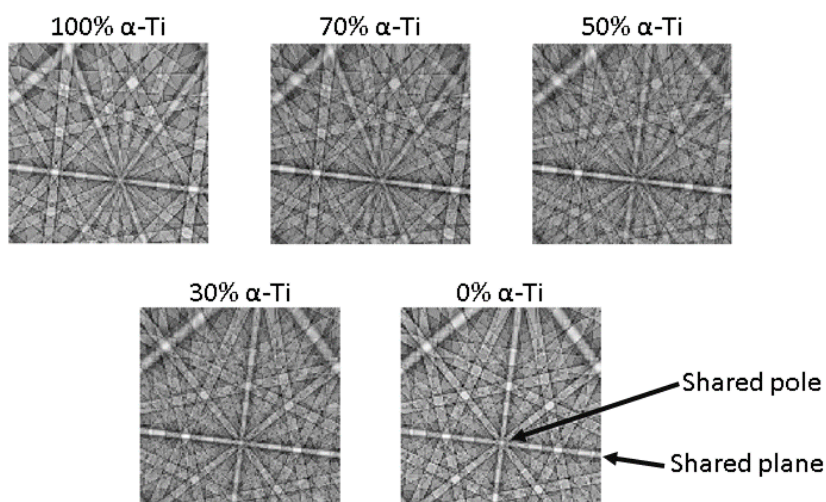


Figure 50: Mixed patterns showing the linear mixing of α -Ti and β -Ti patterns for varying percentages of mixing.

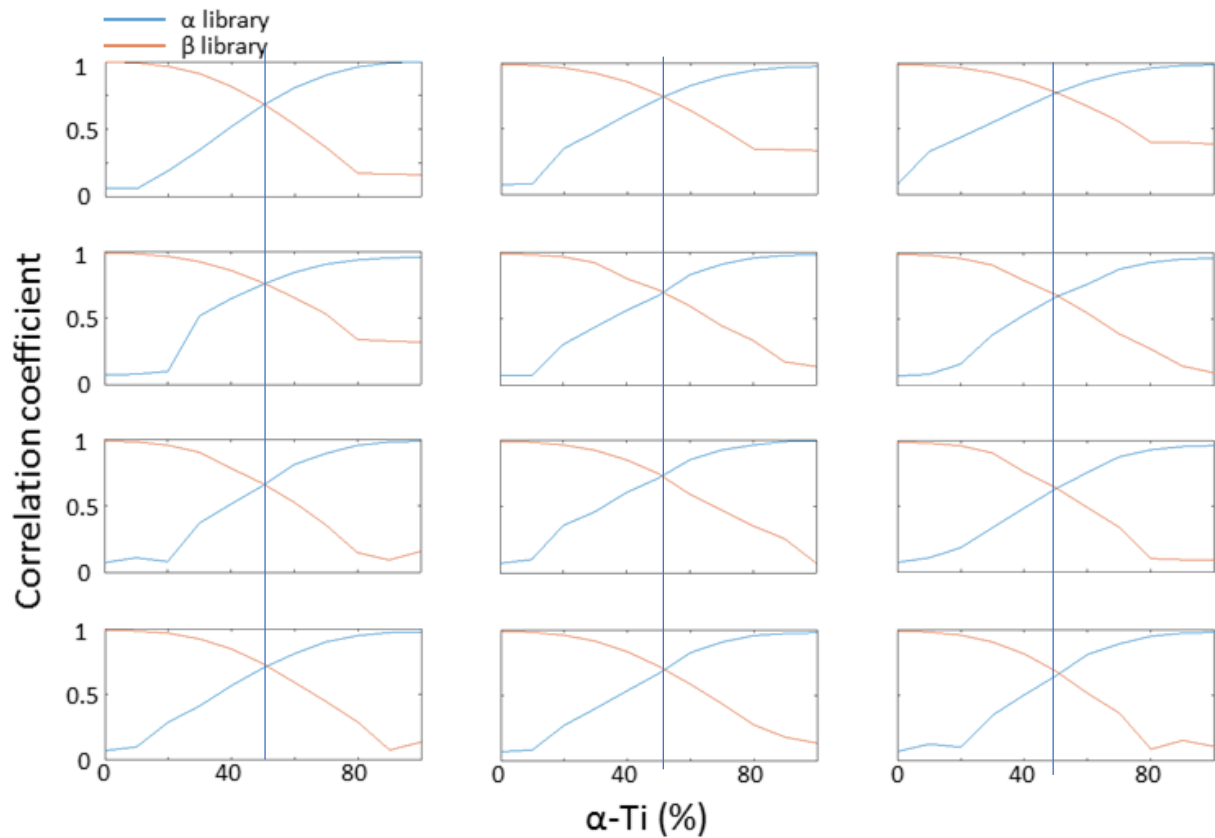


Figure 51: The correlation coefficient as a function of the α -Ti as a percentage of the pattern for each of the 12 ORs. Results show the CC for the α and β libraries, with the 50% pattern mix indicated with a vertical line.

Each of these mixed patterns is templated matched against a single phase template library, and the results from pattern matching are shown in Figure 51. In each case, the correlation coefficient of single-phase test pattern is equal to one. The correlation coefficient of the alternative library varies between 0.1 and 0.4, and this variation is present due to the orientation of the β -crystal and the detector, and which features from the BOR overlap on the EBSD screen. This sharing of features is highlighted in Figure 50.

Note that a linear mixing used here is a reductive approach to understand pattern mixing. In practice the contribution of each pattern will not be linear as shown here. The contribution of each pattern to the mixed pattern will vary based upon the scattering physics and crystal structure. This can be altered by the chemistry, structure and defect density of the two

phases within the interaction volume. Other contributing factors are the Z number of the atoms and relative orientations of the phase (which may be the same phase in a different orientation, not in an orientation). This is because the strength of the EBSD signal is related to the strength of the diffraction signal, which itself is a function of the volume fraction, effective Z-number, crystal quality, and density, as shown in section 10.2.2. This means the accuracy of phase determination might be lessened in a real dataset. In the case of α vs β titanium, the density will likely have the most impact on the diffraction pattern quality.

The major result from Figure 51 is that for a pattern that is either 100% BCC or HCP, the correct library consistently has a significantly higher CC than the incorrect library. For these simulations, the correct solution typically has a correlation coefficient of 1 when a single phase is present, the ‘worst’ (in terms of contrast) match has a cross correlation value of 0.4. When there is pattern mixing, then contrast drops, but has a difference of >0.2 and absolute value of >0.8 when the intensity mix is 70% the parent pattern.

12.3.2 Different Crystal Structures

Next, I explore a more general challenge of how well the method can classify different crystals. There are three significant ways in which a crystal lattice can differ. The geometry, Bravais lattice or lattice constants can all change [36]. Table 2 shows examples of each difference.

Table 2: Examples of the three ways in which a crystal lattice can differ

Materials	Difference	Notes
α/β titanium	Geometry	α –Ti is HCP β –Ti is BCC
α titanium/ β vanadium	Geometry	β –V is BCC

FCC iron (austenite)/BCC iron (ferrite)	Bravais lattice	Both FCC and BCC have cubic unit cells
FCC copper/FCC silver	Lattice constants	For copper: $a = b = c = 3.61$ $\alpha = \beta = \gamma = 90^\circ$ For silver: $a = b = c = 4.09$ $\alpha = \beta = \gamma = 90^\circ$

To show the refined template matching approach is capable of dealing with each of these changes, patterns for each pairing in Table 2 were generated and indexed against the correct and incorrect libraries. E.g, a pattern for α titanium was generated and then indexed against a library generated for α titanium (correct library) and one for β titanium (incorrect library). The pattern is then indexed against both libraries and the peak heights recorded.

For this analysis, all of the cross correlation values were recorded for the library search (i.e. on the limited SO(3) sampling, so the patterns do not perfectly match), and subsequently the top 5% refined of the matches as ranked by the cross correlation value were refined. The refined cross correlation values were recorded and the misorientation between the measured ultimately orientation and the input orientation were calculated. Results from this experiment are shown in Figure 52.

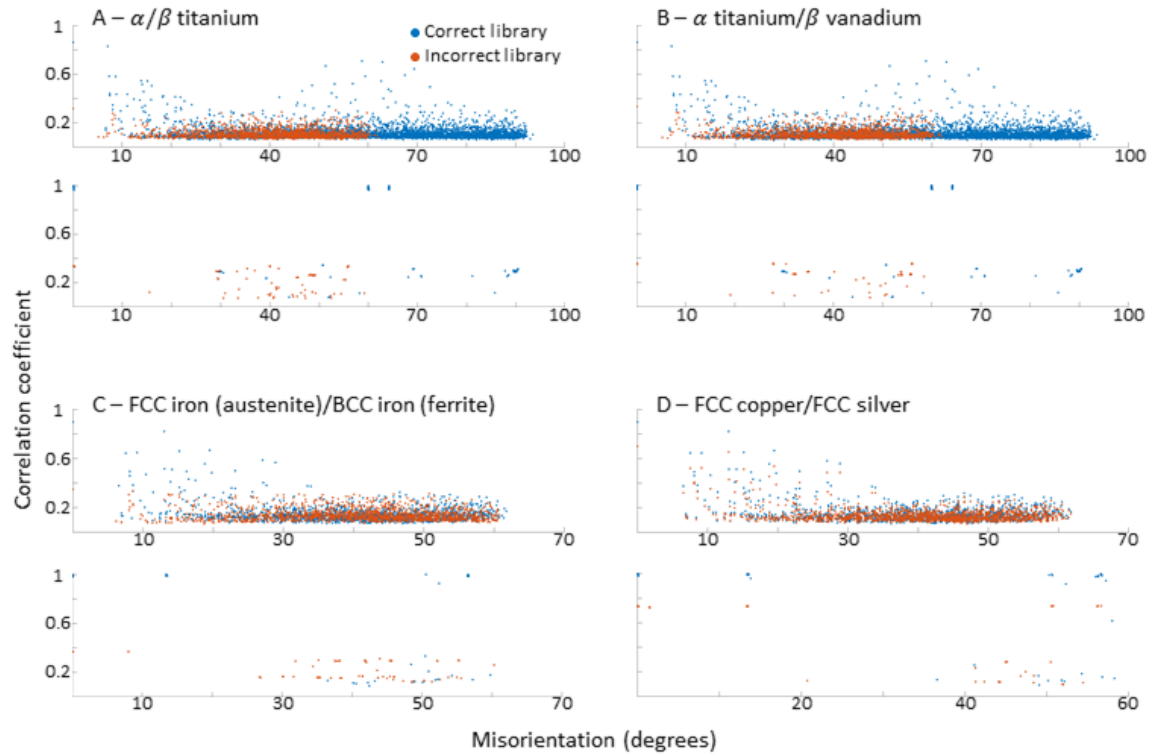


Figure 52: Graphs showing the CC for the top 5% of SO(3) library searches that have been refined against the correct and incorrect libraries for the pattern. The misorientation shown, is the misorientation between the known and correct orientation and the orientation associated with the CC returned. Graph A shows the results for an α -Ti pattern vs an β -Ti library. B is the same pattern vs an α -Ti library and a β -V library. C) shows an Austenitic pattern vs an Austenite and a Ferrite library. And D shows a FCC Cu pattern vs an FCC Cu and FCC Ag library. In all cases the least misorientated CC is the highest. Peaks at higher angles of misorientation show either symmetric or pseudosymmetric orientations of the correct orientation. This suggests the refined template matching can be used to differentiate all three cases of differing phase tested.

Points with low misorientation and the correct phase classification have cross correlation values of close to one for all trials. There are solutions with cross correlation values, for the correct phase, with values equal or close to one, and these correspond to symmetrically equivalent solutions. The incorrect solutions, e.g. for the incorrect library, all have significantly lower cross correlation values for their best match, typically with a coefficient of less than 0.4. This indicates a high contrast is achievable, even with these difficult case studies. The hardest results to see are those for Cu/Ag. This is due to the main bands in the pattern being in similar locations and strengths. In each case, however, the correct library is still higher than the incorrect library. There appear to be issues involving pseudosymmetry

(misorientations $> 0^\circ$, with a CC close to 1), the approach to deal with pseudosymmetry is discussed in chapter 13. The graphs act as a proof of concept and warrant further exploration. Alloying of similar elements, or alterations in lattice constants may yield differing results. As further exploration was not necessary for the main points in this chapter, time restraints on PhD completion prevented me from exploring further.

12.4 Experimental Demonstrations

To demonstrate the effectiveness of phase classification using this approach, an example dual phase titanium map was explored.

Each experimental pattern was background corrected, and then the refined template matching method was performed with the α -phase and β -phase reference patterns. The cross correlation values and ascribed phases, from ranking the highest cross correlation coefficient for the best matches, are shown in Figure 53 and compared with the Hough-based indexing (taken from the on-line Bruker eSprit 2.1 indexing).

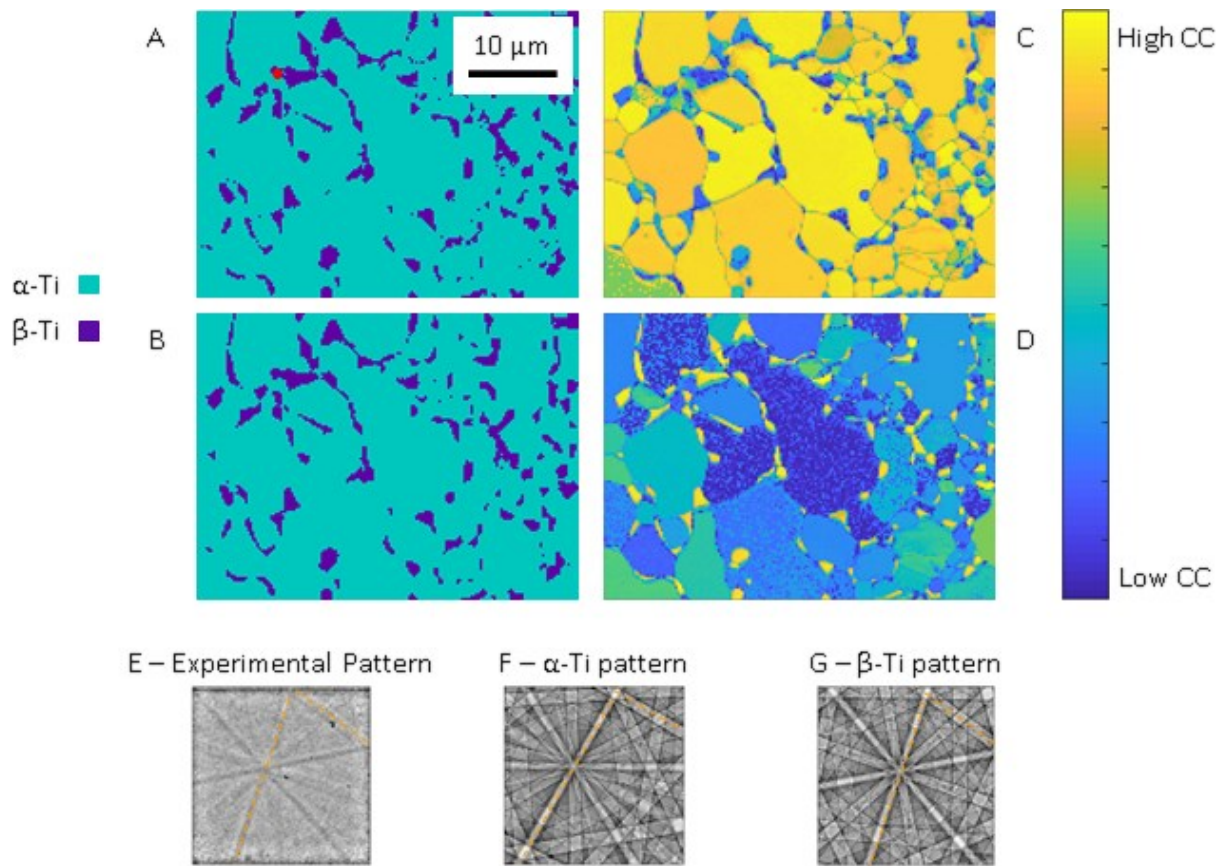


Figure 53: The dual phase titanium map for, A, the Hough based indexing and B the refined template matching approach. The α and β correlation coefficients for each point are shown in C and D respectively. The red point in A shows the location the pattern in E has been taken from, with F and G showing the indexed patterns with the α and β libraries respectively. Bands of interest in E, F and G are highlighted in an orange dashed line.

Figure 53 reveals a microstructure of \sim equiaxed α -phase grains, with regions of beta at the α - α grain boundaries and the triple junctions. The Hough based indexing reveals that the majority of these β -phase regions are indexed as a homogenous β -phase region. However, there are some regions where there are spatially isolated points of indexed α -phase. These regions, as shown with the experimental pattern in Figure 53E, typically have poor quality but identifiable patterns where it is easy to see that the best fitting α -phase pattern (Figure 53 F) is similar to the (correct) β -phase pattern (Figure 53) which is confirmed by the crystal plane in the top right of the pattern (and highlighted in orange).

The map was collected in a standard EBSD set up, with a beam acceleration voltage of 20 keV, a detector distance of 22.18 mm, a beam current of $\sim 1 \times 10^2 \mu\text{A}$, and a total collection time of 42 minutes 3 seconds (~ 120 ms per pattern).

This qualitative assessment, and simple ranking, highlights the potential of the pattern matching method to classify phases more reasonably, but it is limited for general studies as quantitative assessment of contrast is not yet performed, which is what I do in the next section.

12.4.1 Robust Pattern Matching for Phase Classification - Error Analysis

As EBSD is an experimental technique, where many thousands of patterns will be compared, it is useful to have confidence in the classification and to assess associated uncertainty. This section develops and tests a method of assessing how accurately the phase of a pattern can be determined.

In this chapter, I propose the signed contrast, δ_p , as metric for a dual phase pattern matching challenge:

$$\delta_p = \frac{\chi_{1i} - \chi_{2i}}{\chi_{1i} + \chi_{2i}} \quad \text{Equation 59}$$

χ_{1i} is the normalised cross correlation value, obtained from the peak of a 2D FFT based cross correlation of the background corrected, cropped, windowed, and filtered patterns between the test pattern and library 1, and χ_{2i} is the same calculation but against library 2.

This signed contrast metric is compared with the alternative proposed by Ram and De Graef [36], which they call the phase confidence $f \cdot f_i^p$ for the p^{th} phase and the i^{th} pattern is calculated from:

$$f_i^p = \frac{\sum_{j=1}^M w_j^p \overline{a_{lj}}}{\sum_{j=1}^M \overline{a_{lj}}} \quad \text{Equation 60}$$

In the phase confidence metric, the best pattern is matched based upon the highest correlation coefficient $\overline{a_{lj}}$. Next the top M correlation values for each dictionary search are stored. The phase confidence is constructed to calculate a ratio between these such that a weight, w_j^p , of 1 is applied for cross correlation values for the phase with the highest cross correlation value, and a weight of 0 is applied for every other cross correlation value.

Where $\overline{a_{lj}}$ contains the top M correlation coefficients and the associated library from which they originated, and w_j^p is weighting such that $w_j^p = 1$ for phase p and 0 otherwise.

Essentially the phase confidence here is the weighted average of all the correlation coefficients from a given phase against the values of CCs from all CCs for the top M patterns.

Unless otherwise stated, during this paper, when the phase confidence is used, I take $M = 30$ as standard, based on the findings of the original paper [36].

The new metric is proposed as the number, and distribution, of cross correlation values will depend on the sampling of the library and the crystal structure. In the refined template matching method, a sparse library is used (for computational reasons) and refinement is used to upsample this.

This changes how these metrics perform.

- (1) For an extremely sparse SO(3) library, as used in the refined template matching method, the distributions of the CCs of the initial library search are likely to be poor.

- (2) The refinement step may result in multiple seed orientations from the library search to converge on the same ultimate, more correct orientation. Thus, similar cross correlation values will come from multiple initial searches.
- (3) There may be 'wrap around' issues if the refinement upsamples the crystal orientation beyond the search space of the initial fundamental zone. This third issue will cause significant challenges when materials of different crystal symmetries (and therefore numbers of templates) as well as pseudosymmetry issues will adjust the shape of the search space. This is a subtle but important effect for a suitable selection of M in Equation 60).

Furthermore, for both metrics only the 'best' pattern is described but it is not clear whether either phase match is ultimately suitable (i.e. better than random). The addition of a threshold value for a match is proposed to fix this issue and is described in the "Phase Contrast" section.

12.4.2 Phase Contrast

Firstly, I will use simulations to explore contrast when two phases are matched using the refined template matching method and demonstrate how the signed contrast can be used to determine whether the proposed match for the phase (and orientation) is sensible.

I start by simulating two reference patterns using an α -titanium (HCP, $P6_3/mmc$, $a = b = 2.95$, $c = 4.686$, $\alpha = \beta = 90^\circ$, $\gamma = 120^\circ$) and β -titanium (BCC, $Im\bar{3}m$, $a = b = c = 3.3065$, $\alpha = \beta = \gamma = 90^\circ$) in DynamicS and the reference pattern is exported for the input pattern for the refined matching.

The default settings in DynamicS were primarily used. To allow for the use of different software when recreating patterns, these settings are shown in Table 3.

Table 3: The properties for the simulation used in Dynamics

Property	Value
Absorption (\AA)	124
Excitation (\AA)	97
Debye-Waller-B: Crystal	10.3
Debye-Waller-B: Source	0.3
Quality factor (90)	1
Thickness (\AA)	5000

The full diffraction sphere is simulated with a resolution of 1024 x 1024 pixels and exported to be reconstructed as an expected pattern for a given orientation in MATLAB. The reconstruction used a PC of (0.5, 0.3, 0.6), in units of screen length and described in [37].

The screen dimensions for the reconstruction were set to 128 x128 pixels.

Libraries with 7° spacing are then generated for both phases. A pattern size of 128 x 128 pixels, a pattern centre of (0.5, 0.3,0.6) and Euler angles (61°, 53°, −40°) are used for both patterns as in this instance, there is no need to relate the patterns with the BOR. Due to the different reference crystal frames, the patterns generated are different, despite the same seed Euler angles.

These patterns are used to explore what value is suitable as an absolute cut off for a correct match, and to evaluate the phase contrast metrics.

The top 5% of the SO(3) matches were retained and the orientations were refined. Values for the CC are reported in Figure 53.

Firstly, for an α -pattern matching with an α -library we observe that multiple incorrect seeds are found within our data set, with only $\sim 1\%$ above a CC of 0.5. This is not surprising and reflects that the contrast between a good match and a poor match is high. The number of solutions with a CC > 0.9 increases when refinement is used. Multiple of these are from the same seed orientation.

For an α -pattern matching against the β -library there are no solutions where the CC is greater than 0.5, and refinement of the best solutions only results in values of CC which peaks at 0.6.

When the reverse problem is considered, testing β -patterns against the library and associated refinement with the correct and incorrect phase, we observe a similar outcome to testing the α -pattern. There is an additional peak for β -pattern vs β -library, with $\chi = 0.8$ and this is related to the pseudosymmetry match of the $\langle 111 \rangle$ zone axis. The presence of a pseudosymmetric peak may cause issues when the “top 20” solutions for the correct phase used as a quality or reliability metric.

Together these two tests indicate that there is a threshold value of χ which is suitable to cut off matching. However, note that these tests are noise free simulations, where the contrast exactly matches and so the exact values may need to be modified.

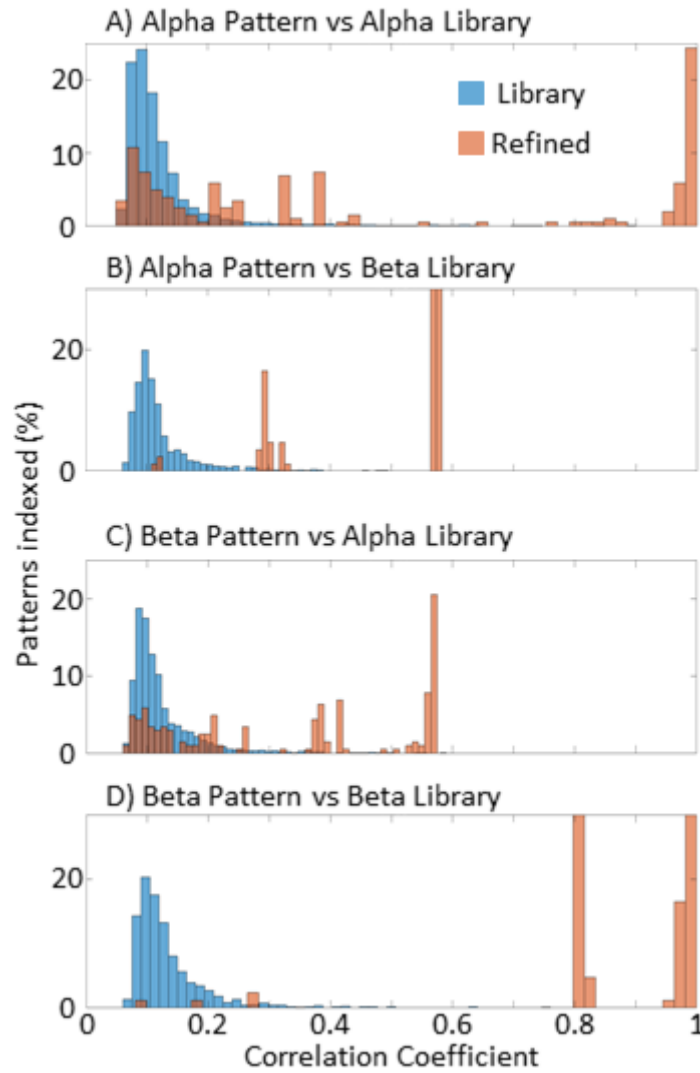


Figure 54: The results of matching an α -titanium pattern against A) an α -titanium library and B) a β -titanium library and a β -titanium pattern against C) an α -titanium library and D) a β -titanium library.

Note that in parallel to my work and in collaboration with me as part of my project, Tom McAuliffe developed a statistical test of the distribution and this is reported in full within his PhD thesis [141]. This analysis determines if the solution suggests is better than random, and is described briefly here.

Firstly, the CCs (χ) for all library matches are recorded and normalised, such that the library normalised CC (Z) is given as:

$$Z = \frac{\log(\chi_{\max}) - \mu}{\sigma}$$

Equation

61

where μ and σ are respectively the arithmetic mean and standard deviation of the respective SO(3) library match.

Plotting the histogram of the distribution of the normalised CC values gives a normal distribution and therefore, if the best value for the library search lies above the 2nd standard deviation, it is 95% certain the value is not a random orientation match, i.e. some features within the diffraction pattern correlate with the experiment. This is shown graphically in Figure 55.

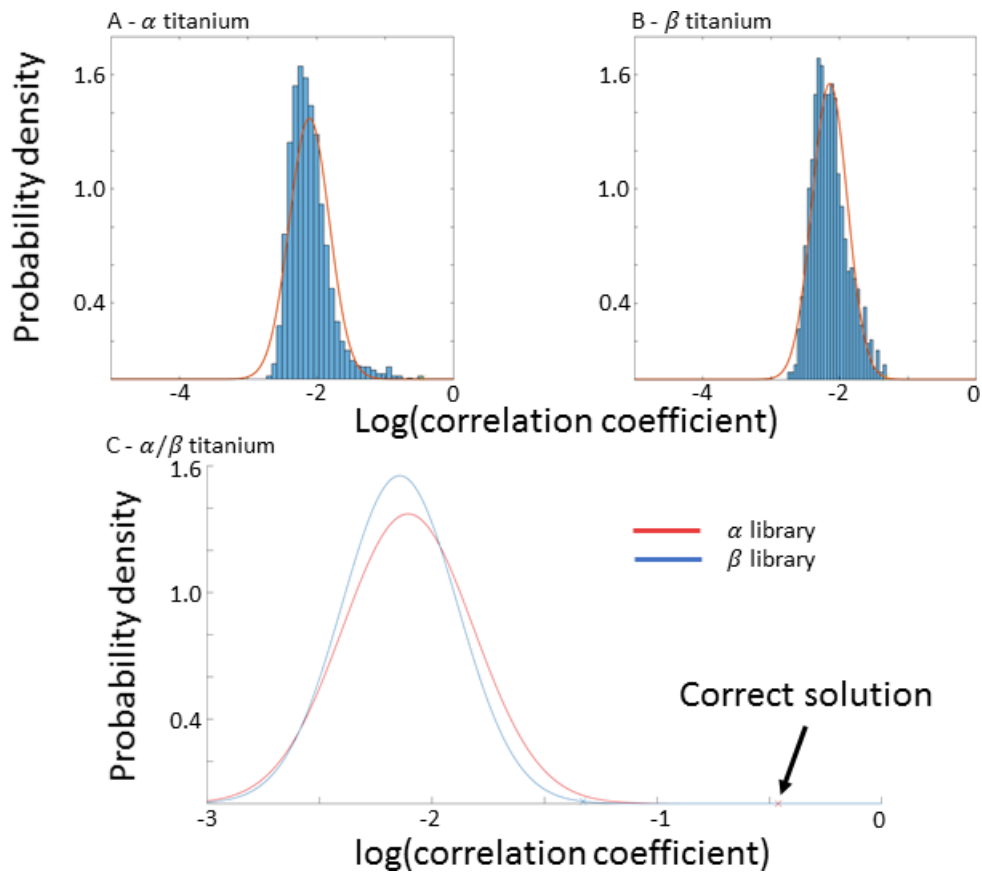


Figure 55: The normalised correlation coefficients for an α titanium pattern library search plotted against A: an α titanium library, B: a β titanium library and C: both libraries. C also shows the locations of the two best matches from the library search. The alpha library is shown to have a better match due to the pattern being further along the x axis.

In my work, the distributions shown in Figure 54 and Figure 55, 0.6 seems to be the cut off limit for CCs in perfect patterns, and when this is repeated for the experimental data (which has increased noise and other contrast) a value of 0.5 can be selected as a suitable cut off for experimental patterns in dual phase titanium. This means that for the experimental data set, if a point has a CC of < 0.5 for both α and β libraries, it is considered to be misindexed. This value is supported by a forescatter electron image of the mapped region, shown in Figure 56 (where the unindexed regions are largely found in the 'dark' areas due to shadowing).

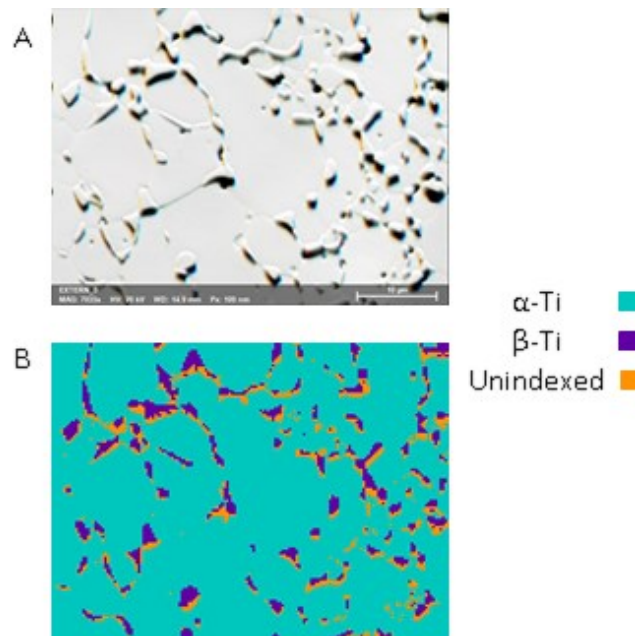


Figure 56: A) An Argus image of the titanium map, with B) the same map as in Figure 53 with the points marked as red below the threshold value

At this point, the best phase has been selected through ranking of the highest cross correlation coefficient for the best matching pattern, and points with a low cross correlation value have been removed using a threshold value as determined from statistical analysis of the measured cross correlation distributions.

Assignment of the phases, above the threshold values, thus far has been determined simply by ranking the cross-correlation coefficients for the best match with library A and library B, provided they are above a threshold (established from the statistical test). However the classification does not address cases where the quality of the match with the second phase is poorer than the first, e.g. due to differences in the intensity distributions within the reference patterns. This motivates evaluation of the signed contrast (Equation 59). This method suggests that the condition for determining the phase requires:

- (1) The correlation coefficient with library A must be greater than a minimum value, established with the statistical test of the SO(3) library.
- (2) The signed contrast for matching the experimental pattern with phase A must be significantly high, and the signed contrast for matching with phase B must be sufficiently low.

This approach can be seen within 2D histogram for all points within the mapped regions, as shown in Figure 57. Here regions that are identified as α -phase have a high correlation coefficient and high contrast, and tend to have poor contrast for the β -phase, and vice versa for those points which are identified as beta phase. However importantly there is now a region where neither phase is a suitable match, and this is clearly demarked. Looking at the map, these regions tend to be the shadowed regions (compare with the foreshatter electron image in Figure 56)

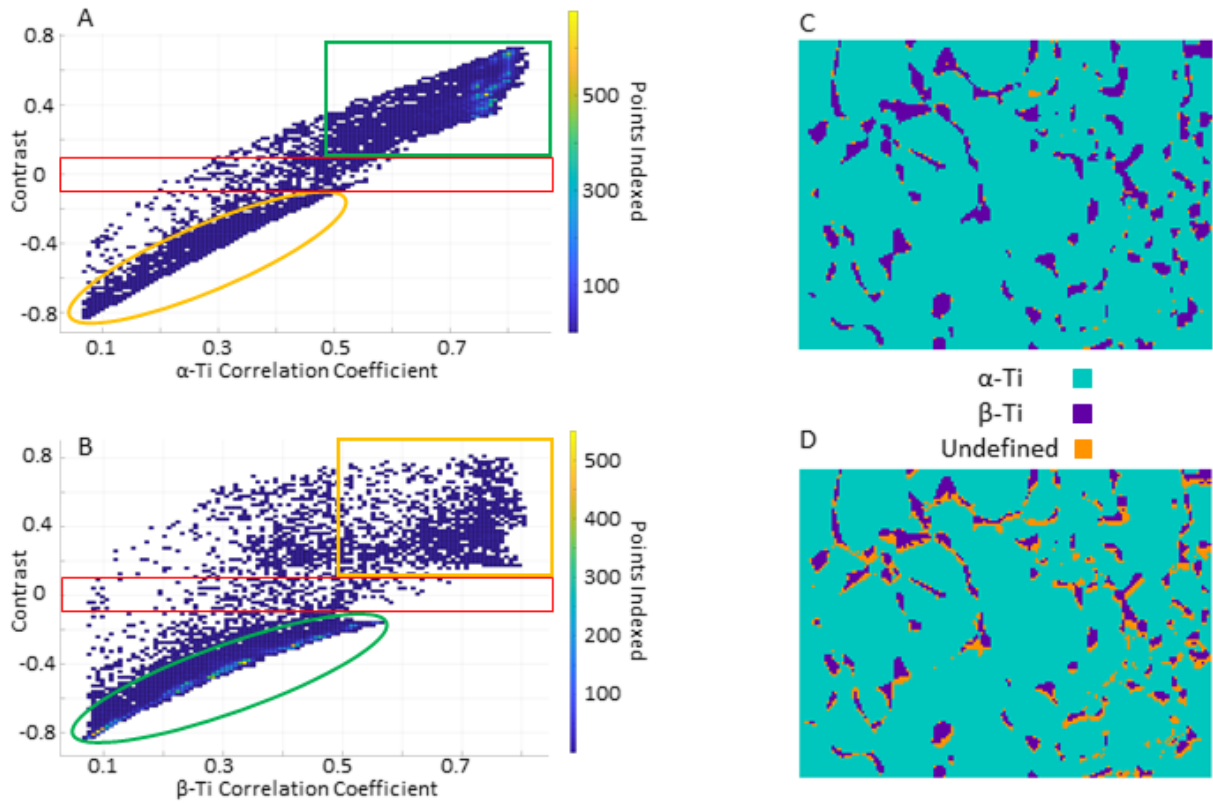


Figure 57: A and B show 3-D histograms of the contrast against the CC of a given library for indexing. The contrast is calculated as in Equation 59, with χ_{1i} as the α library for A and β for B. The colours show the number of points in each bin at a given point. The red boxes show the regions that are removed within a contrast threshold of 0.1 as read from the base of the large clump in A. The area inside the green highlighted section show points with a high contrast and that have a CC above a threshold of 0.5 for the α library and orange boxes show the same for B. C and D show the phase maps for the contrast threshold and the contrast and CC threshold determination methods respectively.

By looking at where the upper and lower pools of good matching level out in Figure 57, a value of 0.1 was taken to be the contrast cut off.

12.4.3 Comparison with the Phase Confidence Metric

It seems prudent now, to test this new phase confidence metric against the previously established phase confidence metric (Equation 60).

As a brief reminder, Equation 60 returns a confidence vector in the form

(phase 1 confidence, phase 2 confidence, ..., phase n confidence) for n phases. The

phase confidence is essentially a weighted average for all of the CC values associated with the phase in question.

To this end, the dual phase titanium data used throughout this chapter has been reindexed and the phase confidence (Equation 60) was calculated for each point after the initial $SO(3)$ library search, and the top M search results refined and the phase confidence calculated again. Note that for $M = 30$ and two phases, this requires an addition 58 (29×2) orientation refinements and is computationally very expensive.

Phase confidence for α and β have been plotted. This can be compared to the CC maps in Figure 53 and a map of the signed contrast at a given point. The results are shown in Figure 58

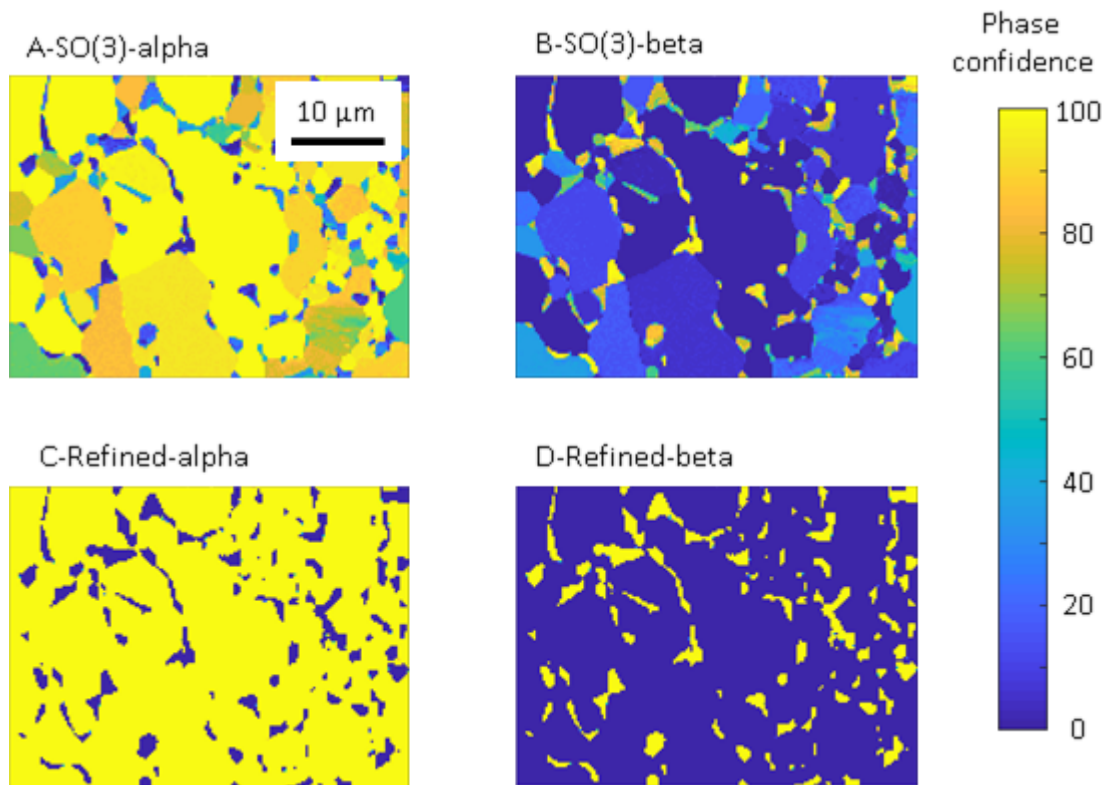


Figure 58: Maps showing the phase confidence described in Equation 60. Map A shows the phase confidence for the initial library search in $SO(3)$ space for an alpha library and B) shows the same for a beta library. The top M patterns from the initial search were then refined and the phase confidence calculated again for the refined step and are shown in map C for the alpha library and D for the Beta.

Figure 58 shows the existing phase confidence, at first glance, appears to be a very good metric for differentiating phases to a high confidence. However, it is likely that this accuracy is falsely inflated due to the nature of the refinement step.

In the experiment the top 30 library results were taken and refined for both libraries. It is possible that distinct orientations in the library search that yielded separate CC values were refined to the same orientation with the same CC value in the refined step. This effectively reduces the M value for the refined approach, which reduces the accuracy of the phase confidence metric, as shown in [36]. This could be fixed by increasing M , however, this would dramatically increase the computational costs associated with the calculation.

The overestimation of the phase certainty using the established metric in Equation 60, prompts the suggestion that the signed contrast metric developed throughout this chapter be used in conjunction with the refined template approach. The additional computational costs with the larger M value needed mean the established metric is unsuited the refinement.

This only applies to the refined matching approach. If you are using the classical dictionary approach, the additional computational costs are minimal and the metric works due to each CC being associated with a unique orientation. It also easily transfers from two to many phases. The approach described in this chapter can be used to examine multiple phases, however to do so, the signed contrast metric can only look at the contrast between the top two candidate libraries.

12.5 Chapter Summary

This chapter has introduced the RTM method to characterise the phase of a pattern.

Through rigorous testing with generated and experimental patterns the method has been shown to correctly identify patterns with different structures, Bravais lattices and lattice constants. The signed contrast and cut off error metric was also introduced and shown to be an effective measure of where misindexed patterns might be.

13 Application of the Refined Template Matching Approach to Pseudosymmetry

Pseudosymmetry is a phenomenon where two distinct crystallographic orientations look similar, such as when they produce similar EBSs which are easily confused. This is described in more detail in section 10.5.8.4.

Pseudo symmetry often happens for cells of lower symmetry, where two distinct orientations look similar as the lower symmetry cell can be described in terms of a unit cell which is of higher order (i.e. more symmetric) and the two distinct orientations would be the same orientation of the higher order cell.

As a simple example, consider a cell with $a = b = 1$ and $c = 0.98$ with $\alpha = \beta = \gamma = 90^\circ$. This cell is tetragonal, but crystal is almost cubic (as c almost equals a and b). This means that a diffraction pattern with the $\langle c \rangle$ axis pointing horizontal would look extremely similar to a pattern with $\langle c \rangle$ pointing along Y , and these would be confused with the third having $\langle c \rangle$ along Z . The challenge of identifying the direction of the $\langle c \rangle$ axis of this cell, and the associated confusion, is related to the pseudo symmetry and the symmetry operators of the higher order cubic unit cell (e.g. the triad axis along the diagonal). This simple case is important, as it is observed for martensite in steels [142], but more complicated challenges can be found in many intermetallic systems. The literature review section goes into more detail about pseudosymmetry.

In intermetallic crystals, the less symmetric crystal can involve not only a change in the lattice parameters but also a change in the distribution of atoms in the unit cell, which results in more complex and subtle variations in the diffraction pattern. For examples some pseudosymmetric patterns even show higher order Loue zone (HOLZ) rings in one orientation that are absent in other (related) orientations. These features can be seen in

experiment, but I note that the version of DynamicS used in this thesis does not typically simulate HOLZ rings and so these features can be used to identify differences between the experimental patterns they will not be used in the formal analysis here.

In this chapter, patterns collected by Yi Cui (of Imperial College London) are examined.

These patterns were collected from an intermetallic particle in a furnace cooled Al-3Fe alloy and the intermetallic particle can be important in understanding the casting process, as well as the performance and life of the part. Yi Cui identified that this particle is $\text{Al}_{13}\text{Fe}_4$, which has monoclinic symmetry [143].

Figure 59 shows two different patterns from two regions in the particle which exhibit pseudosymmetry, such that both patterns can be identified as the same orientation with conventional (Hough-based) EBSD analysis, but manual analysis can be performed to highlight the main features that make them different.

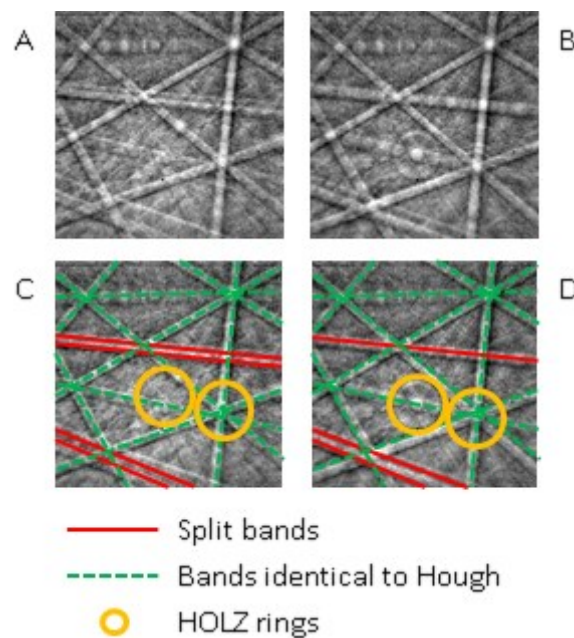


Figure 59: Two patterns exhibiting pseudosymmetry are shown in A and B, with annotations of similar and different features shown in C and D. All highlighted bands would be indistinguishable to the Hough method of indexing. The red highlighted bands are split bands, where the band width and relative intensity differentiate them. The orange circles show the HOLZ rings.

The challenge addressed in this thesis chapter is to create an efficient, and general, approach to classify pseudosymmetry related EBSPs as the correct orientation.

13.1 Al₁₃Fe₄ Unit Cell

Al₁₃Fe₄ is a monoclinic material that exhibits pseudosymmetry. It is used throughout this chapter to demonstrate the effectiveness of the refined template matching approach to indexing a pseudosymmetric pattern, and as such it is important we fully define and understand the unit cell and how it projects as it rotates (section 10.1.1). An unrotated unit cell, and how the \hat{a} , \hat{b} and \hat{c} relate to the sample frame are shown in Figure 60.

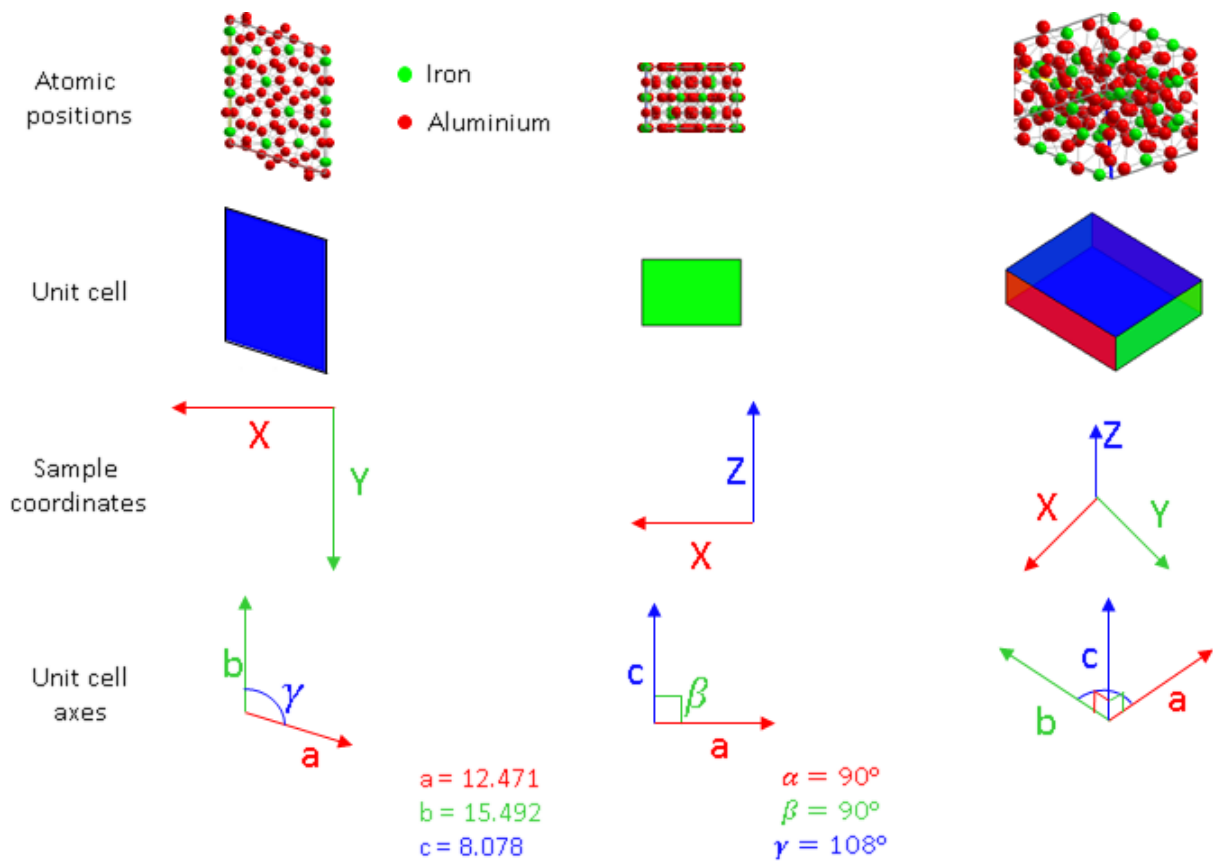


Figure 60: An Al₁₃Fe₄ unit cell, the associated atomic positions and how they relates to the sample frame.

In the analysis of the EBSPs formed by Al₁₃Fe₄ in this chapter, I follow the conventions shown from the crystallographic information file (CIF) as read in the DynamicS software and set $a = 12.471$, $b = 15.492$ and $c = 8.078$, with $\alpha = \beta = 90^\circ$ and $\gamma = 108^\circ$, and I will

show shortly that I can confirm understanding of this cell structure with a reproduction of rotations between cell and diffraction pattern in a MATLAB based tool.

I stress that I follow the CIF convention, as this is different to the description used in MTEX 5.4.0 and Esprit 2.1 where the unit cell parameters are defined as $a = 15.492$, $b = 8.078$ and $c = 12.471$, with $\alpha = \gamma = 90^\circ$ and $\beta = 108^\circ$. Convention would state that the unrotated \hat{c} axis lies parallel to sample \hat{z} axis, and this means there is a rotation of lattice vectors between conventions which needs to be accounted for (and understood).

The cell is explicitly plotted in Figure 60 for the convention I have employed and throughout the chapter, I will follow the convention set up in Figure 60. Note that Figure 60 the cell is coloured such that the:

red plane is normal to the red \hat{a} vector;

green plane is normal to the green \hat{b} vector;

blue plane is normal to the blue \hat{c} vector;

and in the reference configuration (i.e. no rotation) $\hat{c} // Z_s$ and $\hat{b} // Y_s$

Where appropriate the X,Y and Z axes will also be coloured red, green and blue respectively.

This convention is described in more detail in [37].

To aid later discussion, Table 4 shows the locations of each of the atoms in the unit cell, as read from DynamicS.

Table 4: Atomic Coordinates of the $Al_{13}Fe_4$ unit cell, taken from DynamicS

	Atomic positions along		
Atom	\hat{a}	\hat{b}	\hat{c}

Fe	0.382	0.085	0
Fe	0.623	0.402	0
Fe	0.989	0.091	0
Fe	0.986	0.403	0
Fe	0.278	0.320	0.294
Al	0.174	0.065	0
Al	0.282	0.323	0
Al	0.535	0.238	0
Al	0.580	0.074	0
Al	0.961	0.241	0
Al	0.829	0.479	0
Al	0.5	0.5	0
Al	0.773	0.306	0
Al	0.789	0.087	0
Al	0.111	0.185	0.217
Al	0.110	0.368	0.211
Al	0.335	0.178	0.221
Al	0.330	0.492	0.233
Al	0.479	0.363	0.219
Al	0	0	0.25

Finally, as part of the addition to the indexing algorithm to account for pseudosymmetry, I will be using a reduced symmetry library for the initial search. I.e. for a monoclinic cell, such as $\text{Al}_{13}\text{Fe}_4$, a cubic library can be used and then refined to more correct orientation. To aid in

discussion, I have generated an $\text{Al}_{13}\text{Fe}_4$ pattern and the roughly equivalent unit cell orientation in silicon. The orientations used in the reduced library initial search will be for the correct material. However, this demonstrated the symmetry being taken advantage of to reduce the initial search time.

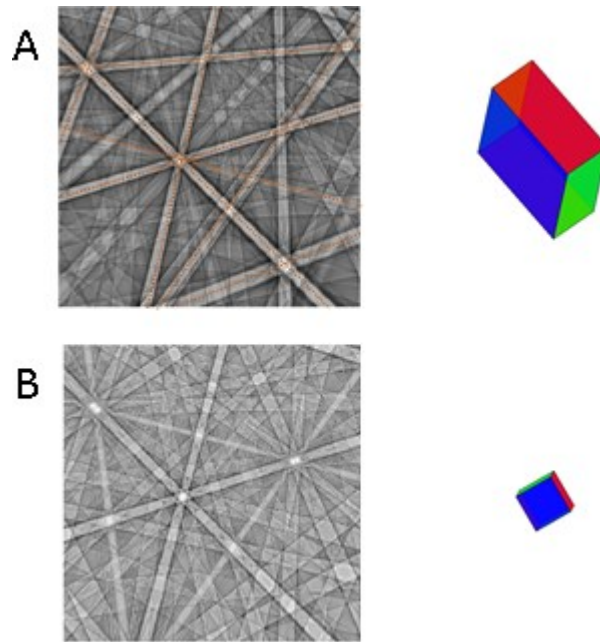


Figure 61) The EBSD and respective unit cells for A) $\text{Al}_{13}\text{Fe}_4$ and B) Si in a pseudosymmetric configuration. All of the bands highlighted in A) have a corresponding band in B and it is this symmetry between the two patterns I take advantage of in the modified indexing algorithm.

13.2 Reference Frames

Lower symmetry crystals are useful to confirm our understanding of the relationship between the diffraction pattern, unit cell, and the microscope, but they are also less forgiving of systematic errors.

This motivates a brief confirmation that we understand the reference frames involved in EBSD, and specifically confirm that the simulated lattice planes match the unit cell and we can rotate the crystal and pattern consistently. This is covered in detail in the literature

review and in [37], but to aid in the discussion of pseudosymmetry they are summarised here.

The main frames are:

- The sample frame (X_s, Y_s, Z_s) – how the sample is oriented with respect to the detector;
- The gnomonic frame (X_{gn}, Y_{gn}, Z_{gn}) – the coordinate system of the EBSD camera with respect to the sample;
- The unit cell frame – the orientation of the unit cell \hat{a}, \hat{b} and \hat{c}) with respect to the cartesian axis system, and this is easy to confuse for a monoclinic cell.

These frames are shown in Figure 62, here I use the conventions as described by Britton *et al.* [37] which are described in section 10.1.1.

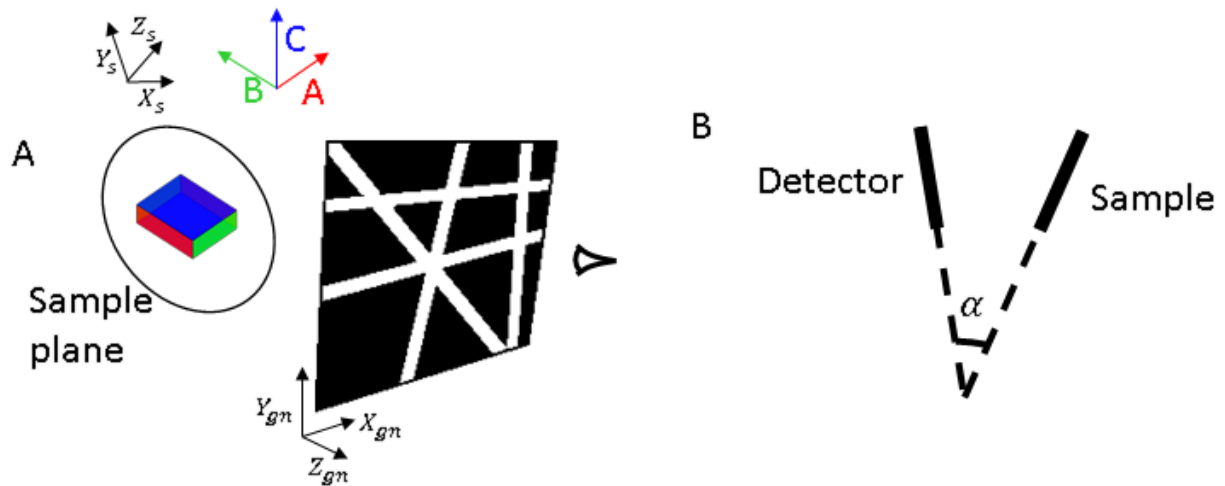


Figure 62: A) The sample plane shown as a circle around a unit cell. The axes show the sample frame and the unit cell frame. The projection of the EBSD in the gnomonic frame is also shown. And B) the rotation (α) about the X axis shared between the sample and gnomonic frames to switch between the two.

13.3 Representing the Orientation of the Unit Cell

Next, I explore the relationship between these frames with a simulation performed entirely in MATLAB (where the conventions are explicitly constructed using AstroEBSD tools). Figure

63 shows the applied rotations of the unit cell in the sample frame, the patterns generated and confirmation of the diffracting planes.

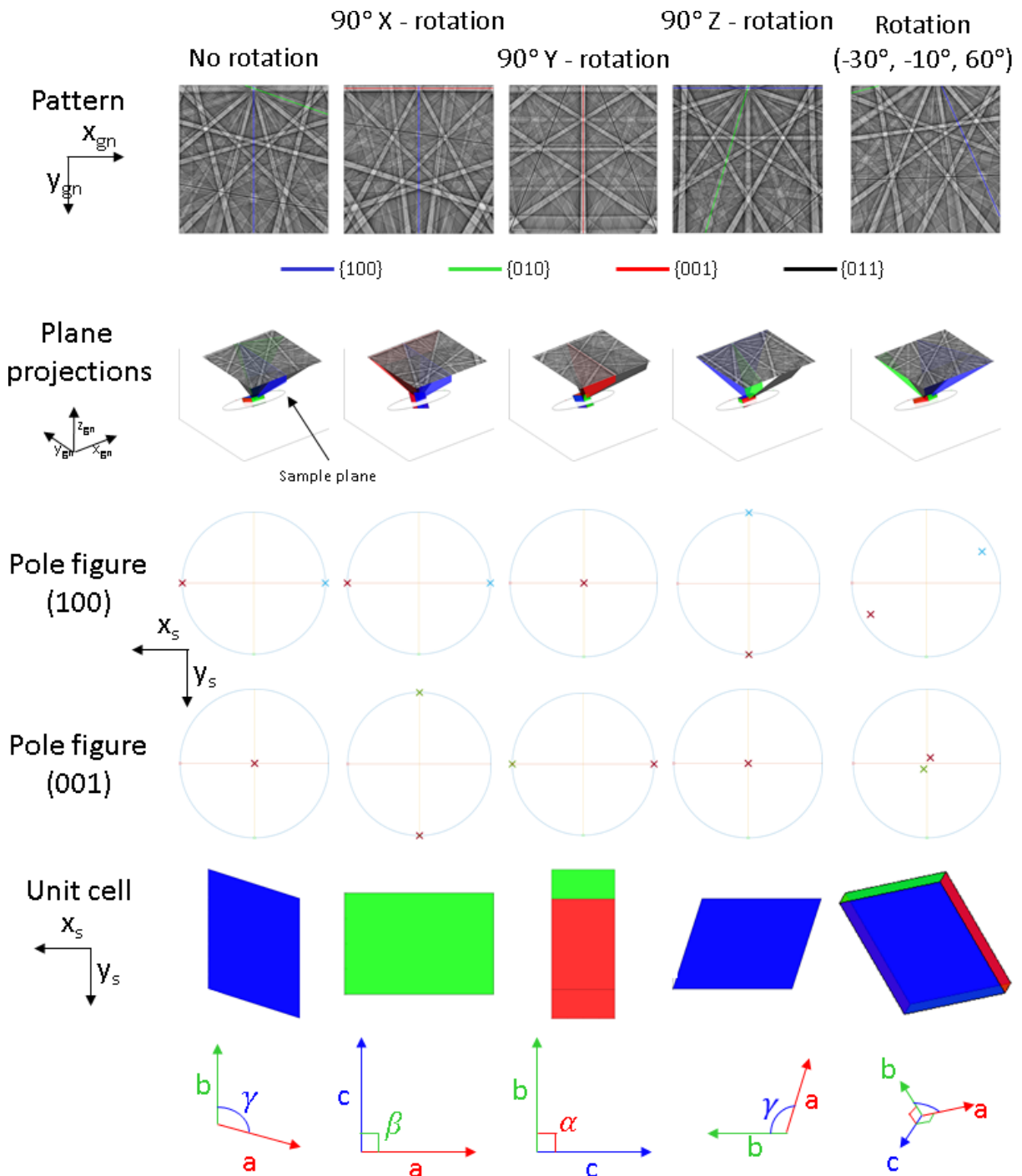


Figure 63: The controlled rotation and representation of a unit cell for $\text{Al}_{13}\text{Fe}_4$. For the $(-30, -10, 60)$ rotation green cross represents the C axis in the positive hemisphere.

Figure 63 confirms that I can rotate the unit cell and represent it in the dynamical diffraction pattern and a known sample frames of reference. It is important to note that I have

confirmed that the simulated bands belong to the correct lattice planes in the dynamical pattern, and their relationship in 3D is shown in the 3D projection. Finally, the unit cell and stereographic projections in the sample frame of reference are included for completeness.

13.4 Resolving Pseudosymmetry with Pattern Matching

Typical analysis of diffraction patterns using the Hough-based routines do not have sufficient resolution to distinguish between pseudosymmetric orientations. Pattern matching methods, which include the dictionary indexing (DI) method [7], can distinguish between pseudosymmetric patterns as they compare intensities within the whole pattern and do not rely on classification based upon (similar) measurements of the interplanar angles

A challenge with these pattern matching approaches is their (relative) computational speed, as many more calculations are needed to determine the final orientation of the pattern. This computation speed is (inversely) dependant on the size of the template library, which is determined not only by the angular spacing of the sample but also the size of the fundamental zone. For comparison, a sampling factor of 2° (a lower limit to the size of the library for the DI method), a cubic cell would need $\sim 77,000$ patterns and a monoclinic cell would need $\sim 900,000$ to find a suitable peak for pattern matching and this means that the time taken to index a pattern from such a library would be far too much to be practical by a general user.

This motivates more efficient searching algorithms where knowledge of the sampling spaces is used to our advantage. One method of reducing the library size for the Dictionary Indexing method was proposed by Pang *et al* [102] whereby the Hough based orientations

are used as seed points for the Dictionary Indexing library and patterns are generated around those seeds.

These refinement methods reduce computation cost, but they do not resolve the pseudosymmetry problem directly. There is potential for us to improve this approach through searching not only the local neighbourhood, but to also include the pseudosymmetry equivalents if the misindexing cases are well known in advance. This can be complicated as the relationship between crystallographic groups can be challenging and require specialist user knowledge.

This motivates a different approach which is explored in this chapter, whereby the EBSD equivalent patterns are sampled between symmetry groups using the higher and lower symmetry spacings, through a brute force method. Once these electron diffraction pseudosymmetries are stored (and this only has to be computed once for a camera geometry), pattern matching of experimental can be performed in the (more efficient) higher symmetry sampling which also employs a coarser sampling frequency due to the size of the peaks, as discussed in chapter 2. Then a reduced number of searches can be performed with the refined template matching approach, applying the EBSD equivalent orientation relationships. The ultimate crystal orientation is selected based upon the orientation highest correlation coefficient (CC) is taken to be the correct orientation.

The process is shown diagrammatically in Figure 64.

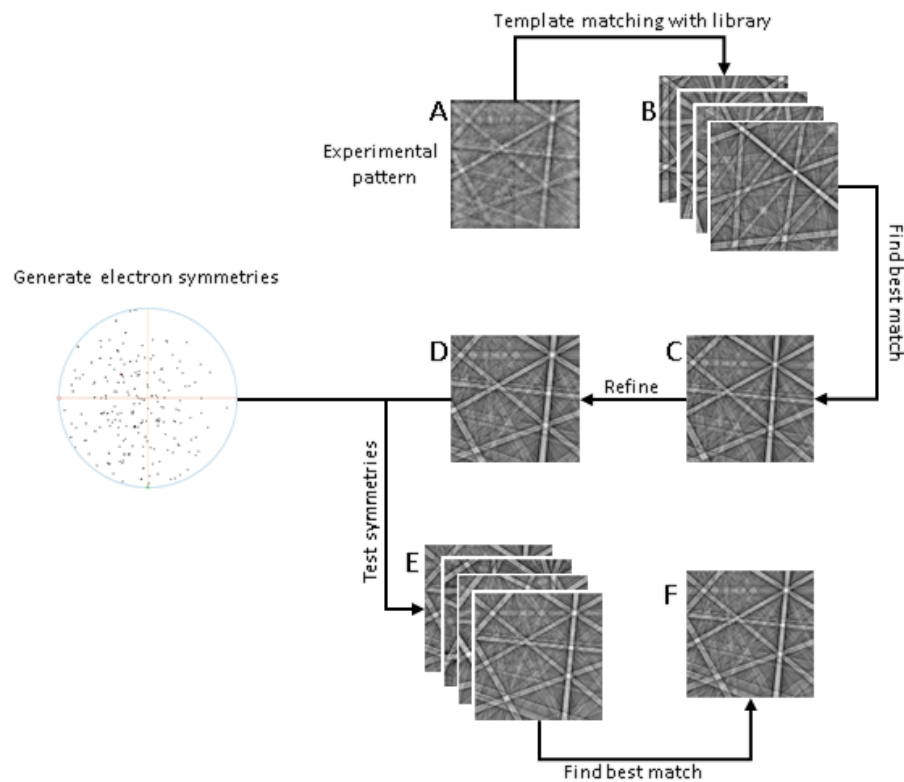


Figure 64: The modified refined template matching to account for pseudosymmetry. A reduced library is first generated and used to get an initial orientation. This is taken as a starting point and symmetrically equivalent rotations are applied and tested. The best match is taken to be the correct orientation

13.5 Electron diffraction pseudosymmetries

The electron diffraction pseudosymmetries are orientations which have similar EBSPs and will be confused within the efficient search space (e.g. the $SO(3)$ search of the higher symmetry fundamental zone). To calculate these pseudosymmetries a brute force method is used.

The brute force method starts with the full monoclinic library, as generated for the pattern matching approach. For this, a lower sampling frequency is required to conduct a thorough search of orientation space. In this instance 5° is used. As this only needs to be performed once per EBSD geometry, for a given unit cell, this does not affect the index time per pattern. This is essentially an extra set up step. This can be seen in Figure 65.

As well as the generation of the library, a reference pattern is generated for a random orientation. The reference pattern is then matched against all points in the library and the CCs recorded for each point, this is shown as a red dot in Figure 65.

Examination of the measured cross correlation values will result in many poorly matched patterns (e.g. with a correlation coefficient of <0.3), but there will be some patterns that are a better match. Cross correlation values numerically close to 1 are symmetric equivalents. Cross correlation values above random matching and lower than 1 can be electron diffraction pseudosymmetries, and these can be thresholded for those which correspond to a sufficiently “good match”. I.e. orientations that have a CC higher than a threshold value are likely candidate orientations for an electron-pseudosymmetric orientation. The threshold value can be determined using Figure 66. The disorientation matrices between the reference pattern and the electron diffraction pseudosymmetries are recorded.

The points above the initial threshold value are then run through a refinement step, as in the standard refined approach described in this thesis. The refinement step migrates the seed orientations in the initial close matches for the electron pseudosymmetries. These refined orientations can again be thresholded using Figure 66. This process is shown in Figure 65.

To account for missed equivalences, the initial seed orientation is switched to the most disoriented point in the initial library and the whole process iterated until the seed starts switching between two seed orientations. This is usually after ~ 5 iterations. The disorientations to the seed orientation become the electron pseudosymmetry equivalent rotations and are stored for the indexing algorithm.

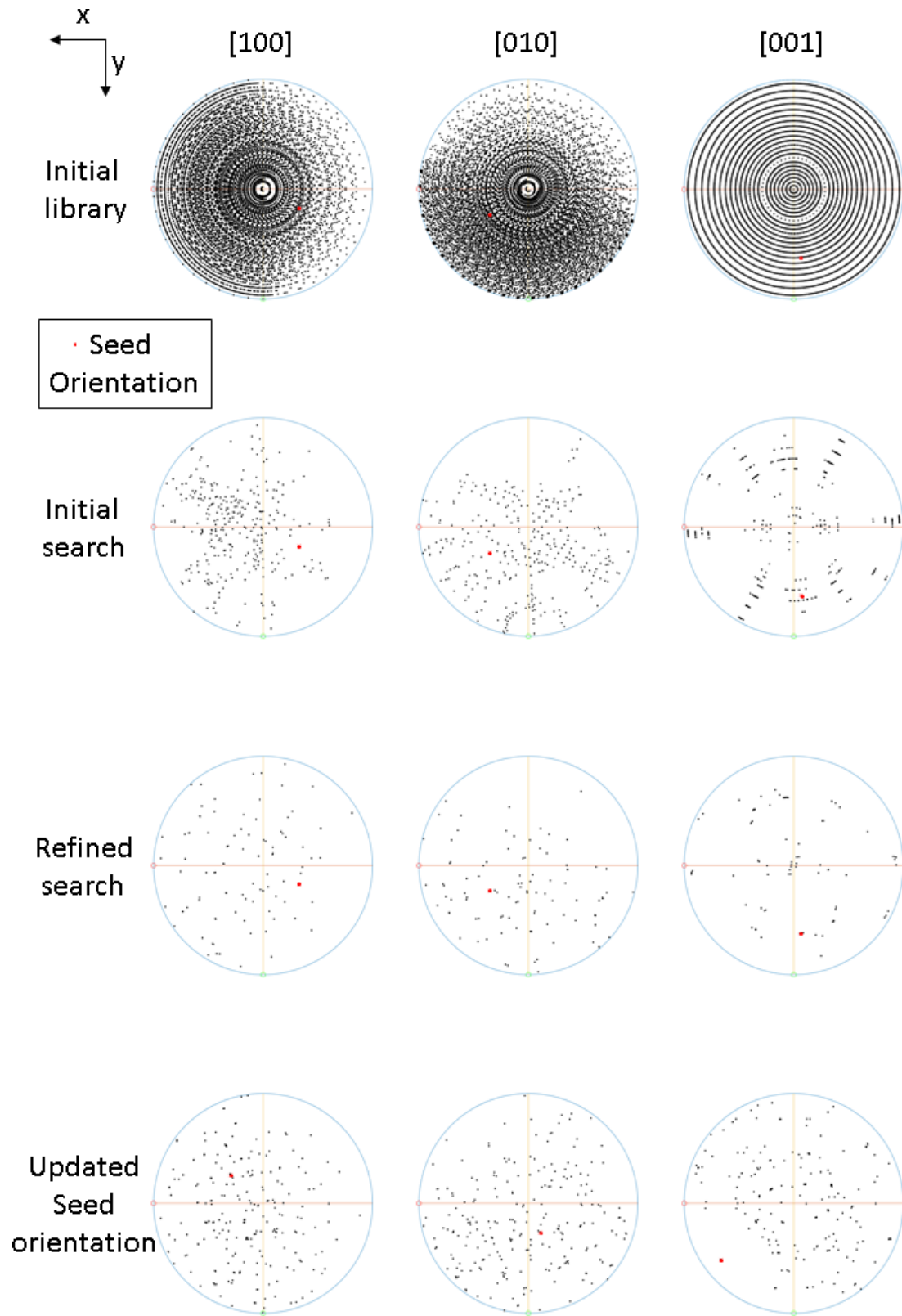


Figure 65: Pole figures showing the full $SO(3)$ library (this is showing a sampling frequency of 8° due to the time needed to plot the full 5° $SO(3)$, however as this is a demonstration, this is sufficient), and initial seed orientation. The results of the first search and thresholding, the refinement and the final result of the first iteration showing a new seed point.

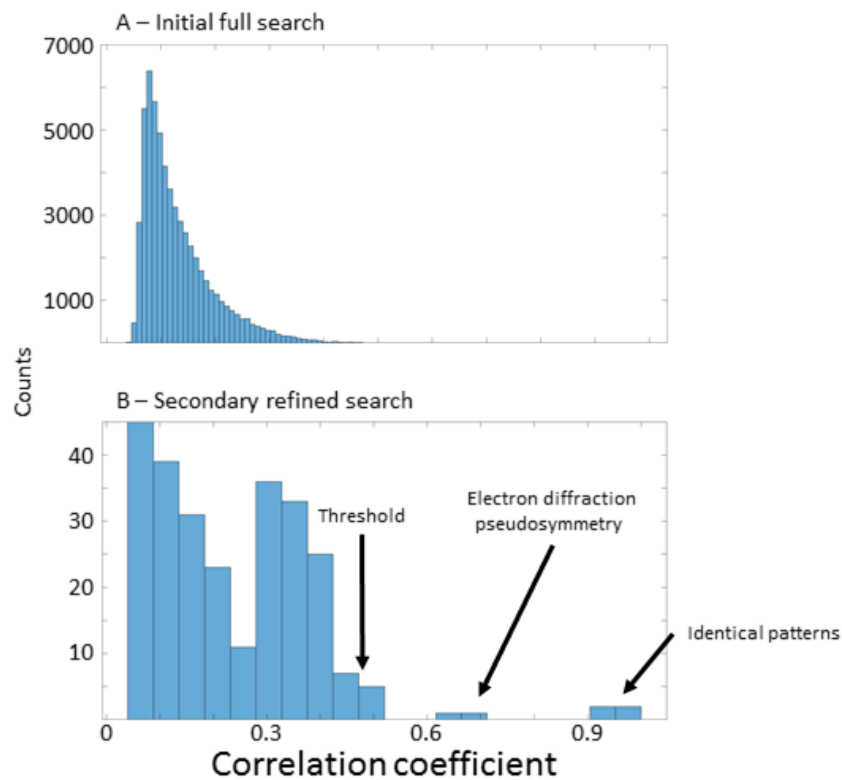


Figure 66: The distribution of the correlation coefficients found in A) the initial search of the whole fundamental zone and b) the distributions of the CCs after the refinement of patterns above the cut off value.

Figure 66 shows the distribution of correlation coefficients for A) the initial library search and B) the refined search. The thresholds used to define a good enough match to refine can be defined from these two graphs. The tail end to the right of Figure 66 A for the initial seed points and the clusters labelled in Figure 66 B for the final refined orientations.

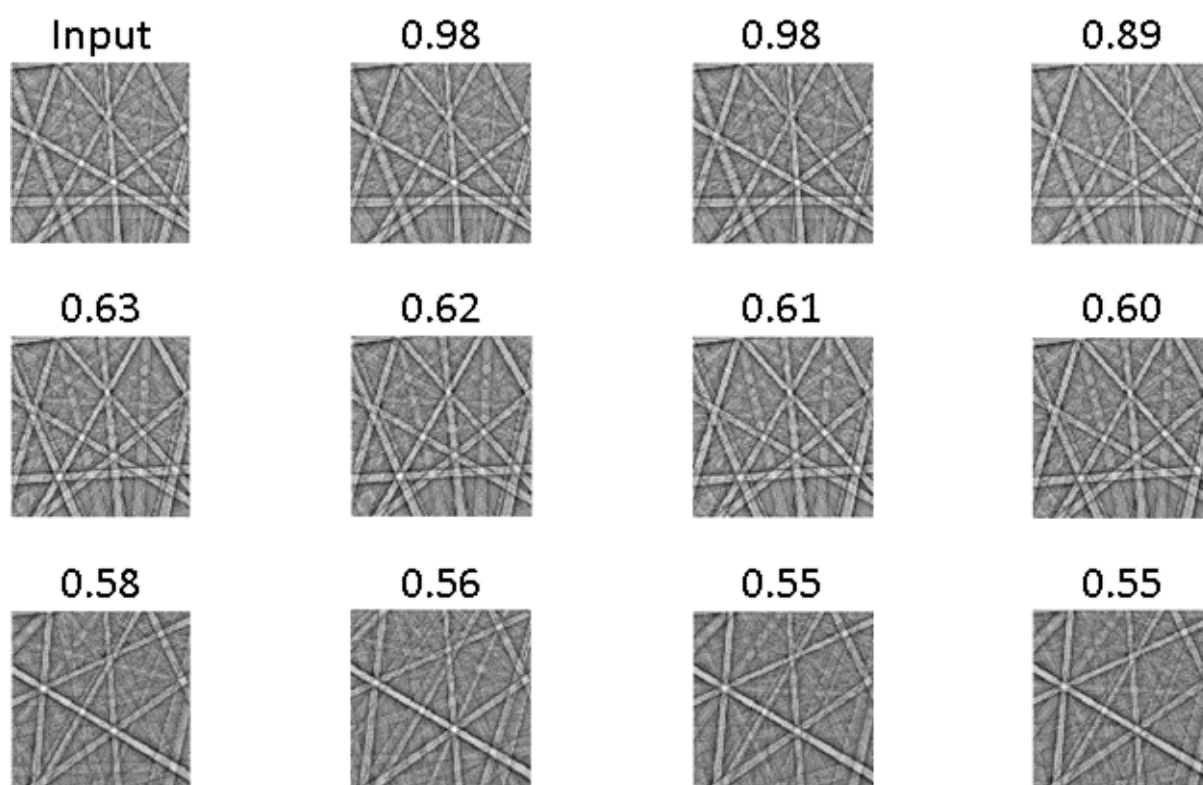


Figure 67: The electron diffraction symmetries for an input pattern and their respective correlation coefficients.

As this operation is performed in the gnomonic space, i.e. with consideration of the camera geometry, there may be electron diffraction pseudosymmetries which are missed due to the choice of input orientation for the reference pattern (e.g. if a long camera length is selected). To address this, the misorientation between the reference (seed) orientation and all points in the library is measured. A new seed orientation is selected which has the largest misorientation angle from the previous seed, and calculation of the electron diffraction pseudosymmetry equivalent orientations is repeated.

Seed selection is continued until the selected seed orientation oscillates between two orientations, which indicates all potential seeds have been searched. Duplicates within the final list of orientation matrices are removed. The final list of orientation matrices can now be stored to disk and used for subsequent calculations.

13.6 Indexing EBSD Data

To demonstrate this approach, the data from the $\text{Al}_{13}\text{Fe}_4$ experiment was used. Visual inspection of these patterns has revealed that there are two easily confused pseudosymmetric crystal orientations within a single region and patterns from these regions were extracted. Figure 68 shows the analysis of one of these patterns.

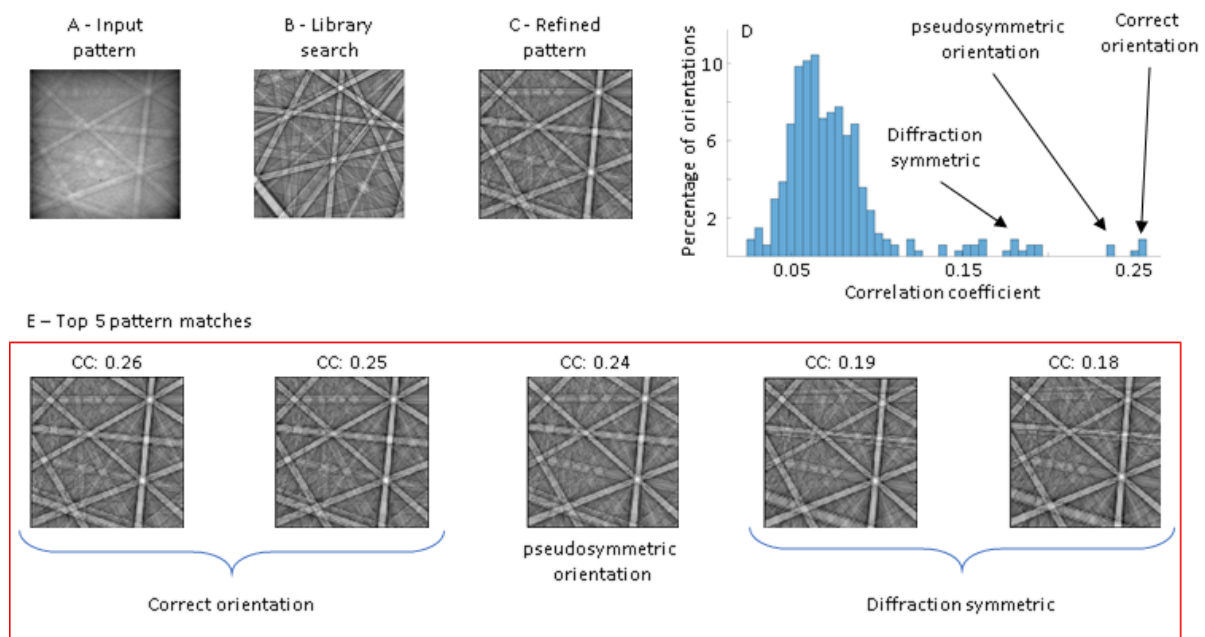


Figure 68: A demonstration of the spread of the symmetric orientations. A) The input pattern leads to an incorrect orientation from B) the sparse library search but is corrected to C) a pattern that matches. The Histogram (D) shows the distribution of the electron diffraction equivalents tested and highlights the main and pseudosymmetric peaks of the distribution. E) Example matches are shown along with their corresponding correlation coefficients. The patterns are labelled such that the peaks they relate to in the histogram are shown.

Figure 68 shows that the initial library search does not appear to resemble the input pattern and as such the orientation is likely incorrect. However, the application of the equivalent rotations leads to a significantly better match. Analysis of the distribution of these matches suggests the best match is significantly better than most of the incorrect results. This can be seen in the histogram in Figure 68 D. This distribution and the visual analysis of the pattern means we can be confident we can correctly identify a pseudosymmetric pattern. The CCs of these patterns appear to be lower than those shown in previous chapters. This is believed to

be caused by a systematic error in the updated algorithm, which, due to time constraints on finishing this thesis has yet to be addressed.

Figure 69 Indexed two similar looking patterns, visual inspection of the bands in each pattern reveals that the orientations are correct. The features within these patterns are similar to those which are demonstrated to be confused as electron diffraction pseudosymmetries, and testing against the alternative values reveals a distribution of cross correlation values (Figure 66) which show that the initial (fast) searchers are less well matched than an alternative.

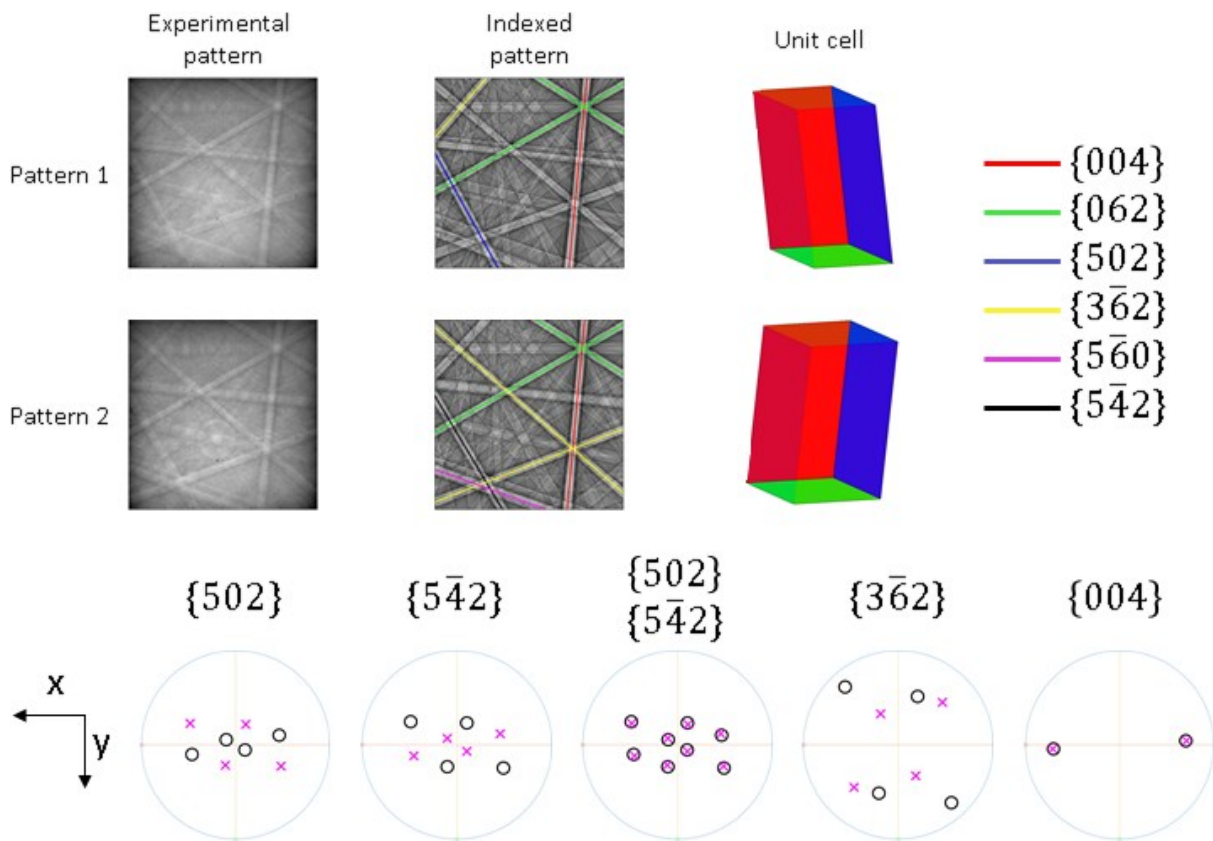


Figure 69: The results of indexing two patterns, the simulated patterns with band overlays are shown for the orientation the indexing returned along with the unit cubes that formed each pattern. The 5 pole figures show the overlapping and similar planes for each pattern, points on the pole figure marked by a black circle are from pattern one and those with a pink x are from pattern two. The axis shown to the left of the pole figures is the axis for the pole figures and also the sample frame for the unit cubes plotted.

The best matched dynamical patterns, and the associated crystal orientations, are shown in Figure 69. Visual analysis of the experimental and simulation patterns confirms that the

algorithm has worked and the correct orientation has been determined for both cases.

Specific features can be explored, such as the horizontal split band in the centre which is present in both the experimental and simulated pattern for pattern one. The equivalent band in pattern two is a single band and this is found to be the case within the simulated pattern. In the bottom left corner of both patterns there is a diagonal split band which is thinner in pattern two and this is also found within the simulated pattern.

As I have the unit cell matched, and can index bands for these patterns, the difference (and similarities) can be observed directly. The $\{004\}$ is parallel in the two patterns, and this is seen in the unit cell (with the parallel green plane) and stereographic analysis. The $\{502\}$ and $\{5\bar{4}2\}$ planes are in a similar location within the EBSs and this is echoed in the pole figures for the associated plane. The fact that they are similar, but not parallel is the confusion that result in electron diffraction pseudosymmetry.

The algorithm was subsequently applied to the entire map, matching each point applied to the whole map from which patterns one and two were taken, the results are shown in Figure 70.

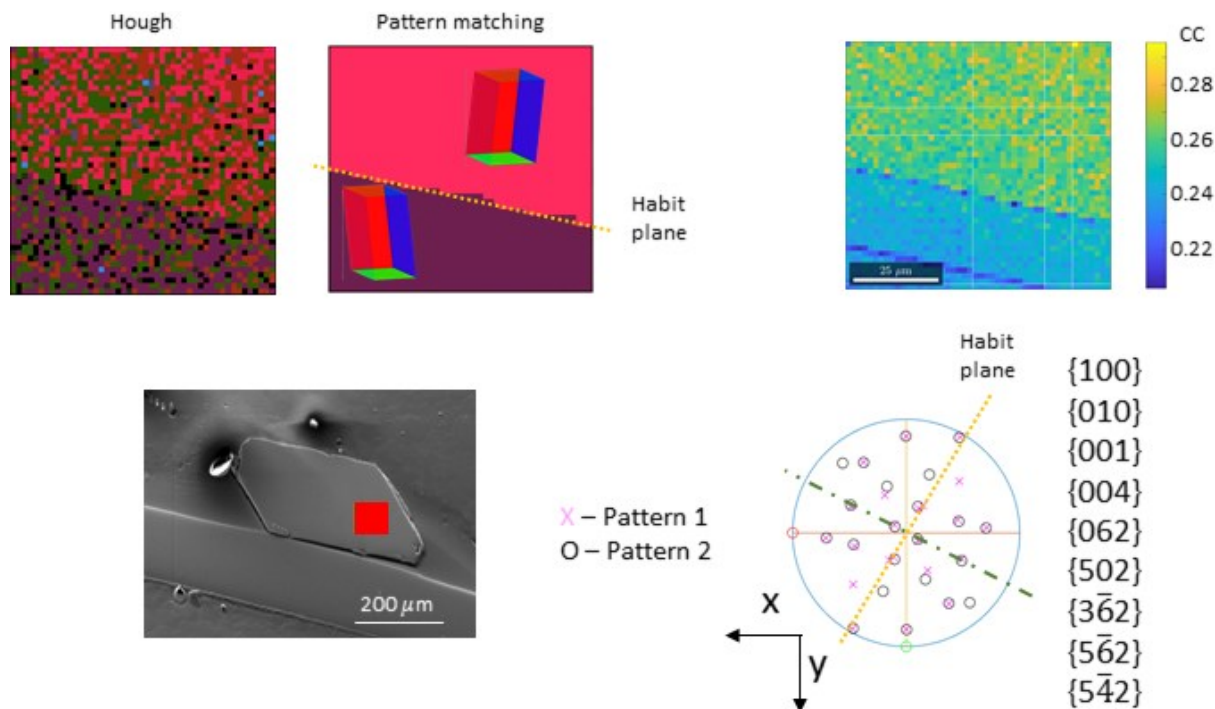


Figure 70: The results of indexing the red segment shown in the backscatter image. The habit plane (plane shared between the two orientations) is shown as an orange dashed line. The Hough matching is shown as an indication of the improvement the modified refined template approach has made. The correlation coefficient map supports the smoothness of the refined map and the pole figure is included for completeness.

The orientation map in Figure 70 shows a uniform electron diffraction pseudosymmetric match for each of the regions. This is an improvement on the Hough based method that has a speckled orientation across the whole map. The EBSFs from each region agree with the uniform orientations shown in the map. Note that the reduction in the cross correlation coefficient here is related to a problem with the normalisation when comparing experiments and simulations for this case, and a manual verification of every single pattern was performed to confirm the result.

The map was collected in a standard EBSD set up, with a beam acceleration voltage of 20 keV, a detector distance of 18.25 mm, a beam current of $\sim 1 \times 10^2 \mu\text{A}$, and a total collection time of 39 minutes 11 seconds (~ 14.5 ms per pattern).

There is a notable, systematic reduction in CC for the lower twin in the grain. I suspect this is a result of the orientation producing an EBSF with many subtle features making it hard to

index. It is also possible the orientation itself diffracts less readily than the upper twin, producing a reduced pattern quality, seen in the CC.

From a material science perspective, this method now enables us to explore specific crystallographic features such as the interfacial plane between the two domains and the relationship between this and the crystal orientations. Coincident points along the trace of the line in Figure 70 (the green dashed line) indicate shared plane normal which are potentially within the interfacial plane and may be important for the orientation relationship present. The perpendicular bisector of this line which goes through the origin is the zone of the interfacial plane normal, and four potential plane normal are observed to fall on this line with the following indices $\{502\}$ and $\{5\bar{4}2\}$

13.7 Summary

This chapter has looked at the problem of determining the correct orientation for a pseudosymmetric pattern. The RTM algorithm has been slightly modified to use a brute force symmetry check, such that prior knowledge of the crystal symmetry is not needed. This allows for a wider user base as people with a less in depth understanding of crystallography can still use it.

14 Direct Electron Detection with a Fixed Detector Angle Stage

Please note that work within this chapter is preliminary in nature due to time restraints on submitting this thesis and to COVID-19 restrictions significantly affecting data collection.

14.1 Introduction

For accurate orientation determination and phase characterisation, it is important to not only have high quality simulations [40], but to also have as high quality experimental patterns as is possible. This is so that the more subtle features of the EBSD can be more readily identified, interpreted and characterised, such as with the pattern matching approach described in the previous three chapters. This motivates developments in detector technology, which are explored in this chapter.

Although it is possible to obtain higher quality patterns by increasing the electron dose on the detector (the combination of voltage and acquisition time) there is a limit, due to inherent inefficiencies in the system and optical blurring. Alternatively, the technology of the detector can be changed.

This chapter looks at the design and testing of a fixed angle stage for use with the Timepix 2 (a hybrid pixel direct electron detector (DED)), to acquire high fidelity patterns, see Figure 71. The chapter continues with using data collected from this detector with the refined template matching approach as described in Chapter 11 to reconstruct a map from a single crystal silicon sample.



Figure 71: The Timepix 2 detector used throughout this chapter. The detector is covered by a protective screen that is slid out of the way when the detector is in use. The ruler is included as a scale for the detector.

14.2 The Stage

Detector motion, with respect to the sample, introduces significant uncertainty in an EBSD experiment [50]. This motivates creation of a fixed geometry, which also can be easily removed and added to a microscope (thus not disturbing other users).

Design of the detector stage has several items to consider:

- (1) Optimum sample-to-detector positioning, and potential to change this based upon the experimental set up.
- (2) The ability to move the sample under the electron beam.
- (3) Mechanical (and thermal) stability.
- (4) Space surrounding the detector and physically not colliding with other items in the microscope, including the pole-piece.

A prototype design was sketched, see Figure 72, which simplifies the geometry of the system significantly. Here the sample is held at a fixed tilt angle with in-plane sample movement, and the detector can withdrawn away from the sample.

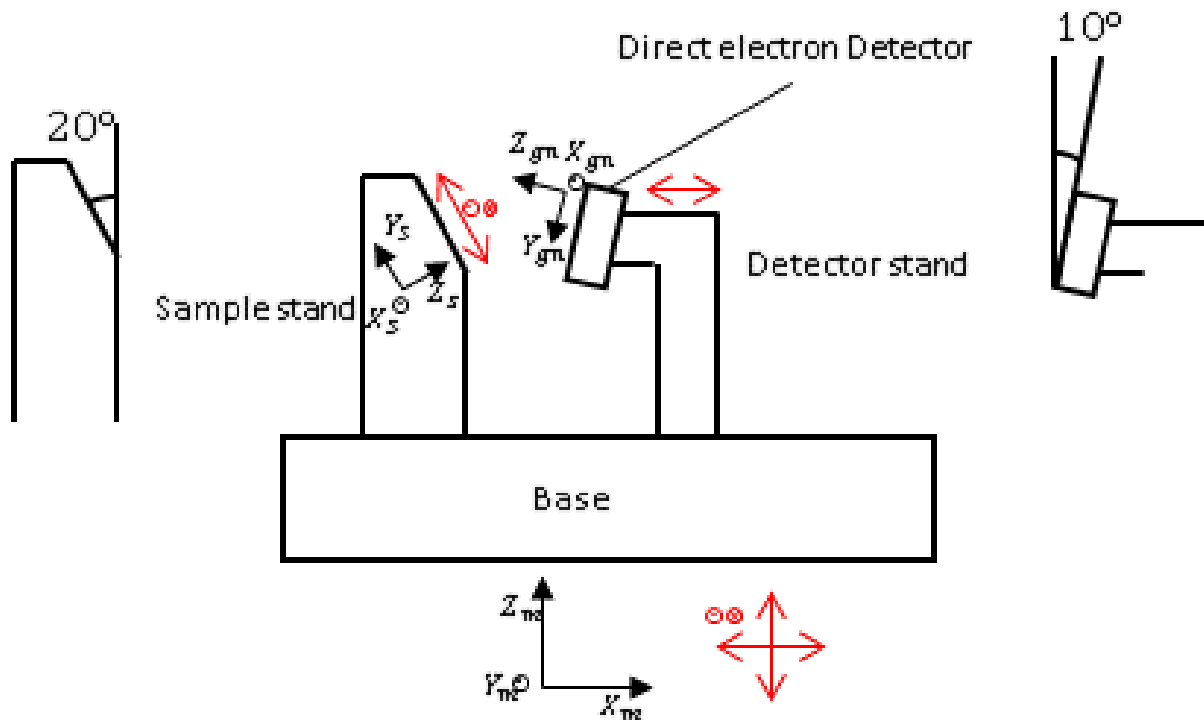


Figure 72: The fixed angle direct electron detector set up with a camera at a fixed angle with respect to the sample. The camera will be able to advance and retract upon the sample, which should be able to move in the sample X/Y plane. The whole assembly will also be able to move in the microscope X/Y/Z planes because of the movement of the microscope stage. The black, solid arrows show the coordinate systems as used throughout this thesis. The red unfilled arrows show the directions of movement of the stage

Constraint in this geometry is advantageous, as this simplifies analysis of the patterns. The detector distance can be selected as needed. The sample height with respect to the detector can be selected based upon where entire sub-stage is located in the microscope, i.e. positioning of the electron beam. Finally, beam and/or stage scanning can be used to map larger areas.

14.2.1 Stage Design

14.2.1.1 Sample and detector movement

The stage uses SmarAct SLC motors to move the camera and the sample. Two stages are connected at right angles for sample X/Y motion; one stage for the detector retraction and advancement. These stages are shown in Figure 73.

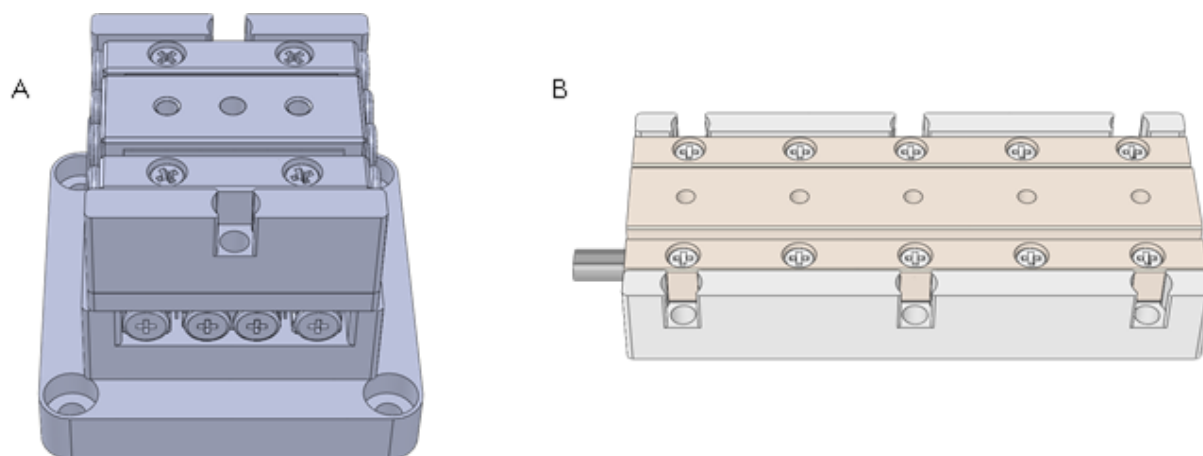


Figure 73: Digital CAD renderings of o A) the SmarAct sample x/y stage and B) the detector z stage

It is important to consider the relationship between the sample and the detector, to ensure the camera has a sensible pattern centre (PC) and can acquire patterns for indexing. The X/Y SmarAct motors are mounted directly below the sample, giving sample X/Y movement. The third stage is used to withdraw the camera, thus enabling selection of the appropriate sample-to-detector distance, and also enable camera retraction experiments which can be used to locate the electron source position.

This design was also constructed to enable stage scanning, i.e. motion of the sample and not the beam, which would enable greater control of the step size, and for a map in which the pattern centre is the same for all patterns (which would simplify substantial parts of the analysis). The precision both the X/Y and Z stages can move is $> 50\text{nm}$ depending on stage settings used [144], [145]. This has not yet been implemented due to time constraints.

14.2.1.2 Base and sample and camera mounting

We have established where the sample and stages should be with respect to each other, now I turn to the design of the connecting parts and mounting this within the electron microscope.

The stage is designed to mount on the conventional stage within the FEI Quanta-650 SEM, primarily providing mechanical stability.

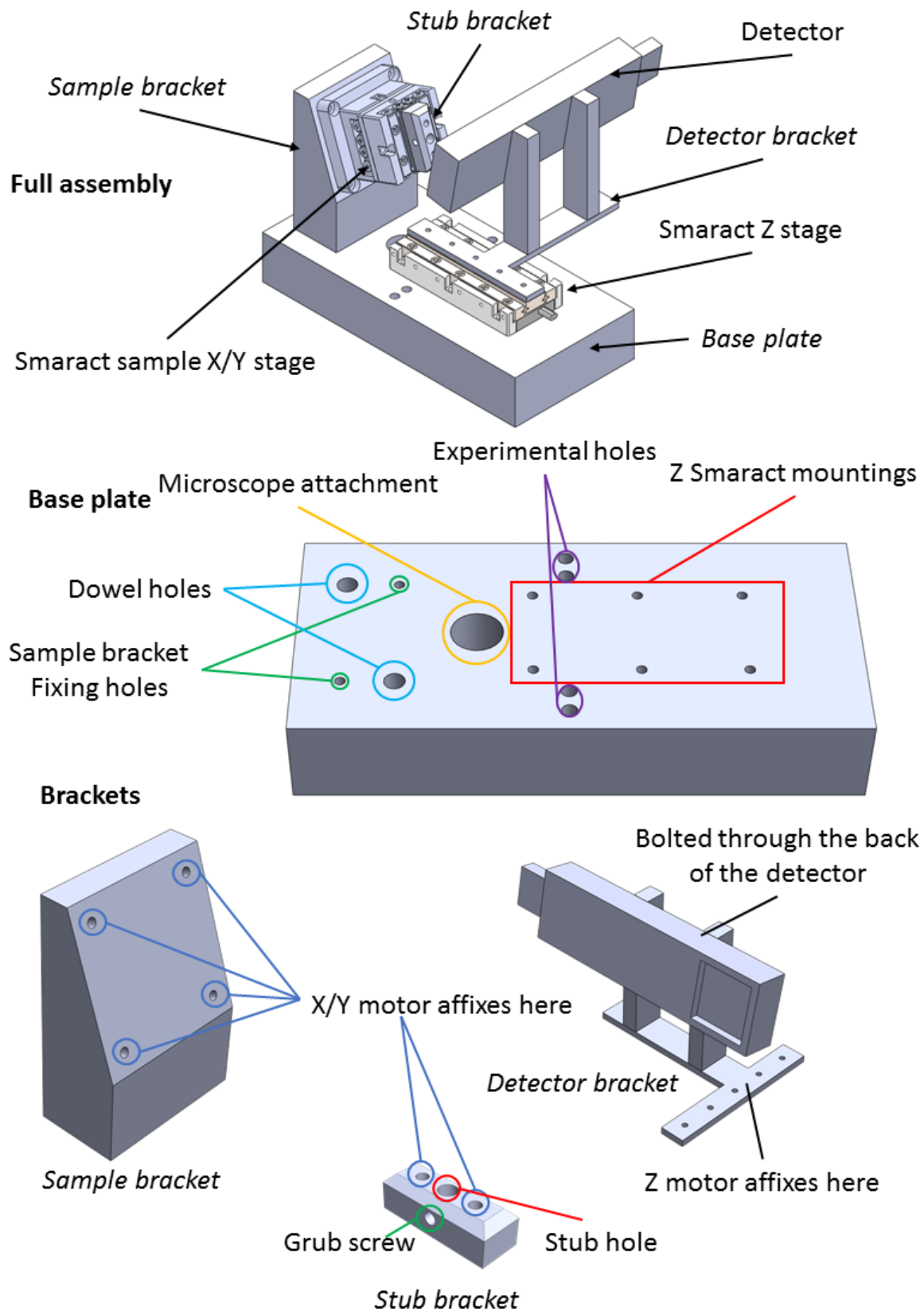


Figure 74: CAD rendering of the designed DED stage, with) overview of the stage with key parts.

The stage was designed to be made of several easy to machine parts, shown in Figure 74:

- (a) The base plate which connects to the Quanta-650 stage, and includes connections to for the sample and detector brackets / SmarAct stages. Also included in this plate are several holes for mounting ancillary devices, such as posts to hold ball bearings in a shadow casting experiment (such as Dingley's balls), or a wire to measure the modulation transfer function (MTF) of the detector (labelled as experimental holes).
- (b) The sample bracket, which connects to the base plate and presents the sample at 20° to the incoming electron beam. Such that the incoming electron beam is incident on the sample at 70° .
- (c) The stub bracket which accepts a pin stub and mounts on the SmarAct sample X/Y stage.
- (d) The detector bracket which connects the detector the SmarAct PCz-stage and presents the detector at an angle of 10° to the incoming beam.

14.2.1.3 The Base Plate

The base plate is a solid block of aluminium with holes drilled into it to allow for the fixing of all the brackets and subsidiary experimental equipment. It also has a hole to attach to the microscope itself. The plate is made from aluminium as it is strong, lightweight and conductive. Importantly, aluminium is also nonmagnetic, and therefore reduces scanning artefacts and focussing issues.

14.2.1.4 The Sample and Stub Brackets

The sample bracket affixes to the base plate and is designed to hold the sample at a 20° angle to the electron beam, as is conventional for an EBSD experiment. The bracket is fixed to the base plate with 2 non-magnetic screws that screw into it through the baseplate and held from underneath. The bracket itself is held in position by two metal dowels. The

sample X/Y SmarAct motors are affixed to the sample bracket and the sample holder attached to the SmarAct motors. The holder is also aluminium and has a main hole for a stub and a secondary hole for a grub screw to keep the sample in position.

14.2.1.5 The detector bracket

The detector bracket attaches to the Z SmarAct using the holes built into the motor itself.

The Stand comes in two parts, a “T” shaped section to attach to the motor and two stands to support the camera. The most stable way to attach the camera was to have two supporting posts which are secured to the DED with screws. To attach these, the innards of the detector were removed, the holes drilled and screwed, and the innards returned. The supports hold the camera to be inclined at a 10° angle, which increases contrast in the pattern.

14.2.1.6 Stage Design Adjustments

As this stage is currently in the prototype phase, initial iterations of the design were made based upon experiments in the chamber:

1. A copper ribbon has been affixed between the sample stand and the stub mount.

This is to allow the electron beam to earth and avoid beam associated drift on the sample. (The SmarAct stages are electrically isolated from the base due to ceramic bearings.)
2. The initial stage base attached to the microscope using a single bolt which passed through the base, and this required rotation of the entire stage to attach it to the base. This was changed to a post which screws into the Quanta-650 stage and then the DED-substage is attached to this post.

3. A peltier has been attached to the rear of the DED chip. This is because the DED becomes hot when in use. The peltier acts as a (active) heat pump to cools the DED down while in use.

14.3 Detector Testing

14.3.1 Modulation Transfer Function

The modulation transfer function (MTF) and the detective quantum efficiency (DQE), are methods of quantifying how well a detector collects the information contained in an EBSD.

The MTF describes the recovery of information for different spatial frequencies, and the DQE determines how much information is lost. Both are described in detail in the Literature review.

The MTF of the detector is of particular importance as a better MTF allows for higher frequency information in the EBSD to be obtained (i.e. the pattern is sharper). This enables fine features such as higher order bands, or the intersection of bands to be identified which can aid in creating new methods of characterisation.

To measure the MTF, a sharp edge can be illuminated and the sigmoid function associated with that edge is measured. In this experiment, illumination is provided from a poorly polished (i.e. flat, but highly deformed) aluminium stub. A thick and straight wire is used to cast a line shadow at an angle on the detector (typically 30 ° to the horizontal, and not at 0. 90 or 45° to the hybrid pixel grid).

The method of Meyer and Kirkland is then used to fit a sigmoid to the edge which is the linespread function, and the MTF is determined from the FFT of the linespread function.

Figure 75 shows an MTF collection pattern and an example determined MTF.

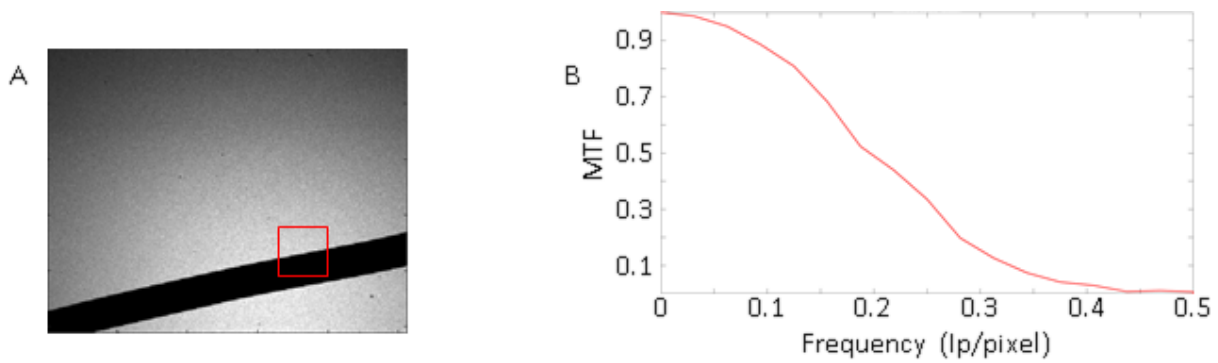


Figure 75A) And example pattern used to obtain an example MTF, shown in B. The line in B is likely not smooth due to the line in A not being entirely straight.

Figure 75 shows a test MTF calculation. The MTF shown will be of reduced quality due to the wire not being perfectly straight, as is the assumption in the MTF calculation. The box shown is the segment from which the linespread was taken, and due to curve in the wire, the MTF is not as smooth as one would expect, it will also be of reduced value, meaning the higher frequency information will still be accessible.

The next step would be to calculate the noise transfer function (NTF) and use this to calculate the DQE, which is, as shown in the literature review is related to the two. The NTF can be calculated by taking a background (as with the MTF calculation without the shadow), retracting it and measuring the difference in signals compared to the expected drop off to get the relation between noise in and noise out to calculate the NTF

14.3.2 Pattern Centre Determination

To measure how well the pattern centre (PC) can be determined for a given pattern, two main tests were attempted. The first involves measurement of the same pattern formed from a single crystal of silicon, and using similar triangles to trace the origin [46]. The second involves insertion of spherical ball bearings, which ideally cast shadows that are ellipses where the major axes point at the source point position and the ratio of major to minor axis length is the detector distance [14].

14.3.2.1 Retraction test

A single crystal of wafer grade silicon was attached to the sample, as this diffracts well and produces high quality patterns with a single orientation. It is also well studied, and easy to identify different crystallographic features and thus find the pattern centre position.

The beam illuminated the sample and the detector was retracted along the PCZ-stage in fixed increments. The SmarAct stage has movement precision of 4 nm, and the pixel size on the detector is 55 μm .

A retraction of 10 mm with 20 increments, i.e. 0.5 mm increments, was performed. Patterns were captured at each point and recorded to disk. As the detector has a physical size of 14.080 mm, this corresponds to a change in PCZ of c. 0.7.

Results from this experiment are shown in Figure 76.

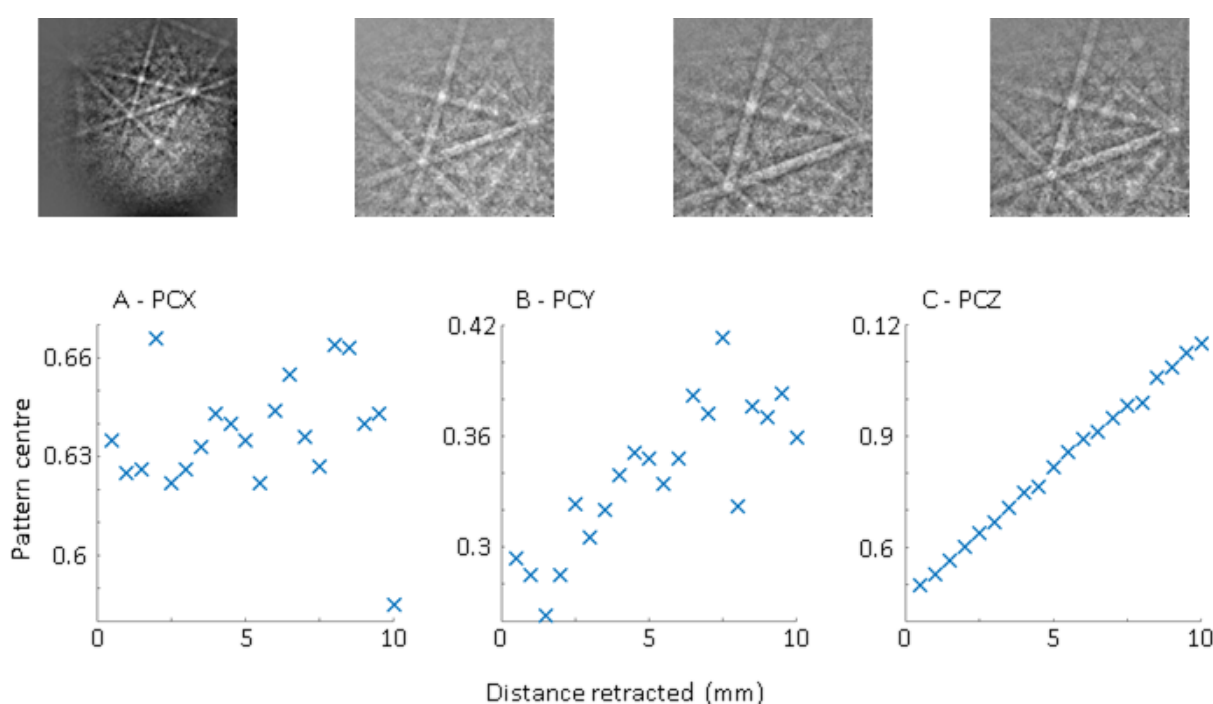


Figure 76: The graphs of A) The PCX B) the PCY and C) the PCZ locations at each retraction. And examples of patterns at various points in the retraction.

Figure 76 shows the expected slope of the retraction. The PCY gradient is likely a result of a slightly sloping base, which will need to be calibrated for.

14.3.2.2 Shadow casting test

An alternative method of finding the PC is to do a shadow casting (Dingley's/pawnbroker's balls) experiment. Whilst it is not necessary to do this extra test, doing so gives another determination of the PC that can be used to confirm the accuracy of the retraction or iterative approaches. The shadow casting also has the advantage of only needed to be done in one position without moving the detector, which could affect the PC if the stage is not completely flat and level. The same Si sample is used as before, but in this case three ball bearings were suspended between the sample and the detector casting three elliptical shadows on the pattern. As described in section 10.1.2, the major axis for each of these shadows should point to the PC.

Ellipse fitting was performed in MATLAB for each of the shadows, but the shadows were not suitable for an accurate determination of the major and minor axis as shown in Figure 77.

This is likely because the shadow was incomplete on the detector (as typically $\frac{3}{4}$ of the perimeter would be needed for a reasonable fit). Due to time, and limited access to equipment because of the COVID-19 pandemic it was not possible to improve this experiment.

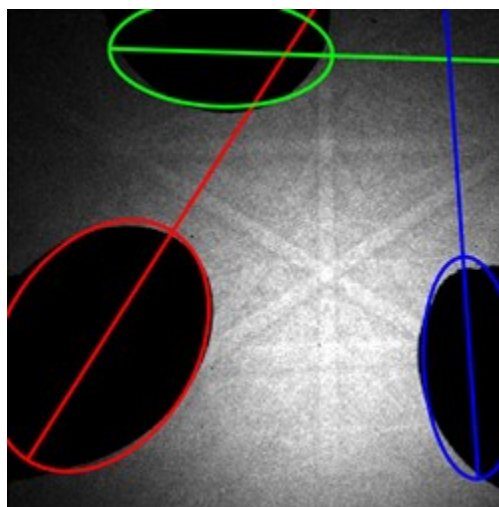


Figure 77: Example pattern with elliptical shadows from ball bearings suspended between the Si sample and the detector. Note the overlaid ellipses misalign with the elliptical shadows due to there being too little of the ellipse showing on the pattern.

The fit of the ellipses in Figure 77 is poor due to there being too little of the ellipse showing in the data for the Hough based MATLAB routine to accurately determine the ellipse parameters. A manual fitting would have been more appropriate given the quality of the data, however, was not attempted due to time constraints on finishing the PhD thesis.

14.4 Detector exposure

In theory a direct detector provides an improved signal to noise as it should have an increased efficiency. This motivates a brief study of the effect of increasing electron dose on the quality of the diffraction patterns, which will impact the time per exposure required to collect a map.

For example, suppose your exposure time is 0.2 s, and a relatively small map of 100 x 100 points is required. The map leads to 10,000 patterns. Giving a total collection time of 2000 s (~33 minutes) plus any overheads incurred. Increasing the time of exposure to 0.4 s will increase the time take for the same map to be 4000 s (~1 hour 6 minutes) plus any overheads.

To explore the effect of exposure time, the single crystal silicon was mapped and at each measurement point, 19 EBSPs were collected each with a integrated collection time of 0.1 s. The microscope was run with a probe current of $\sim 1.3 \times 10^2 \mu\text{A}$. Beam control and pattern capture were performed using 'GUI mouse clicks' within MATLAB (using JAVA to control the Medipix PIXET software and the Bruker eSprit based scan generator) this added significant overhead per pattern between exposures. The 0.1 exposure patterns were each saved within a HDF5 container for offline analysis.

Using MATLAB, these patterns were added together to create composite patterns of higher effective exposure and collection times. The exposure and collection times differ because the overheads associated with pattern collection mean there is an extra 1.4 s of beam exposure between every exposure (as the GUI is very inefficient), and this overhead is pictorially shown in in Figure 78. For analysis, the intensity of the pixels in the pattern were averaged. This was to ensure the intensity of each pattern is similar and there are no artefacts in the analysis from runaway numbers.

Figure 78 shows the collection times and 5 example patterns, which will be used as examples throughout this chapter. Finally, the AstroEBSD background correction routine was used to normalise the intensity of each pattern such that mean of the intensities = 0 and the standard deviation of the intensities = 1. This essentially shifts the mean of the gaussian the intensities that describe an EBSP to be centred on 0 and necessarily means there are negative values for intensity. This intensity shift is also performed on the library and does not affect the results of the pattern matching. The shift in intensities is performed so that there are no artefacts in the matching brought about by significantly differing pattern intensities.

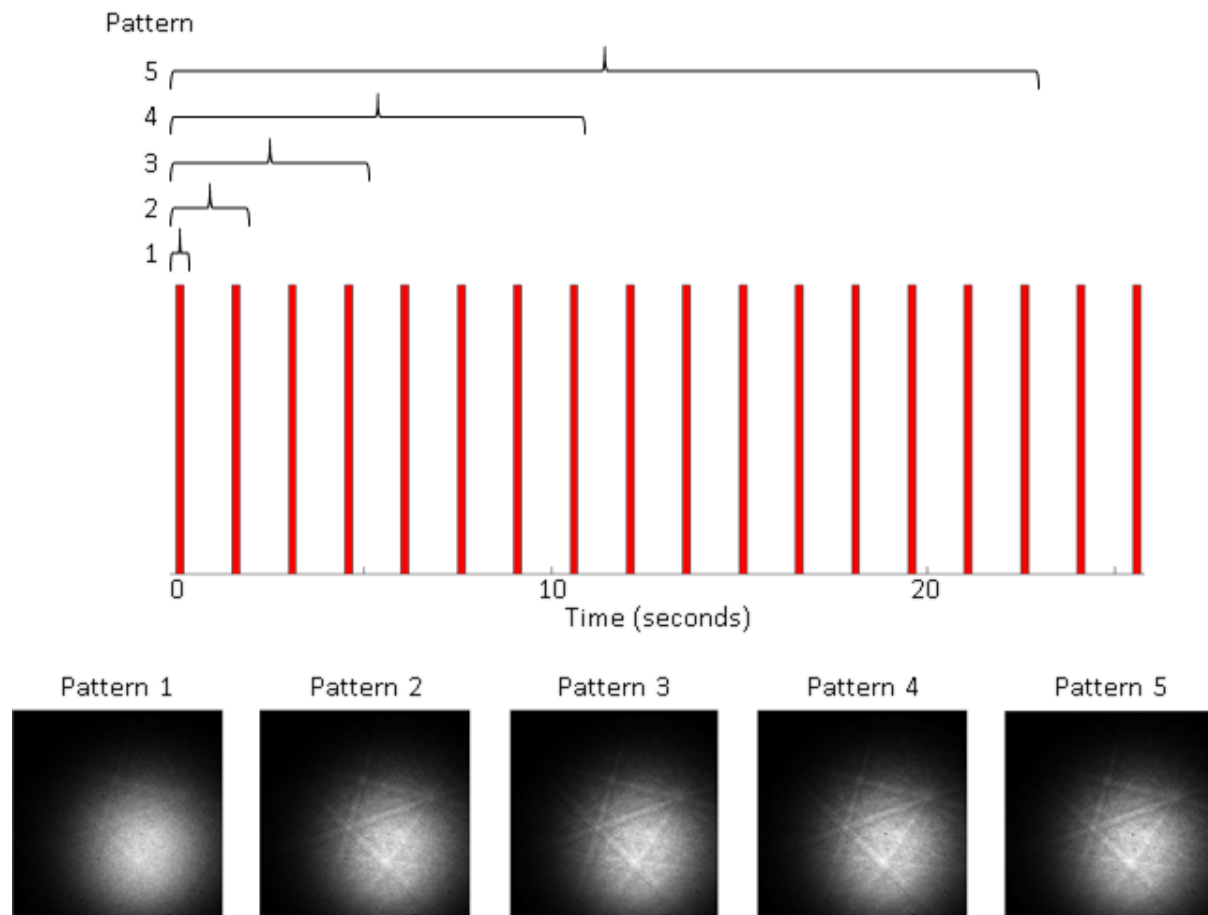


Figure 78: The collection time of patterns 1-5 and the example patterns 1-5. The red bars indicate time when the detector is capturing an image and the space in between is the associated overhead with each pattern collected.

The Patterns were collected on the FEI Quanta SEM with a beam of 20 kV and a spot size of 5.5, and using the Pixet Pro software, set to collect a frame of 0.1 s.

The patterns were then indexed using the RTM method and the correlation coefficient (CC) from the indexing stored. A higher value of the cross-correlation value represents improved matching between experiments and simulations (noting that the geometry could have been optimised further). The resulting graph of CC against effective collection time, shown in Figure 79 gives an initial guide to an ideal exposure time.

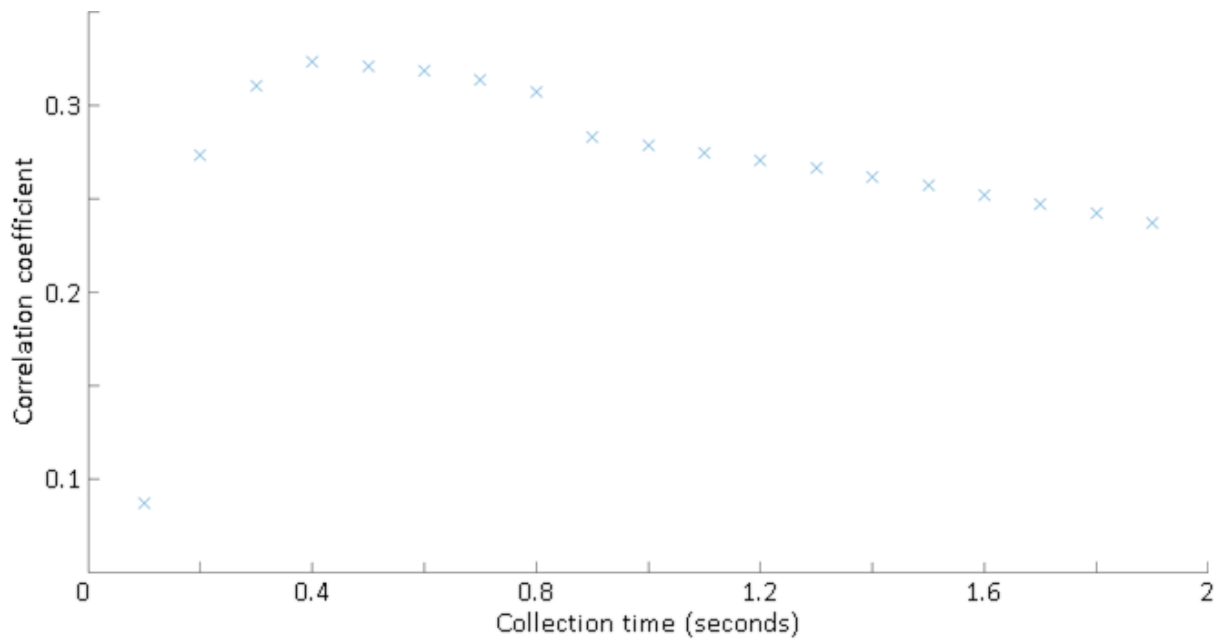


Figure 79: The correlation coefficient with respect to the collection time.

The benefit of a longer exposure is also seen with an increase in the signal that gives rise to the bands as compared to the random read out from the detector. This can be observed through analysis of higher spatial frequency within the diffraction pattern, via 2D Fourier analysis as well as sampling features across a particular band.

Figure 80 shows the raw and background (BG) corrected patterns, histograms of the intensities of the pixels in each pattern, the fast Fourier transform (FFT) of the raw and BG corrected patterns and the BG itself. It also shows these for a simulated pattern that has no background and would be seen in a perfect detector. Figure 81 shows the location of the line scan on the pattern and the results of the line scan for each pattern and for a simulated pattern.

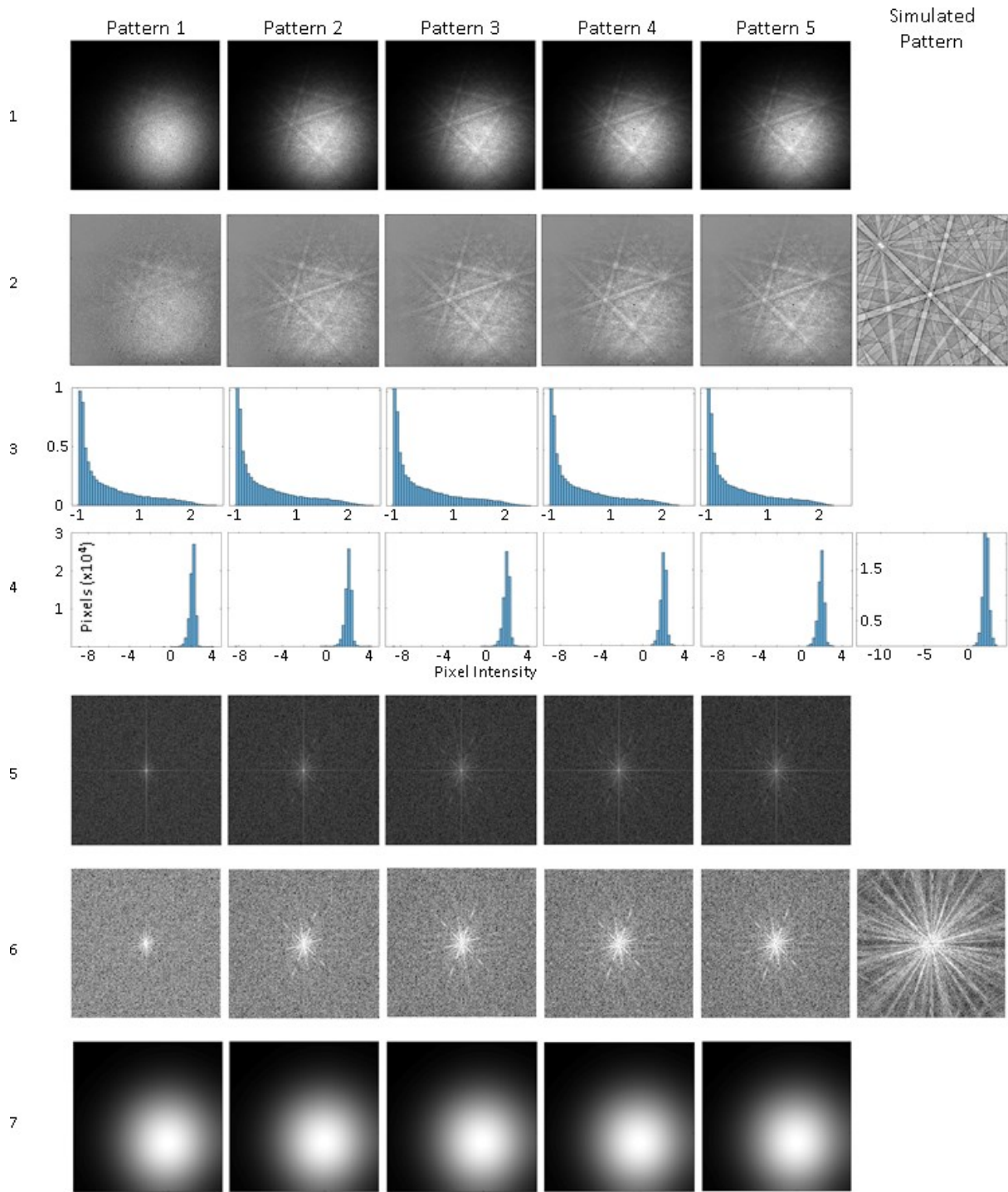


Figure 80: Rows 1 and 2 show the patterns as collected from the detector and the background corrected patterns respectively. The intensities of the pixels in each of the patterns were taken and rows 3 and 4 show the histograms of the collected and the background corrected patterns respectively. Rows 5 and 6 show the FFTs of the collected and background corrected patterns respectively. The horizontal and vertical bands prominent in each FFT in row 5 are an artefact from the fact that the patterns are not periodic. Finally, row 7 shows the background of each pattern. A simulated pattern, histogram and FFT have been included as a reference.

Figure 80 shows that the background is not saturated in any of the images. This can be seen because of the mostly circular white patch in the centre of the background's circle, which

would be irregular if the camera had become saturated. And also that the FFT tends to reach furthest for patterns 3 and 4, which implies higher access to the high frequency information and is related to the MTF of the detector [146].

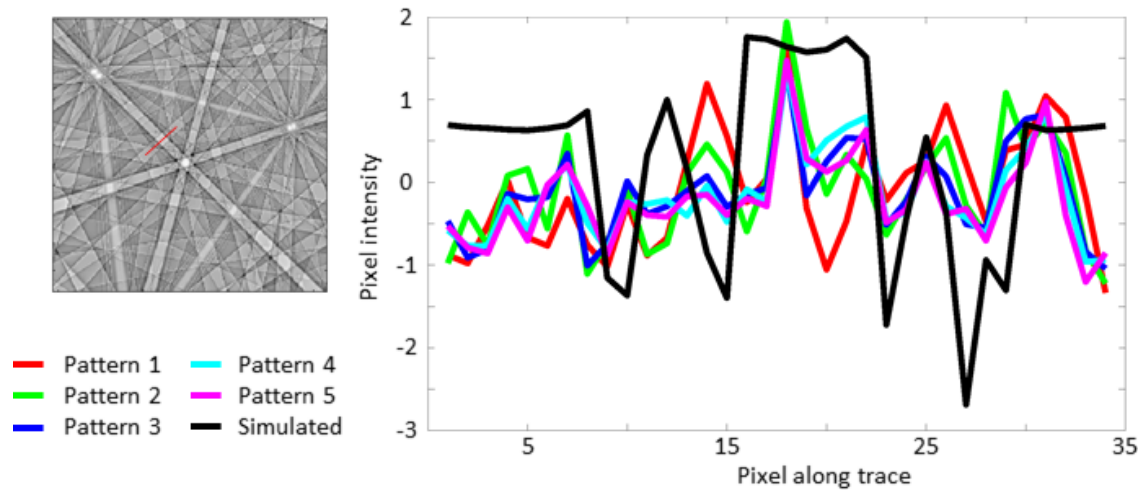


Figure 81: A line scan perpendicular to the $\{220\}$ band and running along the $\{311\}$ band, marked by a red line on the EBSP.

Figure 81 shows that the patterns conform to the simulated line profile in a similar way with pattern 4 being slightly more consistent as it levels off in a similar fashion to the simulated pattern slightly more than the other patterns. This is seen with the general shape of each line scan having a peak at $\sim 7, 18, 25$ and 30 pixels and troughs at $\sim 10, 23$ and 28 pixels. The negative intensities are a result of the 0 mean and 1 standard deviation normalisation performed on the patterns.

The ultimate aim of this section is to determine the exposure time needed to attain a pattern that has a sufficiently high CC that the orientation determination and phase characterisation. Figure 79 peaks at 0.4 s and has a significant drop at around 0.8 s. Suggesting the optimum value of collection to be between these two values. This drop off is likely due to carbon contamination on the sample as a result of the pattern collection method.

Figure 80 shows the FFT spectrum expands the furthest in pattern 3. That is to say, pattern three has more access to the highest frequency terms. As pattern 3 corresponds to a collection time of 0.4 s this sits within the expected time based on the results of Figure 79.

Finally, Figure 81 shows that all patterns with the exception of the first have similar line profiles. However patterns 3 and 4 level out in the most similar fashion to the simulated pattern. Also suggesting ~ 0.4 s ~ 0.8 s are the best collection times.

These combined results suggest a collection time of ~ 0.4 s is optimal to achieve patterns that have a sufficient CC, and are collectable within a reasonable time frame. As the overheads of this experiment also need to be accounted for, 0.4 s is likely an upper bound on what would be optimal for pattern collection.

14.5 Map reconstruction

As EBSD is usually used to gather data from a large area map, it is important to be able to reconstruct a map of data collected on the DED stage designed here.

I have collected a map from a single crystal silicon sample with the aim of reconstructing the data in a usable form.

To collect these maps the Bruker Esprit software was used in spot mode to take control of the electron beam in an FEI quanta. MATLAB was then used to move the beam via Esprit to collect the map.

The information collected from the map was distributed across 3 separate files that needed to be combined in order to construct a map.

The first file is a Bruker information file, which is converted into an HDF5 container. This HDF5 contains the map magnification, surface areas, length and width.

The second file is a HDF5 container created by Pixet pro and contains all of the patterns and pattern information such as the pattern height and width in pixels.

The third file is a MATLAB information file containing the number of points collected in x and y on the map. This in combination with the information in the Bruker HDF5 file can be used to work out the step size in x and y on the map, both in pixels and in μm .

The data is sorted into ascending pattern number order. The pattern numbers are then sorted into a 2-D array so that each point in the 2-D array corresponds to the point on the map from which it was taken.

The pattern centres are determined by the method described in AstroEBSD [5] and are then used to index the patterns, using the RTM method described in Chapter 11. The Orientation maps are then reconstructed using the MTEX add on for MATLAB. The results of this indexing for the Si map are shown in Figure 82.

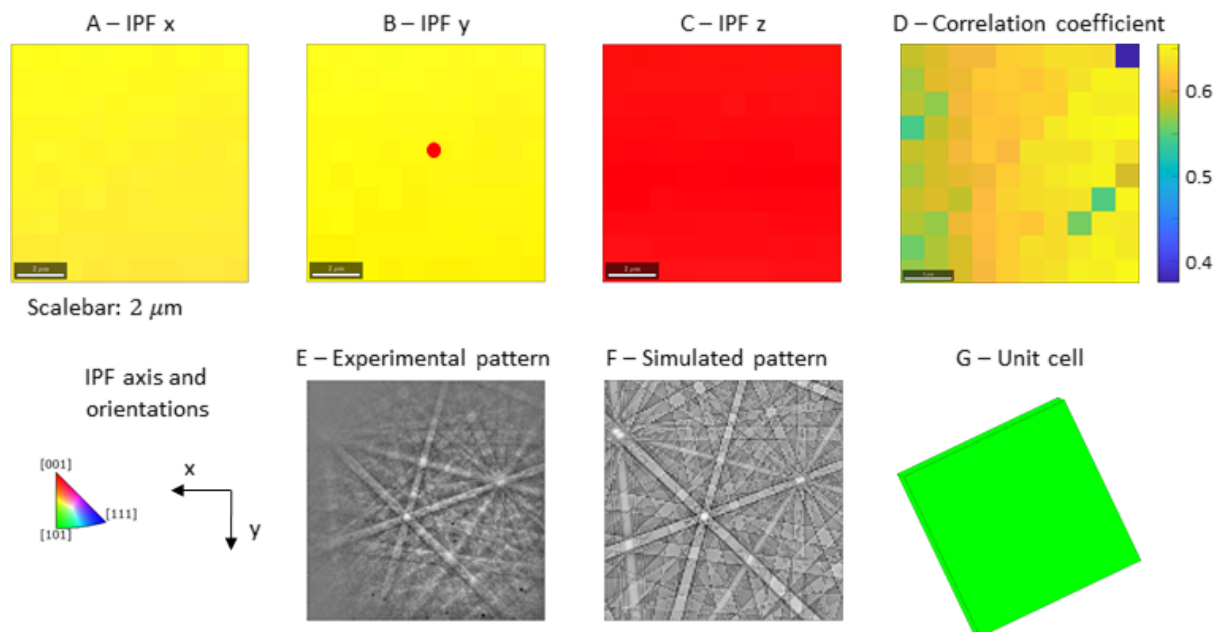


Figure 82: The IPF maps for a single crystal of Si in the A) x, B) y, with the location of the experimental point, and C) z directions and D) a map showing the correlation coefficients of each point. A pattern from E) the detector and F) the result of the indexing taken from the red circle on the IPF y map. And finally G) the unit cell orientation

Figure 82 shows that it is possible to correctly index and reconstruct a map for single crystal silicon. The correlation coefficient map shows a smooth spread of CC, apart from one point, thought to be a spec of dust. The experimental pattern shown is from the centre of the map, marked by a red circle in the IPF γ map, and is a typical pattern and pattern match in the dataset.

The map was collected in a standard EBSD set up, which is the default for the DED stage, with a beam acceleration voltage of 20 keV, a detector distance of approximately 8 mm, a beam current of $\sim 1 \times 10^2 \mu\text{A}$, and a total collection time of 5 minutes 30 seconds (~ 2 s exposure and 1.3 s overhead per pattern).

14.6 Chapter Summary

This chapter has looked at the preliminary development of a DED stage that allows for the collection of high fidelity patterns to allow for improved use of the RTM indexing algorithm described in chapters 1, 2 and 3. The stage has been designed and tested with minor adjustments made, but is still a prototype. Detector tests such as the MTF and PC verification were performed and a map of Si collected, indexed and successfully reconstructed. Work in this chapter has been preliminary in nature due to the COVID-19 restrictions on microscope time.

15 Discussion

The literature review highlighted that there is potential to improve our ability to detect and characterise electron backscatter diffraction patterns with new algorithms and hardware. In this thesis I have developed, and applied, new pattern matching approaches and these are now released within the AstroEBSD open source package (<https://github.com/benjaminbritton/AstroEBSD>).

Chapter 11 demonstrated that use of the 2D-FFT for searching the template library (the reference patterns) is advantageous compared to the NPD approach, as it enables a much more sparsely populated library to be used as the peak required for successful matching is wider and has higher contrast. Further testing of this method for phase classification and pseudo symmetry [147] (or more subtle variations e.g. non centrosymmetric crystals [148]), which is one potential attraction of the pattern matching method in comparison to the Hough/Radon based methods, are explored in chapter 2 and 3.

In the FFT approach, image filtering is explicitly used to assist in drawing out the contrast associated with the orientation data. The background does contain significant information [149] but it is a complicated mix of electron channelling-in, topography, phase, and microscope conditions, and so the RTM elects to discard this information to generate robust and high contrast FWHM and make template matching more successful. In the 2D-FFT this is also computationally in-expensive to implement, and experience with HR-EBSD approaches [75] has proven advantageous.

For the RTM approach to be widely applied, high quality dynamical simulations are required and these are now available courtesy of the work of Winkelmann [53], [61], [66], [67], [148] and the commercial DynamicS package outlined in the literature review. Similar simulation

capability has also been implemented by de Graef and co-workers [10, 11, 24] and are available within EMSoft (<https://github.com/EMsoft-org/EMsoft/wiki/EBSD-Pattern-Simulations>). As a different approach to EMSoft, I have chosen to remove the background from the experimental pattern and match this with a reprojection of a single energy template. This (intentionally) ignores significant instrument variation, such as contrast associated with the take-off angle, but it is relatively robust and interpolation from the reference pattern is quick and sufficient for the present needs of the RTM. I have found that the stereographic projection is sufficient at present, but alternative projections [150]) could be useful particularly in optimising the accuracy of the refinement step.

The $SO(3)$ library generation, using sampling obtained from MTEX [125] has proven sufficient in these cubic examples. Alternative sampling schemes are available (e.g. cubochloric [49]) but these may not be necessary, especially if refinement is used. For lower symmetry materials, the number of orientations in the template library is necessarily larger. It is noted that in borrowing the fundamental zone based $SO(3)$ sampling from MTEX [125], the RTM method has benefited from improvements in the MTEX open source packages to ensure that our sampling remains robust in the future use of the refined template matching approach.

The refinement step I use here is well suited towards ‘conventional’ EBSD geometries, as the solution converges well and the difference in screen centre and pattern centre makes the orientation updates converge well. Trials (not reported here) indicate that a different scheme may be needed when the pattern centre is not within the screen, and this is likely due to the approximation regarding rotation about the Z axis and the screen optical centre. This is a set up mostly seen in off axis TKD.

A sparse set of templates limits the ultimate resolution of the technique, unless a refinement step is implemented, but this reduces the library size significantly which has computation and memory benefits.

Refinement to the output orientation is performed using a fast-iterative approach that exploits the fact that rotations about the sample x and y axes can be approximated as vertical and horizontal shifts in the EBSPs, while rotations about the surface normal can be obtained from a shift along the angular axis of the log polar transform of the EBSPs. This interpolative refinement achieves an ultimate orientation accuracy that is dramatically superior to the initial discrete sampling of the $SO(3)$ space (0.1° as opposed to 2° or even a 7° resolution).

The proposed new approach has been compared to the conventional EBSD patterning indexing (commercially available) Hough based approach and with an existing “Dictionary-Indexing” method.

The size of the peak in the initial matching and the contrast found has significant effects. It makes it easier to find a reliable match, regardless of pattern centre and/or orientation uncertainty. This results in a significant reduction in library size (a factor of 1/25 for cubic symmetry) and results in a speeding up of the indexing and a reduction in the memory overhead. The benefit on memory requirements is simple linear scaling, for a screen size of 128 x 128 pixels, the memory requirements for the NDP is ~5 Gb, and 0.2 Gb for the FFT. For computational times the gain of factor of 1/25 from reducing the library size is offset slightly by the factor ~3 increase in calculation times per pattern required to undertake the more demanding 2D-FFT analysis (see Figure 6). Two iterations of the refinement corrections incur an additional overhead of 0.03 Gb per iteration, the largest additional contribution to this is

the calculation of the log polar transform. If the $\sim 0.1^\circ$ accuracy demonstrated here for the new 2D-FFT based analysis were to be targeted for delivery solely through pattern matching to a discrete template library then the SF of $\sim 3.5^\circ$ and would require a much larger library of 14,232 patterns (compare with 1,600 patterns for 7° and cubic symmetry, i.e. at least 9x faster).

Table 5 details the time and memory requirements needed to index the three maps documented in section 11.6. The apparent similarity in the memory overhead comes from the fact that the library size is the main memory overhead in each indexing. As the library is generated once, the number of images does not affect the memory overhead significantly as storing orientations has relatively low memory costs. Indexing used a 2x Intel Xeon E5-2660 v3 @ 2.60 GHz (i.e. 20 cores). MATLAB 2017a using Windows 10.

Table 5: The time and memory requirements and number of patterns indexed in each of the demonstrative maps.

Map	Time taken	Memory requirements	Number of patterns indexed
Si – Small map – Figure 47	~ 10 mins	~ 0.33 Gb	660
Si – Large map – Figure 48	~ 1 hour	~ 0.33 Gb	2596
Fe – Figure 49	~ 3.5 hours	~ 0.33 Gb	9130

The computational time for the generation of the Library at a SF of 7° , irrespective of the number of cores used in the computer is approximately 10 s. The time taken to generate the library increases rapidly as the SF approaches 0, however, as a SF of 7° is used in this

chapter, library generation time can be neglected. Based on timed runs of EBSD maps, the approximate time, t , for a map to run, depending on the number of cores, c , and the number of patterns to index, n is:

$$t \sim \frac{32}{c}n, \quad \text{Equation 62}$$

For cubic symmetry.

This method of indexing, although slower, is comparable to a Hough based method in accuracy, precision and sensitivity, in some cases exceeding it. This thesis does not claim that this is the ultimate accuracy or speed possible for this method. However, it has demonstrated at least this accuracy, precision and sensitivity using a combination of simulated data, silicon single crystal data and a deformed α -iron sample. There is also potential to use this together with methods such as HR-EBSD where the orientation difference from pattern matching is used as a first step, similar to the approach proposed by Maurice *et al.* [151].

Chapter 12 proposed using the refined template matching approach to classify the potential phase of a pattern, from a list of candidate phases. This improves on the Hough based method for characterisation as the refined method also considers more subtle pattern features, as well as band locations. The method in brief uses the refined template matching described in Chapter 11 with multiple libraries. The library with the highest CC being taken to be the phase of the pattern. The biggest drawback to this method is that potential phases for the material are taken to be known *a priori* and as such this is a classification and not determination method.

To begin, I simulated α and β titanium patterns that were related by a BOR. This was selected to address a specific characterisation challenge found in dual phase titanium alloys, but also as it provides situations where the two phases may be more readily confused. The simulated patterns were linearly mixed and each matched against an α and β library. The results showed that, for a pattern that was 100% α or β a CC of 1 was attained for the correct library. It was also found that the CC for the correct library was consistently higher for the phases making up the highest percent of the pattern. The contrast for each of the libraries was also shown to be significant for patterns made up of above ~60% one phase. Although this experiment ignored how well each phase diffracts, it gives a good indication the method is sensitive enough to correctly distinguish each phase.

Taking this further, simulated patterns from differing crystal structures, Bravais lattices and lattice constants were generated. These patterns were used to demonstrate the refined matching could correctly distinguish these phases.

As EBSD is an experimental technique, it is useful to have a metric by which the reliability of the results can be determined and that has been a theme within this thesis. In this phase classification chapter, the signed contrast was introduced to provide a cut-off CC threshold value which indicates that neither phase suitably matched the experimental pattern without ambiguity. Further work could explore developing this for classification problems where three phases are matched or phases with very similar structures, e.g. ordered and disordered Ni_3Al [152].

From the simulation based experiments, it was determined that a value of 0.6 was a good threshold value, with patterns with a CC below 0.6 being considered misindexed. This value was confirmed via statistical analysis performed by Tom McAuliffe. To account for a reduced

cross correlation based upon differences between simulations and experiments, such as background and lower quality patterns, a threshold of 0.5 was selected for experimental pattern analysis. The value of 0.5 was selected as not only were these points ambiguously indexed (from visual inspections) but the resultant map of non-indexed points matched the “shadows” shown on a foreshattered electron image of the same area. These are regions of significantly reduced pattern quality and error would be expected here.

The signed contrast was then combined with the threshold value, this revealed the random speckling of error that would be expected due to dust or other forms of experimental error.

The value of 0.1 for the contrast was decided upon by via visual analysis of Figure 57.

Furthermore, the signed contrast was compared to an existing metric for a similar approach, referred to in the paper as the phase confidence. The (previously described) phase confidence was shown to give falsely high readings for the refined method due to the sparse library search leading to multiple seed points having the same ultimate solution. The phase confidence calculation also added an additional $(M - 1)n$ refinement steps where n is the number of phases and M is the number of patterns from which the metric is calculated. This means additional phases would significantly increase the time needed to analyse data. The value for M would also need to be drastically increased to account for the sparse library used in this matching.

As the signed contrast with threshold metric gives sensible errors as shown in Figure 56 and Figure 57, requires no additional information to be saved or calculated, and requires little computing power to compute, it is recommended for use with the refined template matching approach.

In the pseudosymmetry chapter, I went on to introduce and test a modified refined template matching algorithm to address the issue of determining the orientation of a pseudosymmetric unit cell.

I used a $\text{Al}_{13}\text{Fe}_4$ unit cell as the case study, and as this is the cell used for demonstration of the method, it is important the relationship between the orientation of the cell and the pattern seen on the screen is understood. Understanding of this relationship was demonstrated by overlaying the expected planes on the generated patterns in Figure 63.

With this understanding in mind, the modified algorithm was described. The algorithm uses a reduced library from a higher symmetry to get a seed point. Pseudosymmetric electron diffraction equivalent orientations are then applied to the library seed orientation to arrive at an ultimate – correct – orientation.

The pseudosymmetric electron diffraction equivalent orientations are calculated using a seed pattern and the whole monoclinic library. They are calculated on the detector, as opposed to on the sphere because the detector set up will affect the pseudosymmetry seen in the pattern. A detector tilt can look like a rotation in the x axis and a retraction will zoom in on the pattern showing more pseudosymmetric features. These changes will affect the diffraction patterns seen and will change the disorientations used to determine the equivalent rotations. In this preliminary work, a cut off correlation coefficient is selected by visual examination of the EBSPs. In practice, potentially this could be selected based upon analysis of the normal distribution and points that are above a statistical threshold, similar to the phase classification approach.

The computational costs of this calculation are relatively small. This is because the rotations only need to be determined once per detector set up. They are saved into computer memory and used in determination of the correct pseudosymmetric orientation.

The algorithm itself has been applied to pseudosymmetric orientations in the chapter. But there are other applications to the algorithm. As a thought experiment, the reduced library could also be used to more efficiently index an HCP material using a cubic library and use the orientation relations to upsample to a reduced number of refinements for the correct symmetry.

All values for the experiment vs simulation correlation coefficients shown in the chapter are uncharacteristically low. The visual examinations of patterns would suggest that values of 0.6 or higher should be expected, and this is potentially a normalisation error. Visual inspection of the patterns confirmed that the solution provided was correct and this was reasonable given the limited data set analysed.

Finally, I developed a prototype stage and direct electron detector system. This was designed to hold a direct detector at a fixed angle to the sample and the chapter highlights preliminary testing of the properties of the stage.

Initially the components of the stage and their overall construction were described. The properties and functionality of each was discussed and improvements to the prototype, through use, mentioned. The stage itself has not changed in functionality, despite small changes made during prototyping. The sample X/Y stage and the detector Z stage all still move in the same way as was initially conceived, however ease of use and issues of pattern drift have been addressed.

An initial estimate of the MTF of the detector was then obtained. This is thought to be a lower limit to the MTF because the wire used in the experiment was not straight. This may cause a discrepancy to the true value, as a straight wire is a key assumption of the method devised by Meyer and Kirkland [118] and used in this thesis. This led to a non-smooth MTF function line being plotted and a falsely low estimate of how well the detector can handle higher frequency information.

Following on from the MTF test, pattern centre analysis was performed using a retraction test and attempted with a shadow casting experiment. The retraction test showed the PCZ behaved as expected, however the shadow casting test was unsuccessful due to difficulty in obtaining a sufficiently well defined elliptical shadow.

Next the optimal electron dose on the detector to obtain a sufficiently high CC, in a reasonable time was calculated. This was done by linear addition and averaging of 19 patterns collected for 0.1 s. Analysis of the CCs, FFTs and line scans of these patterns suggested that 0.4 s is the optimal collection time.

Finally, patterns were taken from a single crystal silicon sample. The patterns were then indexed and successfully reconstructed into a map of the area from which the patterns were taken. This highlights potential of the stage to be used to map larger areas.

16 Conclusions and Future Work

In this thesis, I have presented my development of a new algorithm that can be used to classify diffraction patterns, determine crystal orientations, and disambiguate pseudosymmetry equivalent orientations. This has been combined with development of new EBSD hardware to help improve the quality of patterns obtained. An overview of the contributions of my thesis can be seen in Figure 83.

Figure 83 shows a summary of and relationship between each of these methods.

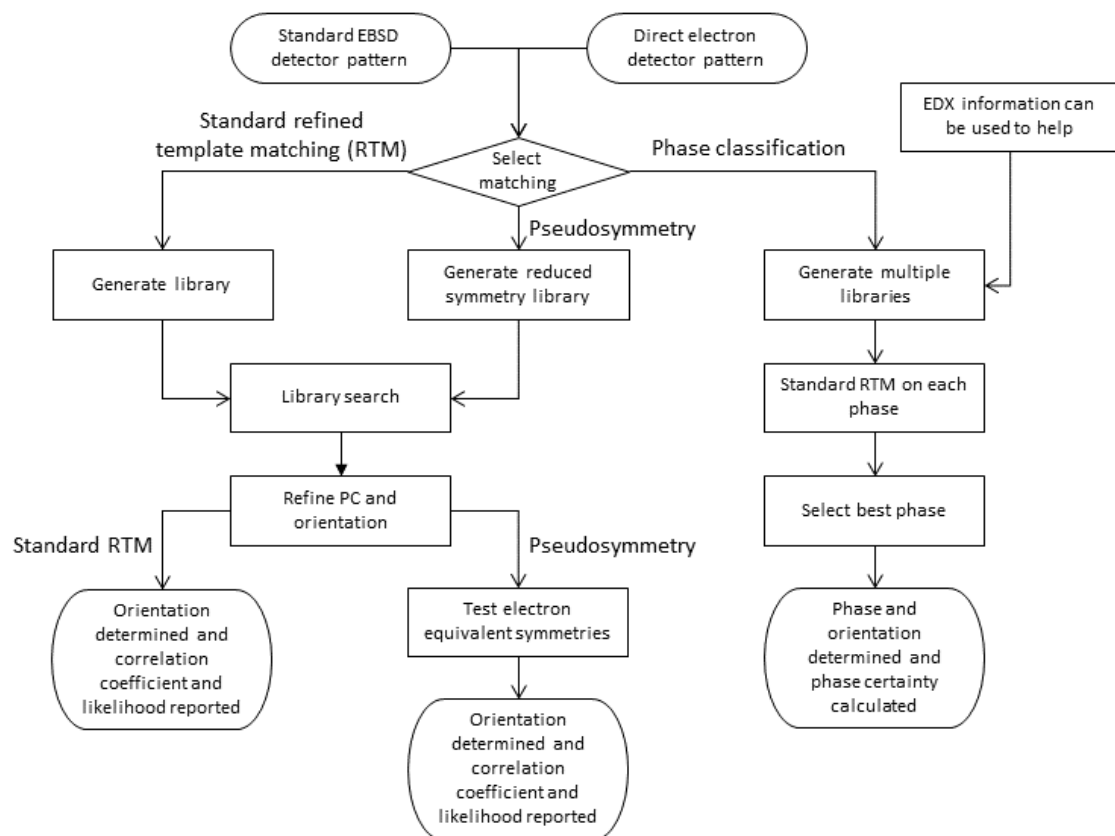


Figure 83: The standard, pseudosymmetry and phase classification branches of the refined template matching approach.

In Chapter 11, I introduced the refined template matching algorithm. This algorithm allows for a FFT-based matching against the fundamental zone of the reference diffraction sphere has significant benefits in terms of reliability in finding a suitable pattern that looks like the

test pattern. The addition of the refinement step allows for an ultimate resolution of c. 0.1° which is unrelated to the spacing of the library ($\sim 7^\circ$). This refinement method has multiple benefits and only a fraction of those have been explored within this thesis. For example, this has the potential to be used to improve the resolution and reliability of Hough-based indexing.

Chapter 12 then applied the algorithm to understand dual phase microstructures and improve reliable classification of the diffraction patterns. A metric to determine how well the phases can be determined from the given libraries was also developed.

In Chapter 13, the algorithm was extended to improve understanding of very similar diffraction patterns, which are often misclassified due to pseudosymmetry. Here a brute force method was used to identify pseudosymmetric equivalents, making the method more widely applicable.

This chapter posed new challenges, as the lower symmetry Al_3Fe crystal was of a low symmetry which is often poorly described in software and in the literature, as the unit cell can be inadvertently rotated. This motivated me clearly establishing conventions between the unit cell, diffracting planes, and the simulated pattern through generation of a full 3D model of the system, and controlled rotations. This was performed all within transparent code within Matlab (and coded using MTEX and AstroEBSD) which should aid future research using these tools.

Finally, I presented preliminary work on a prototype direct electron detector (DED) stage. The DED stage is designed to fit completely inside the chamber of an SEM, keeping the angle between the detector and sample fixed. Design of the stage was performed to optimise the

geometry and provide in built opportunities to calibrate and perform additional experiments beyond 'standard' EBSD data analysis.

I examined a number of patterns, each with a very short exposure time that had been combined to give patterns of a different exposure time to try to determine the optimal exposure time for indexing. This analysis used a combination of pattern, background, intensity histograms, line traces, correlation coefficient and FFT examination to determine the optimal exposure time. It was found this is ~ 0.4 s with the setting used on for Pixet Pro.

Finally, a map of a single crystal silicon was successfully reconstructed using the DED stage and indexing described in this work.

The work in this thesis is used for highly specialised applications of EBSD, in which unit cells of low symmetry, or of very similar phase need to be analysed. For conventional grain boundary detection and orientation analysis, the Hough based method is superior. The Hough based method has a similar accuracy (for highly symmetric unit cells) to the method described here but is significantly faster and as such can be used for real time indexing as the map is collected.

The algorithm introduced in this work represents a significant speed up to the dictionary indexing method. However, there are certain instances in which the dictionary indexing method will outperform the work presented here. Namely, if the PC is offscreen the DI will outperform the refined method. This is due to the refinement step requiring the PC be on screen. This could be a particular problem for off-axis TKD.

The code itself is written in MATLAB and relies on the MTEX plugin. It is freely available now as part of the AstroEBSD package. However, MATLAB and MTEX updates may affect the working of the code.

Finally, the reduced library for the pseudosymmetry needs to be of a lower SF than for conventional pattern analysis. This increases the time needed to index a pattern. The indexing is still faster than the dictionary indexing method, as the dictionary indexing would need a monoclinic library with a small SF to index the pattern correctly.

16.1 Future Work

The work presented in this thesis details a new pattern matching algorithm to analysis EBSPs. I also presented a preliminary design for a direct electron detector setup allowing for high fidelity EBSPs and maps to be acquired. As with any thesis, there remains work that could be explored, I detail the main areas I would have liked to have explored here.

16.1.1 The Refined Template Matching

Chapter three detailed the development and testing of the main algorithm used throughout this thesis. I would have liked to have implemented the library search as a MEX file (a C programming language file readable in MATLAB). This would have sped up the library search. I would also have liked to have spent more time optimising the code for speed (more use of the parallel computing tool box and exporting sections to MEX files would be a good start). This has not been implemented due to time constraints, work on the algorithm took ~ 1.5 years to accurately and reliably index an EBSP, and a further six months to get through the peer review process and get published. At this point, applications of the working algorithm became more useful to work on than speed up of a fast enough and accurate enough algorithm.

16.1.2 Phase Characterisation with the RTM

This chapter focused on the application of the previous algorithm to multiphase materials.

Further work I would have liked to have explored was the application to more real datasets showing >3 phases, differing geometries, Bravais lattices and lattice constants. I would have also liked to have had more rigorous simulated experiments, particularly detailing the effect of changing lattice constants and the ratio between them on the pattern matching coefficients.

This work was not completed due to time constraints and COVID-19 restrictions in place at the time of writing and experimenting.

16.1.3 Pseudosymmetry with the RTM

Chapter 5 focused on the introduction and application of an updated indexing algorithm to look at the problem of pseudosymmetry.

Work in this chapter focused on the $\text{Al}_{13}\text{Fe}_4$ unit cell. Due to time constraints on the PhD, I could only look at this unit cell. I would have liked to have explored other crystal symmetries exhibiting pseudosymmetry, both simulated and experimental. I would also have liked to have extended the work in this chapter to include non-centrosymmetric unit cells. COVID – 19 restrictions also meant I was unable to look at another unit cell experimentally.

Had I had more time in my PhD I would have also implemented an error metric similar to that introduced in Chapter 4, to help determine the correct pseudosymmetric orientation. This metric would have essentially worked as an n-phase material, where n is the number of explored pseudosymmetries.

Finally, there is a bug in the pseudosymmetry code that gives consistently low values for the recorded CC for a close to identical match. Fixing this to make the CCs more consistent with

those in previous chapters would be the next thing I fix. Sadly, time restrictions prevented me from doing so.

16.1.4 Direct Electron Detector Stage

The DED stage described in this chapter is preliminary in nature and as such there are a list of improvements and measurements I would like to implement and test.

1. The addition of stage scanning as opposed to beam scanning.
2. Correct PC determination using the shadow casting (Dingley's balls) method.
3. More accurate measurement of the MTF of the detector.
4. Measurement of the DQE of the detector.
5. Mapping and indexing of a multiphase material.
6. An exposure time test with differing exposure time lengths.

The primary reason these were not completed is due to COVID-19 restrictions in place after the initial stage build and testing.

17 References

- [1] A. J. Wilkinson and T. Ben Britton, "Strains, planes, and EBSD in materials science," *Mater. Today*, vol. 15, no. 9, pp. 366–376, 2012, doi: 10.1016/S1369-7021(12)70163-3.
- [2] "Constraints on the Effective Electron Energy Spectrum in Backscatter Kikuchi Diffraction (arxiv)." <https://arxiv.org/pdf/1810.09525.pdf> (accessed Dec. 01, 2020).
- [3] M. A. Frank, "Functionalization of Steels and other Metallic Materials with Hydrophobic Layers - Influence on Wetting and Corrosion Resistance," 2018.
- [4] T. B. Britton, "Introduction to Crystallography and Diffraction," *lecture notes*. 2011.
- [5] T. B. Britton, V. Tong, J. Hickey, A. Foden, and A. Wilkinson, "AstroEBSD: exploring new space in pattern indexing with methods launched from an astronomical approach," Apr. 2018, Accessed: Jun. 14, 2018. [Online]. Available: <http://arxiv.org/abs/1804.02602>.
- [6] A. Day, "Developments in the EBSD techniques and their application to grain imaging," 1993.
- [7] Y. H. Chen *et al.*, "A Dictionary Approach to Electron Backscatter Diffraction Indexing," *Microsc. Microanal.*, vol. 21, no. 03, pp. 739–752, Jun. 2015, doi: 10.1017/S1431927615000756.
- [8] A. Foden, D. M. Collins, A. J. Wilkinson, and T. B. Britton, "Indexing electron backscatter diffraction patterns with a refined template matching approach," *Ultramicroscopy*, vol. 207, p. 112845, Dec. 2019, doi: 10.1016/j.ultramic.2019.112845.

- [9] A. Winkelmann, "Private communication." 2018.
- [10] M. . Alam, M. Blackman, and D. W. Pashley, "High - angle Kikuchi patterns," 1953.
- [11] J. A. Venables and C. J. Harland, "Electron back-scattering patterns—A new technique for obtaining crystallographic information in the scanning electron microscope," *Philos. Mag.*, vol. 27, no. 5, pp. 1193–1200, 1973, doi: 10.1080/14786437308225827.
- [12] J. A. Venables and R. Bin-Jaya, "Accurate microcrystallography using electron back-scattering patterns, The Philosophical Magazine: A," *J. Theor. Exp. Appl. Phys.*, vol. 35, no. 5, pp. 1317–1332, 1977, doi: 10.1080/14786437708232955.
- [13] C. J. Harland, P. Akhter, and J. A. Venables, "Scientific Instruments To cite this article," 1981.
- [14] S. Biggin and D. J. Dingley, "A general method for locating the X-ray source point in Kossel diffraction," *J. Appl. Crystallogr.*, vol. 10, pp. 376–385, 1977, doi: 10.1107/S0021889877013806.
- [15] D. J. Dingley and G. Ferran, "Application of the Kossel X-ray technique for obtaining crystallographic data in the scanning electron microscope," *Micron (1969)*, vol. 8, no. 3, pp. 145–149, 1977, doi: 10.1016/0047-7206(77)90019-X.
- [16] Dingley, "A comparison of diffraction techniques for the SEM," *Scan. Electron Microsc.*, pp. 273–286, 1981.
- [17] DJ Dingley, "Diffraction from sub-micron areas using electron backscattering in a scanning electron microscope," *Scan. Electron Microsc.*, no. 2, pp. 569–575, 1984.
- [18] D. Dingley, "NoDJ Dingley. Title," in *Inst Phys Conf Series*, 1989, pp. 473–476.

- [19] D. J. Dingley, M. Longden, J. Weinbren, and J. Alderma, "On-line analysis of electronbackscatter diffraction patterns, texture analysis of polysilicon," *Scanning Microsc.*, vol. 1, pp. 451–456, 1987.
- [20] D. J. Dingley, A. Day, and Bewick A, "Application of Microtexture Determination using EBSD to Non Cubic Crystals," 1991.
- [21] V. Randle and A. Brown, "Development of grain misorientation texture, in terms of coincident site lattice structures, as a function of thermomechanical treatments," *Philos. Mag. A Phys. Condens. Matter, Struct. Defects Mech. Prop.*, vol. 59, no. 5, pp. 1075–1089, 1989, doi: 10.1080/01418618908209838.
- [22] T. Watanabe, "Grain boundary engineering: Historical perspective and future prospects," *J. Mater. Sci.*, vol. 46, no. 12, pp. 4095–4115, 2011, doi: 10.1007/s10853-011-5393-z.
- [23] D. J. Dingley, C. Alabaster, and R. Coville, "Phase identification using backscatter kikuchi diffraction in the scanning electron-microscope," in *Inst Phys Conf Series*, 1990, pp. 451–454.
- [24] K. Z. Baba-Kishi and D. J. Dingley, "Backscatter Kikuchi diffraction in the SEM for identification of crystallographic point groups," *Scanning*, vol. 11, no. 6, pp. 305–312, 1989, doi: 10.1002/sca.4950110605.
- [25] K. Z. Baba-Kishi and D. J. Dingley, "Application of backscatter Kikuchi diffraction in the scanning electron microscope to the study of NiS₂," *J. Appl. Crystallogr.*, vol. 22, pp. 189–200, 1989.
- [26] D. J. Dingley, K. Z. Baba-Kishi, and V. Randle, "Atlas of Backscattering Kikuchi

- Diffraction Patterns,” 1995.
- [27] D. J. Dingley and S. I. Wright, “Phase Identification Through Symmetry Determination in EBSD patterns,” in *Electron Backscatter Diffraction in Materials Science*, Springer, 2009, pp. 27–109.
 - [28] S. I. Wright and B. L. Adams, “Automatic analysis of electron backscatter diffraction patterns,” *Metall. Trans. A*, vol. 23, no. 3, pp. 759–767, Mar. 1992, doi: 10.1007/BF02675553.
 - [29] D. Juul Jensen, “An automatic on-line technique for determination of crystallographic orientations by EBSD,” *Int. Conf. Recryst. Met. Mater. Proc.*, 1990.
 - [30] K. Lassen, D. J. JENSEN, and K. CONRADSEN, “Image processing procedures for analysis of electron back scattering patterns,” *Scanning Microsc.*, vol. 6, pp. 115–121, 1992.
 - [31] N. C. Krieger Lassen, D. Juul Jensen, and K. Condradsen, “Automatic Recognition of Deformed and Recrystallized Regions in Partly Recrystallized Samples Using Electron Back Scattering Patterns,” *Mater. Sci. Forum*, vol. 157–162, pp. 149–158, 1994, Accessed: Jun. 24, 2020. [Online]. Available: <https://www.scientific.net/MSF.157-162.149>.
 - [32] R. P. Goehner and J. R. Michael, “Phase Identification in a Scanning Electron Microscope Using Backscattered Electron Kikuchi Patterns.”
 - [33] A. J. Wilkinson, G. Meaden, and D. J. Dingley, “Materials Science and Technology High resolution mapping of strains and rotations using electron backscatter diffraction
High resolution mapping of strains and rotations using electron backscatter

- diffraction," *Mater. Sci. Technol.*, vol. 22, no. 11, pp. 1271–1278, 2006, doi: 10.1179/174328406X130966.
- [34] Y. H. Chen *et al.*, "A Dictionary Approach to Electron Backscatter Diffraction Indexing," *Microsc. Microanal.*, vol. 21, no. 03, pp. 739–752, Jun. 2015, doi: 10.1017/S1431927615000756.
- [35] A. J. Wilkinson, G. Moldovan, T. B. Britton, A. Bewick, R. Clough, and A. I. Kirkland, "Direct Detection of Electron Backscatter Diffraction Patterns," doi: 10.1103/PhysRevLett.111.065506.
- [36] F. Ram and M. De Graef, "Phase differentiation by electron backscatter diffraction using the dictionary indexing approach," *Acta Mater.*, vol. 144, pp. 352–364, Feb. 2018, doi: 10.1016/j.actamat.2017.10.069.
- [37] T. B. Britton *et al.*, "Tutorial: Crystal orientations and EBSD - Or which way is up?," *Mater. Charact.*, vol. 117, pp. 113–126, 2016, doi: 10.1016/j.matchar.2016.04.008.
- [38] A. J. Schwartz, M. Kumar, B. L. Adams, and D. P. Field, "Electron backscatter diffraction in materials science," in *Electron Backscatter Diffraction in Materials Science*, 2009, pp. 21–33.
- [39] S. Singh, "Application of Forward Modeling to Materials Characterization," Carnegie Mellon University, 2017.
- [40] T. B. Britton *et al.*, "Factors affecting the accuracy of high resolution electron backscatter diffraction when using simulated patterns," *Ultramicroscopy*, vol. 110, no. 12, pp. 1443–1453, 2010, doi: 10.1016/j.ultramic.2010.08.001.
- [41] V. Randle and O. Englar, *Introduction to Texture Analysis: Macrotexture, Microtexture,*

and Orientation Mapping, 2nd ed. CRC press, 2000.

- [42] J. A. Venables and R. Bin-jaya, "Accurate microcrystallography using electron back-scattering patterns," *Philos. Mag.*, vol. 35, no. 5, pp. 1317–1332, 1977, doi: 10.1080/14786437708232955.
- [43] "Analysis of a conic." <https://solitaryroad.com/c433.html> (accessed May 13, 2020).
- [44] J. Hjelen *et al.*, "EBSP, PROGRESS IN TECHNIQUE AND APPLICATIONS Royal Norwegian Air Force Academy, N-7004 Trondheim mil, Norway," 1993.
- [45] D. A. CARPENTER, J. L. PUGH, G. D. RICHARDSON, and L. R. MOONEY, "Determination of pattern centre in EBSD using the moving-screen technique," *J. Microsc.*, vol. 227, no. 3, pp. 246–247, Sep. 2007, doi: 10.1111/j.1365-2818.2007.01807.x.
- [46] C. Maurice, K. Dzieciol, and R. Fortunier, "A method for accurate localisation of EBSD pattern centres," *Ultramicroscopy*, vol. 111, no. 2, pp. 140–148, 2011, doi: 10.1016/j.ultramic.2010.10.007.
- [47] KRIEGER LASSEN, "Source point calibration from an arbitrary electron backscattering pattern," *J. Microsc.*, vol. 195, no. 3, pp. 204–211, Sep. 1999, doi: 10.1046/j.1365-2818.1999.00581.x.
- [48] N. C. K. LASSEN and J. B. BILDE-SØRENSEN, "Calibration of an electron back-scattering pattern set-up," *J. Microsc.*, vol. 170, no. 2, pp. 125–129, May 1993, doi: 10.1111/j.1365-2818.1993.tb03331.x.
- [49] S. Singh and M. De Graef, "Orientation Sampling for Dictionary-Based Diffraction Pattern Indexing Methods," *Model. Simul. Mater. Sci. Eng.*, no. 412, pp. 1–22, 2016, doi: 10.1088/0965-0393/24/8/085013.

- [50] R. Hielscher, F. Bartel, and T. Ben Britton, “Gazing at Crystal Balls Æ Electron Backscatter Diffraction Indexing and Cross Correlation on a Sphere,” *J. Appl. Crystallogr.*, vol. 409, no. 2, p. 2019, 2019, doi: 10.1017/S143192761901050X.
- [51] P. G. Callahan and M. De Graef, “Dynamical electron backscatter diffraction patterns. Part I: Pattern simulations,” *Microsc. Microanal.*, vol. 19, no. 5, pp. 1255–1265, Oct. 2013, doi: 10.1017/S1431927613001840.
- [52] H. S. M. Coxeter, *Introduction to Geometry*. John Wiley & Sons, 1961.
- [53] A. Winkelmann, “Dynamical Simulation of Electron Backscatter Diffraction Patterns,” in *Electron Backscatter Diffraction in Materials Science*, Boston, MA: Springer US, 2009, pp. 21–33.
- [54] B. K. (Brian K. Tanner, *Introduction to the physics of electrons in solids*. Cambridge University Press, 1995.
- [55] “No.” https://commons.wikimedia.org/wiki/File:Bragg_diffraction.svg (accessed May 01, 2020).
- [56] A. Winkelmann, T. Ben Britton, and G. Nolze, “Constraints on the effective electron energy spectrum in backscatter Kikuchi diffraction,” *Phys. Rev. B*, vol. 99, p. 64115, 2019, doi: 10.1103/PhysRevB.99.064115.
- [57] C. J. Humphreys, “The scattering of fast electrons by crystals,” *Reports Prog. Phys.*, vol. 42, no. 11, pp. 1825–1887, 1979, doi: 10.1088/0034-4885/42/11/002.
- [58] J. C. H. Spence and J. M. Zuo, *Electron Microdiffraction*. Springer Science, 1992.
- [59] S. L. Dudarev, L.-M. Peng, and M. J. Whelan, “Correlations in space and time and

- dynamical diffraction of high-energy electrons by crystals.”
- [60] H. Bethe, “Theorie der Beugung von Elektronen an Kristallen,” *Ann. Phys.*, vol. 392, no. 17, pp. 55–129, 1928, doi: 10.1002/andp.19283921704.
 - [61] A. Winkelmann, G. Nolze, M. Vos, F. Salvat-Pujol, and W. S. M. Werner, “Physics-based simulation models for EBSD: advances and challenges,” *IOP Conf. Ser. Mater. Sci. Eng.*, vol. 109, no. 1, p. 012018, Feb. 2016, doi: 10.1088/1757-899X/109/1/012018.
 - [62] J. M. Zuo and A. L. Weickenmeier, “On the beam selection and convergence in the method,” *Ultramicroscopy*, vol. 57, p. 375*383, 1995.
 - [63] L. J. Allen and C. J. Rossouw, “Effects of thermal diffuse scattering and surface tilt on diffraction and channeling of fast electrons in CdTe.”
 - [64] C. J. Rossouw, P. R. Miller, T. W. Josefsson, and L. J. Allen, “Zone-axis back-scattered electron contrast for fast electrons,” *Philos. Mag.*, vol. 70, no. 6, pp. 985–998, 1994, doi: 10.1080/01418619408242944.
 - [65] A. Winkelmann, “Dynamical effects of anisotropic inelastic scattering in electron backscatter diffraction,” *Ultramicroscopy*, vol. 108, no. 12, pp. 1546–1550, 2008, doi: 10.1016/j.ultramic.2008.05.002.
 - [66] A. Winkelmann, C. Trager-Cowan, F. Sweeney, A. P. Day, and P. Parbrook, “Many-beam dynamical simulation of electron backscatter diffraction patterns,” *Ultramicroscopy*, vol. 107, no. 4, pp. 414–421, 2007, doi: 10.1016/j.ultramic.2006.10.006.
 - [67] A. WINKELMANN, “Principles of depth-resolved Kikuchi pattern simulation for

- electron backscatter diffraction," *J. Microsc.*, vol. 239, no. 1, pp. 32–45, Jul. 2010, doi: 10.1111/j.1365-2818.2009.03353.x.
- [68] RADON and J., "On the Determination of Functions from their Integrals along Certain Manifolds," *Ber. Verh, Sachs Akad Wiss.*, vol. 69, pp. 262–277, 1917.
- [69] P. Aundal, "General rights The Radon Transform-Theory and Implementation."
- [70] P. Hough, "METHOD AND MEANS FOR RECOGNIZING COMPLEX PATTERNS," Mar. 1962.
- [71] N. Christian and K. Lassen, "Automated Determination of Crystal Orientations from Electron Backscattering Patterns," 1994, Accessed: May 30, 2018. [Online]. Available: http://www.ebsd.info/pdf/PhD_KriegerLassen.pdf.
- [72] V. Tong, J. Jiang, A. J. Wilkinson, and T. Ben Britton, "The effect of pattern overlap on the accuracy of high resolution electron backscatter diffraction measurements," *Ultramicroscopy*, vol. 155, 2015, doi: 10.1016/j.ultramic.2015.04.019.
- [73] C. Tu, "Enhanced Hough transforms for image processing," Université Paris, 2014.
- [74] A. Winkelmann, "Personal Communication." .
- [75] a. J. Wilkinson, G. Meaden, and D. J. Dingley, "High resolution mapping of strains and rotations using electron backscatter diffraction," *Mater. Sci. Technol.*, vol. 22, no. 11, pp. 1271–1278, 2006, doi: 10.1179/174328406X130966.
- [76] T. B. Britton and A. J. Wilkinson, "High resolution electron backscatter diffraction measurements of elastic strain variations in the presence of larger lattice rotations," *Ultramicroscopy*, vol. 114, pp. 82–95, 2012, doi: 10.1016/j.ultramic.2012.01.004.

- [77] A. P. DAY, "Spherical EBSD," *J. Microsc.*, vol. 230, no. 3, pp. 472–486, Jun. 2008, doi: 10.1111/j.1365-2818.2008.02011.x.
- [78] W. C. Lenthe, L. Germain, M. R. Chini, N. Gey, and M. De Graef, "Spherical indexing of overlap EBSD patterns for orientation-related phases – Application to titanium," *Acta Mater.*, vol. 188, pp. 579–590, Apr. 2020, doi: 10.1016/j.actamat.2020.02.025.
- [79] C. Hammond, *The Basics of Crystallography and Diffraction*, 4th ed. Oxford University Press, 2015.
- [80] S. A. Nelson, "External Symmetry of Crystals, 32 Crystal Classes."
<https://www.tulane.edu/~sanelson/eens211/32crystalclass.htm> (accessed May 01, 2020).
- [81] M. De Graef, "Rotations, rotations, and more rotations ... AN OVERVIEW OF ROTATION REPRESENTATIONS AND THE RELATIONS BETWEEN THEM."
- [82] D. Rowenhorst *et al.*, "Tutorial: Consistent Representations of and Conversions Between 3D Rotations."
- [83] V. S. Tong, "EBSD Characterisation of Heterogeneous Microstructures in Zirconium Alloys," Imperial College London, 2016.
- [84] "(No Title)." http://pirate.shu.edu/~wachsmut/Teaching/MATH3626/2015-03/01-rot_matrix_theory.pdf (accessed May 06, 2020).
- [85] A. . Sutton and R. W. Balluffi, *Interfaces in Crystalline Materials*. Clarendon Press, 1995.
- [86] P. Neumann, "REPRESENTATION OF ORIENTATIONS OF SYMMETRICAL OBJECTS BY

- RODRIGUES VECTORS,” 1991.
- [87] J. H. Cho, A. D. Rollett, and K. H. Oh, “Determination of a mean orientation in electron backscatter diffraction measurements,” *Metall. Mater. Trans. A Phys. Metall. Mater. Sci.*, vol. 36, no. 12, pp. 3427–3438, 2005, doi: 10.1007/s11661-005-0016-4.
 - [88] E. B. Dam, M. Koch, and M. Lillholm, “Quaternions, Interpolation and Animation,” 1998.
 - [89] K. Marquardt, M. De Graef, S. Singh, H. Marquardt, A. Rosenthal, and S. Koizumi, “Quantitative electron backscatter diffraction (EBSD) data analyses using the dictionary indexing (DI) approach: Overcoming indexing difficulties on geological materials,” doi: 10.2138/am-2017-6062.
 - [90] A. Winkelmann, G. Cios, T. Tokarski, G. Nolze, and R. Hielscher, “EBSD orientation analysis based on experimental Kikuchi reference patterns,” *Acta Mater.*, vol. 188, pp. 367–385, 2020.
 - [91] T. Tanaka and A. J. Wilkinson, “High Angular Resolution Electron Backscatter Diffraction Studies of Tetragonality in Fe-C Martensitic Steels,” *Microsc. Microanal.*, vol. 24, no. 1, 2018, doi: 10.1017/S1431927618005305.
 - [92] F. CE and N. DE, “Artifacts in energy dispersive x-ray spectrometry in the scanning electron microscope (II),” *Scan Electron Microsc.*, p. 251*258, 1980.
 - [93] W. M. Edwards, “Microstructural and Mechanical Property Modelling for the Processing of Al-Si Alloys,” LoughBourgh, 2002.
 - [94] A. Keshavarzi, W. Wisniewski, and C. Rü, “EBSD and EDX Analyses of a Multiphase Glass-Ceramic Obtained by Crystallizing an Yttrium Aluminosilicate Glass,” 2013, doi:

- 10.1021/am401953j.
- [95] T. G. Woodcock and G. O., "Multi-phase EBSD mapping and local texture analysis in NdFeB sintered magnets," *Acta Mater.*, vol. 59, no. 1026–1036, 2011.
 - [96] C. L. Chen and R. C. Thomson, "The combined use of EBSD and EDX analyses for the identification of complex intermetallic phases in multicomponent Al–Si piston alloys," *J. Alloy. Compunds*, vol. 490, pp. 293–300, 2010.
 - [97] J. Bandy, Q. Zhang, and G. Cao, "Electrophoretic Deposition of Titanium Oxide Nanoparticle Films for Dye-Sensitized Solar Cell Applications," *Mater. Sci. Appl.*, vol. 2, pp. 1427–1431, 2011, doi: 10.4236/msa.2011.210193.
 - [98] T. P. McAuliffe, A. Foden, C. Bilsland, D. Daskalaki Mountanou, D. Dye, and T. B. Britton, "Advancing characterisation with statistics from correlative electron diffraction and X-ray spectroscopy, in the scanning electron microscope," *Ultramicroscopy*, vol. 211, no. January, 2020, doi: 10.1016/j.ultramic.2020.112944.
 - [99] A. J. Wilkinson, D. M. Collins, Y. Zayachuk, R. Korla, and A. Vilalta-Clemente, "Applications of multivariate statistical methods and simulation libraries to analysis of electron backscatter diffraction and transmission Kikuchi diffraction datasets," *Ultramicroscopy*, vol. 196, no. September 2018, pp. 88–98, 2019, doi: 10.1016/j.ultramic.2018.09.011.
 - [100] K. Kaufmann, C. Zhu, A. S. Rosengarten, D. Maryanovsky, H. Wang, and K. S. Vecchio, "Phase Mapping in EBSD Using Convolutional Neural Networks," *Microsc. Microanal.*, pp. 1–11, May 2020, doi: 10.1017/S1431927620001488.
 - [101] A. Foden, A. Previero, and T. B. Britton, "Advances in electron backscatter

- diffraction,” *arXiv*, 2019, doi: 10.5281/zenodo.2609220.
- [102] E. L. Pang, P. M. Larsen, and C. A. Schuh, “Resolving pseudosymmetry in tetragonal ZrO₂ using EBSD with a modified dictionary indexing approach,” 2020. Accessed: May 18, 2020. [Online]. Available: <http://arxiv.org/abs/2003.04476>.
- [103] M. D. Vaudin, “Pseudosymmetry in EBSD Patterns,” 2020, doi: 10.1017/S1431927605500710.
- [104] P. G. Callahan, S. Singh, M. Echlin, J. C. Stinville, T. M. Pollock, and M. De Graef, “Automated Prediction of Pseudo-Symmetry Issues in EBSD,” *566 Microsc. Microanal.*, vol. 24, no. 1, 2018, doi: 10.1017/S143192761800332X.
- [105] M. M. Nowell and S. I. Wright, “Orientation effects on indexing of electron backscatter diffraction patterns,” *Ultramicroscopy*, vol. 103, no. 1, pp. 41–58, 2005, doi: 10.1016/j.ultramic.2004.11.012.
- [106] L. Ryde, “Application of EBSD to analysis of microstructures in commercial steels,” *Mater. Sci. Technol.*, vol. 22, no. 11, pp. 1297–1306, Nov. 2006, doi: 10.1179/174328406X130948.
- [107] K. Mingard, A. Day, C. Maurice, and P. Quested, “Towards high accuracy calibration of electron backscatter diffraction systems,” *Ultramicroscopy*, vol. 111, no. 5, pp. 320–329, 2011, doi: 10.1016/j.ultramic.2011.01.012.
- [108] I. Brough and F. J. Humphreys, “Materials Science and Technology Evaluation and application of a fast EBSD detector Evaluation and application of a fast EBSD detector,” 2013, doi: 10.1179/026708309X12468927349415.
- [109] J. Goulden, P. Trimby, and A. Bewick, “The Benefits and Applications of a CMOS-based

- EBS Detector,” *Microsc. Microanal.*, vol. 24, no. 1, 2018, doi: 10.1017/S1431927618006128.
- [110] “What are CCD or CMOS image sensors in a digital camera? | HowStuffWorks.”
<https://electronics.howstuffworks.com/cameras-photography/digital/question362.htm> (accessed May 19, 2020).
- [111] Meyer, “2) United States Patent45) Date of Patent: (54) (75) (73) (*) (21) (22) (65) (63,” 2011.
- [112] “MerlinEM - Quantum Detectors Ltd.”
<https://quantumdetectors.com/n/products/merlinem/> (accessed May 19, 2020).
- [113] X. Llopart, R. Ballabriga, M. Campbell, L. Tlustos, and W. Wong, “Timepix, a 65k programmable pixel readout chip for arrival time, energy and/or photon counting measurements,” *Nucl. Instruments Methods Phys. Res. Sect. A Accel. Spectrometers, Detect. Assoc. Equip.*, vol. 581, no. 1-2 SPEC. ISS., pp. 485–494, 2007, doi: 10.1016/j.nima.2007.08.079.
- [114] “Compton camera based on Timepix3 technology Recent citations,” doi: 10.1088/1748-0221/13/11/C11022.
- [115] S. Vespucci *et al.*, “Digital direct electron imaging of energy-filtered electron backscatter diffraction patterns,” *Phys. Rev. B*, vol. 92, p. 205301, 2015, doi: 10.1103/PhysRevB.92.205301.
- [116] R. S. Ruskin, Z. Yu, and N. Grigorieff, “Quantitative characterization of electron detectors for transmission electron microscopy,” *J. Struct. Biol.*, vol. 184, no. 3, pp. 385–393, 2013, doi: 10.1016/j.jsb.2013.10.016.

- [117] T. B. Britton, J. Jiang, R. Clough, E. Tarleton, A. I. Kirkland, and A. J. Wilkinson, "Assessing the precision of strain measurements using electron backscatter diffraction - part 1: Detector assessment," *Ultramicroscopy*, vol. 135, pp. 126–135, 2013, doi: 10.1016/j.ultramic.2013.08.005.
- [118] R. R. Meyer and A. I. Kirkland, "Characterisation of the signal and noise transfer of CCD cameras for electron detection," *Microsc. Res. Tech.*, vol. 49, no. 3, pp. 269–280, May 2000, doi: 10.1002/(SICI)1097-0029(20000501)49:3<269::AID-JEMT5>3.0.CO;2-B.
- [119] K.-H. Herrmann and D. Krahel, "The detection quantum efficiency of electronic image recording systems," *J. Microsc.*, vol. 127, no. 1, pp. 17–28, Jul. 1982, doi: 10.1111/j.1365-2818.1982.tb00393.x.
- [120] G. McMullan, A. R. Faruqi, D. Clare, and R. Henderson, "Comparison of optimal performance at 300keV of three direct electron detectors for use in low dose electron microscopy," *Ultramicroscopy*, vol. 147, pp. 156–163, 2014, doi: 10.1016/j.ultramic.2014.08.002.
- [121] G. McMullan, S. Chen, R. Henderson, and A. R. Faruqi, "Detective quantum efficiency of electron area detectors in electron microscopy," *Ultramicroscopy*, vol. 109, no. 9, pp. 1126–1143, 2009, doi: 10.1016/j.ultramic.2009.04.002.
- [122] G. McMullan *et al.*, "Experimental observation of the improvement in MTF from backthinning a CMOS direct electron detector," *Ultramicroscopy*, vol. 109, no. 9, pp. 1144–1147, 2009, doi: 10.1016/j.ultramic.2009.05.005.
- [123] J. A. Mir *et al.*, "Characterisation of the Medipix3 detector for 60 and 80 keV electrons," *Ultramicroscopy*, vol. 182, pp. 44–53, 2017, doi:

- 10.1016/j.ultramic.2017.06.010.
- [124] L. G. Brown, "A survey of image registration techniques," *ACM Comput. Surv.*, vol. 24, no. 4, pp. 325–376, 1992, doi: 10.1145/146370.146374.
- [125] R. Hielscher, H. Schaeben, and IUCr, "A novel pole figure inversion method: specification of the *MTEX* algorithm," *J. Appl. Crystallogr.*, vol. 41, no. 6, pp. 1024–1037, Dec. 2008, doi: 10.1107/S0021889808030112.
- [126] B. E. Jackson *et al.*, "Performance of Dynamically Simulated Reference Patterns for Cross-Correlation Electron Backscatter Diffraction," *Microsc. Microanal.*, pp. 1–14, 2016, doi: 10.1017/S143192761601148X.
- [127] A. Winkelmann, G. Nolze, M. Vos, F. Salvat-Pujol, and W. S. M. Werner, "Physics-based simulation models for EBSD: Advances and challenges," 2016, doi: 10.1088/1757-899X/109/1/012018.
- [128] T. Ben Britton, S. Biroscas, M. Preuss, and A. J. Wilkinson, "Electron backscatter diffraction study of dislocation content of a macrozone in hot-rolled Ti-6Al-4V alloy," *Scr. Mater.*, vol. 62, no. 9, pp. 639–642, 2010, doi: 10.1016/j.scriptamat.2010.01.010.
- [129] T. B. Britton and A. J. Wilkinson, "High resolution electron backscatter diffraction measurements of elastic strain variations in the presence of larger lattice rotations," *Ultramicroscopy*, vol. 114, pp. 82–95, Mar. 2012, doi: 10.1016/J.ULTRAMIC.2012.01.004.
- [130] M. Guizar-Sicairos, S. T. Thurman, and J. R. Fienup, "Efficient subpixel image registration algorithms," *Opt. Lett.*, vol. 33, no. 2, pp. 156–158, 2008, doi: 10.1364/OL.33.000156.

- [131] F. Ram, S. Wright, S. Singh, and M. De Graef, "Error analysis of the crystal orientations obtained by the dictionary approach to EBSD indexing," *Ultramicroscopy*, 2017, doi: 10.1016/j.ultramic.2017.04.016.
- [132] S. Teramoto, T. Asano, N. Katoh, and B. Doerr, "Inserting points uniformly at every instance," *IEICE Trans. Inf. Syst.*, 2006, doi: 10.1093/ietisy/e89-d.8.2348.
- [133] D. Hardin and E. Saff, "Discretizing Manifolds via Minimum Energy Points," *Not. AMS*, 2004.
- [134] H. Niederreiter, *Random Number Generation and Quasi-Monte-Carlo Methods*. Society for Industrial and Applied Mathematics, 1992.
- [135] G. Wolberg and S. Zokai, "Robust image registration using log-polar transform," in *Proceedings 2000 International Conference on Image Processing (Cat. No.00CH37101)*, vol. 1, pp. 493–496, doi: 10.1109/ICIP.2000.901003.
- [136] A. Hast and A. Marchetti, "Rotation invariant feature matching-based on Gaussian filtered log polar transform and phase correlation," in *2013 8th International Symposium on Image and Signal Processing and Analysis (ISPA)*, Sep. 2013, pp. 107–112, doi: 10.1109/ISPA.2013.6703723.
- [137] T. B. Britton *et al.*, "Factors affecting the accuracy of high resolution electron backscatter diffraction when using simulated patterns," *Ultramicroscopy*, vol. 110, no. 12, pp. 1443–1453, 2010, doi: 10.1016/j.ultramic.2010.08.001.
- [138] F. J. Humphreys, Y. Huang, I. Brough, and C. Harris, "Electron backscatter diffraction of grain and subgrain structures - Resolution considerations," *J. Microsc.*, vol. 195, no. 3, pp. 212–216, 1999, doi: 10.1046/j.1365-2818.1999.00579.x.

- [139] F. Ram, S. Zaefferer, T. Jäpel, and D. Raabe, “Error analysis of the crystal orientations and disorientations obtained by the classical electron backscatter diffraction technique,” *J. Appl. Crystallogr.*, vol. 48, pp. 797–813, 2015, doi: 10.1107/S1600576715005762.
- [140] F. Ram, S. Wright, S. Singh, and M. De Graef, “Error analysis of the crystal orientations obtained by the dictionary approach to EBSD indexing,” *Ultramicroscopy*, vol. 181, 2017, doi: 10.1016/j.ultramic.2017.04.016.
- [141] T. P. McAuliffe, “private communication.” 2021.
- [142] G. Nolze, A. Winkelmann, and A. P. Boyle, “Pattern matching approach to pseudosymmetry problems in electron backscatter diffraction,” *Ultramicroscopy*, vol. 160, pp. 146–154, Jan. 2016, doi: 10.1016/j.ultramic.2015.10.010.
- [143] Yi Cui, “Private communication.” 2020.
- [144] “SLC-1720 - Linear Piezo Stage - SmarAct.” <https://www.smaract.com/linear-stages/product/slc-1720#specifications> (accessed Mar. 12, 2021).
- [145] “SLC-1750 - Linear Piezo Stage - SmarAct.” <https://www.smaract.com/linear-stages/product/slc-1750> (accessed Mar. 12, 2021).
- [146] T. B. Britton, J. Jiang, R. Clough, E. Tarleton, A. I. Kirkland, and A. J. Wilkinson, “Assessing the precision of strain measurements using electron backscatter diffraction - part 1: Detector assessment,” *Ultramicroscopy*, vol. 135, pp. 126–135, Dec. 2013, doi: 10.1016/j.ultramic.2013.08.005.
- [147] G. Nolze, A. Winkelmann, and A. P. Boyle, “Pattern matching approach to pseudosymmetry problems in electron backscatter diffraction,” 2015, doi:

- 10.1016/j.ultramic.2015.10.010.
- [148] G. Nolze, C. Grosse, and A. Winkelmann, “Kikuchi pattern analysis of noncentrosymmetric crystals,” *J. Appl. Cryst.*, vol. 48, pp. 1405–1419, 2015, doi: 10.1107/S1600576715014016.
- [149] T. Ben Britton, D. Goran, and V. S. Tong, “Space rocks and optimising scanning electron channelling contrast,” *Mater. Charact.*, vol. 142, pp. 422–431, Aug. 2018, doi: 10.1016/j.matchar.2018.06.001.
- [150] S. Singh, M. De Graef, and D. R. Rosca, “Related content Orientation sampling for dictionary-based diffraction pattern indexing methods Area-preserving projections from hexagonal and triangular domains to the sphere and applications to electron back-scatter diffraction pattern simulations,” *IOP Publ. Model. Simul. Mater. Sci. Eng. Model. Simul. Mater. Sci. Eng.*, vol. 21, p. 16, 2013, doi: 10.1088/0965-0393/21/5/055021.
- [151] C. Maurice, J. H. Driver, and R. Fortunier, “On solving the orientation gradient dependency of high angular resolution EBSD,” *Ultramicroscopy*, vol. 113, pp. 171–181, 2012, doi: 10.1016/j.ultramic.2011.10.013.
- [152] T. P. McAuliffe, D. Dye, and T. Ben Britton, “Spherical-angular dark field imaging and sensitive microstructural phase clustering with unsupervised machine learning,” *Ultramicroscopy*, vol. 219, May 2020, doi: 10.1016/j.ultramic.2020.113132.

18 Appendix 1

To convert between the stereographic (master pattern) frame, and the gnomonic (pattern) frame. For this derivation, a slightly altered representation of the stereographic plane is needed. In this, a line is drawn from the origin to the point on the unit sphere for which the stereographic point needs to be known. The line then continues down the south pole, see Figure 84. The location of the point on the screen also needs to be known with respect to pattern centre (PC) if a pattern is to be generated. The geometry of the PC needed is also shown in Figure 84. In an EBSD experiment the sample is placed on the origin, with the z direction pointing towards the detector.

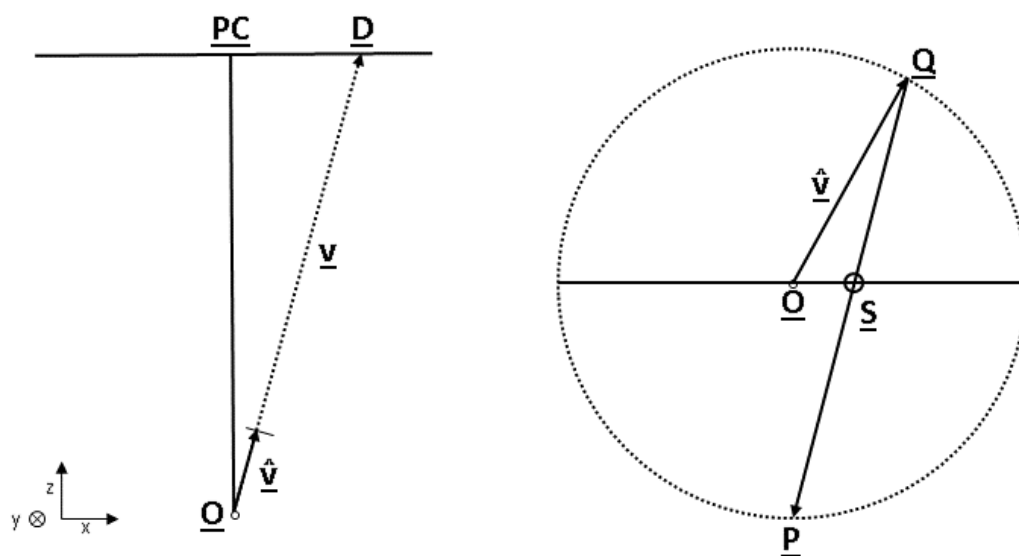


Figure 84: The point \underline{D} , which is a point on the pattern, with respect to the PC and the unit sphere. Important points and vectors are labelled.

Next some definitions are needed:

The pattern centre:

$$\underline{PC} = (x^*, y^*, z^*)$$

The point on the gnomonic plane:

$$\underline{D} = (D_x, D_y, z^*)$$

The origin:

$$\underline{O} = (0,0,0)$$

The vector connecting the origin to point \underline{D} :

$$\underline{v} = (D_x - x^*, D_y - y^*, z^*) = (v_x, v_y, v_z)$$

The magnitude of the vector, \underline{v} :

$$|\underline{v}| = \sqrt{v_x^2 + v_y^2 + v_z^2}$$

The unit vector that lies along vector, \underline{v} :

$$\underline{\hat{v}} = \frac{\underline{v}}{|\underline{v}|} = \left(\frac{v_x}{|\underline{v}|}, \frac{v_y}{|\underline{v}|}, \frac{v_z}{|\underline{v}|} \right) = (\hat{v}_x, \hat{v}_y, \hat{v}_z)$$

The point \underline{Q} is the point at which the unit vector $\underline{\hat{v}}$ meets the unit circle and thus shares the coordinates $(\hat{v}_x, \hat{v}_y, \hat{v}_z)$.

The south pole:

$$\underline{P} = (0,0,-1)$$

And finally the stereographic point be determined, \underline{S} .

To determine \underline{S} , take the line \overrightarrow{QP} and work out the value of the line for $z = 0$.

$$\underline{\overrightarrow{QP}} = \underline{P} - \underline{Q} = \begin{pmatrix} 0 \\ 0 \\ -1 \end{pmatrix} - \begin{pmatrix} \widehat{v}_x \\ \widehat{v}_y \\ \widehat{v}_z \end{pmatrix} = \begin{pmatrix} -\widehat{v}_x \\ -\widehat{v}_y \\ -1 - \widehat{v}_z \end{pmatrix}$$

To work out where the line crosses the z plane, set the starting point to be the south pole and define a scale factor, λ such that

$$\underline{S} = \begin{pmatrix} S_x \\ S_y \\ S_z \end{pmatrix} = \begin{pmatrix} 0 \\ 0 \\ -1 \end{pmatrix} + \lambda \begin{pmatrix} -\widehat{v}_x \\ -\widehat{v}_y \\ -1 - \widehat{v}_z \end{pmatrix}$$

As we are trying to determine the point at which the line passes the z plane, $S_z = 0$. This can be used to determine λ by taking the z values for each vector.

$$S_z = 0 = -1 + \lambda(-1 - \widehat{v}_z)$$

Rearranging gives

$$\lambda = \frac{-1}{1 + \widehat{v}_z}$$

Substituting this value for λ back into the equation for \underline{S} gives

$$\underline{S} = \begin{pmatrix} 0 \\ 0 \\ -1 \end{pmatrix} + \begin{pmatrix} \widehat{v}_x / (1 + \widehat{v}_z) \\ \widehat{v}_y / (1 + \widehat{v}_z) \\ 1 \end{pmatrix}$$

Collecting terms gives:

$$\underline{S} = (\frac{\widehat{v}_x}{1 + \widehat{v}_z}, \frac{\widehat{v}_y}{1 + \widehat{v}_z}, 0)$$

To generate a simulated EBSP from a stereogram you first need to simulate an EBSD experiment and save the diffraction hemisphere as a stereogram. This is essentially now a map of intensities. Select the point of the pattern in the gnomonic plane you wish to know

the intensity of. This gives you the point \underline{D} . The PC is set by you and using the definitions of the vectors, $\hat{\underline{v}}$ can be calculated and from that so can the point \underline{S} . The intensity at point \underline{S} is known and propagates through to point \underline{D}